QSM-CI: An automated continuous QSM challenge

Ashley Wilton Stewart[1], Thuy Thanh Dao[1], Korbinian Eckstein[1], Steffen Bollmann[1,2]

[1]School of Electrical Engineering and Computer Science, The University of Queensland, Brisbane, Australia;
[2]Queensland Digital Health Centre, The University of Queensland, Brisbane, Australia.

Summary: QSM-CI is an online QSM challenge that allows for continuous evaluations using current and future datasets, algorithms, and metrics. This ensures the continued accessibility and relevance of the challenge as new metrics, test data, and reusable algorithms are contributed.

Introduction: Quantitative susceptibility mapping (QSM) involves a complex post-processing pipeline that includes an ill-posed inverse problem. This makes QSM evaluation challenging, with the first QSM challenge[1] using a COSMOS[2] acquisition as the ground truth and the second[3] using a realistic in-silico head phantom[4]. Public challenges like these are great opportunities to involve the QSM community and report on the current landscape of QSM algorithms under a common evaluation framework. However, running these challenges is a lot of effort and there is an opportunity to build an open-source platform for continuous QSM evaluation that is maintained by the community and is always available to submit algorithms, metrics or updated test data and remain relevant into the future. The availability of benchmarked algorithms would also mean that algorithms are straightforward to reuse in future investigations. This work presents a continuous QSM challenge platform called QSM-CI, implemented using GitHub and Back4app, and automated using GitHub Actions. Users can submit algorithms to automatically evaluate against a range of simulated datasets using quantitative metrics and a qualitative Elo rating system.

Methods: The QSM-CI GitHub project includes instructions on how to generate and download test datasets, run QSM algorithms and compute metrics. **The datasets** include simulations for gradient-echo (GRE) magnitude and phase images and other necessary data required for QSM reconstruction, formatted using the Brain Imaging Data Structure[5] (BIDS). These simulations include a susceptibility phantom consisting of cylinders with constant susceptibility values, data derived from a realistic in-silico head phantom[4], and COSMOS acquisitions[6]. **The algorithms** include user-submitted instructions to execute QSM reconstruction pipelines against the BIDS dataset. The current submissions include algorithms available in QSMxT[7]. **The metrics** include the quantitative metrics from the second QSM challenge, including RMSE, NRMSE, HFEN, XSIM[8], MAD, CC and GXE, as well as a qualitative Elo metric. After a user submits or updates one of their algorithms via a pull request, a GitHub Action will automatically run their pipeline against the datasets and evaluate it using quantitative metrics, publishing the metrics to a Parse backend hosted on Back4app. **Qualitative metrics** remain blank until the community contributes to the anonymized evaluation of the final images in a frontend web interface using Niivue for visualization (see **Figure 1**).
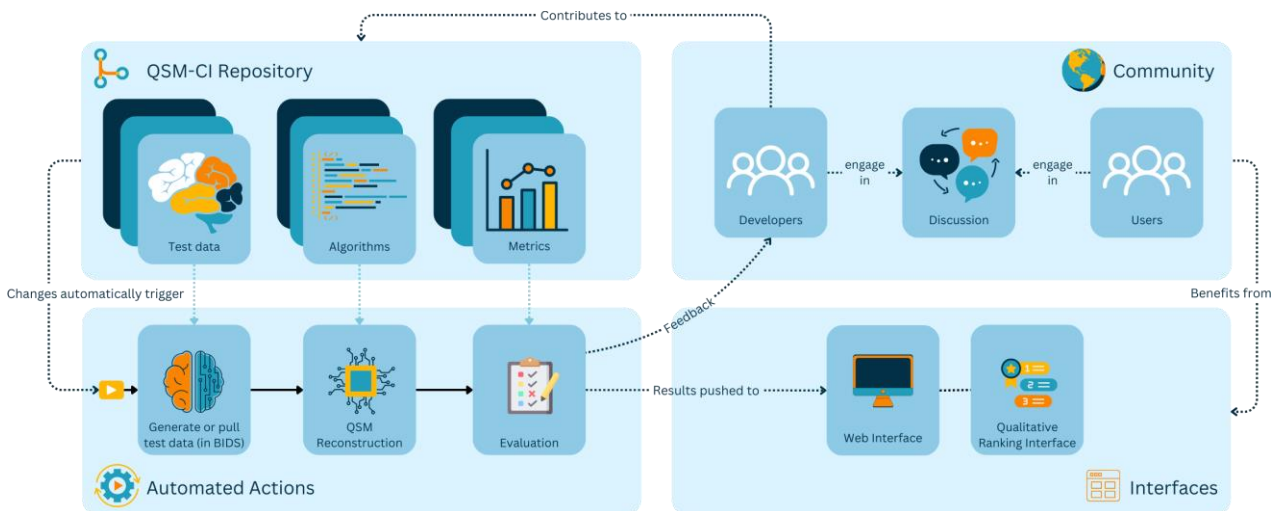

Figure 1: QSM-CI overview. The community of developers maintains the QSM-CI repository. Pushing new algorithms and other updates triggers an automated evaluation. Evaluation results are published to a web interface to benefit QSM users.

Results: Multiple algorithms have been submitted to QSM-CI with metrics automatically computed and published (see **Table 1**). QSM reconstructions can be browsed interactively using the online Niivue-powered viewer, and anonymized qualitative evaluations can be given by users (see **Figure 2**).

Algorithm	RMSE	NRMSE	HFEN	MAD	XSIM	CC	NMI	GXE	ELO
romeo_pdf_tv	0.025	79.923	1.000	0.018	0.204	0.603	1.062	0.656	0.000
romeo_pdf_rts	0.026	82.596	1.000	0.019	0.204	0.566	1.073	0.656	29.872
laplacian_pdf_rts	0.027	83.657	1.000	0.019	0.203	0.549	1.053	0.656	83.150
romeo_vsharp_rts	0.039	45.746	0.267	0.023	0.262	0.917	1.094	0.005	70.450
laplacian_nextqsm	0.040	126.832	1.000	0.031	0.164	0.510	1.039	0.656	-43.336
tgv	0.056	66.210	0.347	0.026	0.308	0.774	1.092	0.007	106.326
laplacian_vsharp_rts	0.091	286.647	1.000	0.072	0.131	0.364	1.023	0.656	-176.467
romeo_nextqsm	0.097	113.662	1.545	0.052	0.189	0.705	1.086	0.027	-13.093

Table 1: Representative QSM results published on QSM-CI based on the currently submitted algorithms.
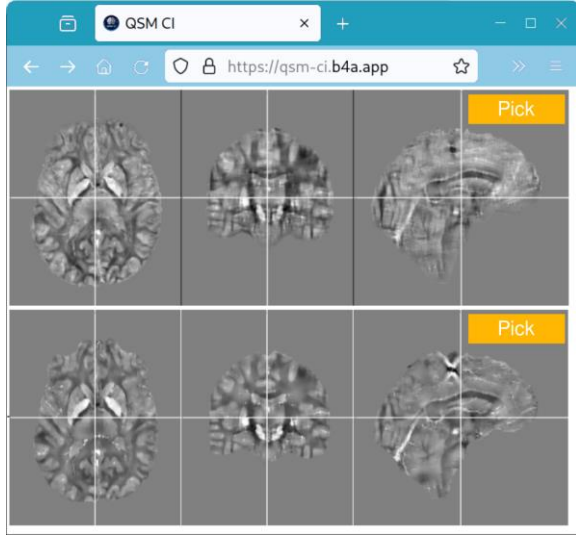
Figure 2: QSM-CI Anonymized qualitative evaluation page. Users select the reconstruction with better perceived image quality.

Discussion and Conclusions: A platform for automatically evaluating QSM algorithms was developed and implemented using GitHub. A frontend interface was developed to display the computed metrics for each algorithm against the test datasets, along with an interactive frontend that uses Niivue to allow users to rate image quality and determine a qualitative Elo ranking. The QSM-CI project provides a proof-of-concept for an always-online QSM challenge platform to streamline the evaluation of QSM algorithms. Published algorithms are straightforward to reuse in investigations using BIDS-structured data. QSM-CI is published at https://github.com/QSMxT/QSM-CI.

References:
[1] T. Liu, P. Spincemaille, L. de Rochefort, B. Kressler, and Y. Wang, "Calculation of susceptibility through multiple orientation sampling (COSMOS): A method for conditioning the inverse problem from measured magnetic field map to susceptibility source image in MRI," Magnetic Resonance in Medicine, vol. 61, no. 1, pp. 196–204, 2009, doi: 10.1002/mrm.21828.
[2] J. P. Marques et al., "QSM reconstruction challenge 2.0: A realistic in silico head phantom for MRI data simulation and evaluation of susceptibility mapping procedures," Magnetic Resonance in Medicine, vol. 86, no. 1, pp. 526–542, 2021, doi: 10.1002/mrm.28716.
[3] Q. C. 2 0 O. Committee et al., "QSM reconstruction challenge 2.0: Design and report of results," Magnetic Resonance in Medicine, vol. 86, no. 3, pp. 1241–1255, 2021, doi: 10.1002/mrm.28754.
[4] A. W. Stewart et al., "QSMxT: Robust masking and artifact reduction for quantitative susceptibility mapping," Magnetic Resonance in Medicine, vol. 87, no. 3, pp. 1289–1300, 2022, doi: 10.1002/mrm.29048.
[5] C. Langkammer et al., "Quantitative susceptibility mapping: Report from the 2016 reconstruction challenge," Magnetic Resonance in Medicine, vol. 79, no. 3, pp. 1661–1673, 2018, doi: 10.1002/mrm.26830.
[6] K. J. Gorgolewski et al., "The brain imaging data structure, a format for organizing and describing outputs of neuroimaging experiments," Sci Data, vol. 3, no. 1, p. 160044, Jun. 2016, doi: 10.1038/sdata.2016.44.
[7] Y. Shi, R. Feng, Z. Li, J. Zhuang, Y. Zhang, and H. Wei, "Towards in vivo ground truth susceptibility for single-orientation deep learning QSM: A multi-orientation gradient-echo MRI dataset," NeuroImage, vol. 261, p. 119522, Nov. 2022, doi: 10.1016/j.neuroimage.2022.119522.
[8] C. Milovic, C. Tejos, P. Irarrazaval, and K. Shmueli, "XSIM, a Susceptibility-Optimised Similarity Index Metric: Validation with 2016 and 2019 QSM Reconstruction Challenge Datasets," in Proceedings of the Joint Annual Meeting ISMRM-ESMRMB 2022 & ISMRT Annual Meeting, London, UK, May 2022. [Online]. Available: https://archive.ismrm.org/2022/2367.html

Automated Deep-Learning-Enabled Segmentation of Intraprostatic Gold Fiducial Markers in the Presence of Calcification for MR-only Radiotherapy Planning

Ashley Stewart[1], Jonathan Goodwin[2,3], Matthew Richardson[2], Simon Daniel Robinson[4,5], Kieran O'Brien[5,6,7], Jin Jin[5,6,7], Markus Barth[1,5,7], Steffen Bollmann[1,5,7,8]

[1]School of Electrical Engineering and Computer Science, The University of Queensland, Brisbane, Australia;
[2]Department of Radiation Oncology, Calvary Mater Hospital, Newcastle, New South Wales, Australia;
[3]School of Information and Physical Sciences, University of Newcastle, Newcastle, New South Wales, Australia;
[4]High Field MR Center, Department of Biomedical Imaging and Image-Guided Therapy, Medical University of Vienna, Vienna, Austria;
[5]Centre for Advanced Imaging, The University of Queensland, Brisbane, Australia;
[6]Siemens Healthcare Pty Ltd, Brisbane, Australia;
[7]ARC Training Centre for Innovation in Biomedical Imaging Technology, The University of Queensland, Brisbane, Australia;
[8]Queensland Digital Health Centre, The University of Queensland, Brisbane, Australia

Summary: We developed a deep learning approach for segmenting intraprostatic gold fiducial markers (FMs) in prostate MRI, integrating multiple contrasts including quantitative susceptibility mapping (QSM) to differentiate FMs from calcifications. This innovation aims to facilitate a streamlined MR-only radiotherapy planning approach, potentially reducing reliance on CT-MRI workflows and lowering healthcare costs.

Introduction: Radiotherapy (RT) planning for prostate cancer (PCa) often uses implanted gold fiducial markers (FMs) for treatment targeting purposes[1]. While FMs aid in CT-MRI workflows, MR-only radiotherapy planning is emerging, reducing costs and offering a streamlined imaging pathway. However, FMs in MRI appear as signal voids, complicating differentiation from other sources of signal voids such as calcifications and bleeds[2,3,4]. This work presents a deep-learning-enabled segmentation across a range of MR contrasts, including phase-based techniques such as quantitative susceptibility mapping (QSM) and susceptibility-weighted imaging (SWI) to exploit susceptibility information. We compare this approach with CT imaging as a baseline, aiming to facilitate a streamlined MR-only RT workflow.

Methods: 25 PCa patients, each with three implanted gold FMs, underwent CT and MRI, including T1-weighted and GRE acquisitions. Calcifications were present in 12 patients, as confirmed by CT. Acquired GRE data were processed using QSMxT[5,6] to produce QSM, SWI[7], and R2* maps. FMs and calcifications were manually segmented using ITK-SNAP[8], with CT as a reference to produce ground-truth labels. 3D U-Nets were implemented using fastMONAI[9] to distinguish between and segment the identified background, calcification, and FM regions. The U-Nets used five levels with channels (16, 32, 64, 128, 256). The loss function combined Dice loss and cross-entropy loss with one-hot encoding applied to the target masks. Performance was evaluated using precision and recall calculated at the FM level using a leave-one-out cross-validation scheme to reliably evaluate the models without the need for a large independent test set. Separate U-Nets were trained for each available contrast.

Results: The trained U-Nets generated segmentations and confidence maps for each label (see **Figure 1**).
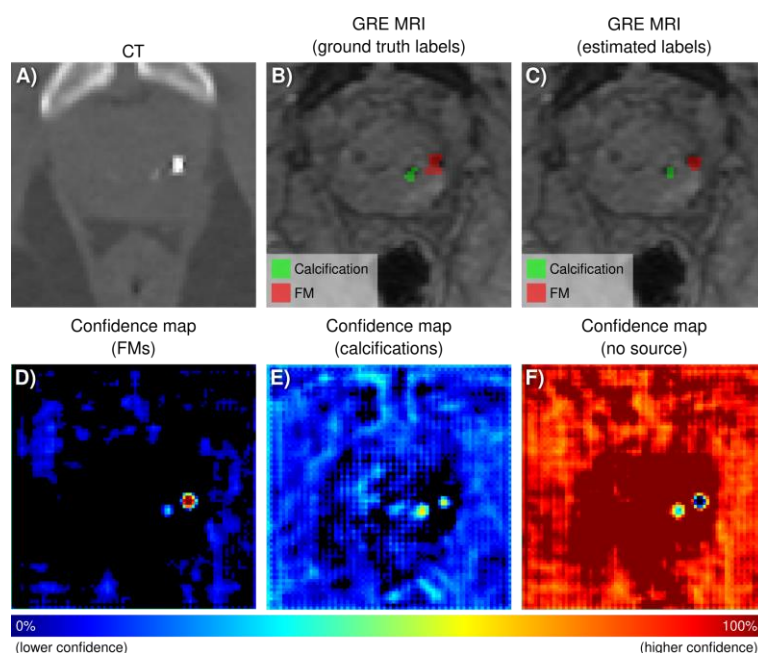
Figure 1: Representative images; cropped axial prostate region. **A)** Reference CT image; **B-C)** GRE magnitude images with overlaid ground-truth and estimated labels produced by the GRE-trained U-Net; **D-F)** Confidence maps generated by the GRE-trained U-Net for each segmentation class. The estimated labels for each source match with the ground truth.

The baseline U-Nets trained on CT achieved perfect recall and 99% precision (see **Table 1**). MRI-based contrasts achieved 92-99% recall and 81-87% precision. This indicates that the MRI-based models reliably identified FMs, but a gap remains in distinguishing them from calcification among the evaluated MR contrasts.

Model	Precision (%)	Recall (%)
CT	99	1
GRE	87	99
SWI	86	96
R2*	87	95
T1w	87	93
QSM	81	92

Table 1: FM identification precision and recall using the GRE-trained segmentation model.

Discussion and Conclusions: MRI can reliably identify intraprostatic gold FMs in our dataset. However, challenges remain in differentiating FMs from sources such as calcification. While susceptibility-based techniques were not always the best-performing, combining information across MR contrasts may improve the result in future. Future work will aim to close the gap in model precision by exploring consensus-based segmentation approaches across U-Nets, hyperparameter tuning, and applying morphological operations to clean model outputs. This will enable tools to automate the segmentation of MR images and streamline the MR-only RT workflow. The code for this work is available open-source via GitHub at https://github.com/astewartau/prostate.

References:
[1] Ng M, Brown E, Williams A, Chao M, Lawrentschuk N, Chee R (2014), "Fiducial markers and spacers in prostate radiotherapy: current applications," *BJU International*, vol. 113, no. S2, pp. 13–20, doi: 10.1111/bju.12624.
[2] Ghose S et al. (2016), "MRI-alone radiation therapy planning for prostate cancer: Automatic fiducial marker detection," *Medical Physics*, vol. 43, no. 5, pp. 2218–2228, doi: 10.1118/1.4944871.
[3] Maspero M et al. (2017), "Evaluation of an automatic MR-based gold fiducial marker localisation method for MR-only prostate radiotherapy," *Phys. Med. Biol.*, vol. 62, no. 20, p. 7981, doi: 10.1088/1361-6560/aa875f.
[4] Gustafsson C, Korhonen J, Persson E, Gunnlaugsson A, Nyholm T, Olsson LE (2017), "Registration free automatic identification of gold fiducial markers in MRI target delineation images for prostate radiotherapy," *Medical Physics*, vol. 44, no. 11, pp. 5563–5574, doi: 10.1002/mp.12516.
[5] Stewart AW et al. (2022), "QSMxT: Robust masking and artifact reduction for quantitative susceptibility mapping," *Magnetic Resonance in Medicine*, vol. 87, no. 3, pp. 1289–1300, doi: 10.1002/mrm.29048.
[6] Langkammer C et al. (2015), "Fast quantitative susceptibility mapping using 3D EPI and total generalized variation," *NeuroImage*, vol. 111, pp. 622–630, doi: 10.1016/j.neuroimage.2015.02.041.
[7] Eckstein K et al. (2021), "Improved susceptibility weighted imaging at ultra-high field using bipolar multi-echo acquisition and optimized image processing: CLEAR-SWI," *NeuroImage*, vol. 237, p. 118175, doi: 10.1016/j.neuroimage.2021.118175.
[8] Yushkevich PA, Gao Y, Gerig G (2016), "ITK-SNAP: An interactive tool for semi-automatic segmentation of multi-modality biomedical images," in *2016 38th Annual International Conference of the IEEE Engineering in Medicine and Biology Society (EMBC)*, pp. 3342–3345, doi: 10.1109/EMBC.2016.7591443.
[9] Kaliyugarasan S, Lundervold AS (2023), "fastMONAI: A low-code deep learning library for medical image analysis," *Software Impacts*, vol. 18, p. 100583, doi: 10.1016/j.simpa.2023.100583.

Mitigation of artefacts arising from the Transceive Phase Assumption in Electrical Properties Tomography

Christian Findeklee[1], Thierry Meerbothe[2,3], Stefano Mandija[2,3], Cornelis van den Berg[2,3], Ulrich Katscher[1]

[1]Philips Research (Hamburg, Germany); [2]Department of Radiotherapy, Division of Imaging and Oncology (UMC Utrecht, The Netherlands); [3]Computational Imaging Group for MR Therapy and Diagnostics (UMC Utrecht, The Netherlands)

Summary: Artefacts arising from the Transceive Phase Assumption (TPA) in Electric Properties Tomography (EPT) can be mitigated by averaging results from a standard reconstruction and a reconstruction using a mirrored B_1 magnitude map.

Introduction: Electrical properties reconstructions require knowledge of the complex RF transmit (TX) field. While determination of the RF TX magnitude B_1 is extensively discussed in literature (see, e.g., [1]), methods to accurately determine the RF TX phase φ from the measurable transceive phase (superposition of TX and receive (RX) phase) are based on multi-RF-transmit systems and too cumbersome for clinical routine (see, e.g., [2]). Thus, φ is typically estimated by half the transceive phase ("Transceive Phase Assumption", TPA). While the TPA is only accurate for symmetric scenarios, typical quadrupolar artefacts appear for approximately symmetric scenarios [3]. This study investigates two approaches to empirically mitigate these quadrupolar TPA artefacts: 1) average two scans with different patient positions, "head first" and "feet first", 2) from a single patient position (as changing patient position is hardly feasible in clinical settings), the corresponding second position is mimicked offline by mirroring the magnitude B_1 of the first position while maintaining its phase φ. These two approaches were evaluated using electro-magnetic field simulations of simple geometrical shapes representing abdomen and legs as well as realistic brain models without and with tumor.

Methods: Complex RF TX and RX field simulations were performed at 128 MHz using a quadrature birdcage coil driven in quadrature and anti-quadrature mode. The transceive phase was calculated by summing quadrature-TX phase and anti-quadrature-RX phase. The simulations were performed twice, corresponding to the "head first" (HF) and "feet first" (FF) position of the patient. No noise was added to the RF fields for better depiction of the TPA artefact and its proposed mitigation.

Four different simulation scenarios were studied: (1) an ellipsoid representing the abdomen (conductivity $\sigma = 0.5$ S/m, relative permittivity $\varepsilon_r = 50$) including an asymmetrically placed smaller ellipsoid representing an inner organ ($\sigma = 0.25$ S/m, $\varepsilon_r = 50$), (2) two parallel cylinders representing legs / knees ($\sigma = 0.25$ S/m, $\varepsilon_r = 50$), (3) a realistic brain model corresponding to a healthy volunteer, (4) a realistic brain model including an asymmetrically placed tumor.

The geometrical shapes (1,2) were simulated with the software package CONCEPT II (Technical University Hamburg-Harburg, Department of Theoretical Electrical Engineering, Germany). The realistic brain models were simulated with Sim4Life (Zurich MedTech, Switzerland) [4]. The truncated Helmholtz equation for the conductivity $\sigma = (\Delta\varphi + \nabla\ln(B_1)\cdot\nabla\varphi) / (\mu_0\omega)$ with Larmor frequency ω and vacuum permeability μ_0 was solved using finite differences [5]. This reconstruction was applied for both positions (HF and measured/mimicked FF).

To mimic the second (FF) position without rotating the object, the B_1 magnitude was mirrored in left/right-direction for each line individually by using the center of each line as pivot point. The phase associated to this mimicked FF position was the same phase as of the HF position. The results of the two reconstructions were averaged after registration based on tissue morphology.

Results: In scenario (1), TPA causes an error of 58/11 mS/m in the outer/inner ellipsoid, which is reduced to 3.5/1.5 mS/m after averaging HF and FF reconstructions and to 18/2.0 mS/m after averaging reconstructions of original/mirrored B_1. For scenario (2), the two reconstruction approaches are identical due to the symmetry of the simulation setup. Thus, the TPA error of 22 mS/m is reduced to 4.2 mS/m for both reconstruction approaches. In scenarios (3) and (4), significant TPA artefacts are found mainly in the CSF of the subarachnoid space between brain and skull. In this area, TPA causes an error of 0.17/0.32 S/m for scenario (3/4), which is reduced to 0.10/0.11 S/m after averaging HF and FF reconstructions and to 0.11/0.13 S/m after averaging reconstructions of original/mirrored B_1. Reconstruction results for scenarios (1) to (3) are shown in the figure.

Discussion and Conclusions: This study shows that a simple approach is able to mitigate artefacts caused by TPA. From the two versions of the approach presented, the version which is based on two different patient positions achieve higher artefact reduction than the version which is based on a single patient position only. However, the measurement of two patient positions is rendered rather impractical in a clinical workflow. The proposed mimicking of the second patient position, even if yielding less accurate results, might be the preferred version as it is quite straight-forward and easy to implement.

In its current form, this study is purely empirical, validating the approach only by a number of simulation examples. Theoretical and experimental validations shall follow in subsequent studies, which will also check the applicability of the approach to permittivity.
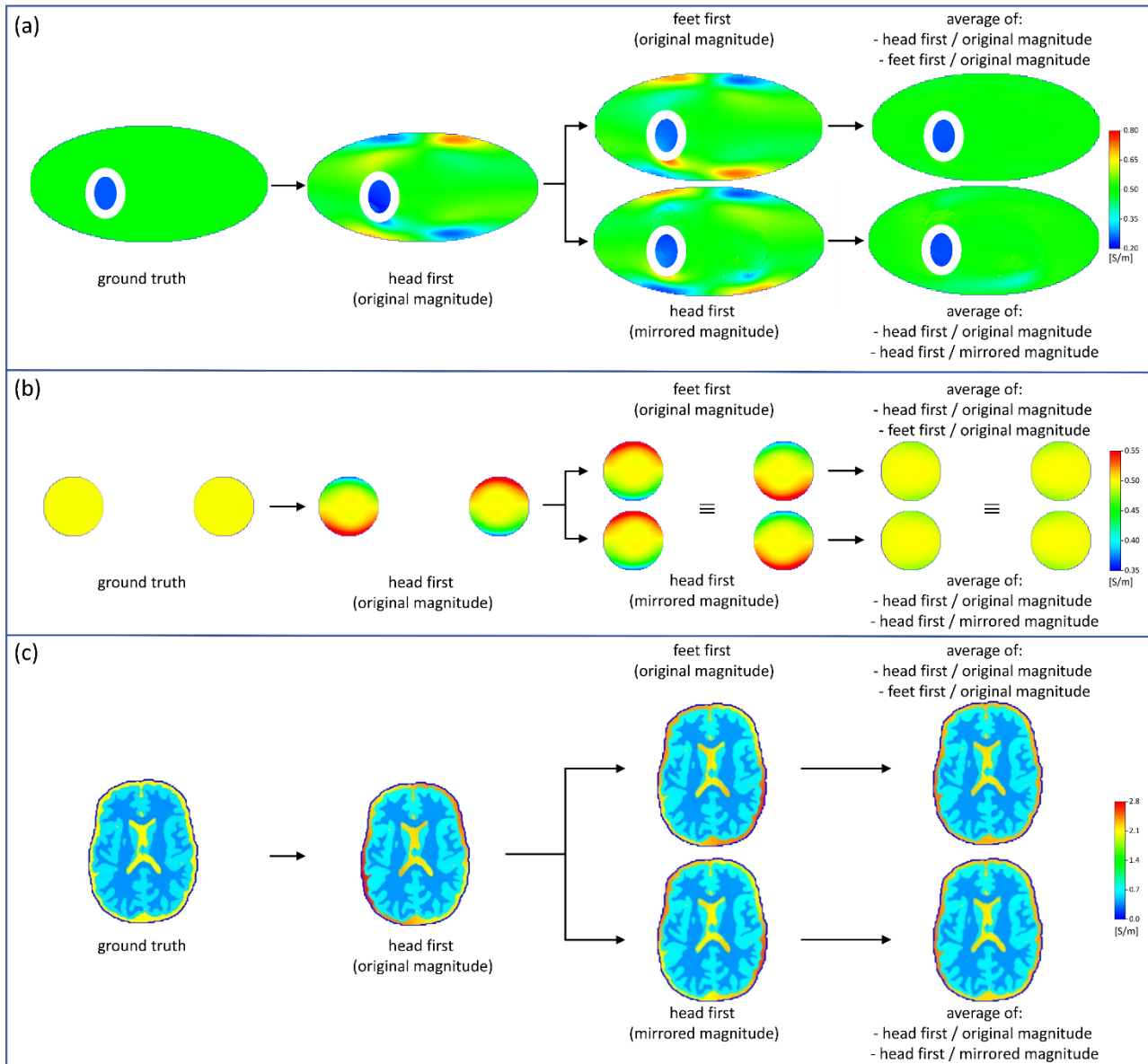
Figure: Simulation results for (a) simple abdominal model, (b) simple leg / knee model, and (c) realistic brain model. Reconstructed conductivity maps from first patient position ("head first", HF) reveal artefacts from the Transceive Phase Assumption (TPA). Reconstructed conductivity maps from second position ("feet first", FF) show artefacts complementary to the artefacts in HF position. The FF position can be mimicked by mirroring B_1 magnitude while maintaining B_1 phase of HF, yielding similar TPA artefacts as found for FF. Thus averaging corresponding conductivity maps clearly reduces TPA artefacts.

References:
[1] Gavazzi S et al. (2019), "Accuracy and precision of electrical permittivity mapping at 3T: the impact of three B_1 mapping techniques," *Magn Reson Med.* vol. 81, pp. 3628–3642, doi: 10.1002/mrm.27675
[2] Katscher U et al. (2012), "B_1-based specific energy absorption rate determination for nonquadrature radiofrequency excitation," *Magn Reson Med.* vol. 68, pp. 1911-1918, doi: 10.1002/mrm.24215
[3] van Lier AL et al. (2014), "Electrical properties tomography in the human brain at 1.5, 3, and 7T: a comparison study," *Magn Reson Med.* vol. 71, pp. 354-363, doi: 10.1002/mrm.24637
[4] Meerbothe TG et al. (2023), "A database for MR-based electrical properties tomography with in silico brain data—ADEPT," *Magn Reson Med.* vol. 1-10, doi: 10.1002/mrm.29904
[5] Katscher U et al. (2017), "Electric properties tomography: Biochemical, physical and technical background, evaluation and clinical applications," *NMR in Biomed*, vol. 30, pp. 3729, doi.org/10.1002/nbm.3729

Multi-Echo Multi-Volume Field Mapping for Computationally Efficient Structural QSM

Patrick Fuchs, Karin Shmueli

Department of Medical Physics and Biomedical Engineering (University College London, London, United Kingdom)

Summary

Multi-volume multi-echo nonlinear fitting provides an efficient approach to combine multiple signal averages. This can greatly reduce the computational overhead of processing large functional datasets for anatomical maps and may be more robust to flow related artifacts.

Introduction

For reconstructing anatomical quantitative susceptibility maps (QSMs), it has been shown that it is more accurate to fit an (off-resonance) field-map across the echoes of a multi-echo acquisition rather than averaging the maps calculated from the separate echoes[1]. Noise propagation through both weighted averaging[2] and nonlinear fitting[3] into field maps and QSM has also been investigated extensively[1]. With novel rapid high-resolution acquisitions many consecutive multi-echo volumes are acquired, which can then be used for functional analysis to investigate temporal changes.

When computing anatomical susceptibility maps from these datasets one can simply reconstruct a QSM at each volume and then take the mean or median over all volumes to provide a map with a slightly improved signal to noise ratio, which can be lacking for high resolution acquisitions[4]. Another approach, which we investigate here, is to fit the field-map not for each volume individually but rather to fit across all the acquired volumes. This could potentially improve the fit for voxels with a low signal to noise ratio, or which suffer from signal dropout in some volumes due to motion. Further, this approach is much more computationally efficient as only a single susceptibility map is computed (involving background field removal and dipole inversion) instead of many.
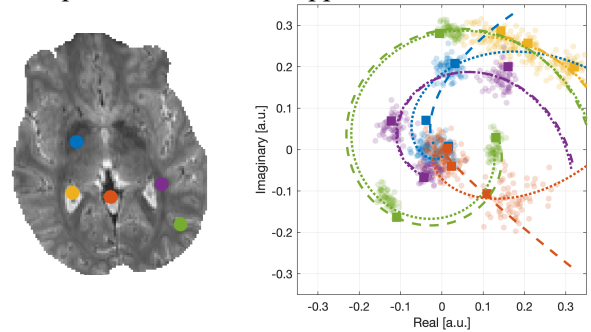

Figure 1 Example fitting results for single volume (solid dots and dotted lines) and all volumes (all dots and dashed lines) for five points in different brain regions (similar coloured dots, left).

Methods

We used a 70 volume 3 echo 2D gradient recalled echo-echo planar imaging acquisition with the following parameters: echo times of 14.8, 39.33, and 63.86 milli-seconds, multi-band acceleration of 3, parallel imaging acceleration of 4, a repetition time of 4.034 seconds, and a field of view of 240 by 219 by 163.8 millimetres, 1.3 mm isotropic voxels, with a bandwidth of 1812 Hz/voxel. The complex data were denoised using tensor-MPPCA denoising[5], before field fitting. Nonlinear fitting is considered here as in the linear case, averaging the fitted map across volumes and fitting across all volumes directly should be identical. This equivalence may not apply to non-linear fitting. Nonlinear fitting was performed using the FIT_PPM_COMPLEX function from the MEDI Toolbox (Update 15-01-2020, Medimagemetric LLC, Cornell, USA)[3,6,7].

Fitted field maps were unwrapped using Laplacian unwrapping[8]. V-SHARP background field removal was applied[9] with a spherical mean value kernel size of 20. Finally, magnetic susceptibility maps were computed using FANSI[10] with a regularisation weight of $2.4 \cdot 10^{-4}$. To compare reconstructed susceptibility values, we segmented the brain using MRICloud[11].
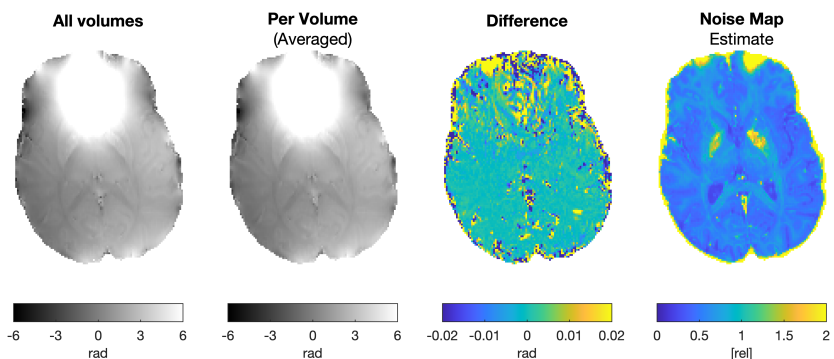

Figure 2: An axial slice of fitted field maps using a fitting across all the data as well as the mean of all field maps fit on single volumes. The difference (computed as all volumes – per volume mean) and a-priori error estimate from the fit across all volumes shown on the right.

Results

Figure 1 shows an example of the nonlinear fitting approach, where essentially a spiral is fit to the target points. We show examples of low

variability (across the volumes) which essentially fit the same curve for both approaches as well as voxels for which there is a large difference between the (chosen) local fit and the fit across all volumes.

Figure 2 shows the field maps from the various fitting approaches. An error estimate output by the nonlinear fitting function[3] is shown together with differences between the fits. The resulting susceptibility maps are compared in Figure 4. This figure also shows the segmentation used to compute the ROI statistics shown in Figure 3.
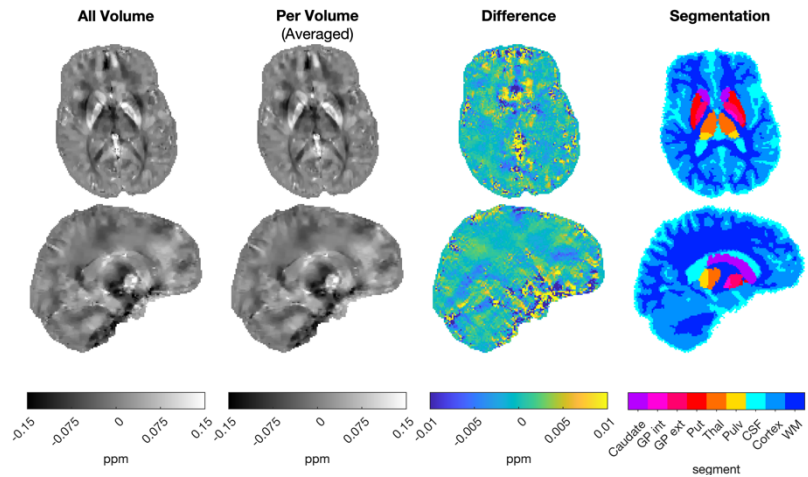

Figure 4 Reconstructed susceptibility maps created by nonlinear fitting across all volumes vs averaging maps created by fitting at each volume and the difference between them. ROIs segmented using MRI Cloud.

Discussion

Figure 3 shows that there was no significant difference in ROI mean susceptibilities for fitting across all volumes compared averaging susceptibility maps fitted and reconstructed for each volume. However, Figure 2 shows susceptibility differences between the two approaches, particularly in and near vasculature and close to the nasal cavity, which suffers from signal drop-out in these types of acquisitions. Since there is no ground truth available, it is impossible to say which of these approaches is more accurate. However, fitting across all volumes is much more computationally efficient and therefore provides a compelling alternative approach.
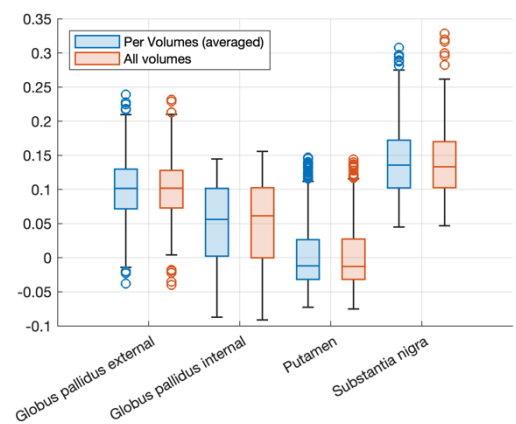

Figure 3 Comparison of susceptibility values from nonlinear fitting across all volumes vs averaging all of the single volume fits in some deep gray matter ROIs.

Conclusion

In a multi-volume acquisition, fitting the field across all the volumes in a single step greatly reduces computational overheads for generating anatomical magnetic susceptibility maps that are almost identical to those created by averaging.

Bibliography

1. Biondetti, E. *et al.* Multi-echo quantitative susceptibility mapping: how to combine echoes for accuracy and precision at 3 Tesla. *Magn. Reson. Med.* **88**, 2101–2116 (2022).
2. Wu, B., Li, W., Avram, A. V., Gho, S.-M. & Liu, C. Fast and tissue-optimized mapping of magnetic susceptibility and T2* with multi-echo and multi-shot spirals. *NeuroImage* **59**, 297–305 (2012).
3. Liu, T. *et al.* Nonlinear formulation of the magnetic field to source relationship for robust quantitative susceptibility mapping. *Magn. Reson. Med.* **69**, 467–476 (2013).
4. Sun, H., Seres, P. & Wilman, A. H. Structural and functional quantitative susceptibility mapping from standard fMRI studies. *NMR Biomed.* **30**, e3619 (2017).
5. Olesen, J. L., Ianus, A., Østergaard, L., Shemesh, N. & Jespersen, S. N. Tensor denoising of multidimensional MRI data. *Magn. Reson. Med.* **89**, 1160–1172 (2023).
6. Kressler, B. *et al.* Nonlinear Regularization for Per Voxel Estimation of Magnetic Susceptibility Distributions From MRI Field Maps. *IEEE Trans. Med. Imaging* **29**, 273–281 (2010).
7. De Rochefort, L., Brown, R., Prince, M. R. & Wang, Y. Quantitative MR susceptibility mapping using piece-wise constant regularized inversion of the magnetic field. *Magn. Reson. Med.* **60**, 1003–1009 (2008).
8. Zhou, D., Liu, T., Spincemaille, P. & Wang, Y. Background field removal by solving the Laplacian boundary value problem. *NMR Biomed.* **27**, 312–319 (2014).
9. Wei, H. *et al.* Joint 2D and 3D phase processing for quantitative susceptibility mapping: application to 2D echo-planar imaging: 2D EPI-BASED QSM. *NMR Biomed.* **30**, e3501 (2017).
10. Milovic, C., Bilgic, B., Zhao, B., Acosta-Cabronero, J. & Tejos, C. Fast nonlinear susceptibility inversion with variational regularization. *Magn. Reson. Med.* **80**, 814–821 (2018).
11. Mori, S. *et al.* MRICloud: Delivering High-Throughput MRI Neuroinformatics as Cloud-Based Software as a Service. *Comput. Sci. Eng.* **18**, 21–35 (2016).

# Mapping cell density with DECOMPOSE-QSM in healthy brain tissues and glioblastoma

Giulia Debiasi[1,2,3], Giovanni Librizzi[4,5], Valentina Visani[2], Marco Castellaro[2], Giuseppe Lombardi[6], Renzo Manara[4,5,7], Alessandra Bertoldo[2,4], Chunlei Liu[3,8]

[1]Department of Surgery, Oncology and Gastroenterology (University of Padova, Padova, Italy); [2]Department of Information Engineering (University of Padova, Padova, Italy); [3]Department of Electrical Engineering and Computer Sciences (University of California, Berkeley, CA, USA); [4]Padova Neuroscience Center (University of Padova, Padova, Italy); [5]Neuroradiology, Department of Neurosciences (University of Padova, Padova, Italy); [6]Department of Oncology (Veneto Institute of Oncology IOV-IRCCS, Padova, Italy); [7]Department of Medicine (University of Padova, Padova, Italy); [8]Helen Wills Neuroscience Institute (University of California, Berkeley, CA, USA)

Summary: DECOMPOSE-QSM estimates sub-voxel susceptibility composition, providing a parameter C_0, that is the volume fraction of tissue susceptibility reference medium. We found high correlation between C_0 maps and NODDI-derived tissue microstructural parameters in both healthy tissues and edema regions of glioblastoma. These findings support $1-C_0$ as a measure of tissue cell density, and DECOMPOSE-QSM may enable high-resolution and fast mapping for tissue cellularity with a single 3D multi-echo GRE sequence.

Introduction: Glioblastoma is one of the most aggressive adult-type tumors of the central nervous system and the prognosis is still very poor. It is radiologically characterized by three tissues including edema that is mainly composed by fluid. The Neurite Orientation Dispersion and Density Imaging (NODDI) diffusion model [1] has been previously applied to investigate the heterogeneity of the non-enhancing tissue in gliomas [2]. The recently developed DECOMPOSE-QSM algorithm [3] for the separation of magnetic susceptibility at voxel level has also provided a new tool to study tissue microstructure. DECOMPOSE-QSM estimates the concentration of the magnetically neutral component (C_0) which is considered the reference medium dominated by extracellular fluid. Therefore, $1-C_0$ represents the intra-cellular volume fraction. Here, we aim to: (i) compare $1-C_0$ maps with NODDI parameters in the healthy tissue to confirm the hypothesis that high C_0 is associated with a low level of cell density or high free water concentration; (ii) investigate the relationship between $1-C_0$ maps and NODDI parameters in the edema tissue of glioblastoma.

Methods: <u>Data:</u> 21 newly diagnosed glioblastoma patients (5/16 F/M, 7/14 R/L, 65±8 years) were scanned on a 3T Philips Ingenia scanner (University Hospital of Padova, Italy) equipped with a 32-channel head-neck coil. The data include a 3D multi-echo GRE sequence (eight echoes $TE_1/\Delta TE$=5/5 ms, TR=44 ms, FA=25°, voxel size=1x1x1 mm^3, FOV=240x240 mm^2); a multi-shell of 116 Diffusion Weighted Images (DWIs) (TE=104 ms, TR=3.7 s, FA=90°, voxel size=2x2x2 mm^3, FOV=112x122 mm^2): 12 images at b=0 s/mm^2 and 8, 32, 64 gradient directions at b-value=300, 1000, 2000 s/mm^2, respectively; and other 3D structural images. <u>Image Processing:</u> Images were bias field corrected, brain extracted and linearly registered to the native T1w space using the Advanced Normalization Tools (ANTs). In T1w space, grey matter (GM) and white matter (WM) segmentations were obtained with SPM12, while segmentation of the deep grey nuclei was generated with FSL. The edema mask was delineated on structural images with an automatic tool [4,5] and masks were checked and modified (if necessary) by an expert neuroradiologist. The T1w image was linearly registered to the first echo of the GRE magnitude image with ANTs and the estimated transformation was applied to the Region Of Interests (ROIs) namely the edema mask, the healthy contralateral WM and the deep grey nuclei (i.e., thalamus, caudate, putamen, pallidum, hippocampus and amygdala). For susceptibility quantification, brain extraction was performed on the first echo GRE magnitude image with FSL. QSM maps were obtained for each echo using STISuite. Phase unwrapping, background field removal and dipole inversion were achieved with Laplacian phase unwrapping [6], V-SHARP [7] and STAR-QSM [8], respectively. The DECOMPOSE-QSM algorithm was used to estimate the C_0 map. After discarding volumes affected by interslice instabilities [9], MRtrix software [10] was employed to carry out the entire pre-processing which included denoising and correction for B0 inhomogeneities, eddy currents and motion. The NODDI model was fitted with a publicly available toolbox [11]. Parametric maps of Neurite Density Index (NDI), Orientation Dispersion Index (ODI) and ISOtropic volume (ISO) were estimated and warped to the first echo GRE magnitude space. <u>Statistics:</u> For correlation analysis, the inverse of the tumor mask was used to exclude any voxel belonging to the tumor that had been wrongly classified as deep grey nuclei by FSL. Pearson's correlation coefficients were
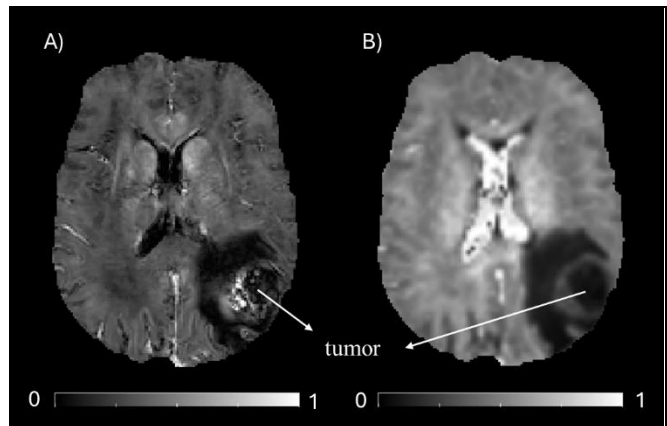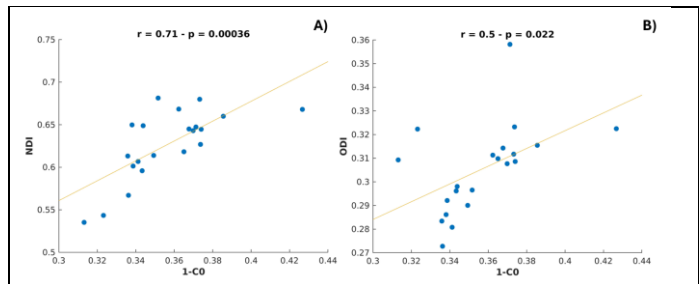

Figure 1 – Representative patient for which $1-C_0$ (A) and NDI (B) maps have been quantified, demonstrating a strong spatial congruence. Bright NDI in the ventricles is a known artifact, which is absent in the $1-C_0$ map.

computed between $1-C_0$ and each NODDI parameter of the ROIs. Multi-comparison correction using the Benjamini-Hochberg procedure was applied to the p-values of the correlation coefficients.

Results: Figure 1 shows the $1-C_0$ and NDI maps of a representative patient, demonstrating a strong anatomical contrast similarity. The common bright NDI artifact in the ventricles is absent in the $1-C_0$ map. Across patients the percentage of voxels that weren't affected by the tumor mask is 97 ± 3 (%). In WM, significant ($p<0.05$) positive associations were found between $1-C_0$ and NDI, and between $1-C_0$ and ODI (Fig. 2). Positive associations between $1-C_0$ and NDI were also observed for all deep gray nuclei, including left and right pallidum, left and right putamen, right amygdala and right hippocampus (Fig. 3). In deep gray nuclei, no significant correlations were observed between $1-C_0$ and either ODI or ISO after correction for multiple comparisons. In the edema regions, $1-C_0$ was positive correlated with ODI and NDI, whereas a negative association with ISO was found (Fig. 4).

Discussion and Conclusions: Our analysis confirmed that C_0 reveals information about the extra-cellular space, which is consistent with the assumption of the DECOMPOSE-QSM model. Particularly, in white matter we found no correlation between ISO and $1-C_0$. This is consistent with the fact that ISO includes both extra- and intra-cellular fluid in which isotropic diffusion is assumed. Instead, there was a strong positive association of $1-C_0$ with NDI. This agrees with the fact that white matter is mainly composed of neurites. Similarly, in the deep gray nuclei, NDI was positively associated with $1-C_0$ bilaterally for pallidum and putamen, while no correlation with ISO was found. In the edema region, while NDI is also positively associated with $1-C_0$, we found that ISO exhibits a strong negative correlation with $1-C_0$, or positively associated with C_0. This association is expected as the edema region is primarily constituted of fluid with relatively low cell densities or neurites. Edema regions may contain brain tissues due to partial volume effect and possibly tumor cells and immune cells. To conclude, we found that $1-C_0$ may serve as a measure of tissue cell density, a biologically and pathologically highly useful characterization of tissue microstructure. In fact, from NODDI we can derive NDI and ISO; with C_0 alone we can distinguish cells and fluid. Taken together these parameters could potentially inform about tumoral tissue microstructure.

Figure 2 – $1-C_0$ vs. NDI (A) and with ODI (B) in white matter. r and p represent the correlation coefficient and the p-value, respectively.
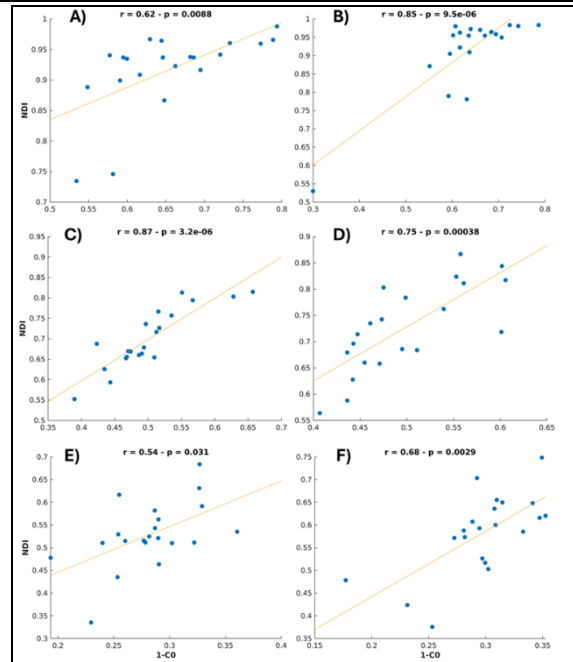
Figure 3 – Significant associations between $1-C_0$ and NDI in left (A) and right (B) pallidum, left (C) and right (D) putamen, right amygdala (E) and right hippocampus (F). r and p represent the correlation coefficient and the p-value, respectively.
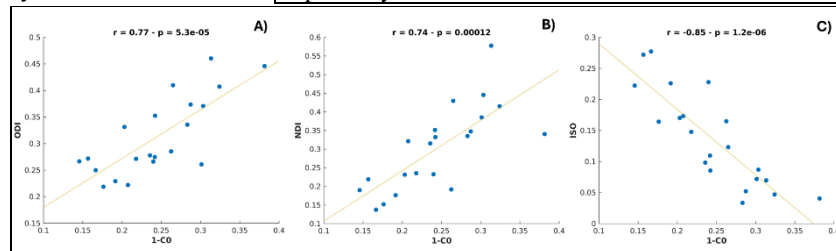
Figure 4 – Correlations between $1-C_0$ and ODI (A), NDI (B) ISO (C) in edema. r and p represent the correlation coefficient and the p-value, respectively.

References:

[1] Zhang H, et al (2012), *Neuroimage,* vol. 61, pp. 1000-16, doi: 10.1016/j.neuroimage.2012.03.072.
[2] Okita Y,et al (2023), *Magn Reson Imaging*, vol. 100, pp. 18-25, doi: 10.1016/j.mri.2023.03.001.
[3] Chen J, et al (2021), *Neuroimage*, vol. 242, doi: 10.1016/j.neuroimage.2021.118477.
[4] Isensee F, et al (2021), *Nat Methods*, vol. 18, pp. 203-211, doi: 10.1038/s41592-020-01008-z.
[5] Pemberton HG, et al (2023), *Sci Rep*, vol. 13, doi: 10.1038/s41598-023-44794-0.
[6] Li W, et al (2010), *Neuroimage*, vol. 55, pp. 1645-56, doi: 10.1016/j.neuroimage.2010.11.088.
[7] Wu B, et al (2012), Magn Reason Med, vol. 1, pp. 137-47, doi: 10.1002/mrm.23000.
[8] Wei H, et al (2015), *NMR Biomed*, vol. 28, pp. 1294-303, doi: 10.1002/nbm.3383.
[9] Bastiani M, et al (2019), *Neuroimage*, vol. 184, pp.801-812, doi: 10.1016/j.neuroimage.2018.09.073.
[10] Tournier JD, et al (2019), *Neuroimage*, vol. 202, doi: 10.1016/j.neuroimage.2019.116137.
[11] NODDI toolbox: http://mig.cs.ucl.ac.uk/index.php?n=Tutorial.NODDImatlab

Exploiting the polysemic nature of the voxel aspect ratio for dimensionality reduction in deep learning based QSM dipole inversion with adaptive convolution

Simon Graf[1,2], Walter A. Wohlgemuth[1,2], Andreas Deistung[1,2]

[1]*Halle MR Imaging Core Facility (Martin-Luther-University Halle-Wittenberg, Halle (Saale), Germany); [2]University clinic and policlinic for Radiology (University Hospital Halle (Saale), Germany)*

Summary: High dimensionality in deep learning models solving QSM-based dipole inversion can be reduced effectively by deploying adaptive convolution and even further with polysemic a priori information, such as the voxel aspect ratio, increasing model robustness and stability therewith.

Introduction: For the computation of quantitative susceptibility maps, the choice of imaging parameters in gradient echo MRI, such as the voxel size and the field-of-view (FOV) orientation, substantially affect the local magnetic field representation and field direction in the acquired volume. Multiple deep learning (DL) models [1, 2] were proposed for solving the ill-posed field-to-susceptibility inversion, however, typically neglecting the impact of these imaging parameters. The adaptive convolution (AC) approach [3] demonstrated the direct incorporation of a-priori information in the network model solving QSM dipole inversion, outperforming conventional DL approaches therewith. By learning the mapping between the imaging parameters and the changes in the local magnetic field associated with the varying acquisition information (Fig. A), AC selects an optimal set of convolution parameters (Fig. B). In this abstract, we investigate the influence of the voxel size encoded in the side information array on susceptibility map computation and test whether a polysemic description of the spatial resolution via the voxel aspect ratio (VAR) is advantageous.

Methods: The adaptive model [3] is built from a modified 3D U-Net [4] with a depth of five layers, 16 initial channels and ELU activation function, where the AC layer includes a multi-layer perceptron to compute the convolution weights from the presented a-priori information (Fig. A). Data augmentation was performed regarding image rotation, flipping, and scaling of three-dimensional susceptibility data sets as well as noise corruption. The models were pre-trained on purely synthetic data sets for 500 epochs, followed by transfer learning (TL) for 30 epochs on in-vivo brain data [3]. The TL data set consisted of 3T [5] and 7T [6] data sets with varying FOV and head orientations. Patch-based training was performed with a batch size of four and the AdamW optimizer [7] for pre-training and TL. Two adaptive models differing only in the presented side information were trained. The Adaptive U-Net Vox received the exact voxel size and FOV orientation, whereas the Adaptive U-Net VAR was presented with the VAR (as defined by: $v_{VARx,y,z} = \frac{v_{x,y,z}}{\max(v_{i=x,y,z})}$) and the FOV orientation.

Results: The computed susceptibility maps of both Adaptive U-Nets resemble the COSMOS ground truth susceptibility (Fig. C). To test the robustness of both Adaptive U-Nets, susceptibility maps were computed with the correct side information array and with modified versions. The Adaptive U-Net VAR generally scores lower NRMSE values as the Adaptive U-Net Vox, which is accompanied with visual changes in the computed susceptibility map (Fig. C, arrows). To further investigate the effects of using the VAR instead of the voxel size, Fig. D illustrates susceptibility maps computed with different absolute voxel sizes but identical VAR. As indicated by the metrics, the quality of computed susceptibility maps degrades for the Adaptive U-Net Vox, but remains constant for the Adaptive U-Net VAR.

Discussion and Conclusions: The assessment of both Adaptive U-Nets on brain data with different voxel sizes and FOV orientations revealed closest agreement with the COSMOS ground truth for the Adaptive U-Net VAR. While the computed susceptibility maps of both models exhibit the typical QSM contrast and depict anatomical structures accordingly, the quantitative image metrics for both data sets and versions of the side information array show the most accurate QSM reconstruction for the Adaptive U-Net VAR. The results clearly demonstrate the dependency of the Adaptive U-Net Vox on the exact voxel-size, where changes substantially affect the susceptibility map quality (Fig. C). We could successfully alleviate this dependency by making use of the VAR (Fig. D). The general idea of AC is to address the dimensionality problem in neural networks by making use of decoupling. In conventional DL-approaches, for each variation of $\vec{s}$, voxel-size and FOV orientation, a neural network (NN) has to be trained during which an N-dimensional feature space is learned. If all variations of $\vec{s}$ are part of the training data, the feature space to be learned expands substantially. AC decouples this problem by attaining the N-dimensional feature space and moving the additional dimensions due to variations in $\vec{s}$ to the filter manifold network (FMN) of the adaptive layer (Fig. B). The FMN learns the feature space of $\vec{s}_{Vox} = [v_x, v_y, v_z, o_x, o_y, o_z]$ by making use of manifold learning, overall reducing the dimensionality, and computes the convolution parameters of the NN. Thus, only a small number of layers in this network are influenced by variations of $\vec{s}$. Summarizing, AC leads to invariance against variations in $\vec{s}$. Exploiting the polysemic

nature of the VAR as side information $\vec{s}_{VAR} = [v_{VARx}, v_{VARy}, v_{VARz}, o_x, o_y, o_z]$ reduces the dimensionality of the FMN's feature space, since multiple voxel-sizes correspond to one VAR. Overall, this leads to an increase in stability and robustness of the NN as reflected by the Adaptive U-Net VAR model. Addressing the so-called curse of dimensionality is an ongoing and crucial challenge in the deployment of NNs. For QSM processing, DL-based approaches are furthermore influenced by the choice of the pre-processing algorithms used, e.g., for phase unwrapping [8] and background field removal [9]. Hence, these results point even more towards the potential of including comprehensive information in the network model to gain further invariance and address the curse of dimensionality therewith.
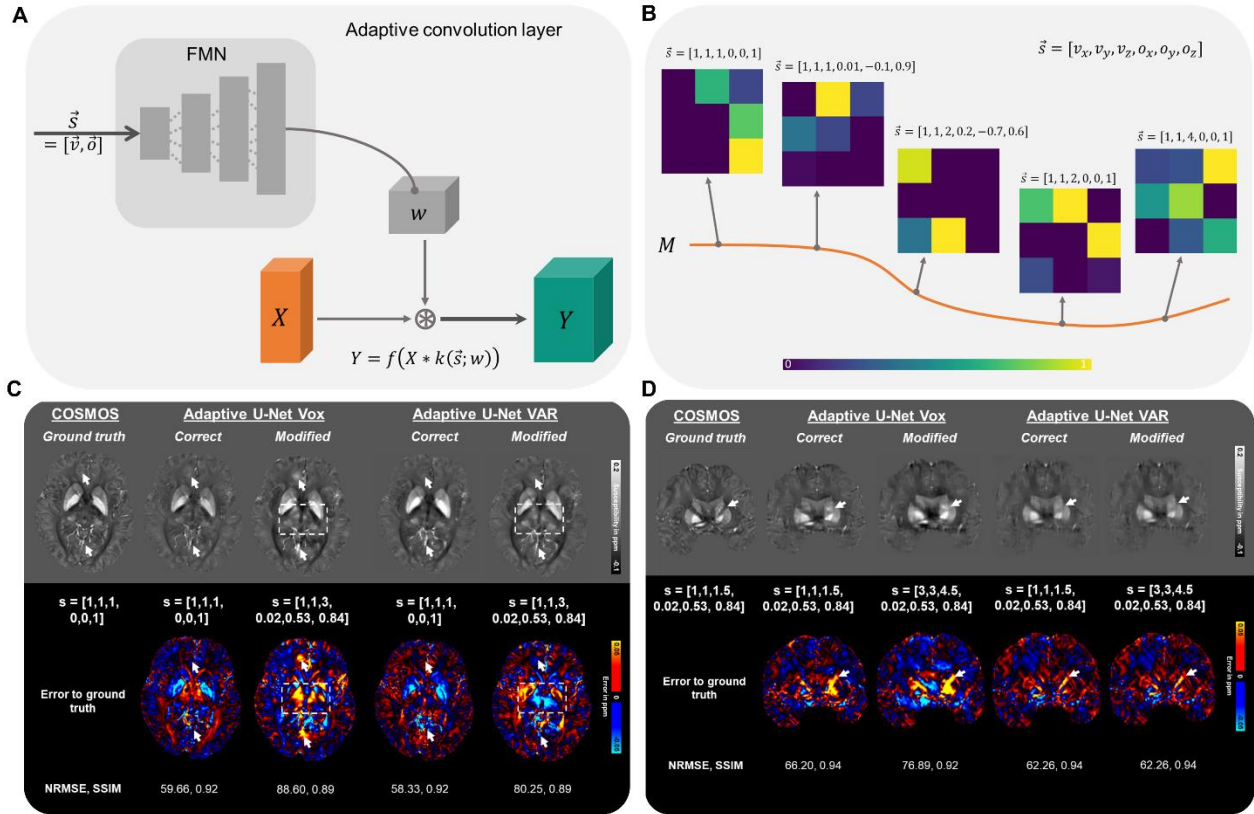
Figures – Adaptive Convolution layers are built from the Filter Manifold Network (FMN) consisting of fully connected linear layers that compute the weights *w* of the convolution kernel (A). Adaptive Convolution (AC) identifies and maps the relationship of the side information $\vec{s}$ (exact voxel size or voxel aspect ratio *v* and FOV orientation *o*) and the changes in the image onto the low dimensional filter manifold, which forms the feature space (B). The Adaptive U-Net Vox, receiving the exact voxel-size, and the Adaptive U-Net VAR, receiving the voxel aspect ratio (VAR), were evaluated on an isotropic purely axial data set (C) and an anisotropic data set with tilted FOV (D). For both data sets, the models were presented with the correct and a modified side information array, where the VAR is identical in D. Arrows and rectangles highlight prominent differences. The NRMSE and SSIM serve as quantitative image metrics. In-vivo brain data provided by [5].

References:
[1] Yoon J, Gong E, Chatnuntawech I, et al. (2018). Quantitative susceptibility mapping using deep neural network: QSMnet. *Neuroimage*, vol. 179, pp.199-206, doi:10.1016/j.neuroimage.2018.06.030
[2] Bollmann S, Rasmussen KGB, Kristensen M, et al. (2019). DeepQSM - using deep learning to solve the dipole inversion for quantitative susceptibility mapping. *Neuroimage*, vol. 195, pp. 373-383, doi:10.1016/j.neuroimage.2019.03.060
[3] Graf S, Wohlgemuth WA and Deistung A (2024). Incorporating a-priori information in deep learning models for quantitative susceptibility mapping via adaptive convolution. *Front. Neurosci*, 18, 1366165, doi: 10.3389/fnins.2024.1366165
[4] Ronneberger O, Fischer P and Brox T (2015). U-Net: Convolutional Networks for Biomedical Image Segmentation.
[5] Shi Y, Feng R, Li Z, et al. (2022). Towards in vivo ground truth susceptibility for single-orientation deep learning QSM: A multi-orientation gradient-echo MRI dataset. *NeuroImage*, vol. 261, 119522, doi: 10.1016/j.neuroimage.2022.119522.
[6] Deistung A, Schäfer A, Schweser F, et. al. (2013). Toward in vivo histology: a comparison of quantitative susceptibility mapping (QSM) with magnitude-, phase-, and R2*-imaging at ultra-high magnetic field strength. *NeuroImage*, vol. 65, pp. 299-314, doi: 10.1016/j.neuroimage.2012.09.055.
[7] Loshchilov I and Hutter F (2017). Decoupled Weight Decay Regularization; 2017
[8] Robinson SD, Bredies K, Khabipova D, et al. (2017). An illustrated comparison of processing methods for MR phase imaging and QSM: combining array coil signals and phase unwrapping. *NMR Biomed*, 30:e3601, doi: 10.1002/Nbm.3601.
[9] Schweser F, Robinson SD, Rochefort L.De, et al. (2017). An illustrated comparison of processing methods for phase MRI and QSM: removal of background field contributions from sources outside the region of interest. *NMR Biomed*, 30.:3604, doi: 10.1002/Nbm.3604

A Deep Learning based Harmonic Field Extension in SMWI with Reduced Spatial Coverage: Feasibility Study

Siyun Jung[1], Sung-Min Gho[2], Soohyun Jeon[1], Jaeyoon Kim[1] and Dong-Hyun Kim[1]

[1]Department of Electrical and Electronic Engineering, Yonsei University, Seoul, South Korea
[2] Imaging Development, Heuron, Seoul, South Korea

Summary: This study evaluates a harmonic field extension network to improve reduced FOV SMWI, enhancing acquisition efficiency and image contrast while mitigating susceptibility value underestimation.

Introduction: Susceptibility map-weighted imaging (SMWI)[1] is an imaging technique that combines magnitude images with quantitative susceptibility mapping (QSM)[2] to enhance the visibility of nigral hyperintensity in the substantia nigra (SN) and improve the contrast of nigrosome-1, both recognized as biomarkers for Parkinson's disease (PD)[3]. However, the current SMWI protocol has a long scan time, which is particularly challenging for PD patients due to their tendency for motion during the scan.

Reducing the Field-of-View (FOV) to focus solely on the substantia nigra region can shorten the scan time (e.g. by approximately 40%). Despite this advantage, severe susceptibility value underestimation has been reported during QSM reconstruction with a limited FOV[4,5], leading to reduced contrast in SMWI. To address this issue, a deep learning based harmonic field extension network[6] has been proposed and successfully applied in limited FOV QSM. This study explores the feasibility of applying these methods to SMWI by comparing limited FOV SMWI with the full FOV SMWI.

Methods:

[Data Acquisition] For training and validation, we acquired data from 15 healthy subjects using a 3T scanner (Vida, SIEMENS, Germany) with a multi-echo 3D GRE sequence. The acquisition parameters were as follows: FOV = 192 × 192 × 144 mm³, spatial resolution = 0.5 × 0.5 × 1 mm³ and TE = 5.30/11.1/16.9/22.7/28.5ms.

[Network Training] Out of the 15 subjects, 12 were used for training the network, 1 was used for validation, and 2 were used as a test set. Background fields were generated through forward calculation of geometric susceptibility sources randomly placed outside the brain ROI. The total fields used for training input were generated by adding the background field to the local field. Finally, the total fields were truncated along the z-axis to a minimal extent containing the substantia nigra (Fig. 1(A)) with masks and randomly cropped into 64 × 64 × 64 sized 3D patches for network training. The network architecture follows the structure of a coarse-to-fine generative model as described in Jung et al[6].

[Evaluation] The final network output was reconstructed into QSM using the V-SHARP[7] and iLSQR[8] methods. Subsequently, we generated the SMWI using a multiplication number of 4 and a susceptibility threshold value of 0.75. For comparison, we evaluated the whole brain SMWI, limited FOV SMWI without harmonic field extension, and our proposed method.

Results: The entire pipeline for reconstructing Limited FOV SMWI using a physics-informed GAN is shown in Figure 1(B). Figure 2 shows the QSM and SMWI results for full FOV, limited FOV, and the proposed harmonic extension method. Our proposed method overcomes susceptibility underestimation in limited FOV situations, resulting in enhanced contrast in both QSM and SMWI results, particularly in the SN (yellow arrow) and red nucleus (RN) (blue arrow). Figure 3 presents the susceptibility intensity plots of QSM and signal intensity plots of SMWI along the orange dotted lines. The QSM and SMWI signal plots from the proposed method were nearly identical to those obtained with full FOV.
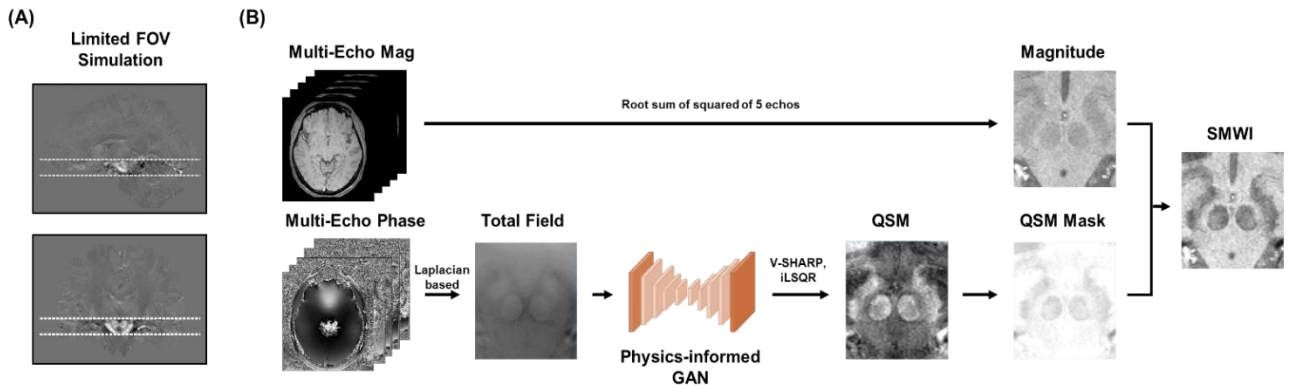
Figure 1. (A) The coronal and sagittal views of the in-vivo subject's QSM with Limited FOV. The location of truncation was manually adjusted for each individual to include the entire SN within the minimal range. (B) The overall pipeline for SMWI with reduced spatial coverage incorporating a physics-informed GAN.
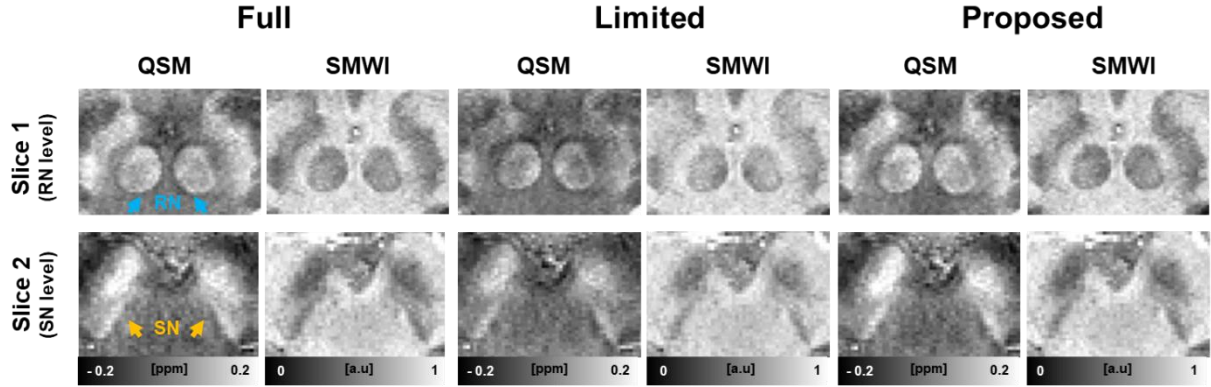
Figure 2. Two slices of QSM and SMWI results in in-vivo data (Slice 1: RN level, Slice 2: SN level).
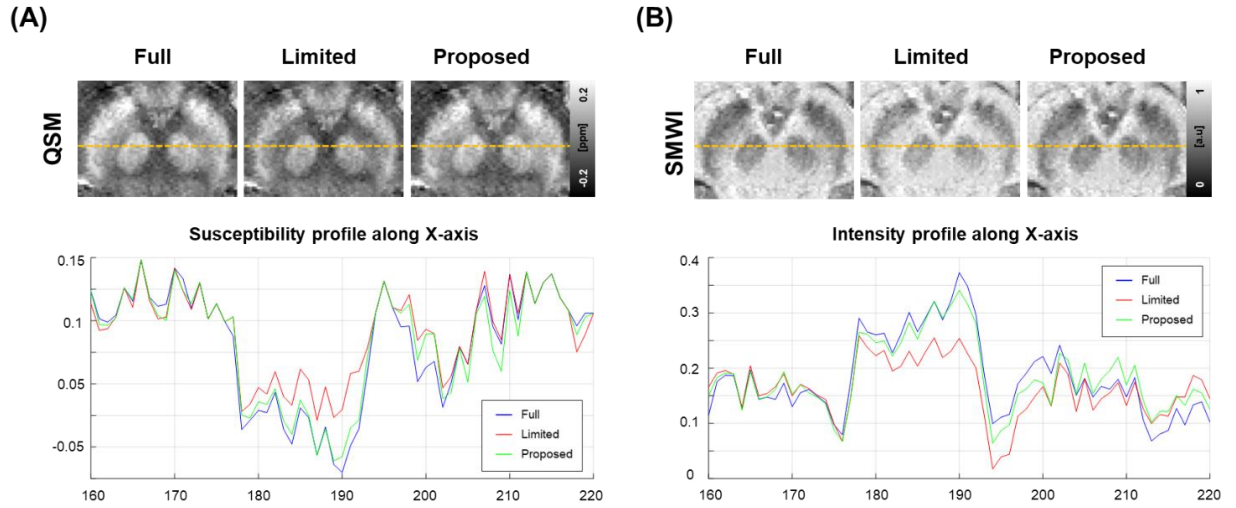
Figure 3. (A) QSM results of in-vivo data (top) and the susceptibility profile along the X-axis (bottom). The cross-sectional line is indicated in orange on the QSM result. (B) SMWI results of in-vivo data and the intensity profile along the X-axis. The cross-sectional line is indicated in orange on the SMWI result.

Discussion and Conclusions: In this study, we explored the feasibility of applying a harmonic field extension method based on a physics-informed GAN to SMWI, comparing limited FOV SMWI with full FOV SMWI. The proposed method significantly reduced scan time (e.g., by approximately 2 min) while enhancing contrast in SMWI through QSM underestimation correction. However, this study focused solely on feasibility and did not include clinical patient data. Future research will apply this method to clinical patient data to assess the impact of enhanced SMWI contrast.

References:
[1] Gho S M, et al. (2014), "Susceptibility map-weighted imaging (SMWI) for neuroimaging," Magnetic resonance in medicine, vol. 72, no. 2, pp. 337-346.
[2] Wang Y, Liu T (2015), "Quantitative susceptibility mapping (QSM): decoding MRI data for a tissue magnetic biomarker," Magnetic resonance in medicine, vol. 73, no. 1, pp. 82-101.
[3] Nam Y, et al. (2017), "Imaging of nigrosome 1 in substantia nigra at 3T using multiecho susceptibility map-weighted imaging (SMWI)," Journal of Magnetic Resonance Imaging, vol. 46, no. 2, pp. 528-536.
[4] Elkady A M, Sun H, Wilman A H (2016), "Importance of extended spatial coverage for quantitative susceptibility mapping of iron-rich deep gray matter," Magnetic resonance imaging, vol. 34, no. 4, pp. 574-578.
[5] Karsa A, Punwani S, Shmueli K (2019), "The effect of low resolution and coverage on the accuracy of susceptibility mapping," Magnetic resonance in medicine, vol. 81, no. 3, pp. 1833-1848.
[6] Jung S, et al. (2024), "Harmonic Field Extension for QSM with Reduced Spatial Coverage using Physics-informed Generative Adversarial Network," NeuroImage, vol. 120528.
[7] Wu B, et al. (2012), "Whole brain susceptibility mapping using compressed sensing," Magnetic resonance in medicine, vol. 67, no. 1, pp. 137-147.
[8] Li W, et al. (2015), "A method for estimating and removing streaking artifacts in quantitative susceptibility mapping," Neuroimage, vol. 108, pp. 111-122.

Exploring functional MRI, B_1 phase, and conductivity changes using phase-based EPT: A Comparative Study with Simulations

Kyu-Jin Jung[1], Chuanjiang Cui[1], SooHyung Lee[1], and Dong-Hyun Kim[1]

[1]Department of Electrical and Electronic Engineering, Yonsei University, Seoul, Republic of Korea

Summary: We explore B_1 phase and conductivity changes during brain activation using 3T MRI and RF simulation. In the simulation, we demonstrate that conductivity exhibit a similar tendency to in-vivo experimental conditions with negative correlation being dominant. Additionally, we found that for low SNR levels, low conductivity activation intensity, or the use of unsuitable EPT reconstruction methods with small kernels can lead to improper detection of conductivity activation.

Introduction: The typical MRI sequence for fMRI is gradient-echo (GE) echo-planar imaging (EPI), based on T2* decay and B_0 phase. Susceptibility, influencing MRI signal intensity through the BOLD effect, does not fully explain detected activations in other fMRI modalities such as spin echo (SE)-EPI and balanced Steady-State Free Precession (bSSFP), which depend on T2 and B_1 phase. A few number of studies have explored the relationship between brain activation and conductivity using phase-based electrical properties tomography (EPT) algorithms, yet the findings remain inconsistent[1,2,3]. Driven by this uncertainty, we investigated the relationship between fMRI signals and conductivity changes, reconstructed from the B_1 phase via SE-EPI and bSSFP sequences using EPT algorithms. We also analyzed trends through RF simulation, which provides a ground-truth reference.

Methods: Ten volunteers participated in a right hand finger-tapping experiment scanned using a 3T MRI system (MAGNETOM Vida, Siemens Healthineers). We utilized 2D GE-EPI, SE-EPI, and bSSFP sequences. Initially, a GE-EPI scan was conducted to capture the BOLD activiation region, selecting a specific slice for observation. This identical slice was consistently targeted in subsequent SE-EPI and bSSFP scans which utilize B_1 phase information. The phase-based EPT algorithm (Poly-Fit) was then applied to the B_1 phase data (Fig. 1). Simulation experiments were performed to mimic the activation state with varying conductivity values in the local gray matter, akin to in-vivo results. These simulations used 1) a cylindrical model with an infinite z-axis to experimentally observe the relationship between phase and conductivity by varying the conductivity values (Fig. 2 (a)), and 2) the human brain model, Duke, to observe the effects of various EPT reconstructions, the noise effects, and situations where both positive and negative conductivity activations occur simultaneously (Fig. 2 (b)).

Results: In Fig. 3 (a), phase changes around the left motor cortex showed a positive correlation similar to BOLD trends, while reconstructed conductivity had a negative correlation. Fig. 3 (b) summarizes the temporal-series signal averages from the non-activated (right motor cortex) and activated (left motor cortex) regions across ten subjects. Fig. 4 displays results from simulated cylinder models, highlighting an inverse relationship between phase and conductivity—increases in conductivity result in phase decreases and vice versa. This observation points to a conductivity variation of -0.04 S/m in the activation regions, akin to in-vivo observations, identified as Model 5. As illustrated in Fig. 5, the brain model showed a similar trend to the cylinder model. Using the brain Model 8, we applied various phase-based EPT algorithms to the B_1 phase with an SNR of 500. In conditions mimicking in-vivo settings, phase information showed small localized negative correlations around the activation regions, potentially leading to inaccurate (positive) conductivity maps when using segmentation-based EPT or with small kernel sizes. Fig. 6 (a) explores correlation maps across different SNR levels for Model 8, with accurate maps only at SNRs above 300. Fig. 6 (b) presents the outcomes when both positive and negative conductivity activations occur simultaneously, indicating that if activation power in Region 2 (positive activation) is below 25% of that in Region 1 (negative activation), displaying both activations is not feasible.

Discussion and Conclusions: We explored B_1 phase and conductivity changes during brain activation. Similar trends in in-vivo and simulation were observed in both B_1 phase and conductivity. This study considered how brain activation might affect conductivity, potentially influenced by ion concentration and blood oxygenation. It is known that ion concentration increases conductivity[4], but other factors (such as red cell[5]/hemoglobin concentrations[6]/reduced CSF volume) may negatively impact this effect. In this study, a negative correlation of conductivity changes was observed to be dominant, but the need to understand which factors have a greater impact on conductivity changes during the brain activation process remains.

References: [1] Jahng G H (2023), "High-frequency Conductivity Signal Changes Measured with Functional MREPT during Visual Stimulation," In proceedings of 2023 ISMRM Annual Meeting & Exhibition, p. 0923. [2] Jung K J (2023), "Investigation of electrical conductivity changes during functional activity of the brain via phase-based MR-EPT: Preliminary observation," In proceedings of 2023 ISMRM Annual Meeting & Exhibition, p. 0922. [3] Luo J (2024), "Preliminary Whole-Brain Functional Electrical Properties Tomography using Gradient-Echo Echo-Planar Imaging," In proceedings of 2024 ISMRM Annual Meeting & Exhibition, p. 3681. [4] Katscher U (2017), "Electric properties tomography: Biochemical physical and technical background, evaluation and clinical applications," *NMR Biomed* Vol. 30, no. 8, p. 3729. [5] Hirsch F G (1950), "The electrical conductivity of blood: 1. Relationship to erythrocyte concentration," *Blood,* Vol. 5, no. 11, p. 1017. [6] Altaf I M & Ahmad A (2017), "Dielectric properties of human blood of patients suffering from iron deficiency anemia," *IJEST.,* Vol. 6, no. 1, p. 916.
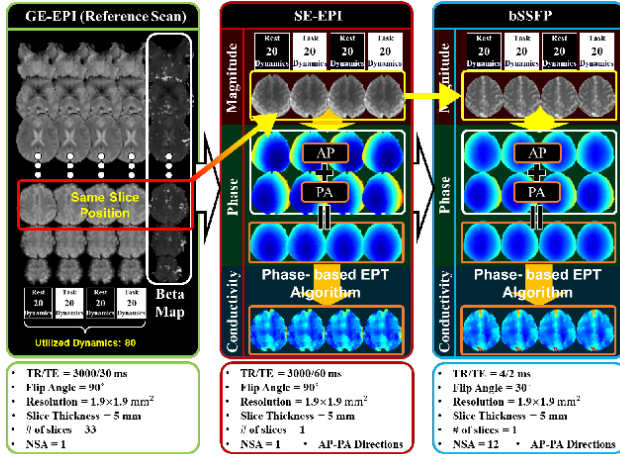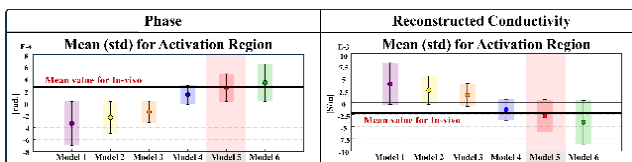
**Figure 1.** MRI scan process for in-vivo experiment (10 volunteers).
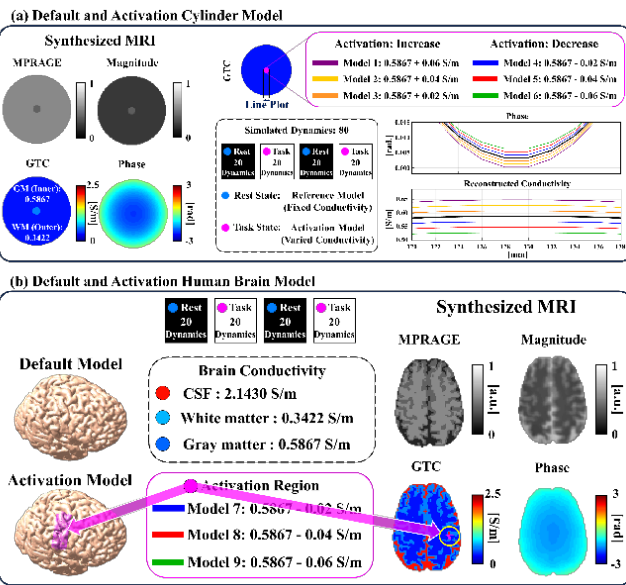
Figure 2. FDTD simulation experiment setting; (a) Cylinder model; (b) Human brain model (Duke).
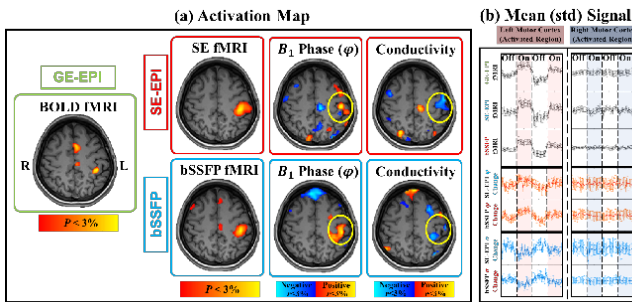

Figure 3. Result for in-vivo experiment; (a) Representative activation map for one volunteer; (b) Mean (std) signals in the motor cortex area for 10 volunteers.


Figure 4. Result for cylinder simulation experiment; Mean and std values in activation regions.
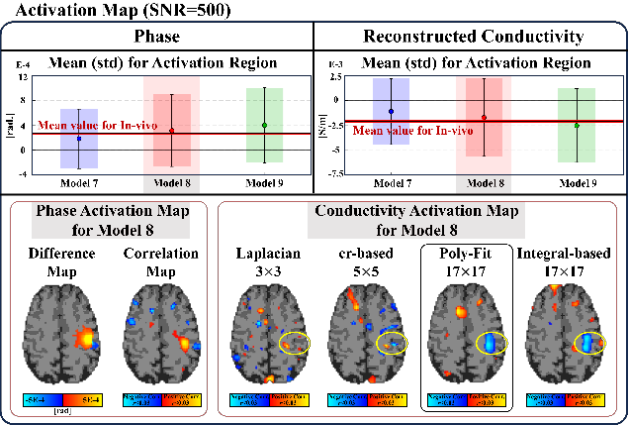
Figure 5. Result for brain simulation experiment; The result includes graphs of the mean and std for activation regions across three different conductivity values for both phase and conductivity. Activation maps are plotted using various phase-based conductivity reconstruction methods; 3×3 Laplacian kernel with gaussian filter; convection-reaction EPT (cr-based EPT); MR-contrast weighted polynomial fitting (Poly-Fit EPT); segmentation based integral EPT (Integral-based EPT)).
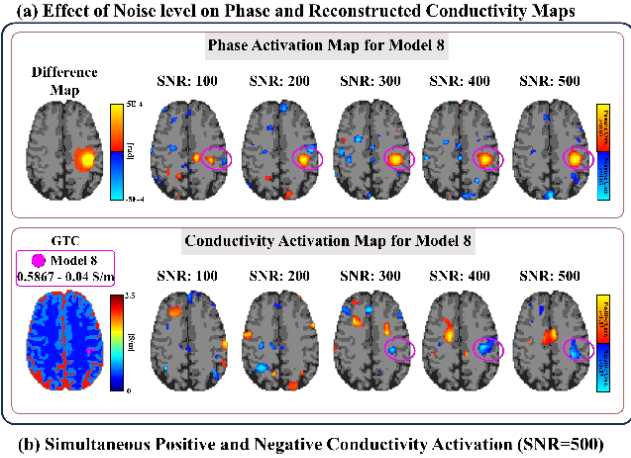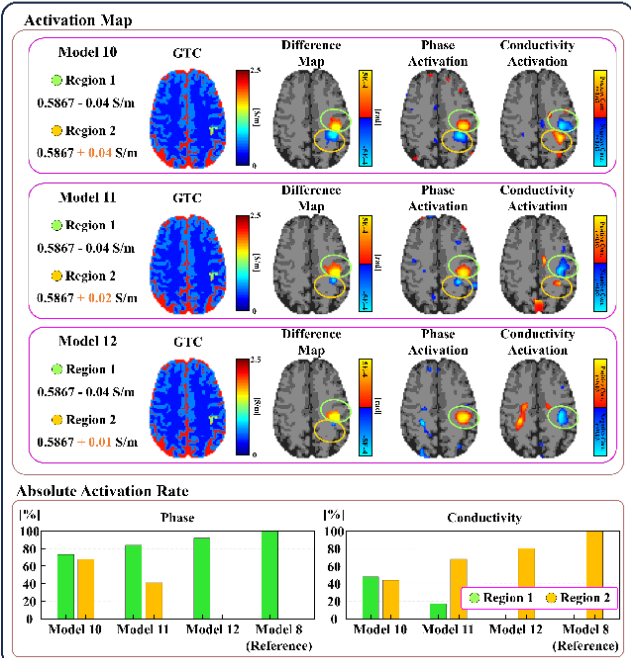
Figure 6. Result for brain simulation experiment; (a) Effects of noise on activations; (b) Effects of simultaneous activations and the absolute activation rate.

QSM based characterization of different kidney stone types and sizes: an ex vivo phantom study

Lion Mücke[1], Frederik B. Laun[1], Guillaume Flé[1], Jennifer Lorenz[1], Alexander Fichte[2], Michael Uder[1], Nadine Bayerl[1*], and Jannis Hanspach[1*]

[1] *Friedrich-Alexander-University Erlangen-Nuremberg, Institute of Radiology, University Hospital Erlangen, Erlangen, Germany;*
[2] *Friedrich-Alexander-University Erlangen-Nuremberg, Department of Urology and Pediatric Urology, University Hospital Erlangen, Erlangen, Germany;*

* shared last authorship

Summary: We present an approach to characterize the magnetic susceptibility of different major kidney stone types, where all examined kidney stones with diameters ≥ 3.4 mm were reliably visualized by QSM. This study represents a first step towards radiation-free, MRI-based detection of kidney stones in clinical routine for suspected urolithiasis.

Introduction: In patients with flank pain and hydronephrosis detected on ultrasound, which strongly suggests urolithiasis, unenhanced CT with ionizing radiation is performed as the reference standard for the detection of kidney stones in routine clinical practice.[1] While CT reliably visualizes most kidney stone types, there are two radiolucent entities: indinavir-induced stones in patients with HIV, and pure matrix stones consisting of proteinaceous material.[1] Therefore, a CT scan may be negative even if kidney stones are present. The most common chemical compositions of kidney stones are calcium oxalate, struvite, calcium phosphate ("carbonate atapatite", CaP), uric acid, and cystine (CY).[1] Recently, two kidney stones of unknown chemical composition, with a size of 9 mm and 10 mm, were visualized in renal MRI using QSM.[2]

The objective of this work was to characterize multiple kidney stone types of known chemical compositions and varying sizes in an ex vivo phantom using quantitative susceptibility maps.

Methods: A total of 21 kidney stones from 21 different patients, each with one of 8 different chemical compositions and diameters ranging from 2.3 mm to 10.6 mm, were investigated. The stones were sorted by patient and type, with each stone having at least one visually identical counterpart in the sample collection. Since the stones were destroyed during the chemical analysis using infrared spectroscopy, one of the additional counterparts was analyzed using QSM instead. Chemical compositions of the kidney stones consisted of: 6× Calcium oxalate monohydrate (CaOx), 5× UA (80% uric acid with 20% Monoammoniumurate), 3× CaP, 2× CY, 2× ST (70% struvite with 30% CaP), 1× 80% CaP with 20% CaOx, 1× CAOx-di (60% Calcium oxalate dihydrate with 40% CaOx), 1× 60% CaP with 40% ST. To ensure consistency regarding the chemical composition, we plan to submit the investigated stones for chemical analysis after finalizing this study. The phantom containing the kidney stones was built by filling a cylindrical plastic box (height 16 cm, radius 6 cm) in four steps with a water-based solution, made of 2% Agar-Agar and 0.5% NaCl. For the first three layers of Agar-Agar solution, 7 of the 21 kidney stones were placed on top of the respective layer after hardening (see Fig. 1). In this way, the stones inside the phantom were sealed without visible air pockets when the next layer was poured on top.

Data were acquired using a multi-echo 3D gradient-echo (GRE) sequence on a 1.5T MRI scanner (MAGNETOM Sola, Siemens Healthineers) with a 20-channel head-and-neck coil (Siemens Healthineers). The acquisition parameters were: TE = 3.08/8.02/12.96/17.90 ms, ΔTE = 4.94 ms, TR = 22 ms, voxel size = 0.8×0.8×0.8 mm³, flip angle = 12°, bandwidth = 320 Hz/px, no acceleration, 7 averages, with a total acquisition-time of 54:06 min.

Calculations for the reconstruction of susceptibility maps were performed in MATLAB (R2022b; MathWorks, USA) utilizing the SEPIA toolbox (with MRITOOLS v3.6.6, MEDI-toolbox downloaded Dec 2022, STISuite_V3.0). First, masks of the phantom were created by thresholding the magnitude images. Phase unwrapping and echo phase combination were performed with ROMEO and optimum weights respectively, before removing the background fields via the VSHARP algorithm (max. radius = 10, min. radius = 3). Finally, the susceptibility maps were reconstructed using MEDI (referenced to the phantom mask, lambda = 50, SMV = 5). The investigated kidney stones were manually segmented via thresholding based on the GRE magnitude image of the first TE. The corresponding mean susceptibility value and the standard deviation (SD) were calculated for each stone.

Results: All kidney stones were clearly visible using QSM and appeared as hypointense regions in the susceptibility map (Fig. 2). The mean susceptibility values of the 21 kidney stones, referenced to the Agar-Agar solution are presented in Fig. 3, together with the respective SD. All investigated stones were diamagnetic compared with the Agar-Agar solution, with mean susceptibility values ranging from -0.82 ppm to -2.47 ppm. Some of the small stones exhibited low susceptibility values close to 0 ppm. The SD were similar for the investigated larger kidney stones. Mean susceptibility values slightly increased with the diameter size of the stones. Excluding sizes ≤ 2.5 mm, the overall mean susceptibility values of the five investigated major chemical compositions are denoted in Table 1. Stones composed of CY and CaP, appeared to be more diamagnetic, lacking clear differentiation due to the large SD. Starting at diameters of 6.2 mm, some

stones visually exhibited noisy inhomogeneities in the susceptibility map (see orange arrows, Fig. 2). This effect increased with larger diameters, regardless of the chemical composition.

Figure 1 Representative layer with 7 kidney stones on top of the hardened Agar-Agar solution, before sealing them in the phantom with the next layer.
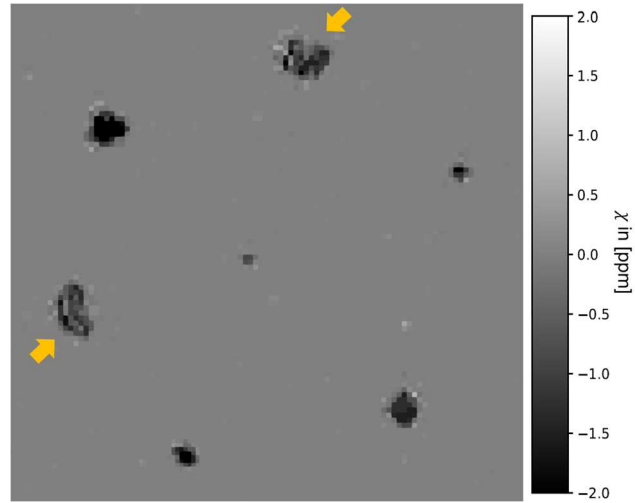
Figure 2 Representative susceptibility map depicting the 7 kidney stones of Figure 1 as hypointense regions, where the largest two (highlighted by orange arrows) visually exhibit noise-like inhomogeneities.
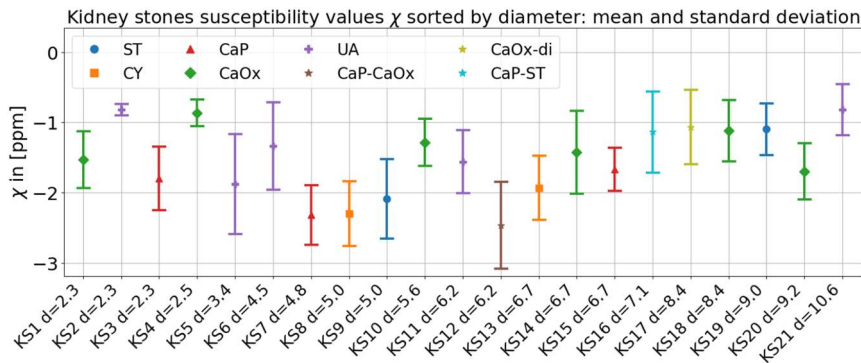
Figure 3 Mean susceptibility values and SD in [ppm] for each of the 21 investigated kidney stones (KS), sorted by diameter (d) in [mm] along the x-axis. Kidney stones of identical chemical composition are displayed in the same color.

Type	Mean susceptibility in [ppm]
CaOx	-1.38 ± 0.94
UA	-1.40 ± 1.20
CaP	-1.99 ± 0.69
CY	-2.12 ± 0.70
ST	-1.59 ± 0.97

Table 1 Mean susceptibility values and SD for the five investigated major types of kidney stones with diameters > 3 mm.

Discussion and Conclusions: This study demonstrated that kidney stones of the five major chemical compositions present as diamagnetic regions compared with a water-based Agar-Agar phantom in susceptibility maps, suggesting that QSM is a reliable MRI technique for detecting kidney stones with diameters ≥ 3.4 mm in vivo. The noisy inhomogeneities might be a result of noise amplification, since the stones provide only little MRI signal.[3] Recently, artifacts caused by air inclusions in the rectum were considerably reduced by a deep learning-based dipole inversion in prostate QSM.[4] As air inclusions are also regions of low SNR, adapting this approach could potentially reduce the noisy inhomogeneities of the investigated kidney stones. Future studies should investigate a larger number of kidney stone types CaP, CY and ST, as well as more infrequent types.[1] Lastly, destroying the kidney stones during chemical analysis gives rise to uncertainties regarding the definite chemical compositions, since the investigated stones can only be analyzed after the study.

We have demonstrated that QSM can visualize all major types of kidney stones, marking a crucial step towards in vivo and radiation-free imaging for suspected urolithiasis in clinical practice.

References:
[1] Cheng et al. (2012), "What the Radiologist Needs to Know About Urolithiasis: Part 1 - Pathogenesis, Types, Assessment, and Variant Anatomy", *AJR,* vol. 198, pp. W540-W547, doi: https://doi.org/10.2214/AJR.10.7285
[2] Schumacher et al. (2024), "Quantitative susceptibility mapping for detection of kidney stones, hemorrhage differentiation and cyst classification in ADPKD", *medRxiv.*, doi: https://doi.org/10.1101/2024.02.24.24303322.
[3] Dimov et al. (2023), "QSM Throughout the Body", *J. Magn. Reson. Imaging*, vol. 57.6, pp. 1621–1640, doi: https://doi.org/10.1002/jmri.28624
[4] Hanspach et al. (2022), "Deep learning–based quantitative susceptibility mapping (QSM) in the presence of fat using synthetically generated multi-echo phase training data", *Magn. Reson. Med.*, vol. 88.4, pp. 1548–1560, doi: https://doi.org/10.1002/mrm.29265

Optimising EPT to Assess Brain Conductivity in Tanzanian Children with Sickle Cell Anaemia at 1.5T

Philippa Sha[1], Jierong Luo[1], Oriana Arsenov[1], Mitchel Lee[1], Fenella Kirkham[2], Karin Shmueli[1]

[1] Department of Medical Physics and Biomedical Engineering, University College London, London, United Kingdom.
[2] Imaging and Biophysics, Developmental Neurosciences, Institute of Child Health, London, United Kingdom.

Summary: Here, we optimised a phase-based EPT pipeline for the first study investigating the effect of SCA on brain tissue conductivity in Tanzanian children at 1.5T. The optimised pipeline, including MP-PCA denoising and automatic selection of the magnitude weighting kernel parameter, produced high-quality conductivity maps throughout a representative sample of 10 subjects and will now allow investigation of conductivities in the full cohort.

Introduction

Sickle cell anaemia (SCA) is a genetic blood disorder that causes haemoglobin to polymerize and red blood cells to become sickle-shaped. SCA is known to affect normal neurocognition, and poses serious risks such as haemorrhagic or ischaemic stroke[1]. This study aims to assess, for the first time, the effect of SCA on brain tissue electrical conductivity (at ~64 MHz). Here, a pipeline for performing phase-based MR Electrical Properties Tomography (EPT)[2] was optimised for complex data originally acquired for quantitative susceptibility mapping at 1.5T[3].

Methods

EPT was optimised in a representative sample: 10 Tanzanian children, 5 with SCA and 5 healthy controls (HCs), aged 12.4 ± 4.1 years, 7/3 male/female, from a total cohort of 163 children with SCA and 47 HCs, aged 12.6 ± 3.9 years.

MRI acquisition: T2*-weighted multi-echo 3D GRE and T1-weighted MPRAGE were acquired at 1.5T (Phillips, Achieva) using either an 8-channel or birdcage RF coil. 3D-GRE sequence parameters were: 5 echoes, TE_1 = 4.28 ms, ΔTE = 4.94 ms, TR = 27.4 ms, resolution = 1.458 x 1.45 8 x 1.5 mm^3, bandwidth = 287 Hz/pixel, flip angle = 15°.

EPT: An existing EPT pipeline[4] was optimised as follows. To account for poorer SNR at 1.5T compared to 3T, MP-PCA denoising[5] was applied to the raw complex images. Field correction[6] was applied to remove 'pseudo-wraps' occurring in the complex image[7]. Complex images were unwrapped using SEGUE[8]. MR transceive phase φ_0 was estimated by extrapolation and unwrapped again using SEGUE. A binary mask was generated from the raw magnitude image at TE2 using FSL-BET[9]. Using integral-form EPT[10], quantitative conductivity maps (QCMs) were reconstructed using 3D quadratic fitting with both magnitude- and segmentation-based weighting (*MagSeg*), for greater edge preservation[4].

Kernel size optimisation: In a conductivity phantom (1mm isotropic resolution, simulated at 128MHz, Sim4Life[11]) with Gaussian noise added to match the SNR of the data (mean = 13.8), the kernel radius for both the differential (k_{diff}) and integral kernels (k_{int}) was varied, between 4-18 mm and 4-32 mm with a stepsize of 1 mm, respectively. Mean absolute error (MAE) and error in the CSF were computed between the resulting conductivity maps and the ground truth.

Segmentation optimisation: For segmentation of grey matter (GM), white matter (WM) and cerebrospinal fluid (CSF), we compared: SPM[12] on the 2nd echo GRE magnitude image (as this was the only echo that provided consistent segmentation), SPM on the co-registered T1-weighted (T1w) image, and FSL-FAST[13] on the same T1w image.

Magnitude weighting optimisation: We compared magnitude echoes 2 and 5 (TE2/5), and the combined-echo magnitude[14]. The value of the δ parameter used for magnitude weighting was varied between 0.15–0.65. We also implemented a new method of varying δ automatically depending on phase noise levels[15].

Results and Discussion

Denoising: Figure 1 shows that, in general, applying MP-PCA denoising resulted in more detailed conductivity maps with greater contrast.

Kernel size: For almost all kernel sizes tested, the minimum MAE and CSF error were obtained at k_{diff} = 15 mm and k_{int} >= 25 mm. Higher k_{int} values achieved an even lower error, but at the risk of over-smoothing within the reconstructed image. Therefore, 25 mm was deemed the best compromise.

Fig. 1: Conductivity maps in an axial slice of a representative HC subject reconstructed without/with MP-PCA denoising. MP-PCA denoising increased GM-WM contrast in some regions (indicated by black arrow).

Segmentation method: Figure 2 shows that, as expected, segmentations using the T1w image provide better contrast between tissue types, especially at GM-WM boundaries. FSL-FAST provided greater detail and a substantial increase (of 0.44 S/m) in median CSF conductivity values, excluding negative values, compared to SPM.
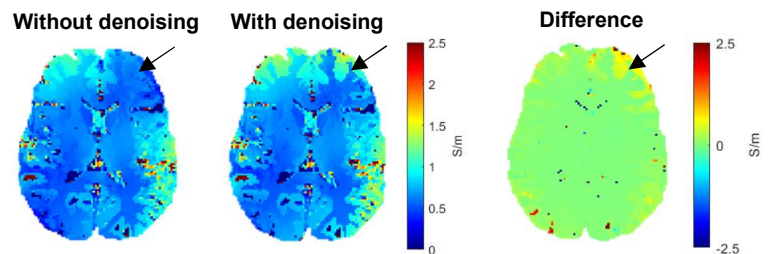
Magnitude method: There was very little visual difference in conductivity maps between using different magnitude-weighting inputs, with combined-echo magnitude providing slightly better GM-WM contrast. For selection of δ, our method of automatically varying δ was optimal in reducing noise.

Preliminary conductivity results in SCA vs HCs: The results of applying the optimised pipeline to the 10 subjects is shown in Figure 3. Although

Fig. 2: Conductivity maps in an axial slice of a representative HC subject using different segmentation methods for EPT segmentation weighting.

there were no statistically significant differences between groups, these preliminary results suggest that children with SCA exhibit greater conductivity compared to healthy controls in both GM and WM, but not in CSF.
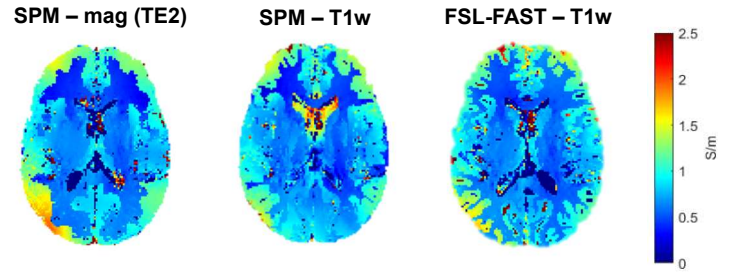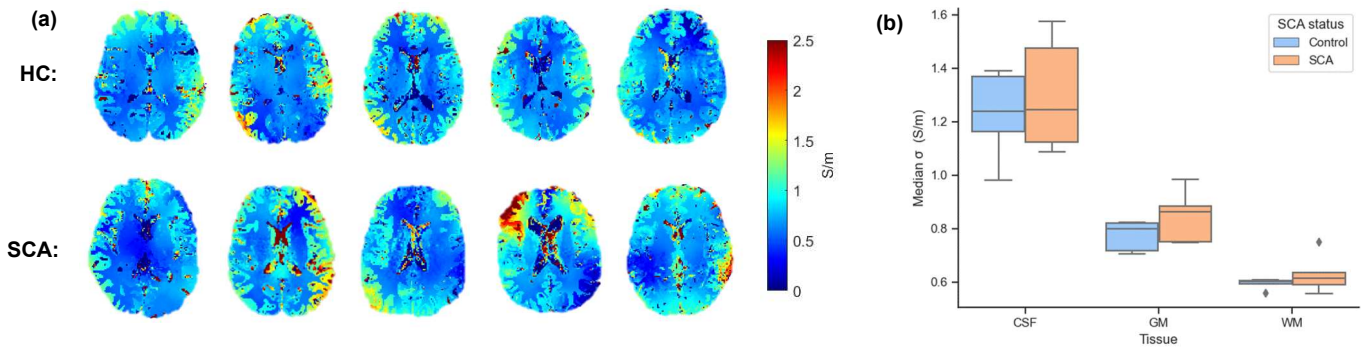

Fig. 3(a): Conductivity maps generated using the optimised EPT pipeline. Fig. 3(b): Median conductivity values for each tissue type, segmented using FSL-FAST on T1w images, excluding negative values.

Conclusion

Here, we optimised a phase-based EPT pipeline to investigate the effect of SCA on brain tissue conductivity, in Tanzanian children at 1.5T. Denoising and field correction were implemented. Optimal reconstruction parameters were found to be: $k_{diff} = 15$ mm, $k_{int} = 25$ mm, FSL-FAST segmentation on the T1w image, and combined-echo magnitude input with automatically varying δ. This pipeline consistently produced high-quality conductivity maps and will now allow investigation of conductivities in the full cohort.

References:

[1] Farooq, S. et al. Neurologic Complications of Sickle Cell Disease. Curr Neurol Neurosci Rep. 2019; 19(4):17.
[2] Katscher, U. et al. Electric properties tomography: Biochemical, physical and technical background, evaluation and clinical applications. NMR Biomed. 2017; 30(8):e3729.
[3] Lee, M. et al. Improved QSM pipeline to investigate the effect of sickle cell anaemia on brain magnetic susceptibility in Tanzanian children at 1.5 Tesla. Proc. Ann Meeting ISMRM 2024; 4828.
[4] Karsa, A. et al. New approaches for simultaneous noise suppression and edge preservation to achieve accurate quantitative conductivity mapping in noisy images. Proc. Ann. Meeting ISMRM 2021; 3774.
[5] Doniza, L. et al. MP-PCA image denoising technique for high resolution quantitative susceptibility mapping (QSM) of the human brain in vivo. Proc. Ann. Meeting ISMRM 2023; 2948.
[6] De Rochefort, L. et al. Quantitative susceptibility map reconstruction from MR phase data using bayesian regularization: Validation and application to brain imaging. Magn Reson Med. 2010; 63:194–206.
[7] Spincemaille, P. et al. Correction of residual echo-to-echo phase inconsistencies in readout phase corrected multi-echo gradient echo for quantitative susceptibility mapping. ISMRM 4th International Workshop on MRI Phase Contrast & Quantitative Susceptibility Mapping. 2016; 46.
[8] Karsa, A. et al. SEGUE: A Speedy rEgion-Growing Algorithm for Unwrapping Estimated Phase. IEEE Trans Med Imag. 2019; 38(6):1347-1357.
[9] Smith, S.M. Fast robust automated brain extraction. Human Brain Mapping. 2002; 17(3):143-155.
[10] Voigt, T. et al. Quantitative conductivity and permittivity imaging of the human brain using electric properties tomography. Magn Reson Med. 2011; 66(2):456-466
[11] Meerbothe, T.G. et al. A database for MR-based electrical properties tomography with in silico brain data – ADEPT. Magn Reson Med. 2023; 91(3):1190-1199.
[12] Ashburner, J. et al. Spm12 manual. Wellcome Trust Centre for Neuroimag. 2014; 2464.
[13] Zhang, Y. et al. Segmentation of brain MR images through a hidden Markov random field model and the expectation-maximization algorithm. IEEE Trans Med Imag. 2001; 20(1):45-57.
[14] Poser, B.A. et al. Investigating the benefits of multi-echo EPI for fMRI at 7T. NeuroImage. 2009; 45(4):1162-1172.
[15] Luo, J. et al. An automatically optimised Gaussian weighting function width for magnitude-weighted phase-based electrical properties tomography (EPT). Proc. Ann. Meeting ISMRM 2024; 137.

Comparison of Susceptibility Source Separation Methods without R_2

Patrick Fuchs, Matthew T. Cherukara, Karin Shmueli

Department of Medical Physics and Biomedical Engineering, University College London, London, United Kingdom

Summary: We compared DECOMPOSE, χ-separation and χ-sepnet: R_2^*-based susceptibility source separation methods. All provided good quality visual maps and source separation for both 5 and 12 echo datasets. χ-sepnet was the most computationally efficient and precise of these methods.

Introduction: Susceptibility source separation methods allow separation of diamagnetic and paramagnetic sources co-located in a voxel. This is possible due to the distinct effects of susceptibility on the tissue relaxation rate and on the magnetic field. These contributions can be used to separate co-located sources whose susceptibilities destructively interfere due to their opposing sign.

The relationship between susceptibility and relaxation rate is not straightforward. This means that, unless the transverse relaxation rate R_2 is mapped separately, to allow direct estimation of R_2' from the R_2^* relaxation rate, assumptions need to be made about the contribution of the susceptibility to R_2^*. In many clinical applications there may not be matched R_2 or spin-echo acquisitions. In these cases, there are currently three published algorithms that allow for an approximate separation of paramagnetic and diamagnetic sources. These are: the DECOMPOSE algorithm from Chen et al.[1], χ-separation and χ-sepnet by Shin et al.[2], and QSM-ARCS by Kan et al.[3]. Of these, all except for the most recently published QSM-ARCS are publicly available[1]. In this abstract, we compared the available algorithms on a 12-echo and a 5-echo dataset to investigate how well their very different approaches relate and highlight potential caveats of the respective methods.

Methods: The methods were compared using acquisitions with a different number of echoes. We acquired 3D-GRE using both 12echoes and 5 echoes on a 3T Prisma system (Siemens AG, Erlangen, Germany) in a healthy volunteer with prior approval from our local ethics committee during a single scan session. The acquisition parameters were: 1 mm^3 isotropic resolution, 15° flip angle, 3-fold parallel imaging acceleration, with a 192×256×176 mm field of view. Echo times were (TE_{first}/ΔTE/TE_{last}) 2,03/1.59/30 and 5/7/38 ms with a bandwidth of 890 Hz/pix and 280 Hz/pix for the 12 and 5-echo acquisitions, respectively. For anatomical segmentation a T1 weighted MPRAGE acquisition with 1mm isotropic resolution was acquired. Since χ-sepnet essentially incorporates a QSMnet[4]-like reconstruction in the separation algorithm and it has been shown that DECOMPOSE is sensitive to the dipole inversion algorithm choice[5] all data were processed using the pipeline provided with χ-sepnet: Laplacian based phase unwrapping[6], V-SHARP background field removal[7] using a mask generated with FMRIB's brain extraction tool[8] (BET), and QSMnet to compute input susceptibility maps. .As χ-separation and χ-sepnet use a combined local field map input (as opposed to separate echoes for DECOMPOSE) the multi-echo phase was combined using non-linear fitting[9] from the MEDI Toolbox prior to the processing described above. To generate the proxy R_2' maps used in χ-separation and χ-sepnet, R_2^* maps were computed using ARLO[10]. Both algorithmic variations of χ-separation are included separately (MEDI+0, and iLSQR regularised, these are not the input QSM methods). All algorithms were run with their default parameters.

To compare the maps several brain regions of interest were segmented. The thalamus, putamen, caudate, globus pallidus and substantia nigra were segmented using MRICloud[11], and the corpus callosum was segmented using FreeSurfer[12] on the T1 image as it is optimal for white matter.

Results: Figure 1 shows a visual comparison of the outputs from the various methods. Figure 2 shows ROI comparisons for four primarily paramagnetic and two primarily diamagnetic regions of interest.

Discussion and Conclusions: Figure 1 shows that the MEDI based χ-separation algorithm suffers from artefacts (highlighted with red dashed circles), originating near the nasal cavity. Further, in the frontal lobe the separated maps look like thresholded bulk susceptibility maps (not shown). This results in no clear delineation of the substantia nigra which is corroborated in Figure 2 where the variance in the substantia nigra is much larger than the variance of any of the other approaches.

---

[1] χ-separation and χ-sepnet can be downloaded from the public repository at https://github.com/SNU-LIST/chi-separation. DECOMPOSE will be formally released with the next version of STI-Suite but is available upon request from the original authors.

The other approaches yield similar visual results, with DECOMPOSE and χ-sepnet appearing least noisy, and χ-sepnet having a notably higher contrast in the diamagnetic component compared to DECOMPOSE. This contrast difference is not reflected in the ROI statistics in Figure 2 which suggest that χ-separation (especially the χ-separation iLSQR based method) yields better apparent separation, that is higher paramagnetic and more strongly diamagnetic (lower) mean values, when compared to the other approaches and the QSM. χ-separation does come with an increased variance, which corroborates the lower visual quality of these maps.

Without a ground truth it is not possible to compare the accuracy of the models. In terms of precision, χ-sepnet generally provides the lowest variance within these ROIs, likely due to its powerful machine-learning-based denoising. DECOMPOSE shows the lowest sensitivity to the number of echoes but takes much longer to compute (multiple hours) χ-sepnet is computationally the fastest, with χ-separation in between those.

References

1. Chen, J., Gong, N.-J., Chaim, K. T., Otaduy, M. C. G. & Liu, C. Decompose quantitative susceptibility mapping (QSM) to sub-voxel diamagnetic and paramagnetic components based on gradient-echo MRI data. *NeuroImage* **242**, 118477 (2021).
2. Shin, H.-G. *et al.* χ-separation: Magnetic susceptibility source separation toward iron and myelin mapping in the brain. *NeuroImage* **240**, 118371 (2021).
3. Kan, H. *et al.* Quantitative susceptibility mapping for susceptibility source separation with adaptive relaxometric constant estimation (QSM-ARCS) from solely gradient-echo data. *NeuroImage* **296**, 120676 (2024).
4. Yoon, J. *et al.* Quantitative susceptibility mapping using deep neural network: QSMnet. *NeuroImage* **179**, 199–206 (2018).
5. Fuchs, P. *et al.* RECOMPOSE – Reproducing DECOMPOSE Using Susceptibility Maps Acquired for Clinical Research. in *Joint Annual Meeting ISMRM-ESMRMB & ISMRT 32st Annual Meeting* (Toronto, Canada, 2023).
6. Zhou, D., Liu, T., Spincemaille, P. & Wang, Y. Background field removal by solving the Laplacian boundary value problem. *NMR Biomed.* **27**, 312–319 (2014).
7. Li, W., Wu, B. & Liu, C. Quantitative susceptibility mapping of human brain reflects spatial variation in tissue composition. *NeuroImage* **55**, 1645–1656 (2011).
8. Smith, S. M. Fast robust automated brain extraction. *Hum. Brain Mapp.* **17**, 143–155 (2002).
9. Liu, T. *et al.* Nonlinear formulation of the magnetic field to source relationship for robust quantitative susceptibility mapping. *Magn. Reson. Med.* **69**, 467–476 (2013).
10. Pei, M. *et al.* Algorithm for fast monoexponential fitting based on Auto-Regression on Linear Operations (ARLO) of data. *Magn. Reson. Med.* **73**, 843–850 (2015).
11. Mori, S. *et al.* MRICloud: Delivering High-Throughput MRI Neuroinformatics as Cloud-Based Software as a Service. *Comput. Sci. Eng.* **18**, 21–35 (2016).
12. Laboratories for Computational Neuroimaging. FreeSurfer. Athinoula A. Martinos Center for Biomedical Imaging.
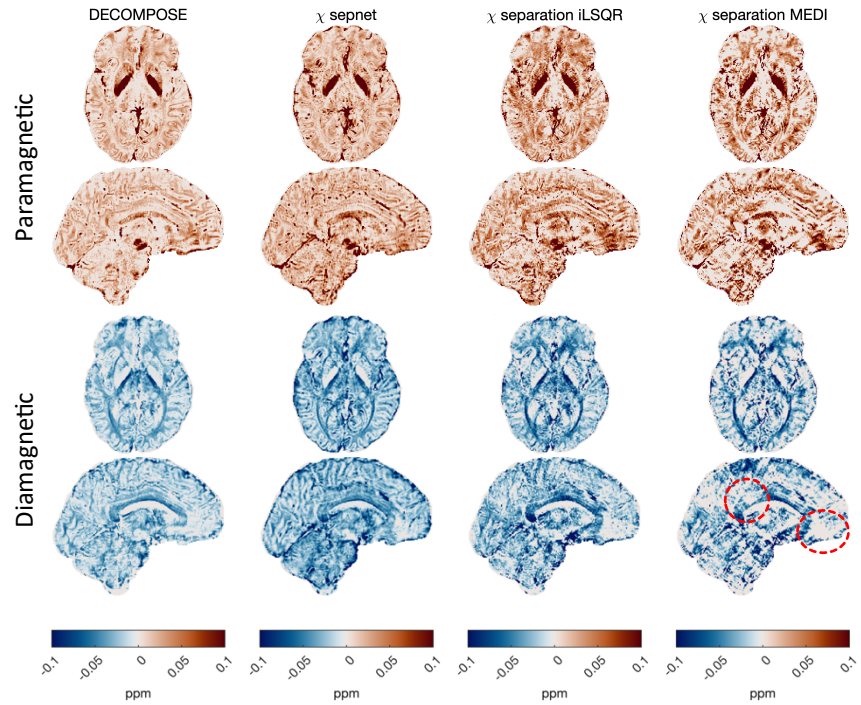
Figure 1 Axial and sagittal slices of the four different source separation algorithms (columns). Paramagnetic (positive) sources at the top, and diamagnetic (negative) sources at the bottom. Data are shown for the 5-echo acquisition. Red circles denote artifacts.

Figure 2 Box plots comparing model outputs for four paramagnetic and two diamagnetic deep brain structures. QSM denotes the input QSMNet reconstruction used in the χ-separation iLSQR and MEDI approaches. DCS: diamagnetic component susceptibility and PCS: paramagnetic component susceptibility.

Bi-parametric Joint Label Fusion:
A Comprehensive Segmentation Tool for Deep Gray Matter in QSM
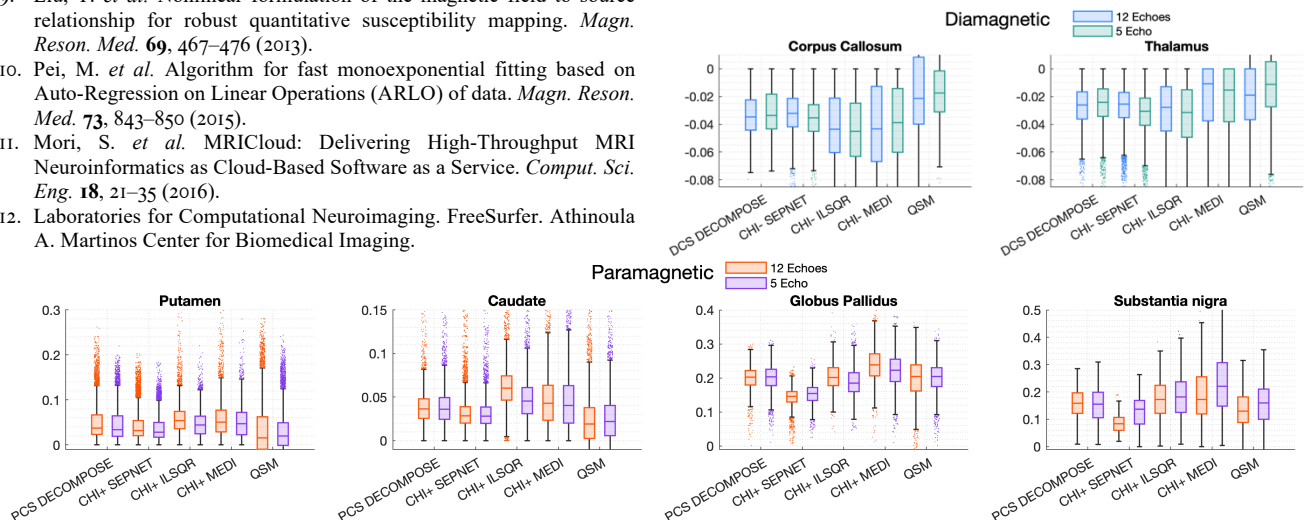
Fahad Salman[1,3], Kevin Thomas[1], Ademola Adegbemigun[1], Niels Bergsland[1], Michael G. Dwyer[1,2], Robert Zivadinov[1,2], and Ferdinand Schweser[1,2]

[1]*Buffalo Neuroimaging Analysis Center, Department of Neurology at the Jacobs School of Medicine and Biomedical Sciences, University at Buffalo, The State University of New York, Buffalo, NY, United States;* [2]*Center for Biomedical Imaging, Clinical and Translational Science Institute, University at Buffalo, The State University of New York, Buffalo, NY, United States;* [3]*Department of Biomedical Engineering, University at Buffalo, The State University of New York, Buffalo, NY, United States*

Summary

We developed a novel method combining bi-parametric (QSM+T1w) and multi-atlas segmentation approaches, significantly improving DGM segmentation accuracy. This method outperformed existing techniques, enhancing QSM-focused clinical and research applications in neurodegenerative diseases.

Introduction

Most publicly available methods for automated deep gray matter (DGM) segmentation are based on T1-weighted (T1w) contrast.[1-7] Studies have demonstrated that low T_1w contrast in some DGM regions can lead to poor segmentation results,[8,9] especially in individuals with neurodegenerative diseases (e.g., multiple sclerosis).[27,28] Systematic segmentation errors can lead to bias in regional susceptibility measurements, especially in the thalamus, which atrophies rapidly in some neurological diseases such as multiple sclerosis, and shows particularly low T_1w contrast.[10,11] To address this limitation, studies proposed bi-parametric[12] (quantitative susceptibility mapping [QSM]+T_1w) and (longitudinal) multi-atlas-based segmentation[13,14] techniques. These approaches were shown to improve DGM segmentation compared to single contrast atlas-based methods (e.g., only T_1w); however, a method combining these promising efforts into a single algorithm is currently lacking.

Hence, we propose to build on the existing work[12-14] by merging bi-parametric and multi-atlas approaches. The combined method was then executed using the Advanced Normalization Tools (ANTs) joint label fusion (JLF)[16], a function which originally segmented regions based on multiple atlases but only accepted one contrast at a time. Therefore, we also extended JLF toward bi-parametric contrast with equal weighting on QSM and T_1w contrast[12]. Our approach performs a regional majority voting system using all bi-parametric atlases' (*N*=9) warp transformation fields to the native subject space (e.g., a segmented region-of-interest [ROI] voxel is true [1] if 80% [7/9] of the atlases agree). These advancements have not yet[13] reached QSM users interested in the DGM segmentation. We compared the segmentation outcomes from our proposed method to state-of-the-art publicly available methods[1,3,5] with manual segmentation as the ground truth (GT).

Methods

<u>Subjects and data acquisition</u>: We used our lab's institutional database inclusive of 4540 and 691 scans with and without neurological disorder, respectively, to generate multiple atlases used for JLF.[16] This principally-retrospective study also enrolled five healthy subject scans for segmentation performance investigation (age average = 25±1 years). The study was approved by the local Ethical Standards Committee at the University at Buffalo, and a written informed consent form was obtained from all participants. All participants' scans were acquired as described previously.[17]

<u>QSM reconstruction</u>: Raw k-space data from a single-echo gradient echo (GRE) were processed using scalar-phase-matching[18], gradient unwrapping[19], best-path unwrapping[20], RESHARP[21] and HEIDI[22] to generate QSM images.

<u>GT segmentations</u>: An experienced rater (K.Th; 2 years of experience) performed manual bi-lateral DGM (caudate, putamen, globus pallidus (GP), and thalamus) segmentations on each subject's native QSM scan (*N*=5).

<u>Multiple (*N*=9) templates for JLF</u>: We rigidly aligned the magnitude GRE images with their respective T1w images (T1wi) using FSL FLIRT.[23] We utilized the resulting transformation matrix to register susceptibility maps to their respective T1wi. These registered QSM and T1wi were then used to generate multiple (9) group-specific bi-parametric templates, utilizing low, medium, and high tertials, each for age, volume, and DGM average-susceptibility from our lab's overall database. Each template included an equal ratio of sex and disease representation, incorporating 60 subject scans per group-specific tertile, adhering to the minimum number of scans required for template generation.[25] All templates were generated using ANTs (antsMultivariateTemplateConstruction2.sh).[24]

<u>JLF-based segmentation</u>: A neuroimaging researcher (F.Sa; 5 years of experience) segmented the DGM regions on the resulting (9) templates utilized for the proposed version of the JLF. All JLF-segmented ROIs were warped to the

native QSM space using majority voting from all (9) warp transformation fields obtained from QSM-T_1w bi-parametric (equal contrast weighting) template to native subjects' QSM registrations.

T_1w-based segmentation: FIRST[1], Freesurfer[3], and SynthSeg[5] were applied to subjects' native T_1wi. Following this, all ROIs were warped back on to subjects' native QSM space using the inverse transformation obtained from the QSM to T_1wi registration.
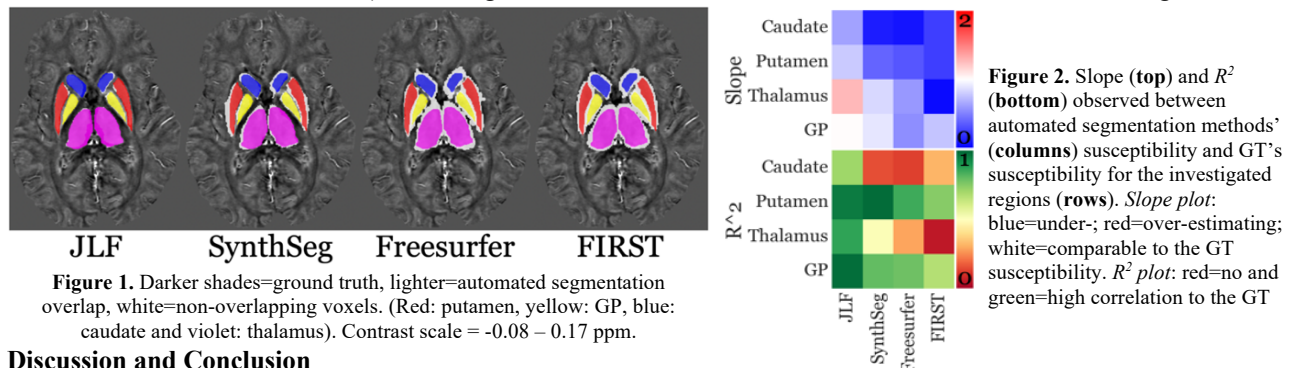
ROI corrections: Corrections ensured each segmentation method matched the GT slice count for consistent analysis.

ROI referencing and analysis: For each ROI, we calculated the regional average susceptibility, referenced it to the whole brain[17], and computed R^2 correlations and slopes compared to the GT. Additionally, we computed overlapping voxels for ROIs from each segmentation method (not displayed), as described earlier.[26]

Results

Figure 1 shows a representative QSM image with automated segmentations (JLF and native T_1w-based methods) overlaid on the GT delineations. Notably, only JLF exhibits minimal voxels outside the GT ROIs (total non-overlap = 8%), while staying within regional boundaries. Other methods extend into the neighboring regions (SynthSeg=33%, Freesurfer=54%, and FIRST=50%), except for the GP ROIs using SynthSeg (visually).

Figure 2 shows that JLF exhibit high correlations (average DGM R^2=0.9) with the GT's regional susceptibility findings. As for the other methods' R^2 correlations, they were at most, moderate (SynthSeg=0.61, Freesurfer=0.51; FIRST=0.45 [weak]). JLF did not under/over-estimate the susceptibility findings compared to the GT (overall DGM slope=1). However, other methods always underestimated the susceptibility by at least 32% (SynthSeg slope=0.68, Freesurfer=0.54, and FIRST=0.48), on average. None of the methods resulted in an overestimation on average.

Figure 1. Darker shades=ground truth, lighter=automated segmentation overlap, white=non-overlapping voxels. (Red: putamen, yellow: GP, blue: caudate and violet: thalamus). Contrast scale = -0.08 – 0.17 ppm.

Figure 2. Slope (**top**) and R^2 (**bottom**) observed between automated segmentation methods' (**columns**) susceptibility and GT's susceptibility for the investigated regions (**rows**). *Slope plot*: blue=under-; red=over-estimating; white=comparable to the GT susceptibility. R^2 *plot*: red=no and green=high correlation to the GT

Discussion and Conclusion

In this study, we introduced a segmentation tool that utilizes both QSM and T_1wi contrasts, which are known to enhance registration, hence, the segmentation outcomes by utilizing the best contrast for deep brain regions in QSM and cortical regions in T_1wi.[12,15] The proposed tool outperformed publicly available segmentation methods.[1,3,5] Native T_1wi image-based segmentations suffers from significant errors, as shown by us and others[11-14], reducing statistical power[11] and potentially masking group differences in prior studies.

In conclusion, our proposed tool offers a versatile segmentation method due to its incorporation of the bi-parametric (QSM-T1w) atlases that span over a wide range of age, volume, and overall DGM susceptibility contrast. Our proposed tool and all atlases (with ROIs) are publicly available at *https://gitlab.com/R01NS114227/antsjointlabelfusion_biparametric.git*. Users should use both contrast atlases to achieve optimal segmentation outcomes. Additionally, one can apply all atlases in combination or select specific atlases based on the characteristics of the subject scan, utilizing our extended version of the ANTs JLF.

References

[1] Patenaude, B. et al. NeuroImage (2011). [2] Klein, A. et al. Front. Neurosci. (2012). [3] Fischl, B. NeuroImage (2012). [4] Dale, A.M. et al. NeuroImage (1999). [5] Billot, B. et al. Medical Image Analysis (2023). [6] Lancaster, J.L. et al. Hum. Brain Mapp. (2000). [7] Mazziotta, J. et al. Philos. Trans. R. Soc. Lond. B Biol. Sci. (2001). [8] Cobzas, D. et al. J. Magn. Reson. Imaging (2015). [9] Feng, X. et al. Magn. Reson. Imaging (2017). [10] Burggraag, J. et al. NeuroImage: Clinical (2021). [11] Lyman, C. et al. J. Neuroimaging (2022). [12] Hanspach, J. et al. J. Magn. Reson. Imaging (2017). [13] Li, X. et al. NeuroImage (2019). [14] Zhang, Y. et al. NeuroImage (2018). [15] Ide, S. et al. Eur Radiol. (2015). [16] Tustison, Nicholas J. et al. Scientific Reports (2021). [17] Salman, F. et al. ISMRM (2024). [18] Robinson, SD. et al. NMR Biomed (2017). [19] Polak, P. et al. ISMRM (2014). [20] Abdul-Rahman, Hussein S. et al. Appl. Opt. (2007). [21] Sun, H. et al. MRM (2014). [22] Schweser, F. et al. NeuroImage (2012). [23] Jenkinson, M. et al. NeuroImage (2002). [24] Avants, BB. et al. Med Image Comput Comput Assist Interv. (2007). [25] Salman, F. et al. ISMRM (2024). [26] https://wiki.biac.duke.edu/mirecc:mireccanat:overlap. [27] Zivadinov, R. et al. Radiology (2018). [28] Hagemeier, J. et al., NeuroImage.(2017).

On the Sensitivity of Quantitative Susceptibility Mapping in Clinical Brain Research

Fahad Salman[1,2], Abhisri Ramesh[1], Thomas Jochmann[1,3], Mirjam Prayer[1], Ademola Adegbemigun[1], Dejan Jakimovski[1], Niels Bergsland[1], Michael G. Dwyer[1,4], Robert Zivadinov[1,4], and Ferdinand Schweser[1,4]

[1]Buffalo Neuroimaging Analysis Center, Department of Neurology at the Jacobs School of Medicine and Biomedical Sciences, University at Buffalo, The State University of New York, Buffalo, NY, United States; [2]Department of Biomedical Engineering, University at Buffalo, The State University of New York, Buffalo, NY, United States; [3]Department of Computer Science and Automation, Technische Universität Ilmenau, Ilmenau, Germany; [4]Center for Biomedical Imaging, Clinical and Translational Science Institute, University at Buffalo, The State University of New York, Buffalo, NY, United States

Summary

This study evaluated the sensitivity of top-rated inversion and background removal algorithms to over-time susceptibility changes in deep gray matter. Our findings emphasize the importance of the algorithmic combination choice in QSM studies, impacting findings beyond demographics and clinical characteristics.

Introduction

Quantitative Susceptibility Mapping (QSM) is increasingly being applied in clinical research, particularly for quantifying brain iron levels in neurodegenerative diseases and studying normal aging.[1-3] To foster QSM's clinical translation, technical consensus recommendations[4] have recently been presented.

Accurate susceptibility measurements rely on precise background field removal (BFR) and dipole inversion.[4] Benchmarking studies have explored similarities, differences, and limitations of BFR and dipole inversion algorithms[5,6,7], demonstrating that algorithms exist that can reconstruct susceptibility maps with high precision and accuracy when compared to a gold standard susceptibility map. However, we claim that previous benchmarking studies have limited practical relevance because they leave a critical question unanswered: **What is the *sensitivity* of algorithms toward the detection of *longitudinal changes* in susceptibility?**

In the present study, we aimed to answer this question by investigating the sensitivity of the most widely used[12-35] and top-ranked (QSM challenge 2.0[7]) algorithms in detecting group-level over-time changes in brain susceptibility. Our research extends a previous investigation presented at the 2023 ISMRM meeting[8] by incorporating additional algorithms, optimizing algorithmic parameters in collaboration with original developers, and a direct comparison to putative age-related brain iron changes reported by Hallgren and Sourander (H&S) in 1958.[9]

Methods

Given the absence of an in-vivo brain susceptibility ground truth, our assessment relied on the assumption that *over-time* DGM susceptibility changes in healthy adults should align with H&S's established aging-related non-heme iron concentration changes.[9]

Participants: We enrolled N=23 healthy subjects who participated in previous studies that included a specific QSM sequence[8,10] when their age was at least 37 years. In this age range, H&S reported increasing iron in globus pallidus (GP), caudate, and putamen, and decreasing iron in the thalamus.[9] Additionally, deep gray matter (DGM) myelin levels are relatively stable in this age range.[37] We enrolled subjects in the order of the date of their first available scan to maximize follow-up time in the final dataset.

Data acquisition: We acquired follow-up images on the same scanner and with the same sequence as the baseline scan.[8] We conducted scan-rescan experiments in five subjects (four repeats with full repositioning).[10]

QSM Reconstruction (single-echo GRE sequence):[38] Best-path unwrapping[11] was followed by six BFR algorithms[12-17], 4th-order polynomial fitting, 21 inversion algorithms applied to each BFR[18-35], and whole brain referencing to minimize variation.[10] For deep-learning (DL) methods, field maps were resampled to isotropic voxel size and rotated to axial orientation.

Statistical analysis: Regional values were obtained as described earlier.[10] We then determined how well over-time DGM susceptibility changes from each algorithmic combination ("*pipeline*") correlated (R^2 values were classified using Cohen's guidelines[39]) with putative H&S DGM iron changes (derived using regional equations provided by H&S).[9] This was computed by converting each subject's regional susceptibility values at baseline and follow-up to iron concentrations using a previously determined conversion factor (13.2 ppb/mg iron/100g-wet-weight for ferritin at 36.5°C; regression equation specific to the gray matter).[40] Following this, we calculated a previously introduced average DGM sensitivity metric[8] (over-time change / reproducibility) for each pipeline (PS).

**Results**

Correlation with and overestimation of putative over-time iron changes (Fig. 1): All but two pipelines demonstrated a significant linear correlation (p<0.05, R^2 threshold=0.02). Out of the remaining 124 pipelines, 71 pipelines (57%)

overestimated putative iron concentrations by at least a factor of two (slope$\geq$2). DirTIK with PDF (slope=1.04), SDI with VSHARP (1.12), RESHARP (1.13), LBV (1.07) and PDF (0.87), and iLSQR with RESHARP (1.07), estimated over-time changes close to the putative iron changes (slope between 0.9 and 1.1). 19 pipelines exhibited low correlations ($R^2 \leq$0.12), 63 exhibited medium correlations ($\geq$0.13 and $\leq$0.25), while the rest (44) showed high correlations ($\geq$0.26). Seven pipelines stood out within the 95th percentile ($\geq$0.35): RESHARP with MATV, AMP-PE, LSQR, MEDI+0, iSWIM, and MEDI+0* (w/o CSF-regularization), and SHARP with MEDI+0 (in descending order).

Overall PS (Fig. 2): Most pipelines detected H&S-consistent over-time changes (non-translucent boxes in heat maps). However, only HEIDI, L1-QSM, LSQR, STAR, iLSQR, and iSWIM were H&S-consistent regardless of the BFR choice.

Most inversion algorithms, except for DeepQSM, QSMnet+, WH-FANSI, and IterTK, exhibited high sensitivity and H&S-consistent over-time changes with SHARP-based BFRs (RESHARP, SHARP, VSHARP). RESHARP+AMP-PE, HEIDI, and LSQR portrayed the highest sensitivity (5.49, 5.38, and 4.97, respectively – 95th percentile).
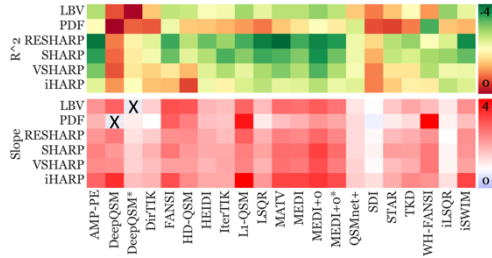
Fig. 1. R^2 (**top**) and slope (**bottom** – white =1) observed between DGM over-time susceptibility changes and putative iron changes. Pipelines within the slope plot that exhibited non-significant Pearson correlation (p>0.05) were excluded (depicted using X in the heatmap). DeepQSM*: in-house developed.
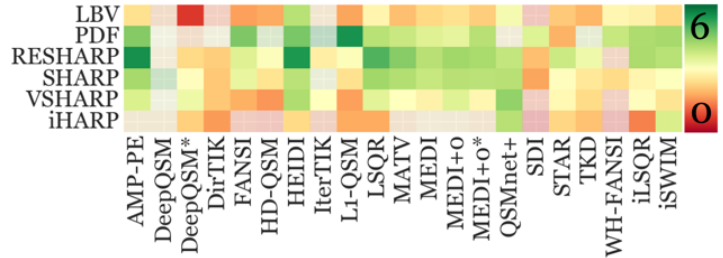
Fig. 2. Average DGM sensitivity metric. Each row corresponds to a BFR algorithm, while each column represents an inversion algorithm. Translucent boxes are indicative of pipelines excluded due to susceptibility changes incompatible with H&S in at least one of the ROIs. Green indicates high sensitivity, while vice versa for red.

Discussion and Conclusion

This study is the first comprehensive analysis of the impact of both BFR and inversion algorithm choice on the detection of *real-world* group-level susceptibility differences. The findings underscore the critical influence of algorithmic choices in QSM processing on ability to detect physiological changes in the brain. This finding has profound implications for clinical research and trials where QSM is used as a biomarker for disease progression. Our study also indicates the need for standardized QSM reconstruction pipeline to enhance comparability across studies.

The potential for bias in study outcomes due to observed discrepancies in over-time changes with some algorithm configurations (Fig. 2 – translucent boxes) is alarming and will require further investigation. Increased robustness of SHARP-based BFRs, in line with the previous findings[36], may be related to the intrinsic low-pass filtering capability and spatial averaging of the spherical convolution. Residual transceiver-phase contributions in our data may have amplified these effects.[4]

In conclusion, pipelines using RESHARP with AMP-PE, HEIDI, or LSQR inversion showed the highest overall sensitivity and, hence, should be considered first-choice for clinical research.

References

[1] Eskreis-Winkler, S. et al. NMR Biomed (2017). [2] Wang, Y. et al. J. Magn. Reson. Imaging (2017). [3] Ravanfar, P. et al. Front. Neurosci. (2021). [4] QSM Consensus Organization Committee. et al. ISMRM Electro-Magnetic Tissue Properties Study Group (2023) [5] Schweser, F. et al. NMR Biomed. (2017) [6] Langkammer, C. et al. Magn. Reson. Med. (2018). [7] QSM Challenge 2.0 Organization Committee; Bilgic, B. et al. Magn. Reson. Med. (2021). [8] Salman, F. et al. ISMRM (2023). [9] Hallgren, B. et al. J. Neurochem. (1958). [10] Salman, F. et al. ISMRM (2024). [11] Abdul-Rahman, H.S. et al. Appl. Opt. (2007). [12] Sun, H. et al. Magn. Reson. Med. (2014). [13] Zhou, D. et al. NMR Biomed. (2014). [14] Liu, T. et al. NMR Biomed. (2011). [15] Schweser, F. et al. Neuroimage. (2011). [16] Li, W. et al. Neuroimage. (2011). [17] Li, W. et al. NMR Biomed. (2014). [18] Huang, S. et al. MRM. (2023). [19] Bollmann, S. et al. Neuroimage. (2019). [20] Karsa, A. et al. ISMRM (2019). [21] Milovic, C. et al. Magn. Reson. Med. (2018). [22] Lambert, M. et al. Magn. Reson. Med. (2022). [23] Schweser, F. et al. Neuroimage. (2012). [24] Li, W. et al. Neuroimage. (2011). [25] Tang, J. et al. Magn. Reson. Med. (2013). [26] Milovic, C. et al. Magn. Reson. Med. (2022). [27] Guo, L. et al. PLoS One. (2018). [28] Liu, J. et al. Neuroimage. (2012). [29] Liu, Z. et al. Magn. Reson. Med. (2018). [30] Jung, W. et al. Neuroimage. (2020). [31] Schweser, F. et al. Magn. Reson. Med. (2013). [32] Wei, H. et al. NMR Biomed. (2015). [33] Wharton, S. et al. Magn. Reson. Med. (2010). [34] Milovic, C. et al. Magn. Reson. Med. (2019). [35] Jochmann, T. et al. ISMRM (2021). [36] Milovic, C. et al. ISMRM (2023). [37] Dvorak, A.V. et al. Sci Rep. (2021). [38] QSM pipeline using the following code: https://gitlab.com/R01NS114227/pi4s. [39] Cohen, J. et al. Current Directions in Psychological Science. (1992). [40] Langkammer, C. et al. NeuroImage. (2012).

Predicting Mesoscopic Larmor Frequency Shifts in White Matter with Diffusion MRI - An In-Silico Monte-Carlo Study

Anders Dyhr Sandgaard[1], Sune Nørhøj Jespersen[1,2]

[1]Center of Functionally Integrative Neuroscience, Department of Clinical Medicine, Aarhus University, Denmark
[2]Department of Physics and Astronomy, Aarhus University, Denmark

Summary: This study aims to validate the orientation dependence of the mesoscopic Larmor frequency shifts from white matter axonal microstructure using Monte-Carlo simulations. Our results confirm that dMRI can account for microscopic magnetic anisotropy from WM microstructure in susceptibility imaging.

Introduction: Magnetic susceptibility imaging offers insights into the chemical composition and microstructural organization of tissue[1]. Estimating susceptibility in white matter (WM) from the MRI signal phase is challenging due to the axonal magnetic microstructure inducing an anisotropic mesoscopic frequency shift $\overline{\Omega}^{\text{Meso}}$ that depends on every axon's direction relative to the B0 field. Our recent work[2,3] (QSM+) illustrates how this anisotropy depends on the axonal fiber orientation distribution function (fODF). However, it has yet to be validated if **a)** the MRI signal phase can be used to estimate the mean magnetic field $\Delta\overline{\mathbf{B}}$ as is assumed in QSM+, and **b)** if the fODF, estimated using diffusion MRI, can predict the anisotropy of $\overline{\Omega}^{\text{Meso}}$ in realistic white matter. These are the goals of this study.

Methods: We conducted Monte-Carlo simulations using eight publicly available mesoscopically sized white matter axon phantoms[4,5] (see figure 1A), segmented from the corpus callosum and cingulum of sham and traumatic brain injury (TBI) rats (four each). Resolution was 0.1μm and the phantom dimensions was roughly $200 \times 100 \times 60$ μm across each of the phantoms. We simulated a Pulsed Gradient Spin Echo (PGSE) experiment, focusing on particles in the intra-axonal space. The PGSE signal was generated with $b = 0,1,3,4,5,7,10$ ms/μm^2, and with $\hat{\mathbf{g}}$ along 30 gradient directions for $b < 5$ ms/μm^2 , and 60 directions for the remaining. The directions were generated using electrostatic repulsion[4]. The diffusion times used were $\Delta = 10, 40, 70, 100$ ms, while the gradient pulse duration was $\delta = 0.83$ μs like the MC time step δ_t. The expansion coefficients $p_{lm}(\Delta)$ of the apparent fODF was estimated by fitting the Standard Model (SM) of Diffusion in WM, modified to include intra-axonal axial kurtosis[6,7]. For part **a)** we investigated the feasibility of estimating $\overline{\Omega}_a(\mathbf{B_0}) = \gamma\hat{\mathbf{B}}^{\text{T}}\Delta\overline{\mathbf{B}}_a(\mathbf{B_0})$, the mean intra-axonal magnetic field, from either the frequency shift $\overline{\Omega}_{\text{MGE}}$ of a multi-gradient echo signal (MGE) at times $t = 0,5,\ldots,40$ ms, or $\overline{\Omega}_{\text{ASE}}$ from an asymmetric spin echo (ASE) with echo time $T_E = 80$ ms and delays $\Delta T_E = 0,5,\ldots,20$ ms. We tested this for 3T and 7T, with $\hat{\mathbf{B}}$ along 13 different directions found by electrostatic repulsion[4], and with $\overline{\chi} = -100$ ppb.[8] The frequencies were estimated from fitting the measured phases to either a linear or third order polynomial. t_{max} and $(\Delta T_E)_{max}$ indicate the maximum time used in the fit. For part **b)** the *l=2* spherical harmonic expansion coefficients $p_{2m}(\Delta)$ of the dMRI estimated fODF were used to estimate $\overline{\Omega}^{\text{Meso}}(\mathbf{B_0}; \Delta)$ with Eq. (1) for each diffusion time Δ. $\overline{\Omega}^{\text{Meso}}(\mathbf{B_0}; \Delta)$ was compared to $\overline{\Omega}_a(\mathbf{B_0})$, estimated directly from the intra-axonal mean magnetic field $\hat{\mathbf{B}}^{\text{T}}\Delta\overline{\mathbf{B}}_a(\mathbf{B_0})$, by computing the normalized RMSE (NRMSE), cf. Eq. (2), normalized by the range of $\overline{\Omega}_a(\mathbf{B_0})$. We also tested the estimation accuracy of $\overline{\chi}$ by measuring $\overline{\Omega}_a(\mathbf{B_0})$ at multiple orientations $\hat{\mathbf{B}}$. This was done by estimating a scalar value β from minimizing the least squares difference described by Eq. (3), such that $\beta = 1$ corresponds to a perfect susceptibility fit.

$$\overline{\Omega}^{\text{Meso}}(\mathbf{B_0}; \Delta, \overline{\chi}) = -\gamma B_0 \overline{\chi} \frac{1}{15} \sum_{m=-2}^{2} p_{2m}(\Delta) Y_2^m(\hat{\mathbf{B}}), \quad (1) \qquad \text{NRMSE}(\Delta) = \frac{\sqrt{\frac{1}{N_{\hat{\mathbf{B}}}} \sum_{\hat{\mathbf{B}}} \left(\overline{\Omega}^{\text{Meso}}(\mathbf{B_0}; \Delta) - \overline{\Omega}_a(\mathbf{B_0}) \right)^2}}{\max\left(\overline{\Omega}_a(\mathbf{B_0})\right) - \min\left(\overline{\Omega}_a(\mathbf{B_0})\right)}, \quad (2)$$

$$\beta(\Delta) = \text{argmin}_{\overline{\chi}'} \sum_{\hat{\mathbf{B}}} \left(\overline{\Omega}^{\text{Meso}}(\mathbf{B_0}; \Delta, \overline{\chi}') - \overline{\Omega}_a(\mathbf{B_0}) \right)^2 / \overline{\chi} \quad (3).$$

Results: a) The results are presented for one SHAM and one TBI brain, showing reproducibility across all eight phantoms. Figure 1B shows mean ratios $\langle \overline{\Omega}_{\text{MGE}}(\mathbf{B_0})/\overline{\Omega}_a(\mathbf{B_0}) \rangle_{\hat{\mathbf{B}}}$ and $\langle \overline{\Omega}_{\text{ASE}}(\mathbf{B_0})/\overline{\Omega}_a(\mathbf{B_0}) \rangle_{\hat{\mathbf{B}}}$ averaged over different $\mathbf{B_0}$ directions. We found $\overline{\Omega}_{\text{ASE}}(\mathbf{B_0})$ estimated $\overline{\Omega}_a(\mathbf{B_0})$ best, especially at 7T, while at 3T, both sequences could estimate $\overline{\Omega}_a(\mathbf{B_0})$ well for all t_{max} and $(\Delta T_E)_{max}$ considered here. **b)** Figure 1C shows great agreement between $\overline{\Omega}_a(\mathbf{B_0})$ and the estimated frequency shift $\overline{\Omega}^{\text{Meso}}(\mathbf{B_0}; \Delta = 70$ ms$)$ at 7T. This is also reflected in an NRMSE of less than 8% for all phantoms. The β value was best estimated when $\Delta = 100$ ms, differing by less than 10% for all 8 phantoms. These

findings suggests that the fODF obtained from diffusion MRI can help account for mesoscopic frequency shifts in MRI measurements

Discussion and Conclusions: Our results demonstrate the potential of using the diffusion-derived fODF to improve estimation of magnetic susceptibility in MRI. By incorporating structural anisotropy into susceptibility models, as in QSM+, we can better understand and interpret MRI data in WM. Future work will focus on validating these findings for extra-axonal water and exploring the impact of more complex microstructural features on susceptibility measurements.
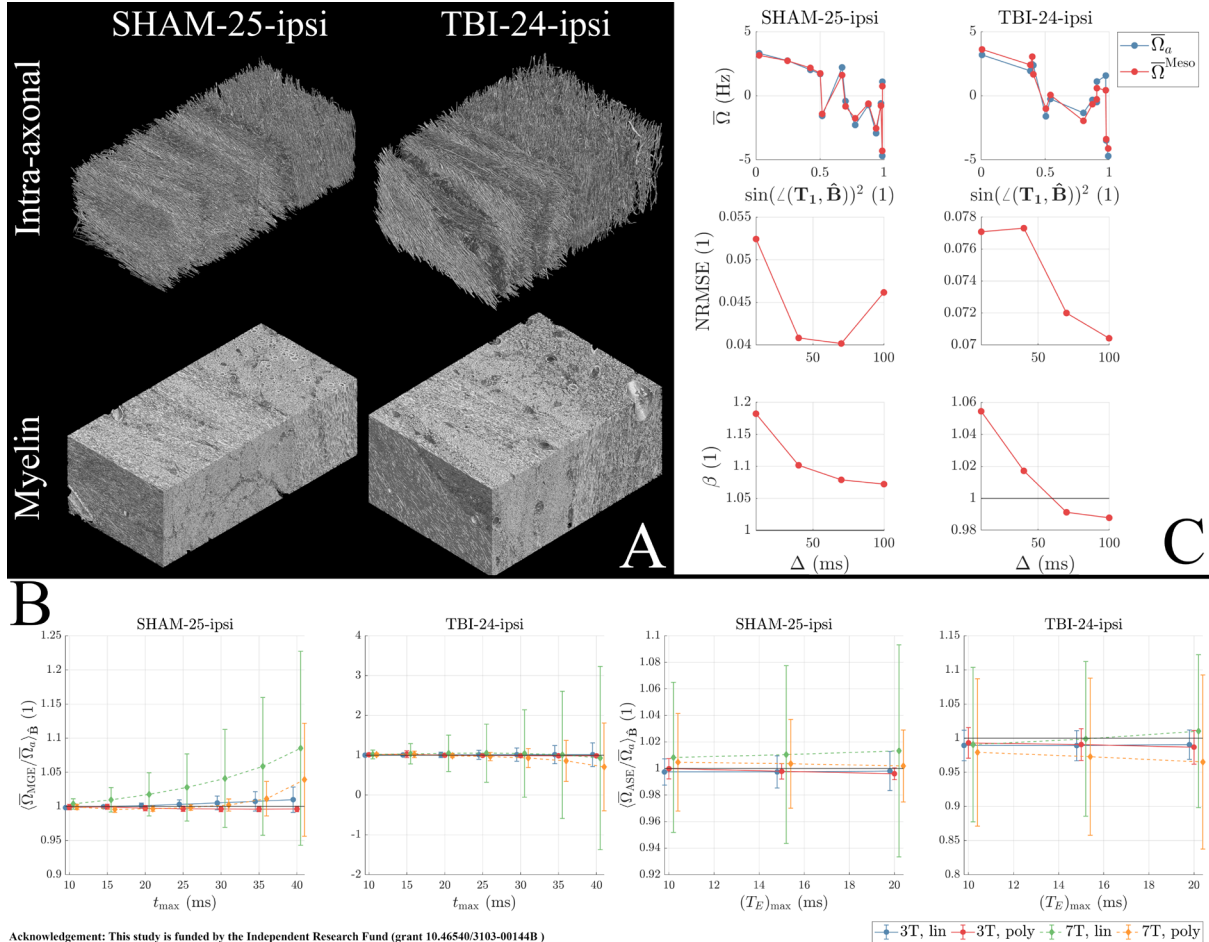
Figures – A: Axon and myelin phantoms used for MC simulation. **B**: Mean ratio across B0 directions between the mean intra-axonal frequency shift $\overline{\Omega}_a$ and the estimated shift from fitting either a 1st or 3rd order polynomial to the phase of the MGE or ASE simulated signal. **C**: First row: Estimated frequency shift $\overline{\Omega}^{Meso}$, cf. Eq. (1), using fODF estimated from simulated dMRI signal. Second row: Normalized RMSE between $\overline{\Omega}_a$ and $\overline{\Omega}^{Meso}$ cf. Eq. (3). Third row: Fitted normalized susceptibility β cf. Eq. (3).

References:
1. Wang Y, Spincemaille P, Liu Z, et al. Clinical quantitative susceptibility mapping (QSM): Biometal imaging and its emerging roles in patient care. *J Magn Reson Imaging*. 2017;46(4):951-971. doi:10.1002/jmri.25693
2. Sandgaard AD, Shemesh N, Kiselev VG, Jespersen SN. Larmor frequency shift from magnetized cylinders with arbitrary orientation distribution. *NMR Biomed*. 2023;36(3):e4859. doi:10.1002/nbm.4859
3. Sandgaard AD, Kiselev VG, Henriques RN, Shemesh N, Jespersen SN. Incorporating the effect of white matter microstructure in the estimation of magnetic susceptibility in ex vivo mouse brain. *Magn Reson Med*. Published online September 29, 2023. doi:10.1002/MRM.29867
4. Abdollahzadeh A, Belevich I, Jokitalo E, Sierra A, Tohka J. DeepACSON automated segmentation of white matter in 3D electron microscopy. *Commun Biol 2021 41*. 2021;4(1):1-14. doi:10.1038/s42003-021-01699-w
5. Abdollahzadeh A, Belevich I, Jokitalo E, Tohka J, Sierra A. Automated 3D Axonal Morphometry of White Matter. *Sci Reports 2019 91*. 2019;9(1):1-16. doi:10.1038/s41598-019-42648-2
6. Olesen JL, Østergaard L, Shemesh N, Jespersen SN. Beyond the diffusion standard model in fixed rat spinal cord with combined linear and planar encoding. *Neuroimage*. 2021;231:117849. doi:10.1016/J.NEUROIMAGE.2021.117849
7. Lee HH, Papaioannou A, Kim SL, Novikov DS, Fieremans E. A time-dependent diffusion MRI signature of axon caliber variations and beading. *Commun Biol 2020 31*. 2020;3(1):1-13. doi:10.1038/s42003-020-1050-x
8. Wharton S, Bowtell R. Effects of white matter microstructure on phase and susceptibility maps. *Magn Reson Med*. 2015;73(3):1258-1269. doi:10.1002/mrm.25189

Impact of Regularization Parameter Choice on Real-World Sensitivity of QSM

Fahad Salman[1,2], Abhisri Ramesh[1], Thomas Jochmann[1,3], Mirjam Prayer[1], Ademola Adegbemigun[1], Dejan Jakimovski[1], Niels Bergsland[1], Michael G. Dwyer[1,4], Robert Zivadinov[1,4], and Ferdinand Schweser[1,4]

[1]*Buffalo Neuroimaging Analysis Center, Department of Neurology at the Jacobs School of Medicine and Biomedical Sciences, University at Buffalo, The State University of New York, Buffalo, NY, United States;* [2]*Department of Biomedical Engineering, University at Buffalo, The State University of New York, Buffalo, NY, United States;* [3]*Department of Computer Science and Automation, Technische Universität Ilmenau, Ilmenau, Germany;* [4]*Center for Biomedical Imaging, Clinical and Translational Science Institute, University at Buffalo, The State University of New York, Buffalo, NY, United States*

Summary

This study evaluated the impact of parameter settings for widely-used background field removal algorithms correction on QSM sensitivity. Our findings demonstrate an urgent need for improved algorithm evaluation and parameter selection procedures.

Introduction

When applying QSM for in vivo medical research, sensitivity to detecting over-time changes is one of the most critical characteristics. A recent study demonstrated variable sensitivity to long-term susceptibility changes in the deep gray matter (DGM) across different inversion algorithms.[1] Interestingly, algorithms that were top-ranked in the latest QSM challenge,[2] i.e. featured small nRMSE against the simulated ground truth, did not exhibit top-ranking sensitivity in the real world. These findings[1] prompted us to hypothesize that the evaluations (nRMSE) performed using a single simulated brain map in the QSM challenge,[2] and widely-used approaches to optimize algorithmic parameters (e.g., L-curve optimization[3]) ***are not effective means to achieve optimal sensitivity in clinical applications***.

In this study, we investigated the sensitivity of the top-ranked[1] BFR algorithms[5-7] over a wide range of regularization (λ) values, including those suggested in the original publications[4] or in email communications with the authors. We also evaluated the widely-used MEDI inversion algorithm[8], known for its visual variability with changes in regularization parameters. Our goal was to determine if the recommended regularization parameters were optimal for the detection of susceptibility changes, thus optimized for clinical applications.

Methods

Theory: Assessing the sensitivity to over-time changes in the absence of in-vivo brain susceptibility ground truth is challenging. Our assessment employed the established aging-related non-heme iron concentration changes reported by Hallgren and Sourander[10] for DGM (thalamus, caudate, putamen, and globus pallidus) in healthy adults. We tested how well susceptibility changes observed with QSM align with the reported concentration changes. Myelin content in DGM was assumed to be stable in our cohort's age range.[11]

Participants and data acquisition: As described previously, N=23 (average age=57±9 [39-73 IQR]) and N=5 (25±1 [24-26]) healthy subjects were enrolled for over-time changes[1] and reproducibility[9] analysis, respectively. The median time between baseline and follow-up scans was 10.0 years [11.5-13.0].

QSM Reconstruction (single-echo GRE sequence): Best-path unwrapping[12] was followed by three BFR algorithms,[5-7] each with 15 λ values uniformly distributed in log-scale (range for SHARP and VSHARP = 0.0031-0.0430; RESHARP = 0.0000001-0.1), including the λ value that was deemed as optimal for each algorithm (SHARP and VSHARP = 0.0074; RESHARP = 0.0001 [recommended by Dr. Hongfu Sun] and 0.005 as per L-curve). Subsequently, 4th order polynomial fitting was applied to RESHARP as per the guidance from its author (Dr. Hongfu Sun). Following BFR, HEIDI,[13] LSQR,[13] and AMP-PE[14] (highly sensitive previously)[1] were applied and whole brain referencing to minimize variation.[9] Additionally, we performed dipole inversion using the MEDI[8] algorithm across a wide range (1-100000) of its λ values on the background corrected field maps from "optimal" λ for each BFR. We termed BFR+inversion as "*pipeline*" in this investigation.

Statistical analysis: We analyzed regional mean susceptibility values using a study-specific bi-parametric QSM-T_1w atlas.[15] We assessed scan-rescan reproducibility by the inter-subject mean of the regional subject-level standard deviation of the scan-rescan susceptibility maps.[9] We quantified sensitivity toward longitudinal changes as the ratio of over-time change to scan-rescan reproducibility.[1]

Results

Figure 1 visualizes the background-corrected field maps from each BFR over a range of λ values. Clear under- and over-regularization are evident in SHARP and VSHARP. As for RESHARP, the tolerance level led to the results

being stagnant around λ=8·10⁻⁷ and lower, without overly under-regularized solutions. Figure 2 shows the effect of the chosen λ on the pipelines' average DGM sensitivity outcome.

<u>Pipeline Sensitivity (PS) (Fig. 2)</u>: Variable sensitivities were observed, ranging from 1.1-6.2 in SHARP (1st panel), 1.0-6.8 in VSHARP (2nd panel), and 2.0-6.9 in RESHARP (3rd panel). SHARP and VSHARP with under- or over-regularized field maps lead to H&S-inconsistent over-time changes (gray boxes). Only RESHARP with HEIDI or LSQR were H&S-consistent over a wide λ-range (exception: 0.01). The highest overall sensitivity in the DGM was achieved with λ = 0.0128 in SHARP, 0.0156 in VSHARP, and 0.001 in RESHARP.

<u>Variable usable λ range (in the 50th percentile)</u>: RESHARP portrayed the highest number (N=6) of λ values (0.0001-0.012) that showcased good sensitivity, while only N=5 and 4 values portrayed good sensitivity for SHARP (0.0085-0.0191) and VSHARP (0.0104-0.0191), respectively.

<u>Sensitivity of "optimal" λ</u>: Compared to the highest sensitivity outcome, SHARP (red λ value in Fig. 2) and VSHARP (red) achieved 36% and 52% lower sensitivity with the "optimal" λ value, respectively. RESHARP achieved 23% (red) and 14% (orange) lower sensitivity with the "optimal" λ, compared to the highest sensitivity. For the MEDI algorithm, the effect of different λ values on sensitivity was low compared to the effects of BFR regularization (top three panels of Fig. 2).
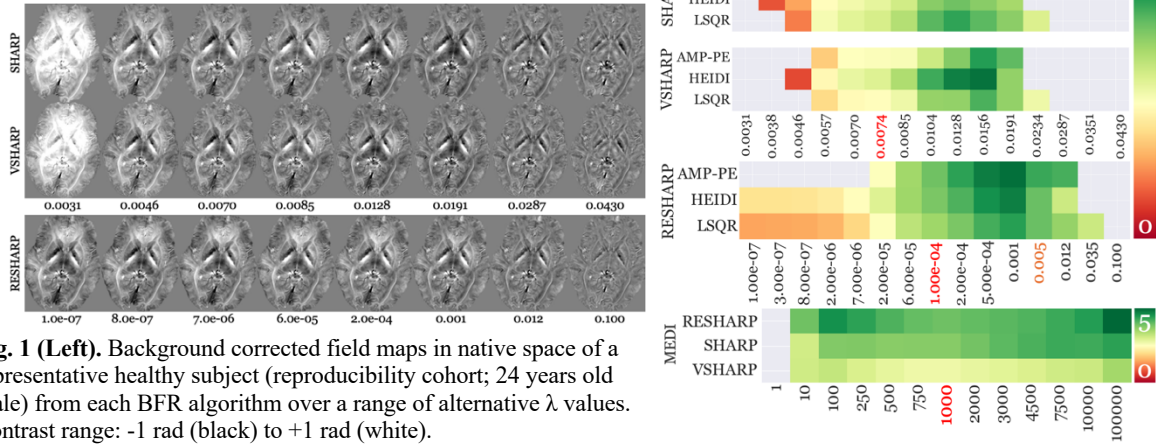
Fig. 1 (Left). Background corrected field maps in native space of a representative healthy subject (reproducibility cohort; 24 years old male) from each BFR algorithm over a range of alternative λ values. Contrast range: -1 rad (black) to +1 rad (white).

Fig. 2 (Right). Average DGM Sensitivity Metric. <u>Panels</u>: BFR (first 3; last is MEDI inversion). <u>Rows</u>: inversion algorithms (MEDI: BFRs in rows). <u>Columns</u>: λ values; red for author-suggested, orange for L-curve obtained values. Pipelines with incompatible regional changes are masked (gray). Green=high sensitivity, red=low.

Discussion and conclusion: This study is the first comprehensive analysis of how over- and under-regularization in BFR and inversion steps affect the detection of real-world group-level susceptibility differences.

Our findings suggest that neither L-curve nor RMSE optimization methods lead to the optimal algorithmic configuration for detecting susceptibility differences in a clinical scenario, thus limiting their practicality in research or clinical settings

Nonetheless, the approach used in this study is not feasible to use for optimizing algorithms for every lab due to the limited availability of a dataset like ours. Therefore, future research should focus on clinically applicable ways of optimizing the parameters that go beyond the approaches used today, such as L-curve/RMSE. Moreover, we advocate the QSM committee to shift their focus on developing numerical models that account for over-time changes, rather than focusing on a single brain at a single time point.[2] These models could be useful for both comparing inter-/intra-algorithmic performances and for optimizing them. This strategy, in turn, would aim to promote standardized QSM pipeline usage while enhancing robustness in detecting group differences and over-time changes in both control subjects and patients with neurological diseases.

References

[1] Salman, F. et al. Sensitivity. ISMRM (2024) [2] QSM Challenge 2.0 Organization Committee; Bilgic, B. et al. Magn. Reson. Med. (2021). [3] Hansen, PC. et al. Computational Inverse Problems in Electrocardiology (2002). [4] Ozbay, PS. et al. NMR Biomed. (2017). [5] Li, W. et al. Magn Reson Med. (2011). [6] Schweser, F. et al. Neuroimage. (2011). [7] Sun, H. et al. Magn. Reson. Med. (2014). [8] Liu, T. et al. IEEE Trans Med Imaging (2012). [9] Salman, F. et al. Reproducibility. ISMRM (2024) [10] Hallgren, B. et al. J. Neurochem. (1958). [11] Dvorak, A.V. et al. Sci Rep. (2021). [12] Abdul-Rahman, HS. et al. Appl. Opt. (2007) [13] Schweser, F. et al. Neuroimage. (2012). [14] Huang, S. et al. MRM. (2023). [15] Hanspach, J. et al. MRI (2017).

Magnetic Susceptibility Source Separation in the Head and Neck: Comparing Gradient Echo Methods

Matthew T. Cherukara, Patrick Fuchs, Karin Shmueli

Department of Medical Physics and Biomedical Engineering, University College London, London, UK

Summary

We compared three magnetic susceptibility source separation algorithms applied to multi-echo gradient echo data in the head and neck in 10 subjects. Inter-subject variance and contrast of the resulting source separation varied across algorithms tested. χ-sepnet achieved clear muscle-fat contrast in the neck and low susceptibility variance in the glands.

Introduction

Recently, several techniques have been proposed to quantify the relative contributions to magnetic susceptibility (χ) of paramagnetic and diamagnetic compartments within each voxel.[1-7] Such techniques typically rely on the assumption that R_2' is related to absolute susceptibility, while phase is affected by both para- and diamagnetic sources.[6] As such, many source-separation techniques require a spin-echo-based R_2 estimate, or make simplifying assumptions about the relationship between R_2 and R_2^*.[1,2,5] The DECOMPOSE method fits multi-echo data to a three-pool model to estimate susceptibility sources without the need for R_2'.[4] These techniques have been used in the brain,[7] but the head and neck (HN) region presents unique challenges including fat-water phase artefacts, and greater air-tissue interfaces, flow effects, and physiological motion. In this study, we compared the results of susceptibility source separation using three methods applied to GRE data in the head and neck.

Methods

This analysis was applied retrospectively to four-echo GRE data acquired from ten healthy subjects using a 3T Achieva system (Philips, Netherlands). Acquisition parameters were: $TR = 22$ ms, $TE_1 = \Delta TE = 4.61$ ms, flip angle $12°$, resolution $1.25 \times 1.25 \times 1.25$ mm, $FOV = 240 \times 240 \times 240$ mm. Complex data were denoised using MP-PCA[8] and fit across echoes.[9] Field maps were unwrapped using SEGUE[10] and background fields removed using V-SHARP[11] with a 22mm kernel width. QSMs were calculated using Star QSM[12] and the results were used to calculate para- and diamagnetic maps using χ-separation (with iLSQR regularization)[3] and χ-sepnet. The above pipeline was applied to GRE data from each echo individually, and the resulting single-echo QSMs were used to estimate para- and diamagnetic signal compartments using DECOMPOSE.[4]

Regions of interest (ROIs) in the brain (thalamus, caudate nucleus, putamen, and globus pallidus) were segmented automatically from first-echo magnitude GRE images using FSL FIRST[13] and ROIs in HN (submandibular gland, parotid gland, and several lymph nodes) were obtained by manual segmentation checked by an experienced radiologist. Average values of paramagnetic and diamagnetic susceptibility were compared in each ROI.

Results

Figure 1 shows a visual comparison of the source separation methods in a representative subject. Each method achieved source separation, although the contrast varies. χ-sepnet achieved clear muscle-fat contrast in the posterior neck (yellow and red arrows). DECOMPOSE produced more uniform values in the ROIs.

Figure 2 shows average values of component susceptibilities in each ROI.
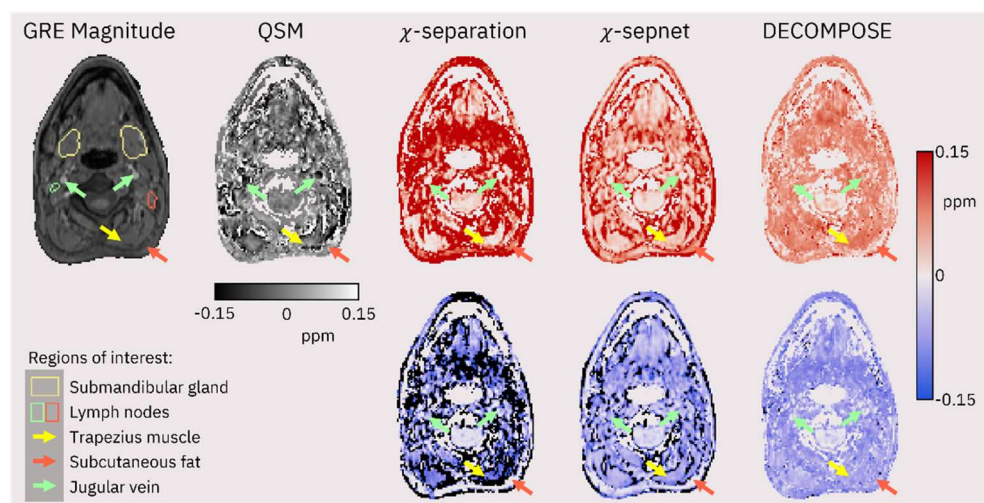
Figure 1. Axial slices of the neck from one subject showing GRE first-echo magnitude data (with ROIs outlined), susceptibility map from Star QSM, and para- and diamagnetic susceptibility maps from three separation algorithms.
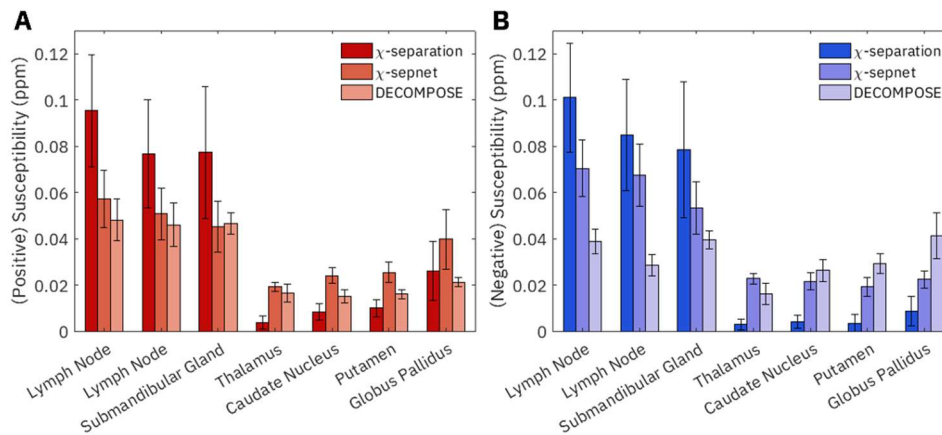
Figure 2. Mean paramagnetic (**A**) and diamagnetic (**B**) compartment susceptibilities in HN and brain ROIs. Error bars indicate standard deviation across 10 subjects.

Discussion and Conclusions

The challenges of QSM in the neck are exemplified by the Star QSM results, where the submandibular gland has large χ variations, and in the posterior neck there are strong fat-water effects at the muscle boundaries (Figure 1, yellow arrow). These phenomena propagate into the para- and diamagnetic susceptibility maps produced by χ-separation, where the χ component values are higher than other methods in the neck (probably driven by noise, Figures 1 & 2) but lower in the brain (Figure 2).

DECOMPOSE estimated paramagnetic χ components with lower variance than the other methods in all ROIs except the thalamus. Diamagnetic χ values from DECOMPOSE had lower variance in HN ROIs, but in deep-brain ROIs χ-sepnet produced the most consistent diamagnetic results. Across all ROIs, the total χ from DECOMPOSE was more diamagnetic than the results of other methods (not shown). Venous vessels such as the internal jugular veins (Figure 1, green arrows) have strong signal in the first-echo GRE magnitude and are expected to be strongly paramagnetic due to the presence of deoxyhemoglobin, but they are not obviously elevated in paramagnetic component maps, likely due to inflow effects.

There are several limitations to this study. The DECOMPOSE multi-compartment model ideally uses five echoes for fitting and is underdetermined with this four-echo dataset. χ-sepnet was trained on brain data at 1-mm resolution, and so may not perform optimally on these 1.25-mm-resolution data. Finally, there are no ground truth values available, nor comparable source-separated results in the literature, so it is necessary to rely on visual inspection and differences across subjects to compare these methods qualitatively.

In conclusion, susceptibility source separation using only GRE data is possible in the head and neck, but further work is needed to validate the resulting maps and regional values.

References

[1] Schweser F et al. (2011). "SEMI-TWInS: Simultaneous extraction of myelin and iron using a T_2^*-weighted imaging sequence," *Proc. ISMRM* 19, #120.
[2] Lee J et al. (2017). "Separating positive and negative susceptibility sources in QSM," *Proc. ISMRM* 25, #0751
[3] Shin H et al. (2021). "χ-separation: Magnetic susceptibility source separation toward iron and myelin mapping in the brain," *NeuroImage*, 240: 118371.
[4] Chen J, Gong N, Chaim K T, Otaduy M C G, Liu C (2021) "Decompose quantitative susceptibility mapping (QSM) to sub-voxel diamagnetic and paramagnetic components based on gradient-echo MRI data," *NeuroImage*, 242: 118477.
[5] Dimov A V et al. (2022). "Susceptibility source separation from gradient echo data using magnitude decay modelling," *J. Neuroimaging*, 32(5), pp.852-859.
[6] Li Z et al. (2023). "APART-QSM: An improved sub-voxel quantitative susceptibility mapping for susceptibility source separation using an iterative data fitting method," *NeuroImage* 274, 120148.
[7] Ji S et al. (2024). "Comparison between R2'-based and R2*-based χ-separation methods: A clinical evaluation in individuals with multiple sclerosis," *NMR Biomed.* May 2024, e.5167.
[8] Doniza L et al. (2023). "MP-PCA image denoising technique for high resolution quantitative susceptibility mapping (QSM) of the human brain in vivo," *Proc. ISMRM* 32, #2948.
[9] Liu T et al. (2013). "Nonlinear formulation of the magnetic field to source relationship for robust quantitative susceptibility mapping," *Magn. Reson. Med.* 69(6), pp.1581-1593.
[10] Karsa A, Shmueli K (2019). "SEGUE: A speedy region-growing algorithm for unwrapping estimated phase." *IEEE Trans. Med. Imaging* 38(6), pp.1347-1357.
[11] Liu T et al. (2011). "A novel background field removal method for MRI using projection onto dipole fields (PDF)," *NMR Biomed.* 24(9), pp.1129-1136.
[11] Wu B et al C (2011). "Whole brain susceptibility mapping using compressed sensing." *Magn. Reson. Med.* 24, pp.1129-1136.
[12] Wei H et al. (2015). "Streaking artifact reduction for quantitative susceptibility mapping of sources with large dynamic range." *NMR Biomed.* 28(10), pp.1294-1303.
[13] Patenaude B et al. (2011). "A Bayesian model of shape and appearance for subcortical brain," *NeuroImage* 56(3), pp.907-922.

Temperature Effects in the Magnetism of Paramagnetic Species in Brain Tissue Sample: An EPR Study

André Avanzine[1], José Henrique Monteiro de Azevedo[1], Fábio Seiji Otsuka[2], Maria Concepcíon García Otaduy[2], Carlos Ernesto Garrido Salmon[1]

[1]*Department of Physics (USP, Ribeirão Preto, Brazil);* [2]*Medical School (HCFM—USP, São Paulo, Brazil)*

Summary: EPR can detect paramagnetic ions in human brain tissue. These ions could contribute to the contrast found in QSM. The acquisition of EPR spectra of several brain regions evaluated the magnetic behavior of Fe^{3+}, copper and ferritin simulated peaks with variable temperature. Copper peaks absorption showed to be the most linear with the inverse of temperature between different subjects, while high-spin iron and ferritin behavior is more heterogeneous.

Introduction: The increasing of metals accumulation in the human brain, mainly iron and copper, is naturally caused by the aging process [1]. The disbalance of these concentrations can induce cellular death or the development of neurodegenerative diseases, such as Parkinson and Alzheimer. In the last decade, researchers have developed qMRI techniques, such as "Quantitative Susceptibility Mapping" (QSM), to quantify the magnetic susceptibility [2]. Yet, the contrast source of this technique is under investigation. "Electron Paramagnetic Resonance" (EPR) is technique sensitive to paramagnetic ions, such as Fe^{3+} high-spin (FeHs), copper (*Cu*) and ferritin systems (Ft), an iron-based protein. These paramagnetic ions could strongly contribute to the contrast found in human brain QSM. This study aims to investigate the magnetic behavior as function of the temperature of paramagnetic species in human brain tissue. Few studies tried the following described methodology, but at that time, they just had few brain regions and just one typical subject [3].

Methods: Gray matter sample from 9 different brain regions was extracted from 8 *ex-vivo* subjects (ages between 50-80 y.o.) and then lyophilized to remove ~80% of water content. EPR spectra were acquired in a X-band spectrometer in 9.15 GHz frequency, 2 mW of power, field sweep from 50 mT to 550 mT (modulation = 1 mT), with single acquisition time of 2 minutes in several temperatures from -80℃ to 20℃ (steps of 20℃). The spectra pre-processing steps included the subtraction of cavity signal and baseline correction, followed by the simulation of each peak (FeHs, *Cu* and Ft) using EasySpin matlab toolbox. Absorption values of the spectra were calculated by the 2nd integral from each simulated peak.

Results: Figure 1.a shows the results of a single brain structure (left putamen) for one typical subject, while figure 1.b shows the absorption patterns of the same brain structure for all typical subjects.
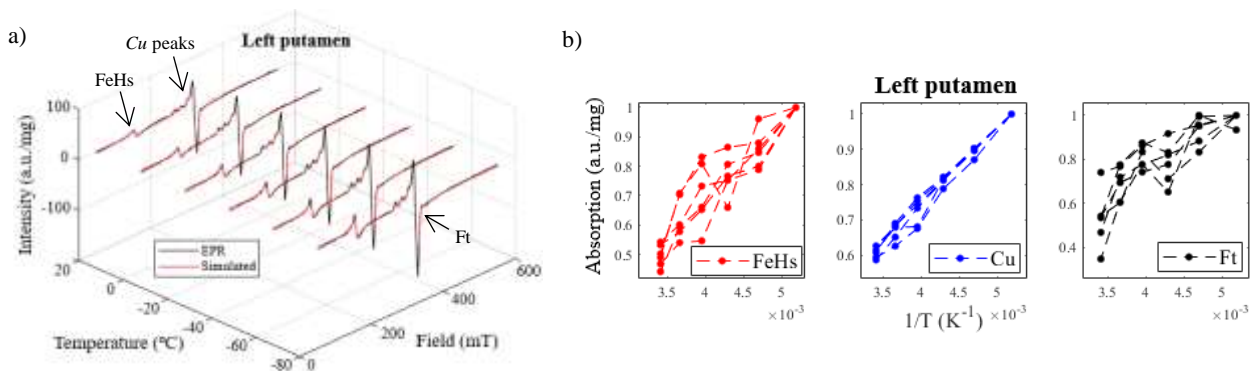
Figure 1 – (a) EPR spectra and simulated curves at different temperatures for left putamen of one typical subject; (b) Absorption as a function of the inverse of temperature for FeHs, *Cu* and Ft (2nd integral of the simulated peak) of left putamen for all typical subjects.

Discussion and Conclusions: The left putamen EPR spectra maintained its peak shape characteristic throughout the temperatures in this range, which all FeHs, *Cu* and Ft peaks slightly increased their intensity amplitude with the decrease of temperature, showing dependence of these paramagnetic species with this variable. The 2nd integral produced strong linear behavior in *Cu* peaks absorption with temperature between all the subjects, representing a classical Curie paramagnetism ($\chi = C/T$, where χ is the magnetic suceptibility, C is the Curie constant and T is the temperature), while FeHs and Ft follows other magnetic behavior and are heterogeneous between different subjects. As both had similar line-shaped pattern, it could be that Ft components has some impact in FeHs environment in all explored temperatures, or vice-versa.

Some researchers studied the Ft absorption behavior in wider temperature intervals [3],[4]. Bussoni et al. [4] used similar EPR analyzes for Ft absorption as a function of temperature in human-liver sample, from 5 K to 210 K. They found a non-linear curve whose maximum absorption value was obtained at 100 K, which was called "blocking temperature", and from that point to lower temperatures, the absorption values dropped again. This results showed that Ft is a iron-protein in which its magnetic behavior changes over wide temperature ranges, which was not observed in FeHs and Cu environments at all. However, the Cu magnetic behavior showed to be the most linear and stable with temperature. Our results expressed here was also observed in the other 8 brain regions available for all typical subjects.

References:

[1] Hallgren, B. et al., "The effect of age on the non-haemin iron in the human brain". Journal of Neurochemistry, vol. 3, no. 1, pp. 762-772, 2015. doi:10.1111/j.1471-4159.1958.tb12607.x

[2] Langkammer, C. et al. "Quantitative susceptibility mapping (QSM) as a means to measure iron? A post mortem validation study". NeuroImage, vol. 62, no. 3, pp. 1593-1599, 2012. doi:10.1016/j.neuroimage.2012.05.049

[3] Otsuka, F. S. et al. "Quantification of paramagnetic ions in human brain tissue using EPR". Brazilian Journal of Physics, vol. 52, no. 4, pp. 272-276, 2022. doi:10.1007/s13538-022-01098-4

[4] Bussoni, L. et al. "In-depth magnetometry and EPR analysis of the spin structure of human-liver ferritin: from DC to 9 GHz". Physical Chemistry Chemical Physics, vol. 25, no. 40, pp. 27694-27717, 2023. doi:10.1039/d3cp01358h

Paramagnetic and Diamagnetic Susceptibility as a Novel Possible Biomarker for Assessing Striatal Dopaminergic Pathway Dysfunction in Prodromal Alpha-Synuclein Disease

Oliver C. Kiersnowski[1], Laura Falcitano[1], Francesco Calizzano[2], Pietro Mattioli[1,2], Beatrice Orso[2], Federico Massa[1], Mattia Losa[1], Andrea Diociasi[1], Stefano Raffa[1], Gianmario Sambuceti[1,2], Silvia Morbelli[3], Elisa Pelosin[2], Laura Avanzino[2], Chunlei Liu[4], Matteo Pardini[1,2], Dario Arnaldi[1,2], Luca Roccatagliata[1,2], Mauro Costagli[1,2]

[1]IRCCS Ospedale Policlinico San Martino, Genova, Italy; [2]University of Genova, Genova, Italy; [3]University of Turin, Turin, Italy; [4]University of California, Berkeley, USA

Summary: Paramagnetic and diamagnetic component susceptibility correlate with DAT-SPECT Z-scores in the substantia nigra and striatum. Therefore, source-separated susceptibility holds promise as a biomarker for assessing dysfunction of the striatal dopaminergic pathway, key for the evaluation of prodromal and overt alpha-synuclein disease.

Introduction: Parkinson's disease (PD) and dementia with Lewy bodies (DLB) are part of a group of neurodegenerative diseases that exhibit abnormal accumulation of the protein alpha-synuclein (aSyn) in the brain[1]. Degeneration of substantia nigra (SN) neurons, a biomarker for neuronal aSyn diseases[2], leads to dysfunction in the striatal dopaminergic pathway, assessed clinically using the dopamine transporter (DAT) single photon emission tomography (SPECT) scan[3]. Patients with prodromal forms of aSyn diseases, including rapid eye movement behavioural disorder (RBD) and prodromal DLB (pDLB), are at high risk of developing overt aSyn diseases[4]. DAT-SPECT is a predictor of phenoconversion[5]: Z-score analysis from DAT-SPECT aids in both the diagnosis of overt neuronal aSyn and the risk assessment of phenoconversion of prodromal aSyn diseases. Quantitative susceptibility mapping (QSM)[6] has identified changes in magnetic susceptibility (χ) in the SN between healthy controls and overt aSyn diseases, e.g. PD[7,8], and recent work has identified SN χ changes in RBD patients[9]. Striatal binding ratios (SBRs), measured from DAT-SPECT in the striatum, have been shown to significantly correlate with χ in the striatum in overt aSyn patients[10] and χ in the SN in RBD patients[9]. However, QSM provides bulk χ estimates averaging the effects of paramagnetic (χ^+) and diamagnetic (χ^-) sources. For the first time, we used the novel susceptibility-source separation technique DECOMPOSE[11], alongside standard QSM, to investigate changes in mean χ, the paramagnetic and diamagnetic component susceptibility (PCS and DCS, respectively) and R_2^* among prodromal and overt aSyn patients compared to healthy controls. We investigate the correlations between susceptibility measures (χ, PCS and DCS) and DAT-SPECT Z-scores, to test if source-separated magnetic susceptibility can be a potential biomarker for assessing the quality of the nigrostriatal pathway in prodromal aSyn patients.

Methods: A total of 78 subjects, including 23 healthy controls (HC), 30 prodromal aSyn (RBD & pDLB) and 25 overt aSyn (PD & DLB) (OaSyn) patients were included. All subjects underwent a multi-echo 3D-GRE MRI sequence on a 3T Siemens MR system with eight echoes at TE1/ΔTE = 5.6/5.6 ms; TR = 51 ms; FA = 18º; 1 mm isotropic resolution; 224x224x144 matrix size; GRAPPA = 2; PF = 6/7 in both PE directions; BW = 340 Hz/px; adaptive coil combine; TA = 8 m 45 s. Subjects with prodromal aSyn disease also underwent a DAT-SPECT scan and were further split into prodromal-negative (PNaSyn: 11 subjects) and prodromal-positive (PPaSyn: 19 subjects) groups based on having a normal or altered DAT-SPECT, respectively, using a threshold Z-score = -1 in the most affected putamen[12]. Age-corrected DAT-SPECT Z-scores in the whole left and right striatum, caudate and putamen were recorded. Susceptibility maps from standard QSM were reconstructed according to the RIN Neuroimaging Network consensus[13]. PCS and DCS maps were calculated using DECOMPOSE[11]. Regional average χ, PCS, DCS and R_2^* in the SN, caudate, putamen and striatum (caudate and putamen) were measured. ROIs were segmented using MRI Cloud[14,15]. Regional values were age-corrected by residualizing the effect of age from a linear fit within each region in the HC group. One-way ANOVA comparing age-corrected χ, PCS, DCS and R_2^* values across all four groups were carried out. To explicitly compare mean SN values across all groups, post-hoc pairwise t-tests with false discovery rate (FDR) correction were performed. Within the prodromal group, DAT-SPECT Z-scores of left and right ROIs were linearly correlated via multiple linear regressions with left and right χ, PCS and DCS in the SN, caudate, putamen and striatum.
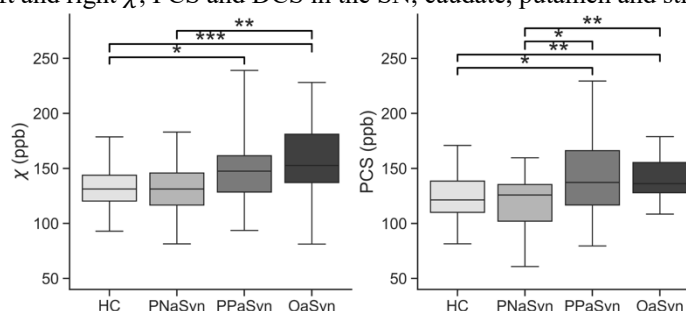
Figure 1 – Age-corrected χ and PCS in the substantia nigra against disease group. Post-hoc and FDR-corrected t-tests indicate higher χ and PCS in the PPaSyn and OaSyn groups compared to the HC and PNaSyn groups, and higher PCS in the PPaSyn group than the PNaSyn group. There were no significant differences in R2* and DCS between groups (not shown).

Results: ANOVA tests indicated significant differences between groups in χ and PCS with post-hoc t-tests revealing significantly higher SN χ and PCS in OaSyn and PPaSyn patients compared to HCs (Figure 1). OaSyn patients also had higher SN χ and PCS than PNaSyn patients, but PPaSyn patients only had higher PCS than PNaSyn patients without a significant difference in χ. Significant negative correlations were found between DAT-SPECT Z-scores in the striatum, putamen and caudate with χ and PCS in the SN (Figure 2, top row), with correlation strength consistently higher for PCS compared to χ. Additional correlations were identified between DAT-SPECT Z-scores and DCS in the striatum and putamen (Figure 2, bottom row).
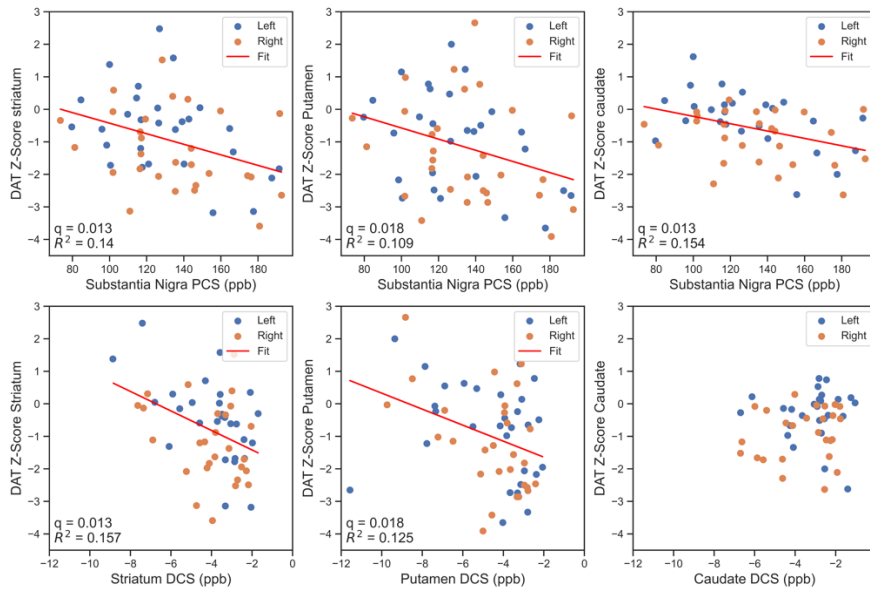
Figure 2 – DAT-SPECT Z-scores in the striatum, putamen, and caudate correlate with PCS in the substantia nigra (top row). The same correlations were found for χ (not shown). These are attributable to iron accumulation in the SN. Z-scores correlate significantly with DCS in the striatum and putamen (bottom row), attributable to neuronal loss in the striatum. These results show that both SN PCS and striatal DCS may act as a novel non-invasive MRI biomarker for assessing dysfunction of the nigrostriatal pathway.

Discussion and Conclusions: Significant increases in SN χ and PCS in OaSyn and PPaSyn patients compared to HCs agree with literature[9,16] and are attributable to iron accumulation. Increases in SN PCS between PPaSyn and PNaSyn patients, with and without altered DAT-SPECT, respectively, suggest that susceptibility-source separation by DECOMPOSE can detect more subtle differences between prodromal aSyn disease compared to standard QSM. It also indicates that DECOMPOSE can identify PCS alterations in prodromal patients prior to exhibiting symptoms of overt aSyn. This is reinforced by the absence of a significant difference between PPaSyn and OaSyn patients, suggesting that the alteration of the SN begins in the prodromal phase of aSyn. This furthers the finding by Li et al[17] that iron accumulation occurs early in the PD disease trajectory, whereby SN χ differences were observed between PD patients and HCs, but not between PD patients of different stages, i.e. stage I vs stage IV. Furthermore, we identified significant negative correlations between χ and PCS in the SN with DAT-SPECT Z-scores in the striatum, putamen and caudate in prodromal aSyn patients. The deterioration of the dopaminergic pathway as assessed by DAT-SPECT is linked to the deterioration of the nigrostriatal neurons that originate in the SN and project into the striatum. Therefore, it is not surprising that a lower Z-score, reflecting higher dysfunction, would correlate with a higher iron content in the SN, given that iron in the SN induces cell loss and aSyn aggregation[18]. We also identified correlations between DAT-SPECT and DCS in the striatum and putamen. DCS is a biomarker of diamagnetic material, χ^-, such as myelin, which sheaths neurons, therefore, a loss of neurons due to deterioration or atrophy would result in a reduced DCS. Given these findings and that DAT-SPECT is costly, limited in its availability and exposes patients to ionizing radiation, χ, and in particular, PCS and DCS holds promise as an alternative, less invasive biomarker to measure nigrostriatal pathway damage in aSyn disease.

References: [1] Brás I C, Outeiro T F (2021), *Cells*, vol. 10(2), pp. 1-19, doi:10.3390/cells10020375. [2] Simuni T, et al. (2024), *Lancet Neurol.*, vol. 23(2), pp. 178-190, doi:10.1016/S1474-4422(23)00405-2. [3] Seibyl J P, Kuo P (2022), *Neurology*, vol. 99(7), pp. S61-S67, doi: 10.1212/WNL.0000000000200786. [4] Postuma RB, et al. (2019), *Brain*, vol. 142(3), pp. 744-759, doi:10.1093/brain/awz030. [5] Arnaldi D, et al. (2021), *Brain*, vol. 144(1), pp. 278-287, doi: 10.1093/brain/awaa365. [6] Shmueli K (2020), *Quantitative Magnetic Resonance Imaging 1st ed*, Elsevier. [7] An H, et al. (2018), *J Neurol Sci*, vol. 386, pp. 46-52, doi:10.1016/j.jns.2018.01.008. [8] Thomas G E C, et al. (2020), *J Neurol Neurosurg Psychiatry*, pp. 418-425, doi:10.1136/jnnp-2019-322042. [9] Varga Z, et al. (2024), *Hum Brain Mapp*, vol. 45(5), doi:10.1002/hbm.26675. [10] Uchida Y, et al. (2020), *Movement Disorders, vol.* 35(8), pp. 1396-1405, doi:10.1002/mds.28077. [11] Chen J, et al. (2021), *Neuroimage*, vol. 242, doi: 10.1016/j.neuroimage.2021.118477 [12] Lanfranchi F, et al. (2023), *Eur J Nucl Med Mol Imaging*, vol. 50(4), pp. 1090-1102, doi:10.1007/s00259-022-06069-0. [13] Lancione M, et al. (2022), *Physica Medica,* vol. 103, pp. 37-45, doi:10.1016/j.ejmp.2022.09.012. [14] Mori S, et al. (2016), *Comput Sci Eng*, vol. 18(5), pp. 21-35, doi:10.1109/MCSE.2016.93. [15] Li X, et al. (2019), *Neuroimage*, vol. 191, pp. 337-349, doi:10.1016/j.neuroimage.2019.02.016. [16] Langkammer C, et al. (2016), *PLoS One*, vol. 11(9), pp. 1-13, doi:10.1371/journal.pone.0162460. [17] Li K, et al. (2021), *Neurology*, vol. 96(15), pp. 2181, doi:10.1212/WNL.96.15_supplement.2181. [18] Li W, et al. (2011), Neurotox Res, vol. 19(3), pp. 435-442, doi:10.1007/S12640-010-9187-x

Impact of Respiratory and Cardiac Physiological Noise Correction on EPI Phase Image Timeseries for functional QSM

R. Allen Waggoner[1], Oliver C. Kiersnowski[2], Kenichi Ueno[1], Luca Roccatagliata[2,3], Chisato Suzuki[1], and Mauro Costagli[1,2,3]

[1]RIKEN Center for Brain Science, Wakoshi, Japan;
[2]IRCCS Ospedale Policlinico San Martino, Genova, Italy;
[3]University of Genova, Genova, Italy

Summary: Respiratory and cardiac noise affects 2D-EPI phase images more than magnitude images and is found to be echo-dependent, with longer echo times suffering from a greater level of both respiratory and cardiac noise. Cardiac-based noise is found to collocate with blood vessels, most easily visible at shorter echo times. Therefore, pre-processing for functional QSM should employ physiological noise correction to better observe functional activations.

Introduction: Functional QSM (fQSM) is a relatively recent extension of traditional QSM[1–3] to functional brain mapping[4–7] and data for fQSM is typically obtained using a 2D-EPI sequence, i.e. the same acquisition sequence as that for conventional functional MRI (fMRI) blood-oxygenation level dependent (BOLD) imaging. However, instead of identifying activations based on T_2^*-weighted signal changes from the magnitude of the complex MRI signal as is done in conventional fMRI, it leverages on the information embedded in the phase. fQSM offers additional information to that of BOLD contrast. The main advantages of fQSM over fMRI include providing a quantitative measure of magnetic susceptibility changes over time, and the images are virtually void of the spurious, nonlocal signal alterations, known as blooming artefacts, that are commonly present in conventional fMRI[8]. Taken together, these two properties enable fQSM to provide a *quantitative* assessment of a *precisely localized* response.

BOLD fMRI data are often affected by unavoidable physiological noise arising from respiration and cardiac-based noise, which can reduce the visibility of true neuronal activation and sometimes appear as false activations themselves[9]. Data is often denoised using some sort of physiological noise modelling, for example with the well-established RETROICOR approach that utilises external recordings of the cardiac and respiratory signal[10]. For typical fMRI data acquired at 3T, this correction, which relies on the signal magnitude only, reduces the temporal variance by 5 to 10%[11]. The impact of physiological noise is known to affect EPI phase to a greater extent than the magnitude signal[12,13], however, the effect of physiological noise *correction* (PNC) and in particular its effect on EPI-phase and fQSM, has not been thoroughly investigated. Here we present data demonstrating that PNC has a much larger impact on the phase data than on magnitude data, and that the difference PNC makes is echo-time dependent for both magnitude and phase data.

Methods: Multi-echo 2D-EPI data was acquired on a Siemens Prisma MRI scanner. Subjects were presented with flickering checkerboard stimuli with a stimulus duration of 0.5 s and an inter-stimulus interval of either 16 or 24 s. Four male subjects (average age, 47.2 years) underwent three functional runs, each one consisting of 200 to 205 functional volumes. For each time volume, 4 echoes were acquired with TE = 14.4, 35.3, 56.1, 77.0 ms and TR = 1.6 s. Sixty slices with thickness of 2.0 mm were acquired with a Field of View of 220 mm and imaging matrix of 110×110, resulting in voxels of size 2.0×2.0×2.0 mm³. A multiband factor of 4, iPat of 3, and 7/8 partial Fourier were used. For all EPI runs, both magnitude and phase images were saved. For PNC, pulse oximetry and respiration data were acquired simultaneously with the EPI scans using a BioPac MP150 system. For PNC, the real and imaginary components of the complex-valued images were fed to an in-house RETROICOR program, separately. The phase images were calculated from the resulting physiological noise-corrected real and imaginary images.

To assess the PNC effectiveness, relative variance (σ_r^2) maps were calculated as follows: a variance (σ^2) map for both magnitude and SEGUE[14] unwrapped phase images at each TE was reconstructed by calculating the variance of the time-series for each voxel. Variance maps were calculated both before and after PNC was applied; the relative variance is then the ratio of the PNC-corrected data variance map to that of the uncorrected data, that is: $\sigma_r^2 = \sigma^2_{\text{afterPNC}} / \sigma^2_{\text{beforePNC}}$. The expected values of σ_r^2 are in the range between 0 and 1 and the smaller σ_r^2 is, the more effective PNC was for that voxel.

Results: Figure 1 shows relative variance maps of the phase data for a representative functional run for one subject. Images in the first row show the relative variance maps that underwent PNC using both the cardiac and respiratory signals. PNC has a larger impact at longer TE values, as is evident via visual inspection of the σ_r^2 maps, which also show smaller average σ_r^2 values in the brain mask for longer TEs. The impact of PNC on phase data is over four times larger than that on the magnitude data: for comparison, the respective σ_r^2 maps for PNC on magnitude data are shown in Figure 2.

Images in rows 2 and 3 of Figure 1 represent the σ_r^2 maps of phase data when either only the respiratory or the cardiac signals are used for PNC, respectively. These images demonstrate that the majority of the correction originates from the

use of the respiratory signal. At longer TE values, some anatomical details start to become apparent in the relative variance maps of phase images, such as the cerebrospinal fluid in the ventricles. The dominant contribution to this effect originates from the respiration signal. The cardiac signal contributes to the reduction of the relative variance of phase image timeseries by a much smaller extent, and its effect does not increase as clearly with TE. Indeed, the contribution of the cardiac signal to the reduction of the relative variance of phase image is most apparent at short TE, in anatomical structures that co-locate with blood vessels (Figure 1, red circles).
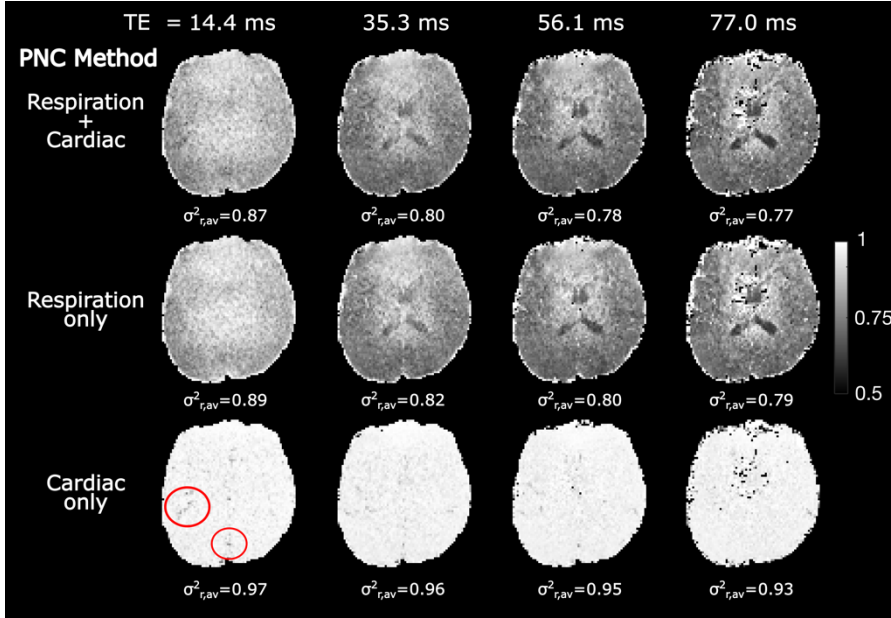
Figure 1: The effect of physiological noise correction for both respiratory and cardiac noise signals on EPI phase and their echo time dependence. As the echo time increases, a greater amount of respiratory and cardiac noise is removed (top row) with average relative variance ($\sigma^2_{r,av}$) of 0.87 compared to 0.77 for the first and last echoes, respectively. The same trends are found for separate respiratory and cardiac correction (middle and bottom rows). Cardiac noise correction co-locates with blood vessels, which is observable at earlier echo times compared to later echo times (red ellipses).
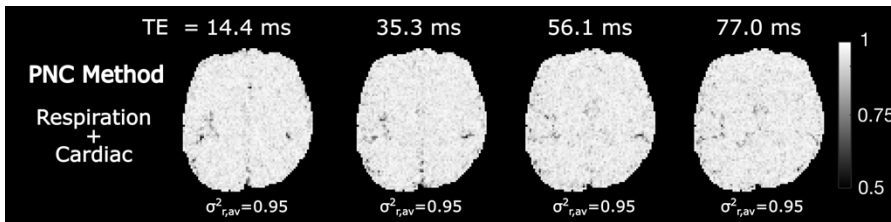
Figure 2: The effect of PNC on the EPI magnitude. Compared to phase (Figure 1), magnitude images are not as affected by respiration and cardiac noise correction and show less echo time dependence.

Discussion and Conclusions: These results show that physiological noise correction has a larger impact on functional phase data than magnitude data. This is an indication that the image phase is more impacted by physiological noise than the image magnitude, which is in line with the known effect of noise on phase compared to magnitude[12,13]. Therefore, PNC using RETROICOR successfully identifies and removes physiological noise from phase and PNC should be included as an important step in the pre-processing pipeline of fQSM data. Future work will investigate the effects of PNC on fQSM activations.

References: [1] Reichenbach JR, et al. (2015), *Clin Neuroradiol*, vol. 25, pp. 225-230, doi:10.1007/s00062-015-0432-9. [2] Shmueli K (2020), *Quantitative Magnetic Resonance Imaging 1st ed*, Elsevier. [4] Bilgic B, et al., (2024), *Magn Reson Med,* vol. 91(5), pp. 1834-1862, doi:10.1002/MRM.30006. [4] Sun H, et al. (2017), *NMR Biomed*, vol. 30(4), doi: 10.1002/nbm.3619. [5]: Balla DZ, et al. (2014), *Neuroimage*, vol. 100, pp. 112-124, doi: 10.1016/j.neuroimage.2014.06.011. [6] Costagli M, et al., (2019), *IEEE Trans Radiat Plasma Med Sci*, vol. 3(4), pp. 516-522, doi:10.1109/TRPMS.2019.2894262. [7] Lancione M, et al., (2021), *Neuroimage*, vol. 244, pp. 118574, doi:10.1016/J.NEUROIMAGE.2021.118574. [8] Özbay PS, et al. (2016), *Neuroimage*, vol. 137, pp. 52-60, doi: 10.1016/j.neuroimage.2016.05.013. [9] Birn RM, et al. (2009), *Neuroimage*, vol. 47(3), pp. 1092-1104, doi:10.1016/J.NEUROIMAGE.2009.05.030. [10] Glover, G.H, et al. (2000), *Magn Reson Med*, vol. 44, pp. 162-167, https://doi.org/10.1002/1522-2594(200007)44:1<162::AID-MRM23>3.0.CO;2-E. [11] Bancelin D, et al. (2023), *Hum Brain Mapp*, vol. 44(3), pp. 1209-1226, doi:10.1002/HBM.26152. [12] Petridou N, et al. (2009), *Magn Reson Imaging*, vol. 27(8), pp. 1046-1057, doi:10.1016/J.MRI.2009.02.006. [13] Hagberg GE, et al. (2012), *Neuroimage*, vol. 59(4), pp. 3748-3761, doi:10.1016/J.NEUROIMAGE.2011.10.095. [14] Karsa A, Shmueli K. (2019), *IEEE Trans Med Imaging*, vol. 38(6), pp. 1347-1357, doi:10.1109/TMI.2018.2884093

Removing the Effect of BOLD Magnitude Signal Changes from Functional Electrical Properties Tomography (fEPT)

Jierong Luo[1], Jannette Nassar[1], Oriana Arsenov[1], Patrick Fuchs[1], and Karin Shmueli[1]

[1]Department of Medical Physics and Biomedical Engineering (University College London, London, United Kingdom)

Summary: We show that previously observed fEPT activations may be attributable to BOLD magnitude contrast introduced by temporally dynamic T_2^*-weighted (T_2^*w) input kernels used for EPT reconstruction. We show that fEPT activations persist even when using temporally invariant input kernels.

Introduction: Phase-based electrical properties tomography (EPT), which calculates tissue electrical conductivities from the MRI transceive phase (φ_0)[1], has shown potential to detect brain functional activations[2-7]. However, the biophysiological mechanisms underlying the observed conductivity changes remain unclear[6]. We recently demonstrated fEPT[7] using a general linear model (GLM) approach with the canonical hemodynamic response function (HRF)[8], by reconstructing each brain conductivity map in the time series using the MagSeg EPT method[9] to minimise noise and boundary artefacts. In this method, the φ_0 gradient was first estimated by polynomial fitting[10] then the conductivity was calculated via the surface integral of the gradient[11]. Within each dynamic of the time series, the CNR-optimal echo-combined[12] T_2^*w magnitude image was used to weight of the polynomial fitting, and tissue segmentations[13] from this image were used to restrict the 3D kernels for the fitting and the integration surface. Although significant conductivity changes were observed within primary visual cortex[7], it is unclear whether those variations may have arisen from the temporally varying T_2^*w magnitude weights and tissue segmentations. Therefore, here we compared three methods to reconstruct conductivity maps using temporally static (invariant) magnitude weights and tissue segmentations, and investigated the effect of temporally dynamic (varying) T_2^*w inputs on fEPT.

Methods: Four healthy volunteers (HVs) were scanned using a high-resolution multi-echo GRE-EPI sequence[14] at 3T, with a visual stimulus paradigm of an 8 Hz flickering checkerboard alternated with a white screen in 15.6 s blocks. The complex data were used to calculate φ_0, as described previously[7] and above. To provide temporally invariant kernels, we performed optimal echo-combination[12] of the T_2^*w magnitude images for each volume (dynamic) and calculated the mean over all 70 volumes. T_1w images were acquired using a 1-mm isotropic MPRAGE sequence. We then reconstructed conductivity maps using MagSeg[9] with different magnitude (Fig. 1a) and segmentation (Fig. 1b) kernels using: a) T_2^*w magnitude from each dynamic (temporally dynamic with T_2^*w); b) mean T_2^*w (temporally static with T_2^*w); c) T_1w image (temporally static with T_1w); and d) mean T_2^*w magnitude weighting and T_1w-segmentation.

To measure the reconstructed EPT quality, we calculated the temporal signal-to-noise ratio (tSNR) of each conductivity map time series. To avoid any bias introduced by preprocessing[14], no filtering or smoothing was applied to the conductivity maps prior to the functional analysis. We analysed the EPT time series using SPM12[8] as reported previously[7] and compared the functional activation results. As a control for spurious fEPT activations, ME GRE-EPI data were also acquired in one of the volunteers without a visual stimulus, and processed identically.
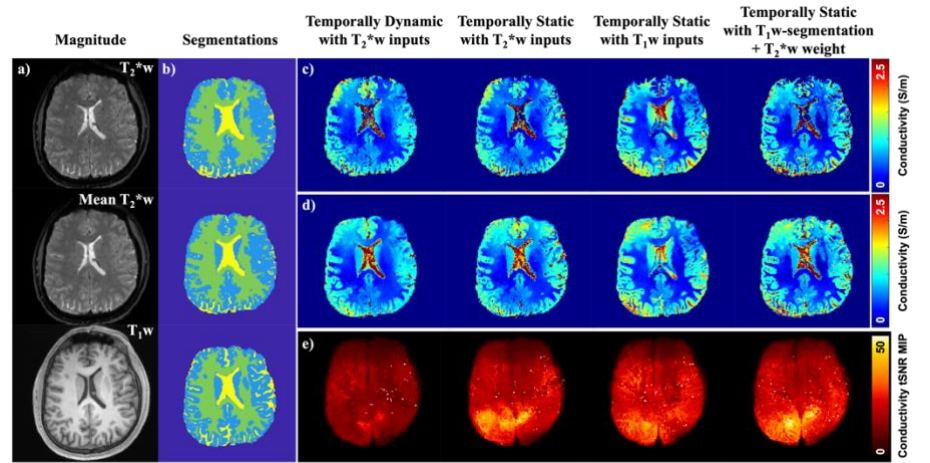
Figure 1 – In HV1, different magnitude images used to weight the polynomial fitting (a); Tissue segmentations derived from corresponding magnitude images in Fig. 1a using SPM[13] (b); Single-volume EPT maps reconstructed using different inputs for magnitude weighting and tissue segmentation (c); Temporal median conductivity maps over 70 coregistered EPT maps (d); Maximum intensity projection (MIP) of the temporal SNR (tSNR) of the 70 coregistered EPT maps (e).

Results and Discussion: While EPTs reconstructed with different inputs are visually comparable (Fig. 1c-d), the reconstructions using temporally static inputs demonstrate higher tSNR (Fig. 1e). In all subjects, compared with EPTs with dynamic T_2^*w inputs (Figs. 2a and 3a), using static inputs provided more localised clusters of functional activations in fEPT, with the activations within visual area largely reduced or absent (Figs. 2b-d and 3b-d). Fewer activations than with static T_2^*w inputs (Figs. 2b and 3b) were found with static T_1w inputs (Figs. 2c and 3c) or with T_1-based segmentation

(Figs. 2d and 3d). Only very few scattered voxels were activated in the absence of a visual stimulus (Fig. 2e), suggesting activated fEPT clusters with static inputs (Figs. 2b-d, 3b-d) are not due to type 1 error. The reduced activations within the primary visual cortex in fEPT with static vs. dynamic inputs suggests that magnitude BOLD contrast may have contributed via magnitude weights and/or tissue segmentations to the fEPT activations observed when using temporally dynamic T_2^*w inputs for MagSeg EPT reconstruction. We also observed inter-subject variability in fEPT (Figs. 2 and 3), regardless of the magnitude weighting and tissue segmentations inputs used for EPT reconstruction.
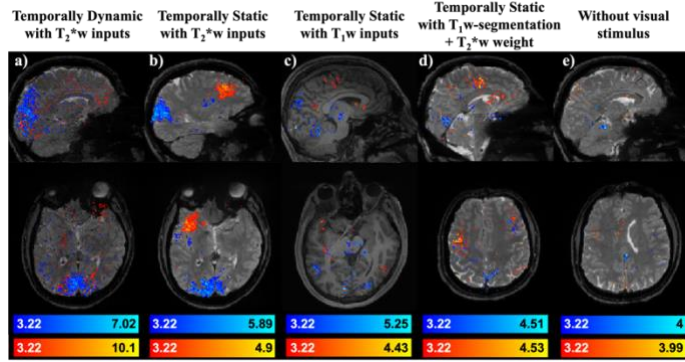
Figure 2 – Positive (red) and negative (blue) functional activations in HV1. The maximum intensity projection (MIP) of T-statistics ($p<0.001$) for: EPT time series reconstructed using different tissue segmentations and magnitude weighting inputs (a-d); EPTs reconstructed using temporally static T_2^*w inputs from an acquisition without visual stimulation (e).
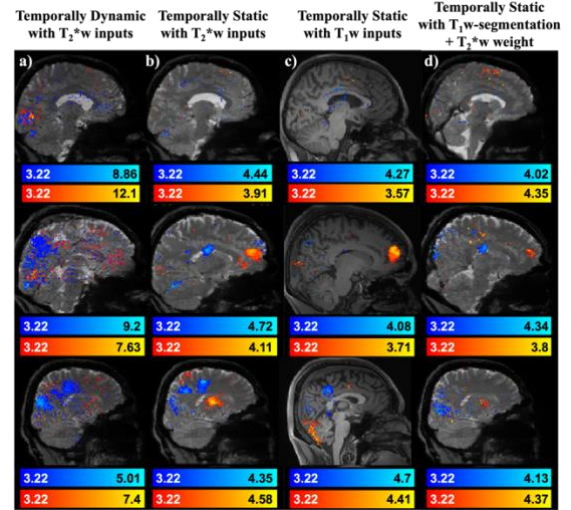
Figure 3 – Positive (red) and negative (blue) functional activations in HV2 (top), HV3 (middle) and HV4 (bottom). MIP of T-statistics ($p<0.001$) for the EPT time series reconstructed using different tissue segmentations and magnitude weighting inputs (a-d).

Conclusions: We have demonstrated that BOLD contrast in T_2^*w magnitude images may have contributed to apparent fEPT activations obtained using a GLM with a canonical HRF, via temporally dynamic T_2^*w magnitude inputs for EPT reconstruction. Using temporally static inputs, fEPT activations were still found in various brain regions, but with large inter-subject variability.

References:
[1] Katscher U and Van den Berg C A T (2017), "Electric properties tomography: biochemical, physical and technical background, evaluation and clinical applications," *NMR Biomed.*, vol. 30, pp. e3729, doi: 10.1002/nbm.3729.
[2] Helle M and Katscher U (2019), "Electrical properties tomography based functional magnetic resonance imaging (EPT-fMRI)," *Proc. Ann. Meeting ISMRM 2019*, Abstract 3759.
[3] Schmidt R (2019), "Electrical conductivity as a potential mean to decouple the hemodynamic response from fMRI," *Proc. Ann. Meeting ISMRM 2019*, Abstract 3777.
[4] Jung K J, et al. (2023), "Investigation of electrical conductivity changes during functional activity of the brain via phase-based MR-EPT: Preliminary observation," *Proc. Ann. Meeting ISMRM 2023*, Abstract 0922.
[5] Jahng G H, et al. (2023), "High-frequency conductivity signal changes measured with functional MREPT during visual stimulation," *Proc. Ann. Meeting ISMRM 2023*, Abstract 0923.
[6] Rae C D, et al. (2024), "Functional conductivity imaging: quantitative mapping of brain activity," *Proc. Ann. Meeting ISMRM 2024*, Abstract 1293.
[7] Luo J, et al. (2024), "Preliminary whole-brain functional electrical properties tomography using gradient-echo echo-planar imaging," *Proc. Ann. Meeting ISMRM 2024*, Abstract 3681.
[8] Friston K J, et al. (1995), "Statistical parametric maps in functional imaging: a general linear approach," *Hum. Brain Mapp.*, vol. 2, pp. 189-210, doi: 10.1002/hbm.460020402.
[9] Karsa A, and Shmueli K (2021), "New approaches for simultaneous noise suppression and edge preservation to achieve accurate quantitative conductivity mapping in noisy images," *Proc. Ann. Meeting ISMRM 2021*, Abstract 3774.
[10] Lee S K, et al. (2015), "Theoretical investigation of random noise-limited signal-to-noise ratio in mr-based electrical properties tomography," *IEEE Trans. Med. Imaging*, vol. 34, pp. 2220-2232, doi: 10.1109/TMI.2015.2427236.
[11] Voigt T, et al. (2011), "Quantitative conductivity and permittivity imaging of the human brain using electric properties tomography," *Magn. Reson. Imaging*, vol. 66, pp. 456–466, doi: 10.1002/mrm.22832.
[12] Poser B A, et al. (2006), "BOLD contrast sensitivity enhancement and artifact reduction with multiecho EPI: parallel-acquired inhomogeneity-desensitized fMRI," *Magn. Reson. Med.*, vol. 55, pp. 1227–1235, doi: 10.1002/mrm.20900.
[13] Ashburner J and Friston K (2005), "Unified segmentation," *NeuroImage*, vol. 26, pp. 839-851, doi: 10.1016/j.neuroimage.2005.02.018.
[14] Kiersnowski O C, et al. (2024), "Rapid high resolution integrated structural and functional susceptibility and conductivity mapping in the human brain," *Proc. Ann. Meeting ISMRM 2024*, Abstract 188.
[15] Mandija S et al. (2024), "The first MR electrical properties tomography (MR-EPT) reconstruction challenge: preliminary results of simulated data," *Proc. Ann. Meeting ISMRM 2024*, Abstract 182.
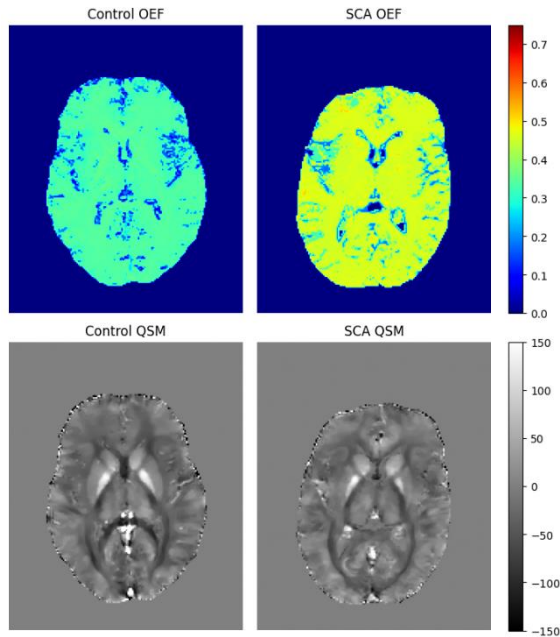
Haematocrit-Corrected QSM + qBOLD Reveals Globally Elevated Brain Oxygen Extraction Fraction in Sickle Cell Anaemia

Mitchel Lee[1*], Isabelle Hawley[2*], Fenella Kirkham[2], Karin Shmueli[1]

[1]*Medical Physics and Biomedical Engineering, University College London, London, UK; [2]Developmental Neurosciences, Institute of Child Health, University College London, London, UK; *Joint First Authors*

Summary: QSM + qBOLD oxygen extraction fraction (OEF) mapping is applied to sickle cell anaemia (SCA), revealing widespread OEF increases throughout the brain. Low haematocrit in SCA is shown to drive elevated OEF estimates.

Introduction: Sickle cell anaemia (SCA) is a genetic blood disorder defined by the presence of abnormal sickle haemoglobin, which becomes polymerized in the deoxygenated state. Complications in the brain, such as stroke, cognitive deficit and chronic neuropathic pain, occur secondary to microcirculatory obstruction, ischaemia and inflammation [1]. A key marker of brain health is the cerebral metabolic rate of oxygen consumption ($CMRO_2$), determined by the product of cerebral blood flow (CBF), arterial oxygen content (CaO_2) and tissue oxygen extraction fraction (OEF) [2]. Autoregulatory mechanisms in the brain can lead to increases in CBF and/or OEF to maintain sufficient $CMRO_2$ levels for brain function in situations of increased metabolic demand, or, in the context of SCA, reduced CaO_2 due to anaemia [3]. CBF increases are well documented in SCA [4], but studies of OEF in SCA show diverse results, with microvascular shunting, in which elevated flow reduces time for blood-tissue oxygen exchange, potentially explaining findings of reduced OEF [5].


Figure 1: Left: OEF map and QSM (ppb) in a representative control subject. Right: OEF map and QSM in a representative SCA patient

Several imaging methods exist to estimate OEF in the brain, with invasive ^{15}O PET representing the gold standard [6]. Previous work investigating OEF changes in SCA have found conflicting results, primarily due to differences in calibration models used in T2 relaxation under spin tagging (TRUST) methods [7,8]. Prior studies using QSM based measurements have found reduced venous oxygen saturation in the straight and superior sagittal sinuses, consistent with elevated OEF [8]. In addition, studies using asymmetric spin echo (ASE) sequences to map voxel-wise OEF found significantly elevated OEF compared to controls, particularly in regions vulnerable to stroke [9, 10].

QSM + qBOLD (QQ), a novel MRI technique for OEF mapping, combines the phase (QSM) and magnitude (qBOLD) information from multi-echo gradient echo (ME-GRE) sequences and has been found to provide comparable OEF estimates to the gold-standard [11]. An extension to the QQ method, QQ-CCTV [12], combines temporal clustering, in which voxels with similar magnitude signal evolution are assumed to have similar model parameters, and tissue-type information, where clusters are divided into grey matter, white matter and CSF components. Total variation regularization is further used in model fitting to impose spatial smoothness.

In this work, we used QQ-CCTV to investigate OEF changes in the brain in SCA. This builds on previous work applying QQ to the paediatric subset of our study cohort [13], by accounting for the effect of reduced haematocrit in SCA patients on the estimated OEF values.

Methods: 90 SCA patients (18.0±9.9 years, 44 male) and 33 healthy age and race matched controls (18.9±10 years, 16 male) were imaged on a 3T Siemens Magnetom Prisma system with a 64-channel head RF coil. 3D ME-GRE images were acquired with parameters: $TE_1 = 3$ms, $\Delta TE = 4$ms, 7 echoes, TR = 38ms, flip angle = 15°, resolution = 1.15 x 1.15 x 1.15 mm^3. T1-weighted MP-RAGE images were also acquired at 1 mm^3 resolution.
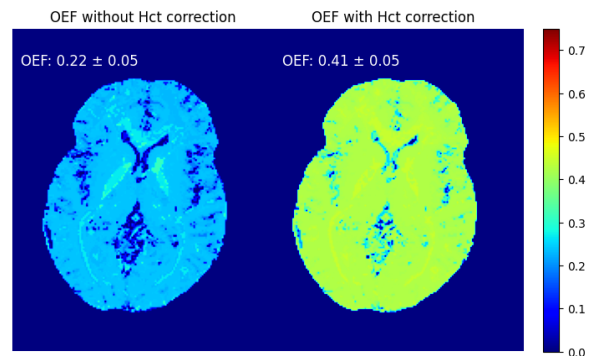
Figure 2: Left: OEF map calculated in a 15-year-old female SCA patient using default haematocrit value (47%). Right: OEF map calculated in the same patient using measured venous haematocrit of 26%. The mean whole-brain OEFs (mean±sd) are shown beside each map.

The QQ-CCTV algorithm was applied to estimate OEF maps and QSMs from the ME-GRE magnitude and phase data. QSMs were obtained using a MEDI toolbox pipeline, consisting of linear phase gradient correction, nonlinear field fitting, region-growing phase unwrapping, projection onto dipole fields (PDF) background field removal and CSF-referenced MEDI+0 dipole inversion [14]. The combined QSM and qBOLD cost function was then minimized to jointly estimate

Figure 3: *Left: Whole-brain OEF as a function of Hct with fitted linear (blue) and power law (red) curves and 95% confidence intervals. Right: Box plot of whole brain OEF in SCA patients and controls, with (***) indicating statistical significance at p<0.001.*

venous blood oxygenation (Y_v), transverse relaxation rate (R_2), non-blood susceptibility (χ_{nb}), venous blood volume fraction (v) and initial signal intensity (S^0). OEF was estimated from Y_v as OEF = $1-Y_v/Y_a$, where Y_a is the arterial blood oxygenation, assumed to be 0.98 for both SCA patients and controls.

For the SCA patients, venous haematocrit (Hct_v) values were taken from the closest blood test to the MRI scan date. Measurements of Hct_v were not available for the controls in this study, so reference values were obtained from the literature [15]. Capillary haematocrit (Hct) was estimated as a constant fraction of Hct_v, taken to be Hct = 0.759 * Hct_v for both SCA patients and controls. We investigated the relationship between Hct_v and mean whole-brain OEF by linear regression and compared OEF values between patients and controls. Independent of changes to other variables, OEF is expected to vary inversely with Hct (OEF $\propto$ 1/Hct). Therefore, a power law model was also fit to the data.

Results: SCA patients had significantly lower haemocrit (26.6±4.9%) than controls (40.4±2.5%). Example SCA and control OEF maps and QSMs are shown in Figure 1. An example SCA OEF map calculated with and without correction for low haematocrit is shown in Figure 2, showing increased OEF throughout the brain when Hct is accounted for. Figure 3 shows a plot of mean whole-brain OEF as a function of Hct, fitted linear and power law curves and corresponding fit parameters. Both models identified a significant negative relationship between OEF and Hct, with the power law model exponent estimated to be -0.69±0.05. Whole-brain OEF in SCA (40.9±7.9%) was significantly elevated compared to controls (30.9±4.9%), as shown in the box plot in Figure 3.

Discussion and Conclusions: We found significantly elevated OEF throughout the brain in SCA, with whole brain OEF measures agreeing with previous results from ASE OEF mapping studies [9,10]. The inclusion of measured haematocrit in the QQ model resulted in large increases in OEF in the SCA patients (Fig. 2) compared to our previous work [13]. The deviation of the exponent of the fitted power law model (Fig. 3) from -1 suggests that coupled changes to other QQ parameters in SCA may partially mediate the relationship between OEF and Hct. Future work will investigate these relationships further. We aim to apply this method to a separate SCA study in which control haematocrit measurements are available, overcoming the limitation of estimated Hct in controls in this study. These results will also be combined with ASL CBF mapping to obtain regional measures of $CMRO_2$, to further elucidate mechanisms of brain injury in SCA.

References:
[1] Rees, David C et al. "Sickle-cell disease." *Lancet*, vol. 376,9757 (2010): 2018-31. **[2]** Rodgers, Zachary B et al. "MRI-based methods for quantification of the cerebral metabolic rate of oxygen." *Journal of cerebral blood flow and metabolism*, vol. 36,7 (2016): 1165-85. **[3]** Wood, John C; Brain O2 reserve in sickle cell disease. *Blood* 2019; 133 (22): 2356–2358. **[4]** Stotesbury, Hanne et al. "MRI detection of brain abnormality in sickle cell disease." Expert review of hematology vol. 14,5 (2021): 473-491. **[5]** Afzali-Hashemi, Liza et al. "Assessment of functional shunting in patients with sickle cell disease." *Haematologica* vol. 107,11 2708-2719. 1 Nov. 2022. **[6]** Fan, Audrey P et al. "Quantification of brain oxygen extraction and metabolism with [15O]-gas PET: A technical review in the era of PET/MRI." *NeuroImage* vol. 220 (2020): 117136. **[7]** Bush, Adam M et al. "Diminished cerebral oxygen extraction and metabolic rate in sickle cell disease using T2 relaxation under spin tagging MRI." *Magnetic resonance in medicine* vol. 80,1 (2018): 294-303. **[8]** Murdoch, Russell et al. "A Comparison of MRI Quantitative Susceptibility Mapping and TRUST-Based Measures of Brain Venous Oxygen Saturation in Sickle Cell Anaemia." *Frontiers in physiology* vol. 13 913443. 29 Aug. 2022. **[9]** Fields, Melanie E et al. "Regional oxygen extraction predicts border zone vulnerability to stroke in sickle cell disease." *Neurology* vol. 90,13 (2018): e1134-e1142. **[10]** Fields, Melanie E et al. "Functional Connectivity Decreases with Metabolic Stress in Sickle Cell Disease." *Annals of neurology* vol. 88,5 (2020): 995-1008. **[11]** Cho, Junghun et al. "Cerebral oxygen extraction fraction (OEF): Comparison of challenge-free gradient echo QSM+qBOLD (QQ) with 15O PET in healthy adults." *Journal of cerebral blood flow and metabolism* vol. 41,7 (2021): 1658-1668. **[12]** Cho, Junghun et al. "Temporal clustering, tissue composition, and total variation for mapping oxygen extraction fraction using QSM and quantitative BOLD." *Magnetic resonance in medicine* vol. 86,5 (2021): 2635-2646. **[13]** Hawley, Isabelle et al. "A novel MRI technique to estimate cerebral Oxygen Extraction Fraction in children with Sickle Cell Anaemia and Controls", *Proceedings of the 18th International Child Neurology Congress* (2024) **[14]** Liu, Zhe et al. "MEDI+0: Morphology enabled dipole inversion with automatic uniform cerebrospinal fluid zero reference for quantitative susceptibility mapping." *Magnetic resonance in medicine* vol. 79,5 (2018): 2795-2803. **[15]** Castro, O L et al. "Age- and sex-related blood cell values in healthy black Americans." *Public health reports* vol. 102,2 (1987): 232-7.
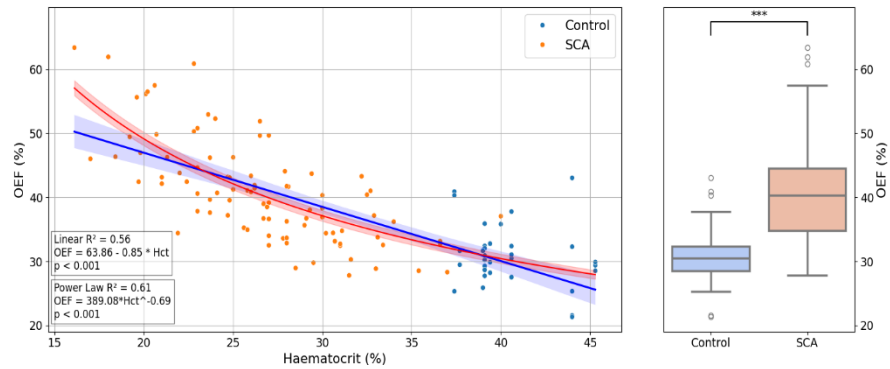
A fast method for B_1^+ predictions from measured data to evaluate Electrical Properties Tomography reconstruction

Thierry G. Meerbothe[1,2], Kyu-Jin Jung[3], Chuanjiang Cui[3], Dong-Hyun Kim[3], Cornelis A.T. van den Berg[1,2], Stefano Mandija[1,2]

[1]Department of Radiotherapy, Division of Imaging and Oncology (UMC Utrecht, Utrecht, The Netherlands); [2]Computational Imaging Group for MR Therapy and Diagnostics (UMC Utrecht, Utrecht, The Netherlands); [3]Department of Electrical and Electronic Engineering (Yonsei University, Seoul, Republic of Korea)

Summary: We developed a physics-based method to assess electrical properties (EPs) reconstructions based on the discrepancy between measured and predicted B1+ fields from reconstructed EPs maps. This can be used to increase confidence for both physics based and deep learning based in-vivo reconstructions.

Introduction: In MR Electrical Properties Tomography (EPT), Electrical Properties (EPs, conductivity σ and relative permittivity ε_r) are reconstructed from measured complex radiofrequency B_1^+ fields. Physics-based reconstruction methods are widely used, but generally suffer from noise and errors at tissue interfaces, which lead to large variations in the reconstructed EP maps. On the other hand, deep learning based reconstructions are more robust to these errors, but suffer from generalization problems (e.g. lower accuracy in pathologies). Overall, it is difficult to evaluate EPT reconstructions in-vivo, since ground truth EPs are not available. These problems lead to low confidence in the reconstructed EPs, which hampers clinical translation.

To solve these problems, we presented a physics-based method to evaluate EPs reconstructions by computing complex B_1^+ maps based on EPs as input and using the discrepancy between the measured and predicted B_1^+ maps as quality metric [1]. Here, we refined the methodology, validated the model with simulated and measured data and further investigated the effect of erroneous input EPs on the resulting discrepancy maps.

Methods: Under the assumption $\partial B_z=0$, the EPs are related to the measureable complex B_1^+ field by [2]:

$$-\nabla^2 B_1^+ = \omega^2 \mu_0 \varepsilon_c B_1^+ - \left(g_x + ig_y\right)\left(\frac{\partial B_1^+}{\partial x} - i\frac{\partial B_1^+}{\partial y}\right) - g_z \frac{\partial B_1^+}{\partial z}$$

ω=Larmor frequency $\varepsilon_c= \varepsilon_0\varepsilon_r - i\sigma/\omega$ (complex permittivity)	μ_0=vacuum permeability $g_{x,y,z} = \partial_{x,y,z}\ln(\varepsilon_c)$

By approximating the derivative operators with central finite difference (FD) schemes, the complex B_1^+ field in a certain voxel can be expressed in the complex permittivity ε_c and the B_1^+ field of neighboring voxels, yielding a recurrent relation:

$$B_{i+1} = \frac{AB_i}{\frac{6}{h^2} - \mu_0\omega^2 E}$$

B [N x 1]=B_1^+ vector at iteration i and i+1 A [N x N]=Sparse FD operators on off-diagonal	E [N x 1]=Complex permittivity h=Resolution

This relation is then recurrently applied while imposing closed loop Dirichlet boundary conditions (BC) for B (retrieved from MRI measurements), until the difference between subsequent iterations is below convergence limit C, at which point the B_1^+ matching the EPs and BCs has been estimated.

The estimated B_1^+ field is dependent on the EP map used as input. Therefore, the discrepancy $D_\phi = \widehat{\phi^+} - \phi^+$ and $D_M = |\widehat{B_1^+}| - |B_1^+|$ between the estimated and measured B_1^+ phase and magnitude give information about the error in input EPs. Such discrepancy maps give an indication how good the total fields match, but they do not show localized errors in the underlying EPs. Analogous to phase/magnitude only EPT, this can instead be represented by the 2nd order derivative of the discrepancy maps: $L_\varphi = \nabla^2\left(S(D_\phi)\right)/\mu_0\omega$ and $L_M = \nabla^2\left(S(D_M)\right)/\mu_0\omega$, where S is a (Gaussian) smoothing function to overcome noise effects.

Three experiments were done: **1:** to validate the model, model accuracy and error maps were studied using simulated brain data (Sim4Life, ZMT Zurich) [3], where ground truth EPs were used as input, both with and without the assumption $\partial B_z=0$. **2:** to test the model sensitivity in measurement setting, 3 spherical phantoms with known EPs (σ=0.41, 0.51, 0.61 S/m, ε_r=78) were scanned with a 3 T Ingenia CX (Philips Healthcare, Best, The Netherlands). The transceive phase was acquired using a 3D bSSFP (1 mm³ isotropic resolution); $|B_1^+|$ was acquired using DREAM (1x1x3 mm³ resolution). Next, B_1^+ maps were estimated and evaluated (D_φ maps) for all combinations of reference EPs and measured complex B_1^+ maps. **3:** to show the application of model evaluation in practice and to see if known EPT errors can be identified with evaluation, Helmholtz EPT (H-EPT) with 11x11x11 kernel mean smoothing (both phase only and complex) is done for sphere 3.

Results: *Figure 1* shows the accuracy of the model estimation (which takes ~30 seconds for a volume with ~ 1 million voxels) with and without B_z, using the ground truth EPs as input. Complex B_1^+ estimations show accurate results in the realistic case (when excluding non measureable B_z), but expanding the model by including B_z further decreases the discrepancies, as expected. These low errors validate the model and show how the B_z term influences B_1^+ predictions.
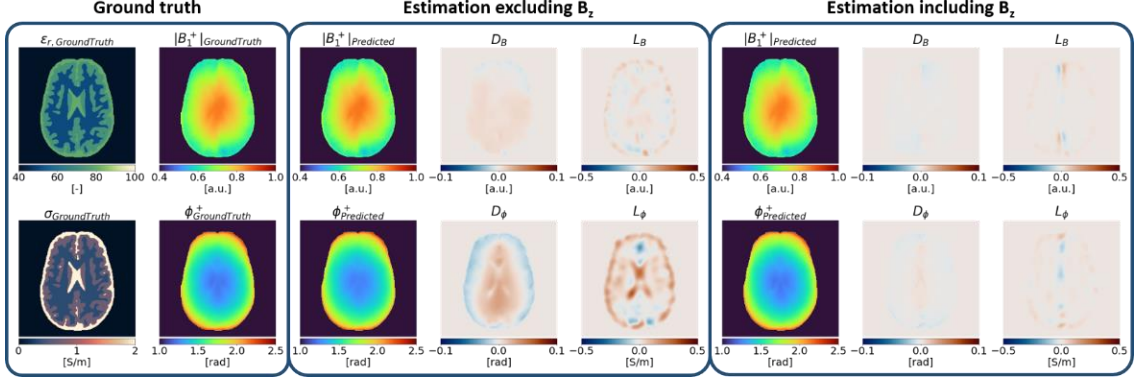

Figure 1: Model validation using simulated brain data. Estimations without B_z show a small discrepancy between measured predicted B_1^+ fields, especially around the ventricles. This is resolved by including B_z, showing that the model is accurate in simulation setting.

Figure 2 shows discrepancy maps (D_ϕ) for the sphere phantoms. For every sphere, three B_1^+ estimations were done, using all reference conductivity values. It is clear that for the correct input EPs, discrepancies are low, while differences increase for larger errors in input EPs. This experiment indicates that the method is capable of detecting errors in conductivity maps below 0.1 S/m.

Figure 3 shows the application of the evaluation pipeline for H-EPT reconstruction. With GT EPs as input, errors in D_ϕ are low. With phase only EPT as input, known to overestimate EPs, larger errors are observed in the D_ϕ and L_ϕ maps. H-EPT shows a lower error in comparison, reflecting the known higher accuracy of $|B_1^+|$ inclusion. Additionally, larger errors can be seen (see arrows) on the right side of the phantom, corresponding to an area with a reconstruction from an imaging artifact. This illustrates the capability of the method to indicate areas with erroneous conductivity reconstructions.
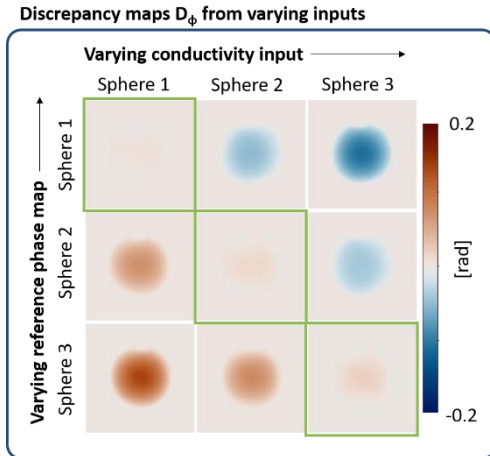
Figure 2: Sphere phantom experiment, including three spheres with varying conductivity. Correct input EPs gives low differences (diagonal), while incorrect input EPs give higher differences (off-diagonal).
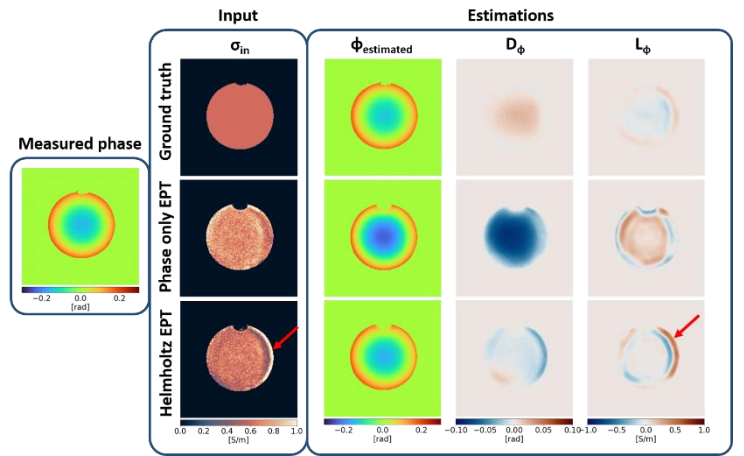
Figure 3: Evaluation of the error in estimated phase maps using as input: GT EPs (first row), filtered phase only H-EPT (second row) and filtered H-EPT (third row). Arrows indicate erroneous conductivity reconstruction as result of an imaging artifact.

Discussion and Conclusions: In this work, we have shown that accurate B_1^+ prediction from input EPs is possible using the developed model despite the absence of B_z information. We have also demonstrated in measurements that the method is capable of distinguishing conductivity differences of 0.1 S/m in phantoms. A disadvantage of the method is the need for inclusion of the relative permittivity, which is more difficult to estimate with EPT. For the phantom experiments in this work we solved this by using water permittivity as input. Additionally, further work should focus on application of the method in-vivo.

References: [1] Meerbothe TG et. al. "Complex B1+ field predictions to evaluate Electrical Properties Tomography Reconstructions". *In: Proceedings 33rd ISMRM Singapore* 2024

[2] Liu, Jiaen, et al. "Electrical properties tomography based on B₁ maps in MRI: principles, applications, and challenges." *IEEE Transactions on Biomedical Engineering* 64.11 (2017): 2515-2530.

[3] Meerbothe TG et. al. "A database for MR-based electrical properties tomography with in silico brain data—ADEPT." *Magn. Reson. Med.* 91.3 (2024): 1190-1199.

Exploring flow-induced displacement artifacts for vessel artifacts in χ-separation

Taechang Kim[1], Jongho Lee[1]

[1]*Department of Electrical and Computer Engineering (Seoul National University, Seoul, Korea, Republic of)*

Summary: This study reveals that erroneous R_2^* values in vessels caused by flow-induced displacement artifacts are a potential source of vessel artifacts in χ-separation maps, as demonstrated through a computer simulation and an *in-vivo* experiment.

Introduction: χ-separation is an advanced quantitative susceptibility mapping (QSM) method that generates para- (χ_{para}) and diamagnetic susceptibility maps (χ_{dia}), potentially reflecting iron and myelin distribution, respectively [1]. However, the reconstructed susceptibility maps report inaccurate values within and near large vessels, which is regarded as errors called vessel artifacts. This study explores flow-induced displacement artifacts [2–4] in multi-echo GRE as a potential source of vessel artifacts in χ-separation, utilizing a computer simulation and an *in-vivo* experiment.

Methods:

[Flow phantom simulation] To assess the effect of flow-related displacement artifacts to the R_2^* maps, a phantom simulation was conducted. The simulation consisted of three steps:

(1) Phantom construction A 3D phantom was created with two compartments: static compartment and flowing compartment. The voxel size of the phantom was $1 \times 1 \times 1$ mm^3 and the matrix size of the phantom was $50 \times 30 \times 50$. Each voxel in the static compartment contained 10 spins, while each voxel in the flowing compartment included 100 spins. The flowing spins moved at a velocity of 20 cm/s within the flowing compartment (Fig. 1a, red arrows).

(2) Simulated data acquisition Assuming the phase offset and field inhomogeneity are negligible, the k-space signal at time t is expressed as follows:

$$s(t) = \int m\big(\mathbf{r}(0)\big) \cdot e^{-R_2^* t} \cdot e^{-j \cdot \gamma \int_0^t \mathbf{G}(\tau) \cdot \mathbf{r}(\tau) d\tau} d\mathbf{r} \qquad (Eq.\,1).$$

where $m(\mathbf{r})$ is the magnetization of a spin at position $\mathbf{r}$, γ is the gyromagnetic ratio, $\mathbf{G}$ is the imaging gradient fields, and R_2^* is the transverse relaxation rate. Using a simplified multi-echo GRE monopolar sequence (Fig. 1a), the phase evolution of each spin was calculated at each time step ($\Delta t = 0.08$ ms). The k-space signal was then determined using ($Eq.\,1$) by summing the complex signals from all spins. Echo times were set to be 6, 14, 22, 30, 38 and 46 ms, and the transverse relaxation rate (R_2^*) was set to 25 Hz. The simulated k-space data were then Fourier transformed to acquire the multi-echo complex images.

(3) R_2^* fitting An R_2^* map was generated by fitting a mono-exponential decay curve to the multi-echo magnitude images in a voxel-wise manner. The fitting was conducted using a nonlinear least squares solver (*lsqnonlin*, MATLAB 2016b). Two ROIs were defined: one within the flowing compartment (Fig. 1c, red box in R_2^* map) and the other near the flowing compartment (Fig. 1c, blue box in R_2^* map). Signal decay curves for each ROI were then analyzed.

[*In-vivo* experiment] An *in-vivo* experiment was performed to explore the effect of the flow-induced displacement artifacts on χ-separation. One subject data from a previous study was used (local IRB approved) [1]. The data included $1 \times 1 \times 1$ mm^3 multi-echo GRE data with 6 head orientations (flow compensated on the first echo only) and $1 \times 1 \times 2$ mm^3 2D multi-echo spin-echo (MESE) data. Phase processing was conducted adhering to the QSM consensus paper [5]: phase unwrapping – ROMEO [6], echo combination – weighted echo averaging [7], background field removal – V-SHARP [8]. An R_2^* map was generated by voxel-wisely fitting a mono-exponential decay function, and an R_2 map was created by dictionary matching using StimFit [9]. The R_2' map was calculated ($R_2' = R_2^* - R_2$), and negative values were set to zero. Finally, χ_{para} and χ_{dia} maps were reconstructed using χ-separation-COSMOS [10].

Results: As shown in the magnitude images in Fig. 1b, the flowing compartment shifts in the phase encoding direction as echo time increases. When the R_2^* map and signal decay curves within and near the flowing compartment are examined (Fig. 1c), the signal in the flowing compartment disappears as echo time increases (Fig. 1c, red box in decay curve), resulting in an erroneously elevated R_2^* for mono-exponential fitting. Conversely, the signal increases along with echo time in a nearby static compartment where the flowing compartment signal has shifted (Fig. 1c, blue box in decay curve), causing R_2^* to converge to near-zero.

Large vessel regions in the *in-vivo* data are illustrated in Fig. 1d. The erroneously increased R_2^* values in vessel regions and decreased R_2^* values near vessel regions, caused by flow-induced displacement artifacts, propagate to R_2', leading to vessel artifacts in both χ_{para} and χ_{dia} maps.

Discussion and Conclusions: Based on the biophysical model of χ-separation [1], χ-separation algorithm with erroneously increased (or decreased) R_2' results in overestimated (or underestimated) χ_{para} and χ_{dia}. Our experiments demonstrate that flow-induced displacement artifacts cause erroneous R_2^*, leading to inaccurate R_2', and consequently erroneous χ_{para} and χ_{dia} maps. Therefore, flow-induced displacement artifacts are one of the potential sources of vessel artifacts in χ-separation.

While not discussed in this study, more factors may induce vessel-related artifacts. Field inhomogeneity due to susceptibility differences between vessels and tissues, which was ignored in this study, also induces blurring in the readout direction, potentially affecting the R_2^* maps [4]. Additionally, because regions with flow do not satisfy the static dephasing regime assumed by χ-separation [1], estimating susceptibility values in vessels becomes more challenging. Recently (ISMRM 2024, Singapore, abstract #2457), a vessel segmentation algorithm for χ-separation was proposed to exclude vessel artifacts for reliable χ-separation analysis.
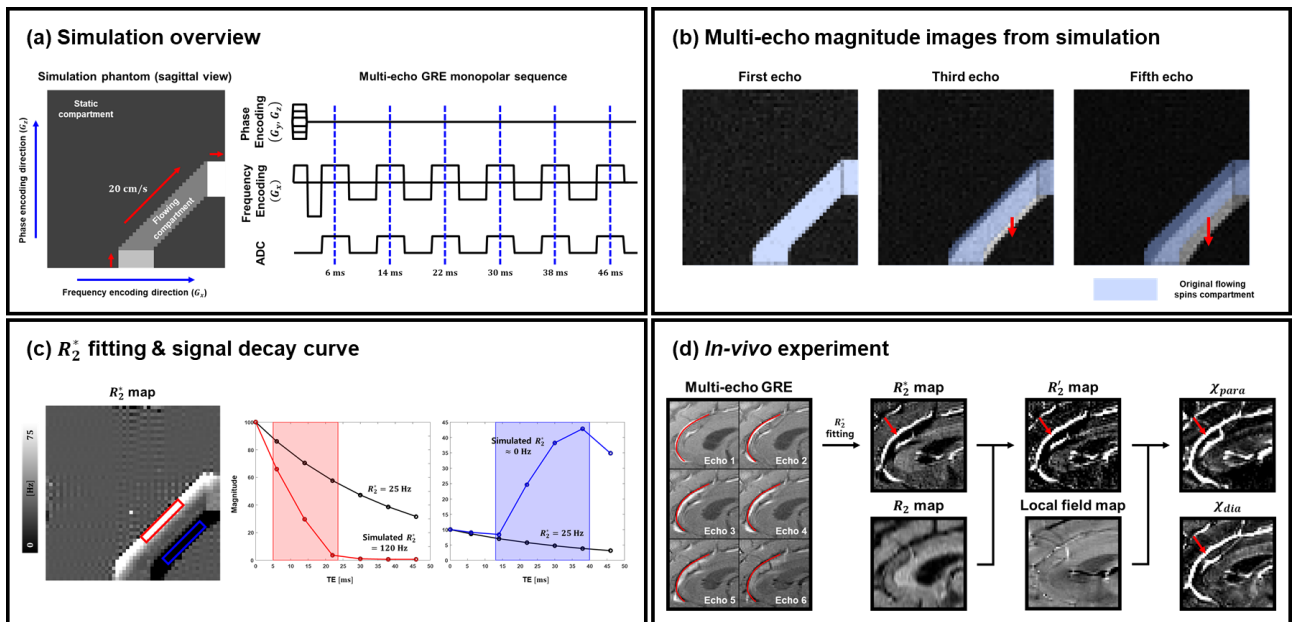
Figure 1. (a) The simulation phantom and multi-echo GRE monopolar sequence. (b) Multi-echo magnitude images from the simulation. The flowing compartment shifts in the phase encoding direction. (c) R_2^* fitting & signal decay curve. The signal absence due to shift of the flowing compartment results in increased R_2^* values, whereas signal increase in the nearby static compartment causes R_2^* values to converge to near-zero. (d) *In-vivo* experiment. Vessel artifacts in χ-separation maps exhibit a similar tendency to artifacts in the R_2^* map, implying that flow-induced displacement artifacts can be a potential source of vessel artifacts.

References:
[1] Shin, H.-G. (2021), "χ-separation: Magnetic susceptibility source separation toward iron and myelin mapping in the brain," *NeuroImage*, vol. 240, p. 118371.
[2] Larson, T. C. (1990), "Spatial misregistration of vascular flow during MR imaging of the CNS," *ASNR*
[3] Nishimura, D. G. (1991), "On the nature and reduction of the displacement artifact in flow images," *Magn. Reson. Med.*, vol. 22, no. 2, pp. 481-492.
[4] Xu, B. (2014), "Flow compensated quantitative susceptibility mapping for venous oxygenation imaging," *Magn. Reson. Med.,* vol. 72, no. 2, pp 438-445.
[5] QSM Consensus Organization Committee (2024), "Recommended implementation of quantitative susceptibility mapping for clinical research in the brain: A consensus of the ISMRM electro-magnetic tissue properties study group," *Magn. Reson. Med.*
[6] Dymerska, B. (2021), "Phase unwrapping with a rapid opensource minimum spanning tree algorithm (ROMEO)," *Magn. Reson. Med.,* vol. 85, no. 4, pp. 2294-2308
[7] Wu, B. (2012), "Fast and tissue-optimized mapping of magnetic susceptibility and T2* with multi-echo and multi-shot spirals," *NeuroImage*, vol. 59, no. 1, pp. 297-305.
[8] Wu, B. (2012), "Whole brain susceptibility mapping using compressed sensing," *Magn. Reson. Med.,* vol. 67, no. 1, pp. 137-147.
[9] Lebel, R. Marc. (2012), "StimFit: A toolbox for robust T2 mapping with stimulated echo compensation," *ISMRM 20th Annual Meeting, Melbourne, Australia, 2558.*
[10] Shin, H.-G. (2022), "chi-separation using multi-orientation data in invivo and exvivo brains: Visualization of histology up to the resolution of 350 um," *Joint Annual Meeting ISMRM-ESMRMB & ISMRT 31st Annual Meeting, London, UK, 0771.*

Synthesized Histology Images of Myelin and Iron Stainings from 7T Multi-Contrast MRI

Sutatip Pittayapong[1,2], Simon Hametner[2], Beata Bachrata[1,3], Romana Höftberger[2], Günther Grabner[1]

[1]Department of Medical Engineering (Carinthia University of Applied Sciences, Klagenfurt, Austria); [2]Department of Neurology (Medical University of Vienna, Vienna, Austria); [3]Karl Landsteiner Institute for Clinical Molecular MR in Musculoskeletal Imaging (Vienna, Austria)

Summary: Multi-contrast MRI, combined with deep learning, can synthesize myelin and iron stainings, giving ex vivo information for insights into histology and more.

Introduction: Myelin and iron are key to understanding neurodegenerative diseases[1]. However, these substances can be assessed by histology only[2]. A non-invasive magnetic resonance imaging (MRI) reveals these brain tissue properties in different contrasts. QSM and R2* are promising contrasts for analyzing iron in deep gray matter, but the QSM shows a negative correlation with myelination for white matter regions[3]. Thus, understanding the connection between the brain's microscopic structure and the properties of in vivo MRI still needs to be improved. Our research could support this field by using deep learning to synthesize myelin and iron stainings from various MRI contrasts. This technique can enhance our understanding of brain development, function, and diseases, offering a promising future for medical imaging and histology.

Methods: This study was approved by the ethics committee of the Medical University of Vienna (EK Nr. 1727/2014). A human cadaver head of an 88-year-old female was imaged using a 7T Siemens MAGNETOM system. T1 weighted images were acquired using an MP2RAGE sequence, and a multi-echo gradient echo was used to create QSM and R2* images. After the MRI, the brain was prepared for histological staining. Myelin staining was performed using the Luxol fast blue with periodic acid Schiff method; iron staining was performed using the diaminobenzidine-enhanced Turnbull blue (TBB) staining method[3]. All stainings were digitized at a resolution of 800 pixels per inch (0.03175 mm/pixel) using an Agfa Duoscan® photo scanner and saved uncompressed in "tif" format.

Histogram matching was performed before MRI to histology registration to increase registration accuracy. Registration between myelin stainings and T1-weighted images was performed using a combination of manual landmarks and non-linear registration using the minc-toolbox[4]. All MRI contrasts were transformed into the histology space using the T1 to myelin transformation.

All MR images were downsampled to 256 x 256 pixels, followed by skull stripping with fslbet[5] and corrected for B1 inhomogeneity with N4BiasFieldCorrection[6]. Normalization of all means equal to zero and a standard deviation of 1 was performed to increase the model's generalizability. The training subject was divided into 80 slices for training and each 10 for validation and testing. Data augmentation for rotation and scaling was performed to increase the training dataset to 160.

Firstly, T1, R2*, and QSM were used as the input images, and myelin staining as a ground truth. The Generative Adversarial Network (GAN) was established with seven inner residual blocks. The attention layer was attached to the last three layers to capture the long-distance dependency of crucial details. Adam optimizer was used for both generator and discriminator with initial learning rates at 0.0001 and 0.0004, respectively. The different rates helped to stabilize the model's training. L1 loss and perceptual loss were added besides conventional adversarial loss to increase the performance of capturing image fidelity.[7]. The network was trained for 12,500 iterations until it converged. According to a study by Fukunaga et al., myelin and iron could exist in the same voxel[8]. Therefore, the myelin staining image was another input for iron staining synthesized model training. The generated myelin from the first model was used as an input for the iron prediction at the inference step.

Peak Signal-to-Noise Ratio (PSNR) was used to evaluate the quality of the reconstructed image, and Structural Similarity Index (SSIM) was used to assess the perceptual quality of the synthesized image.

Results: The GAN models could generate myelin and iron histology stainings from multi-contrast MRI (Figure 1c-d). Adding myelin histology as input to the model contributed to better results for iron staining prediction (Table 1). Moreover, despite the limited training dataset, the network provided good results for other ex vivo and in vivo datasets (Figure 2e-h) with the limitation of including micro details of histology that need improvement. A combination of T1, R2*, and QSM gave lower PSNR and SSIM; when using only T1 as input, the model could predict overall brain anatomy, but including R2* and QSM added more details in synthesized images, especially deep gray matter region which has different iron content between ex vivo and in vivo subjects (Figure 1i-j).

Discussion and Conclusions: These synthesized histology stainings offer detailed ex vivo information, which could be extended to various tissue properties. More training subjects are necessary to improve network performance. Overcoming limitations requires first improving image registration between MRI and histology stainings. Additionally, the color version of histology stainings could provide richer information than the grayscale image. By employing deep learning techniques, we generated brain histology images by combining MR data from various contrasts, contributing to identifying essential markers in histology.

	Myelin Staining		Iron Staining	
	PNSR ↑	SSIM ↑	PNSR ↑	SSIM ↑
T1	**26.25**	**0.85**	24.32	0.77
T1 + R2* + QSM	25.92	0.85	24.54	0.77
T1 + R2* + QSM + Myelin Staining			**25.06**	**0.79**

Table 1 – PSNR & SSIM using different contrasts as an input to the model for both myelin and iron stainings prediction.
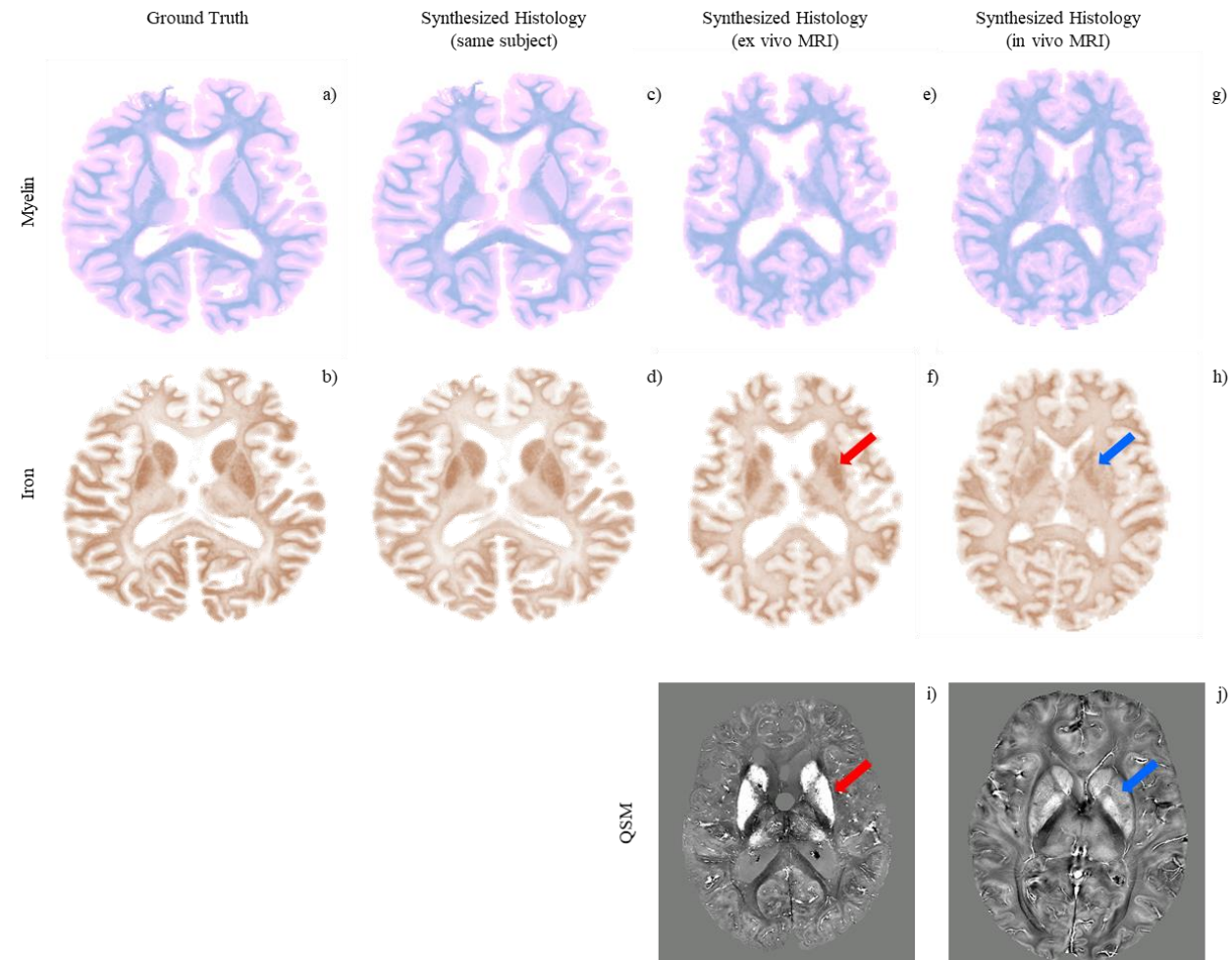
Figures 1 – Synthesized myelin (c) and iron (d) stainings compared to the ground truth (a and b) - testing slice of the same subject. Synthesized myelin (e) and iron (f) stainings from another ex vivo - and (g, h) from another in vivo MRI dataset. QSM images of the ex vivo (i) and of the in vivo MRI dataset (j) – note the increased iron in the putamen (f and i; red arrow) for the ex vivo and the decreased iron (h and j; blue arrow) in the in vivo images. Please note that image processing was done using gray-scale images – for visualization purposes, they were converted to the known color spaces.

References: [1] O'Callaghan J, et al. *NeuroImage*. 2017;159:334-345; [2] Hametner S, et al. *Annals of neurology*. 2013;74:848-861; [3] Hametner S, et al. *NeuroImage*. 2018;179:117-133; [4] Vincent RD, et al. *Frontiers in neuroinformatics*. 2016;10:35; [5] Smith SM. *Human brain mapping*. 2002;17:143-155; [6] Tustison NJ, et al. *IEEE transactions on medical imaging*. 2010;29:1310-1320; [7] Johnson J, et al. In: Leibe B, et al., eds. *Computer Vision – ECCV 2016*. Vol. 9906. Cham: Springer International Publishing; 2016:694-711. *Lecture Notes in Computer Science*; [8] Fukunaga M, et al. *Proceedings of the National Academy of Sciences of the United States of America*. 2010;107:3834-3839

χ-separation (chi-separation) toolbox v1.0:

updates compared to the beta version and advanced functionalities

Sooyeon Ji[1], Kyeongseon Min[1], Hyeong-Geol Shin[2,3], Jun-Hyeok Lee[5], Minjun Kim[1], Se-Hong Oh[4], and Jongho Lee[1]

[1]Department of Electrical and Computer Engineering, Seoul National University, Seoul, Korea, Republic of[1]; [2]Department of Radiology, Johns Hopkins University School of Medicine, Baltimore, MD; [3]F.M. Kirby Research Center for Functional Brain Imaging, Kennedy Krieger Institute, Baltimore, MD; [4]Department of Biomedical Engineering, Hankuk University of Foreign Studies, Yongin, Korea, Republic of; [5]Seoul National University College of Medicine, Seoul, Republic of Korea

Summary: The χ-separation toolbox v1.0 equipped with advanced functionalities enables handy reconstruction of high-quality para- and diamagnetic susceptibility maps, fostering utilization of χ-separation across diverse applications.

Introduction: χ-separation,[1] a method to separate positive and negative susceptibility sources, demonstrated the ability to offer clinically valuable information.[1–3] For the handy application of the χ-separation algorithm to existing or new datasets, there is an increasing need for a toolset that generates high-quality χ-separation. To address this, we developed the χ-separation toolbox v1.0 (Figure 1), extending on the previously developed beta version. The toolbox provides a user-friendly graphic user interface (GUI)-based application of χ-separation, including χ-separation algorithms as core functionality, and new advanced processing options to enhance the quality of the χ-separation results.

Methods

Input/output Complex 3D multi-echo GRE (mGRE) data with DICOM or NIFTI formats are accepted as input. For DICOM input, the relevant parameters (B0 direction, center frequency, voxel size, echo times) are automatically read from the DICOM header. For NIFTI format, the parameters except for B0 direction and voxel size must be manually filled in. An R2' (=R2*-R2) or R2* map, QSM, local field map, and a brain mask may be provided as optional inputs. The outputs of the toolbox are the separated χ_{para} and χ_{dia} maps.

Preprocessing of input data When an R2' or R2* map is not provided, an R2* map is calculated from the mGRE data by fitting an exponential function to the decay curve. The brain mask is calculated using BET (FSL, FMRIB, Oxford, UK)[4] when not provided.

For pipelined phase processing, existing toolboxes must be downloaded.[5–8] The toolbox GUI provides two options for pipelined phase unwrapping: ROMEO[9] followed by weighted echo averaging,[10] or non-linear complex fit[11] followed by SEGUE.[12] For background field removal, VSHARP[13] is pipelined in the GUI.

Core functionality (Figure 1)

- **χ-sepnet:** Two neural-net implementations of χ-separation is included: χ-sepnet-R2' and χ-sepnet-R2*. χ-sepnet-R2* can be used when R2' map is not available.
- **χ-separation:** When an R2' map is available, the toolbox provides two in-house algorithms for optimization-based χ-separation: χ-separation-MEDI and χ-separation-iLSQR. The first option uses the MEDI-regularizer[14] for optimization, following the original paper.[1] The second option calculates χ-separation maps based on iLSQR.[15]
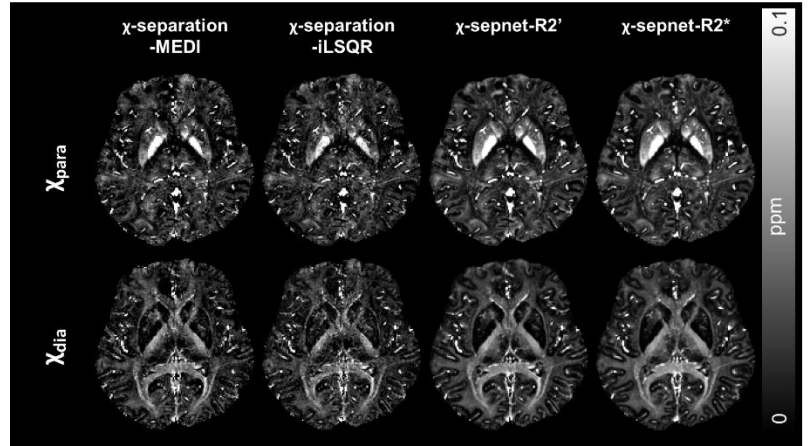

Figure 1. Results of the four chi-separation methods
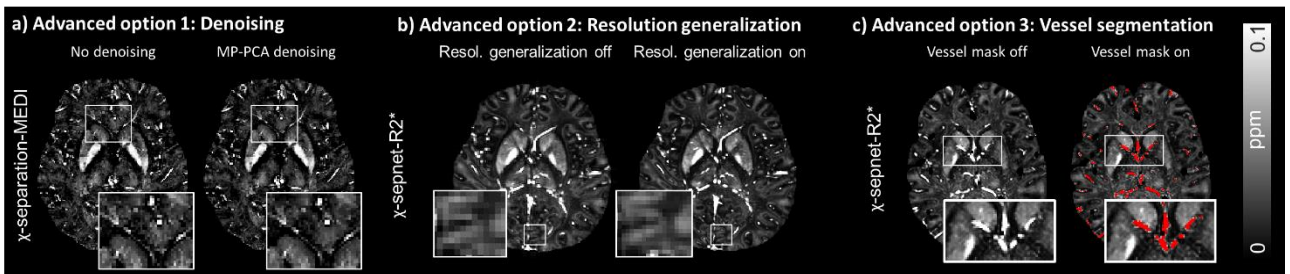

Figure 2. The results of the three advanced processing options

Advanced processing options (Figure 2)

- **Denoising:** Denoising options are provided to compensate for low signal to noise ratio of mGRE magnitude data used for R2* mapping. The first is Marchenko-Pastur principal component analysis (MP-PCA) denoising, which takes advantage of the intrinsic redundancy of the multi-echo images[16].

- **Resolution generalization for χ-sepnet:** An option to utilize the "resolution generalization" pipeline[17] is provided, which enables the inference of data that has higher or lower resolution than that of the training data (i.e., 1 mm^3), including anisotropic resolution. When using χ-sepnet for reconstruction, by enabling this option, χ_{para} and χ_{dia} maps are reconstructed at the input resolution, without spatial information loss. When this option is disabled, the input local field map is down-sampled to the network-trained resolution (1 mm^3) for inference.

- **Vessel masking:** χ-separation maps suffer from vessel artifacts. These vessels may hamper the accurate calculation of ROI values, leading to less interpretable results. The toolbox provides an option to generate vessel masks that can be used to mask out vessels for group analysis.
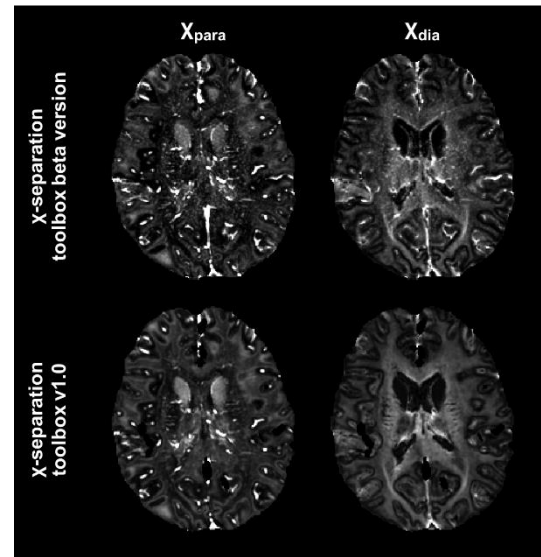
Figure 1. Improvement compared to the beta version

Conclusion

The χ-separation toolbox v1.0 enables GUI-based χ-separation application, providing core χ-separation algorithms and advanced processing options. The advanced options offer high-quality χ-separation with fewer artifacts and less noise, and also a tool for more accurate analysis. In particular, the comparison between the results from version 1.0 vs. beta version clearly demonstrates the improvement. The toolbox is uploaded in GitHub (https://github.com/SNU-LIST).

References:

1. Shin HG, Lee J, Yun YH, et al. χ-separation: Magnetic susceptibility source separation toward iron and myelin mapping in the brain. *NeuroImage*. 2021;240:118371. doi:10.1016/j.neuroimage.2021.118371

2. Shin HG, R, Seo J, et al. Imaging multiple sclerosis histopathology using susceptibility source separation: a postmortem brain study. In: *Proceedings of the 30th Annual ISMRM Meeting*. London; 2022.

3. Kim W, Shin HG, Lee H, et al. χ-Separation Imaging for Diagnosis of Multiple Sclerosis versus Neuromyelitis Optica Spectrum Disorder. *Radiology*. 2022;307(1):e220941. doi:10.1148/radiol.220941

4. Jenkinson M, Beckmann CF, Behrens TEJ, Woolrich MW, Smith SM. FSL. *Neuroimage*. 2012;62(2):782-790. doi:10.1016/j.neuroimage.2011.09.015

5. Releases · korbinian90/CompileMRI.jl. https://github.com/korbinian90/CompileMRI.jl/releases. Accessed November 7, 2023.

6. Chunlei Liu — UC Berkeley. https://chunleiliulab.github.io/software.html. Accessed November 7, 2023.

7. Cornell MRI Research Lab Research Interests. https://pre.weill.cornell.edu/mri/pages/qsm.html. Accessed November 7, 2023.

8. SEGUE available from XIP. https://xip.uclb.com/product/SEGUE. Accessed November 7, 2023.

9. Dymerska B, Eckstein K, Bachrata B, et al. Phase unwrapping with a rapid opensource minimum spanning tree algorithm (RO-MEO). *Magn Reson Med*. 2021;85(4):2294-2308. doi:10.1002/mrm.28563

10. Wu B, Li W, Avram AV, Gho SM, Liu C. Fast and tissue-optimized mapping of magnetic susceptibility and T2* with multi-echo and multi-shot spirals. *NeuroImage*. 2012;59(1):297-305. doi:10.1016/j.neuroimage.2011.07.019

11. Liu T, Wisnieff C, Lou M, Chen W, Spincemaille P, Wang Y. Nonlinear formulation of the magnetic field to source relationship for robust quantitative susceptibility mapping. *Magn Reson Med*. 2013;69(2):467-476. doi:10.1002/mrm.24272

12. Karsa A, Shmueli K. SEGUE: A Speedy rEgion-Growing Algorithm for Unwrapping Estimated Phase. *IEEE Trans Med Imaging*. 2019;38(6):1347-1357. doi:10.1109/tmi.2018.2884093

13. Wu B, Li W, Guidon A, Liu C. Whole brain susceptibility mapping using compressed sensing. *Magn Reson Med*. 2012;67(1):137-147. doi:10.1002/mrm.23000

14. Liu T, Liu J, Rochefort L de, et al. Morphology enabled dipole inversion (MEDI) from a single-angle acquisition: Comparison with COSMOS in human brain imaging. *Magn Reson Med*. 2011;66(3):777-783. doi:10.1002/mrm.22816

15. Li W, Wang N, Yu F, et al. A method for estimating and removing streaking artifacts in quantitative susceptibility mapping. *NeuroImage*. 2015;108:111-122. doi:10.1016/j.neuroimage.2014.12.043

16. Veraart J, Novikov DS, Christiaens D, Ades-aron B, Sijbers J, Fieremans E. Denoising of diffusion MRI using random matrix theory. *Neuroimage*. 2016;142:394-406. doi:10.1016/j.neuroimage.2016.08.016

17. Ji S, Park J, Shin HG, Yoon J, Kim M, Lee J. Successful generalization for data with higher or lower resolution than training data resolution in deep learning powered QSM reconstruction. In: *Proceedings of the 31st Annual ISMRM Meeting*. Toronto; 2023:4168.

Susceptibility- and structure-based investigation of deep gray matter in common types of degenerative cerebellar ataxias

Andreas Deistung[1,2], Simon Graf[1,2], Dominik Jäschke[3,4], Sophia L. Göricke[5], Walter A. Wohlgemuth [1,2], Dagmar Timmann[3]

[1] University Clinic and Outpatient Clinic for Radiology, Department for Radiation Medicine, University Hospital Halle (Saale), Halle (Saale), Germany; [2] Halle MR Imaging Core Facility, Medical Faculty of Martin-Luther-University Halle-Wittenberg; [3] Department of Neurology and Center for Translational Neuro- and Behavioral Sciences (C-TNBS), Essen University Hospital, Essen, Germany; [4] Department of Radiology and Nuclear Medicine, University Hospital Basel, Basel, Switzerland; [5] Institute of Diagnostic and Interventional Neuroradiology, Essen University Hospital, Essen, Germany

Summary: Investigation of susceptibility and volume changes in deep gray matter (GM) nuclei across common types of degenerative cerebellar ataxia to explore the presence of an ataxia-type specific deep GM-based signature.

Introduction: Degenerative cerebellar ataxias are slowly progressive disorders that affect the cerebellum and cerebellar pathways to various degrees [1]. Little is currently known about iron metabolism and its potential contribution to pathology in cerebellar ataxias. While QSM revealed different patterns of abnormalities in volume and iron concentration in the dentate nuclei [2] across different types of ataxia, also pathological evidence for impairment of specific deep GM nuclei in the cerebrum and midbrain in ataxia exists [3, 4]. In the present exploratory cross-sectional study, QSM and T_1w imaging were used to measure tissue magnetic susceptibility (indicating iron concentration) and structural volume in deep gray matter (caudate nucleus, globus pallidus [GP], putamen, red nucleus [RN], substantia nigra [SN], subthalamic nucleus [STN], thalamus, nucleus accumbens, dentate nucleus [DN]), respectively, in common types of degenerative cerebellar ataxias.

Methods: Eighty-four patients with spinocerebellar ataxias (SCA1, SCA2, SCA3, SCA6), 15 patients with Friedreich ataxia (FRDA) and nineteen patients with multiple system atrophy, cerebellar type (MSA-C) as well as one hundred twenty-six healthy controls underwent 3T-MRI and clinical assessments. A total of 16 SCA1, 14 SCA2, 24 SCA3, 25 SCA6, 15 FRDA, and 18 MSA-C patients were included. Multi-echo gradient-echo imaging (TE_{1-4}=6.47ms/17.23ms/27.99ms/38.75ms, TR=62ms, voxel size=0.5mm×0.5mm×0.5mm) for QSM and T_1w imaging (MP-RAGE, voxel size=1mm×1mm×1mm, TE=3.26ms, TR=2530ms, TI=1100ms, FA=7°) for deep GM segmentation were performed at 3T (MRI-PET system, Siemens Healthineers). Volumes of interest (VOIs) of deep GM were segmented automatically by applying DBSegment to T_1w data [5]. The individual segmentations were transferred to the susceptibility maps by applying the rigid transform matrix computed between the T_1w data and gradient-echo magnitude data employing advanced normalization tools (ANTs). To control for differences in head size, the total intracranial volume (TIV) was estimated from the T_1w images using the standard pre-processing pipeline of the Computational Anatomy Toolbox 12 (CAT12). The deep GM VOIs were then corrected via residualization as described in [2]. Consequently, standardized residuals are used as estimates of the volume corrected for head size. Independent linear models were set-up with susceptibilities or volumes obtained from the nine deep GM regions as dependent variables for each specific patient group and their matched controls. Each model included intercept, anatomical region (categorial variable), group (categorial variable: patient or control) and age as predictors as well as the region – group interaction.

Results & Discussion: Susceptibilities and TIV-corrected volumes of deep GM areas, shown in Figure 1, revealed different changes across disease types. Susceptibilities did not vary significantly in SCA3 and SCA6 compared to their controls, being mostly in line with findings by Marvel et al. [6], who investigated a smaller cohort (n_{SCA3} = 10, n_{SCA6}=6, $n_{control}$ = 9) with 7T MR imaging. While we observed slightly higher susceptibilities in SN in SCA3 and lower susceptibilities in DN in SCA6, they did not reach statistical significance (p > 0.05). We observed lower susceptibilities in SN and STN in FRDA patients than in controls, while the other deep GM nuclei did not show statistical changes. Contrary to our study, Harding et al. [4] observed higher susceptibilities in DN and RN in FRDA (30 patients vs. 33 controls). We found a moderately higher susceptibility in more circumscribed parts of the dentate nuclei in FRDA (see [2]). However, at the level of the entire dentate, susceptibilities were not significantly different from controls (Fig. 1A). Susceptibility values were significantly higher in GP, RN, SN and DN in SCA1 compared to matched controls. In SCA 2, only susceptibilities in SN were higher compared to controls. In MSAC, only the susceptibility in DN was higher compared to controls. The deep GM regions with increased susceptibility in the patients mostly showed volume loss in the same regions, indicating increases in iron concentration rather than iron content. Atrophy of deep GM is a more common observation than variations in the susceptibility. In future, we will employ voxel-based analysis to explore the presence of patterns of local susceptibility and volume variations within deep GM nuclei. This will also help to explain the observed differences to previous studies [4, 6]. In addition, associations to clinical scores describing severity of impairments of motor and cognitive functions will be carried out to investigate the potential of deep GM volume and susceptibility to serve as biomarker.
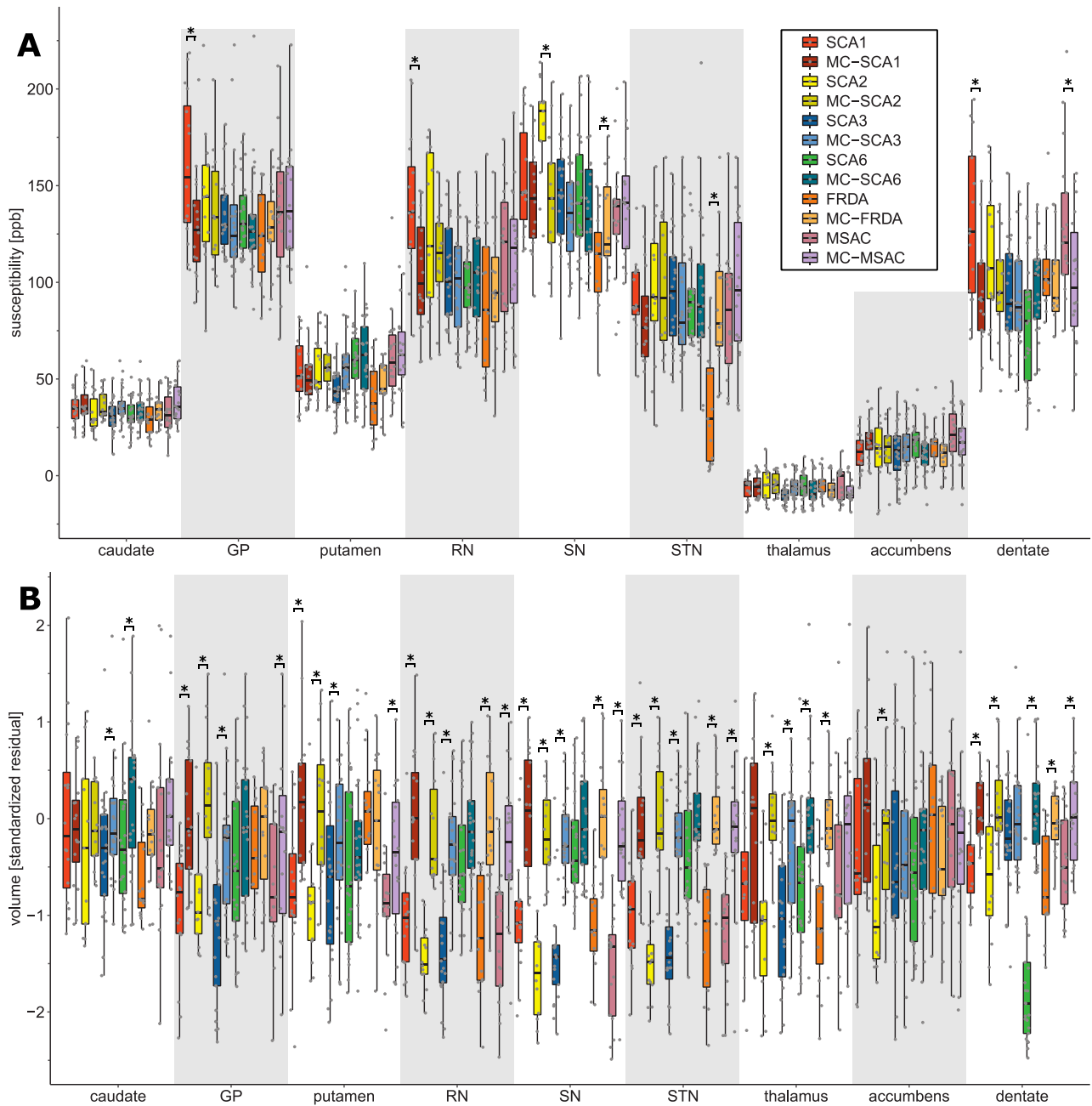
Figure 1: VOI-based group comparisons for susceptibility (A) and volume measures (B) of deep GM. Boxplots are shown for the different ataxia subgroups and the matched control groups (MC). Standardized residuals of total intracranial volume (TIV) corrected volumes are presented in (B). Statistical significance between patients and controls is indicated by asterisks (* – p < 0.05).

Conclusion: Subcortical tissue atrophy and iron dysregulation in individuals with cerebellar ataxia encompass not only regions of established pathology in the cerebellum, but also extend to midbrain and cerebral structures.

References:
[1] T. Klockgether, "Sporadic ataxia with adult onset: classification and diagnostic criteria," *The Lancet. Neurology,* vol. 9, no. 1, pp. 94-104, Jan 2010, doi: 10.1016/S1474-4422(09)70305-9.
[2] A. Deistung *et al.*, "Quantitative susceptibility mapping reveals alterations of dentate nuclei in common types of degenerative cerebellar ataxias," *Brain Communications,* 2022, doi: 10.1093/braincomms/fcab306.
[3] K. Seidel, S. Siswanto, E. R. Brunt, W. den Dunnen, H. W. Korf, and U. Rub, "Brain pathology of spinocerebellar ataxias," *Acta neuropathologica,* vol. 124, no. 1, pp. 1-21, Jul 2012, doi: 10.1007/s00401-012-1000-x.
[4] I. H. Harding *et al.*, "Tissue atrophy and elevated iron concentration in the extrapyramidal motor system in Friedreich ataxia: the IMAGE-FRDA study," *Journal of neurology, neurosurgery, and psychiatry,* vol. 87, no. 11, pp. 1261-1263, Nov 2016, doi: 10.1136/jnnp-2015-312665.
[5] M. Baniasadi *et al.*, "DBSegment: Fast and robust segmentation of deep brain structures considering domain generalization," *Hum Brain Mapp,* vol. 44, no. 2, pp. 762-778, Feb 1 2023, doi: 10.1002/hbm.26097.
[6] C. L. Marvel *et al.*, "Quantitative susceptibility mapping of basal ganglia iron is associated with cognitive and motor functions that distinguish spinocerebellar ataxia type 6 and type 3," *Front Neurosci,* vol. 16, p. 919765, 2022, doi: 10.3389/fnins.2022.919765.

Motion-robust, high-resolution fetal T$_2$*-weighted imaging from 2D EPI

Beata Bachrata[1,2,3], Günther Grabner[1], Simon Daniel Robinson[2,4], Thomas Kau[5]

[1] Department of Medical Engineering, Carinthia University of Applied Sciences, Klagenfurt, Austria, [2] High Field MR Centre, Department of Biomedical Imaging and Image-Guided Therapy, Medical University of Vienna, Austria, [3] Karl Landsteiner Institute for Clinical Molecular MR in Musculoskeletal Imaging, Vienna, Austria, [4] Christian Doppler Laboratory for MR Imaging Biomarkers, Department for Biomedical Imaging and Image-Guided Therapy, Medical University of Vienna, Austria, [5] Department of Radiology, Landeskrankenhaus Villach, Austria

Summary

Super-resolution 2D EPI imaging enables high-resolution fetal T2*-weighted imaging free of motion artefacts and offers the potential of high-quality SWI and QSM imaging.

Introduction

Fetal MRI has been shown to improve the assessment of congenital anomalies, particularly in neurological applications[1,2]. Due to the fine anatomy and extensive motion, fetal MRI requires high-resolution acquisition and fast, motion-robust sequences.

T$_2$*-weighted imaging, along with SWI and QSM, enables the assessment of blood vessel malformations, haemorrhages, calcifications, and reduced blood oxygenation, for instance. Several studies have demonstrated the potential of fetal QSM and SWI imaging, but they relied on slow, gradient-echo acquisitions, which provided only low resolution and required multiple re-acquisitions to obtain images free from excessive motion artefacts[3–7].

We have previously shown that, in the adult brain, orthogonal 2D EPI acquisition with thick slices can be combined into a high-resolution QSM image using an iterative non-linear co-registration approach[8]. This allowed motion-robust T$_2$*-weighted imaging with high nominal resolution. Although this approach removed the distortions inherent in EPI, it suffered from increased blurring, which hindered the visualisation of vessels and potentially of very small susceptibility sources. Super-resolution (SR) methods, based on linear registration and posing image reconstruction as an inverse problem[9,10], offer the potential for sharper results and the possibility to correct slice-to-slice motion[11–13], which may otherwise deteriorate results in fetal imaging.

We aim to achieve motion-robust high-resolution T$_2$*-weighted, SWI and QSM imaging in fetuses to improve the assessment of various congenital anomalies. We assess the possibility of replacing the conventional GRE acquisition with 2D EPI and enhancing the resolution and signal-to-noise ratio using super-resolution techniques. This requires optimizing the EPI acquisition parameters for contrast and SR performance, as well as ensuring the reliability of phase data. Additionally, the SWI and QSM reconstructions need to be optimized for fetal neuroimaging applications.

Methods

One pregnant female volunteer at 34 weeks of pregnancy underwent a clinical MRI examination and the additional scans described here, which were acquired for research purposes. A 3T Siemens Vida scanner was used with an 18-channel flexible coil combined with a 32-channel spine coil. The fetus was diagnosed with agenesis of the corpus callosum associated with colpocephaly. Written informed consent was provided by the participant, and the study was approved by the Ethics Committee of the Federal State of Carinthia.

Three orthogonal (sagittal, coronal and axial) 2D EPI scans were acquired, each with 3 repetitions, TE = 41 ms, TR = 5.5 s, resolution = 1.0 x 1.0 x 3.0 mm, no slice-gap, matrix = 240 x 240, 32 slices, partial Fourier of 6/8 and parallel imaging acceleration of R = 2.

An axial 2D GRE, optimized for the clinical setting, was acquired for comparison, with TE = 19.8 ms, TR = 592 ms, resolution = 0.98x0.98x3.6 mm, matrix = 256x256x24, parallel imaging acceleration of R = 2 and TA = 56.8 s.

For the super-resolution, NiftyMIC reconstruction[11,14] was used to reconstruct a sharp, high SNR, 1.0 mm isotropic image from all nine (3 orthogonal scans of 3 repetitions) 2D EPIs with thick slices.

The SWI and QSM images were reconstructed from the original EPIs with thick slices (without the use of super-resolution). For SWI, CLEAR reconstruction[15,16] was used with a smoothing sigma of 12 voxels and a phase scaling strength of 2. For QSM, the Sepia toolbox[17,18] was used with Laplacian phase unwrapping[19], background field-removal using VSHARP[20], and dipole inversion with STAR[17,21].

Results and Discussions

While the GRE images suffered from motion artefacts and low contrast of the brain structures with different susceptibilities, the EPI images showed enhanced delineation of small veins without quality degradation due to motion artifacts. The slice-to-slice motion within the individual EPI scans and the motion between repeated EPI acquisitions

were effectively corrected by SR reconstruction, resulting in sharp, 1mm-isotropic EPI images. The SR EPI imaging further improved the delineation of veins and potentially other susceptibility sources in all three planes (Figure 1).

The SWI and QSM images derived from EPI acquisitions with thick slices showed enhanced contrast to veins and demonstrated the potential for deriving high-quality SWI and QSM images from EPI data (Figure 2). Nevertheless, the SWI images also exhibited increased noise, and accurate susceptibility estimation has previously been shown to require high-resolution imaging[22]. In the future, we will focus on enabling the super-resolution reconstruction of high-pass filtered phase data and local fields to exploit the SNR and resolution benefits associated with super-resolution in SWI and QSM imaging.
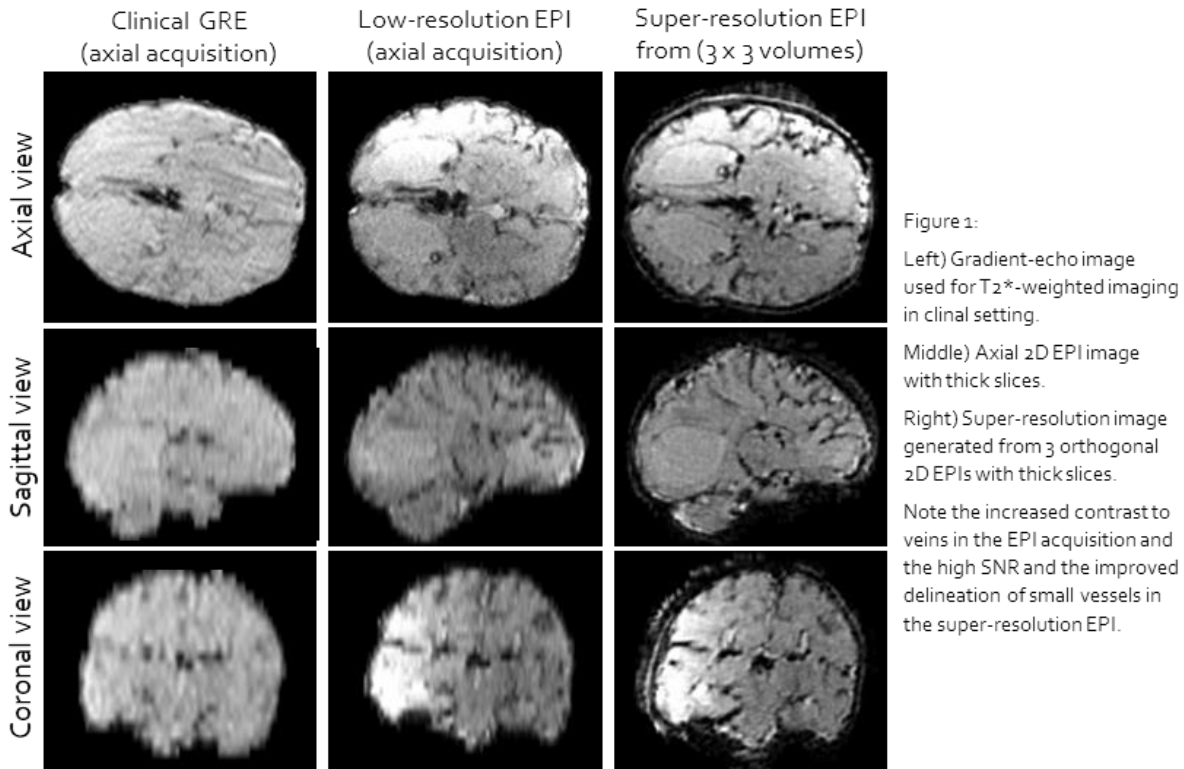

Figure 1:

Left) Gradient-echo image used for T2*-weighted imaging in clinal setting.

Middle) Axial 2D EPI image with thick slices.

Right) Super-resolution image generated from 3 orthogonal 2D EPIs with thick slices.

Note the increased contrast to veins in the EPI acquisition and the high SNR and the improved delineation of small vessels in the super-resolution EPI.
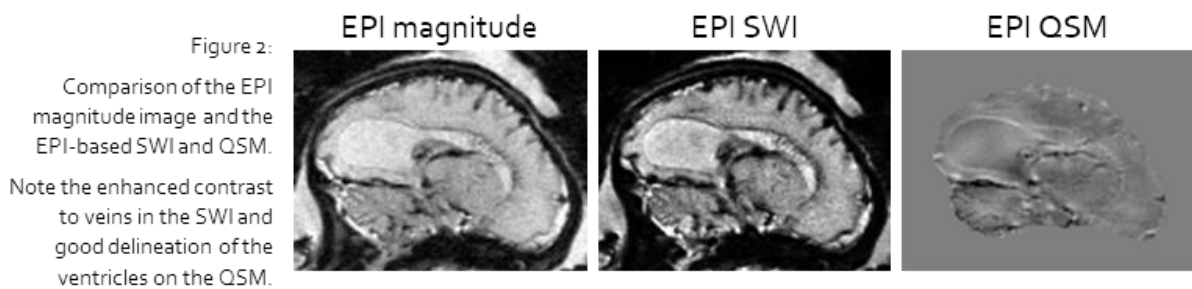

Figure 2:

Comparison of the EPI magnitude image and the EPI-based SWI and QSM.

Note the enhanced contrast to veins in the SWI and good delineation of the ventricles on the QSM.

Conclusions

We have demonstrated that EPI can be used for high-quality T2*-weighted fetal imaging. By combining 2D EPI with super-resolution reconstruction, we achieved high-resolution, motion-robust imaging, enhancing the delineation of small veins and other susceptibility sources. Future work will focus on the super-resolution reconstruction of phase data to maximize SNR and image resolution in SWI and QSM imaging.

Acknowledgements

References: [1] Kul S et al, J Magn Reson Imaging 2012;35(4):882-890; [2] Rossi AC et al, Ultrasound Obstet Gynecol 2014;44(4):388-393; [3] Neelavalli J et al, J Magn Reson Imaging 2014;40(4):949-957; [4] Neelavalli J et al, J Magn Reson Imaging 2014;39(4):998-1006; [5] Sun T et al, Magn Reson Imaging 2021;80:21-25; [6] Yadav BK et al, Eur Radiol 2019;29(4):2017-2026; [7] Dai Y et al, Clin Radiol 2014;69(10):e392-e397; [8] Bachrata B et al, NeuroImage 2023;283:120419; [9] Greenspan H et al, Magn Reson Imaging 2002;20(5):437-446; [10] Fiat D, US patent 2001, #US 6,294,914 B1; [11] github.com/gift-surg/NiftyMIC; [12] github.com/Medical-Image-Analysis-Laboratory/mialsuperresolutiontoolkit; [13] github.com/SVRTK/SVRTK; [14] Ebner M et al, NeuroImage 2020;206:116324; [15] Eckstein K et al, Neuroimage 2021;237:118175; [16] github.com/korbinian90/CLEARSWI.jl; [17] Chan KS et al, Neuroimage 2020;227:117611; [18] github.com/kschan0214/sepia; [19] Schofield MA et al, Opt Lett 2003;28(14):1194-1196; [20] Li W et al, NeuroImage 2011;55(4):1645-1656; [21] Li W et al, Neuroimage 2015;108:111-122; [22] Karsa A et al, Magn Reson Med 2019;81(3):1833-1848

fQSM versus fMRI: A Comparative Analysis of Activations in Veins

Jannette Nassar[1], Oliver C. Kiersnowski[1], Patrick Fuchs[1], Karin Shmueli[1]

[1] Department of Medical Physics and Biomedical Engineering, University College London, London, United Kingdom

Summary: This study demonstrates that multi-echo fQSM detects fewer activated voxels in cerebral venous vessels compared to conventional fMRI. This suggests fQSM may be less dominated by large veins and identifies activated voxels more localized in the visual cortex.

Introduction: Functional quantitative susceptibility mapping (fQSM) detects blood oxygenation changes related to neuronal activation "upstream" of the magnitude signal, offering a complementary perspective to conventional fMRI. FQSM reveals the blood susceptibility changes that underlie conventional Blood Oxygenation Level Dependent (BOLD) activation: fQSM is based on a linear dependence of susceptibility on blood oxygenation, unlike the non-linear dependence of conventional BOLD fMRI based on the signal magnitude [3, 4]. Therefore, fQSM may improve the localization of neuronal activity [1, 2], and detect less activation in large draining veins [4]. Hence, here, we aimed to investigate whether fQSM is less affected by signals arising in venous vessels than fMRI.

Methods: Image acquisition: We acquired 70 multi-echo 2D GRE EPI volumes in 7 healthy volunteers, age 27.7 ± 3.8, using a 3T Siemens-Prisma system with a 64-channel head coil, with 1.3 mm isotropic resolution; GRAPPA=4; MB=3; partial Fourier 6/8; TE=14.8, 39.33, 68.86 ms; TR=4034 ms; TA = 6 min 15 s [5]. To maximize the BOLD signal, we employed a standard visual stimulation paradigm, with a conventional block design. The stimulation consisted of a (black and white) checkerboard flickering at 8Hz in 15.6 s blocks alternating with rest blocks of 15.6 s.

Data processing steps included the generation of brain masks using FSL BET [6] on the second echo magnitude images, followed by single-voxel erosion. For magnitude-based fMRI, multi-echo magnitude images were combined using T_2^*-weighted echo summation [7]. QSMs were calculated for each volume by: non-linear fitting of the complex data [8]; Laplacian phase unwrapping [9]; intra- and inter-slice background field removal with 2D+3D V-SHARP[18,19]; and dipole inversion using non-linear total variation regularisation (FANSI, $\alpha = 2 \times 10^{-4}$) [11].

Functional Analysis: We used SPM12 [12, 13] for fMRI and fQSM analysis [14]. Spatial pre-processing involved (1) rigid-body realignment of the echo-combined magnitude images to the first image in the time-series to correct for motion. The resulting transformations were then applied to the corresponding absolute susceptibility maps. (2) Spatial smoothing with a 4-mm FWHM Gaussian kernel to enhance SNR and statistical power [15]. A general-linear model (GLM) was reconstructed with a regressor for the visual stimuli. Significant activations were identified by thresholding t-score maps to create fMRI and fQSM activation maps using a threshold of $p<0.05$ with Family Wise Error (FWE) correction and no restriction on minimum cluster size.

A mask to highlight highly paramagnetic venous vessels was computed by thresholding at the 99th percentile of the susceptibility distribution. An axial maximum intensity projection (MIP) of the venous vessel mask is shown in Figure 1c. The number of activated voxels detected by fQSM and fMRI were compared, specifically focusing on those within the venous vessel regions. We calculated the percentage of venous vessel voxels that were activated in fQSM v. fMRI.

Results & Discussion: As shown in Fig. 2a, fMRI generally shows higher brain activation than fQSM, and there is significant variability in the number of activated voxels among the volunteers for both methods. Figs 1f, g and 2b show that there were fewer activated voxels in the venous vessels region and a lower percentage of activated venous voxels with fQSM compared to fMRI in all subjects. This suggests that fQSM activations are less contaminated by venous voxels. A major limitation of this study is the creation of the venous mask by thresholding the QSM distribution which clearly includes non-vascular strongly paramagnetic structures (Fig 1c). Future work will involve more sophisticated vessel masking [16], [17], [18].
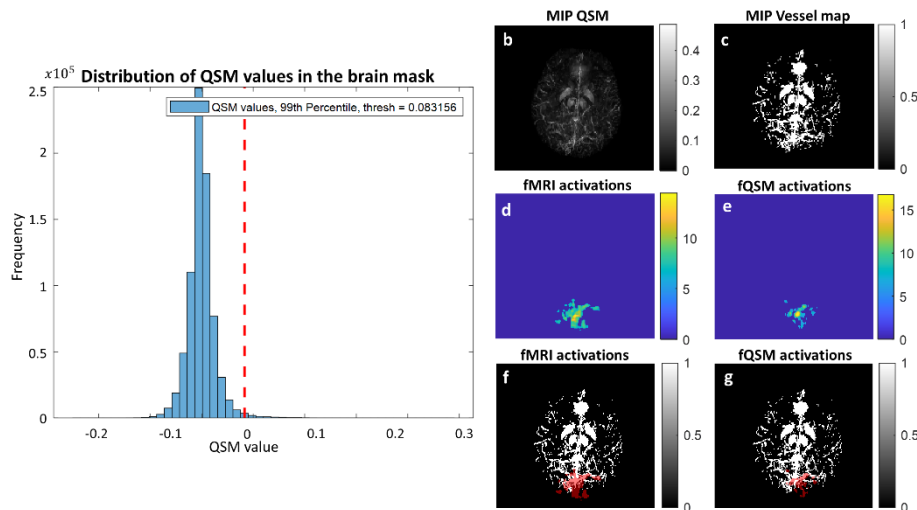
Figure 1. (a). Distribution of QSM values in the brain mask, showing the 99th percentile threshold used to compute the venous vessel mask, in one volunteer. MIPs of the QSM map and the vein mask are shown in (b) and (c) respectively, and MIPs of the fMRI and fQSM activations in (d) and (e) respectively. The MIP of the fMRI and fQSM activations overlaid on a MIP of the vein mask are shown in (f) and (g), respectively.
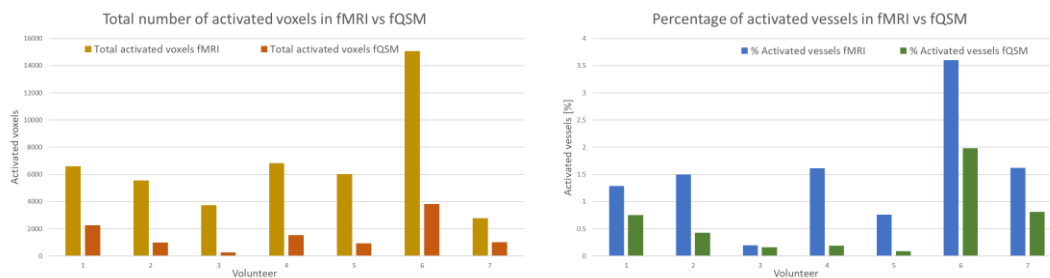
Figure 2. (a). Number of activated voxels in fMRI vs fQSM in all seven volunteers, (b) Percentage of activated vessels in fMRI vs fQSM.

Conclusions: In this first study to employ multi-echo fQSM, in all seven volunteers, fQSM had fewer activated voxels in veins than conventional fMRI, indicating that fQSM is more localized and less contaminated by activations in large veins.

References:

[1] V. Jain, O. Abdulmalik, K. J. Propert, and F. W. Wehrli, "Investigating the magnetic susceptibility properties of fresh human blood for noninvasive oxygen saturation quantification," *Magnetic Resonance in Medicine*, vol. 68, no. 3, pp. 863–867, 2012, doi: 10.1002/mrm.23282.

[2] P. S. Özbay *et al.*, "Probing neuronal activation by functional quantitative susceptibility mapping under a visual paradigm: A group level comparison with BOLD fMRI and PET," *Neuroimage*, vol. 137, pp. 52–60, Aug. 2016, doi: 10.1016/j.neuroimage.2016.05.013.

[3] D. Z. Balla *et al.*, "Functional quantitative susceptibility mapping (fQSM)," *Neuroimage*, vol. 100, pp. 112–124, Oct. 2014, doi: 10.1016/j.neuroimage.2014.06.011.

[4] S, Straub, "Functional quantitative susceptibility mapping for layer specific activation, Program Number: 3127," *ISMRM 2024*.

[5] Kiersnowski O C, et al., "Rapid high resolution integrated structural and functional susceptibility and conductivity mapping in the human brain," *Proc. Ann. Meeting ISMRM 2024, Abstract 188.*, 2024.

[6] S. M. Smith, "Fast robust automated brain extraction," *Hum Brain Mapp*, vol. 17, no. 3, pp. 143–155, Nov. 2002, doi: 10.1002/hbm.10062.

[7] B. A. Poser, M. J. Versluis, J. M. Hoogduin, and D. G. Norris, "BOLD contrast sensitivity enhancement and artifact reduction with multiecho EPI: Parallel-acquired inhomogeneity-desensitized fMRI," *Magnetic Resonance in Medicine*, vol. 55, no. 6, pp. 1227–1235, 2006, doi: 10.1002/mrm.20900.

[8] T. Liu, C. Wisnieff, M. Lou, W. Chen, P. Spincemaille, and Y. Wang, "Nonlinear formulation of the magnetic field to source relationship for robust quantitative susceptibility mapping," *Magnetic resonance in medicine*, 2013, doi: 10.1002/mrm.24272.

[9] M. A. Schofield and Y. Zhu, "Fast phase unwrapping algorithm for interferometric applications," *Opt Lett*, vol. 28, no. 14, pp. 1194–1196, Jul. 2003, doi: 10.1364/ol.28.001194.

[10] W. Li, B. Wu, and C. Liu, "Quantitative susceptibility mapping of human brain reflects spatial variation in tissue composition," *NeuroImage*, vol. 55, no. 4, pp. 1645–1656, Apr. 2011, doi: 10.1016/j.neuroimage.2010.11.088.

[11] "Fast nonlinear susceptibility inversion with variational regularization - Milovic - 2018 - Magnetic Resonance in Medicine - Wiley Online Library." Accessed: Nov. 07, 2022. [Online]. Available: https://onlinelibrary.wiley.com/doi/10.1002/mrm.27073

[12] K. J. Friston, A. P. Holmes, K. J. Worsley, J.-P. Poline, C. D. Frith, and R. S. J. Frackowiak, "Statistical parametric maps in functional imaging: A general linear approach," *Human Brain Mapping*, vol. 2, no. 4, pp. 189–210, 1994, doi: 10.1002/hbm.460020402.

[13] J. Ashburner, "SPM: A history," *NeuroImage*, vol. 62, no. 2, pp. 791–800, Aug. 2012, doi: 10.1016/j.neuroimage.2011.10.025.

[14] J. Nassar and et al, "Optimising Functional Quantitative Susceptibility Mapping (fQSM): The Effect of Multiband Acceleration and Absolute vs. Signed QSM," *Proc. Ann. Meeting ISMRM 2024, Abstract 3415*.

[15] M. K. Chung, "Gaussian kernel smoothing." arXiv, Nov. 29, 2021. doi: 10.48550/arXiv.2007.09539.

[16] "Gap-free segmentation of vascular networks with automatic image processing pipeline - ScienceDirect." Available: https://www.sciencedirect.com/science/article/pii/S0010482517300173?via%3Dihub

[17] "Optimization of quantitative susceptibility mapping for regional estimation of oxygen extraction fraction in the brain - McFadden - 2021 - Magnetic Resonance in Medicine - Wiley Online Library." Available: https://onlinelibrary.wiley.com/doi/10.1002/mrm.28789

[18] A. P. Fan *et al.*, "Quantitative oxygenation venography from MRI phase," *Magnetic Resonance in Medicine*, vol. 72, no. 1, pp. 149–159, 2014, doi: 10.1002/mrm.24918.

Quantitative susceptibility mapping as a novel biomarker of hemorrhage and renal function decline in autosomal dominant polycystic kidney disease

Karl Schumacher[1,2], Martin R. Prince[1], Yi Wang[1], Alexey Dimov[1]

[1]Weill Cornell Medicine, Department of Radiology, New York, NY, USA;
[2]Santa Clara University, Department of Bioengineering, Santa Clara, CA, USA

Introduction: ADPKD is the most common hereditary kidney disease affecting over 500,000 people in the US alone[1], and characterized by uncontrolled formation of fluid-filled cysts causing compression and obstruction of nephrons and progressive decline of glomerular filtration rate (GFR). The critical task in clinical management of ADPKD is the identification of patients at higher risk of rapid kidney function decline[2]. The only FDA-approved biomarker for this risk stratification is height-adjusted total kidney volume (htTKV)[3]. However, htTKV is only a coarse global measure and doesn't inform on vital pathogenic factors, including cyst types and distribution[4], kidney fibrosis and inflammation[2].

Recently, we and others have demonstrated that the presence of hemorrhagic cysts is strongly associated with rapid progression of chronic kidney disease[5,6]. At present, hemorrhagic cysts are detected as hyperintense on T1-weighted (T1w) and hypointense on T2w images in conventional MRI protocol. However, these conventional MRI intensity characteristics are highly unspecific for interpreting hemorrhage and particularly is unable to differentiate between hemorrhagic and dense proteinaceous cysts due to similar T1/T2 shortening effects[7,8]. Herein, we present preliminary cross-sectional data that demonstrate strong association between QSM and decreased eGFR in ADPKD patients, supporting further longitudinal studies to confirm this finding.

Methods: This study was performed under an Institutional Review Board (IRB) approved retrospective protocol. All subjects (n = 34, 12 male, 22 female) met the diagnostic criteria for ADPKD [9,10] and underwent imaging at 3T on a clinical MR scanner (GE Healthcare, Waukesha, WI) using a body phased array coil between July 2021 and March 2023. The imaging protocol included axial and coronal T2-weighted fast spin echo sequences (voxel size = $0.78{\times}0.78{\times}4$ mm^3, echo time (TE) = 92 ms, repetition time (TR) = 1010 ms, flip angle (FA) = 130°, readout bandwidth (rBW) = 355 Hz/pixel) and a 3-dimensional multiecho gradient echo IDEAL/IQ sequence (matrix size = $224{\times}224{\times}30$ interpolated to $512{\times}512{\times}60$; voxel size = $0.78{\times}0.78{\times}4$ mm^3, first TE = 1.2 ms, echo spacing (ΔTE) = 1.1 ms, #TE = 6, TR = 8.3 ms, rBW = 390 Hz/pixel). This axial multiecho GRE acquisition was performed as two acquisitions each with a separate breathhold, to cover the entire abdomen and pelvis. In 8 subjects T1-weighted 3D FSPGR sequence acquired with the following parameters: voxel size = $0.74{\times}0.74{\times}3$ mm^3, TE = 1.8 ms, TR = 4.9 ms, FA = 12°, rBW = 558 Hz/pixel. Data was successfully acquired in 34 ADPKD patients; 1 subject was excluded from the analysis due to severe motion artifacts. Subjects with simultaneously available T1w and T2w images were screened for the presence of T1 hyper- and T2 hypointense lesions consistent with the classic presentation of cystic hemorrhage [5,8]. Identified cysts were referenced to QSM and their appearance on susceptibility maps was classified as either hypo-, iso- or hyperintense, and the number of cysts in each class was recorded.
To quantitatively examine the relation between eGFR decline and QSM, eGFR was fit against the htTKV, and number of hyperintense hemorrhagic cysts N_+ using stepwise regression adjusting for age, sex and mutation status.

Results: T1w and T2w images were reviewed in 8 subjects for the presence of complex cysts. The total of 121 T1 hyper/T2 hypointense cysts classically identified as hemorrhagic were found. 52 (43%) cysts appeared hyperintense ($\approx$0.3 ppm) on QSM consistent with the presentation of hemorrhage (Fig. 1A, yellow arrows); 60 (49%) cysts were isointense with respect to simple cysts and normal kidney parenchyma (Fig. 1A, red arrows), while the remaining 9 (7%) were hypointense ($\approx$-0.2 ppm) (Fig. 1B). As paramagnetism of blood products is much larger it than diamagnetism of protein-based materials, the iso- and hypointense cysts were considered to be non-hemorrhagic.
Both htTKV (fixed effect=-0.014, 95%CI -0.027...-0.001, $p<0.05$) and N_+ (fixed effect=-1.69, 95%CI -2.78...-0.60, $p<0.001$) were independent predictors of the eGFR, with number of hemorrhagic cysts being the most significant one. Having more than 10 hemorrhagic cysts was associated with 50% reduction in eGFR without statistically significant increase in htTKV (Fig. 2)

Discussion and Conclusions: Overall, our preliminary data directly demonstrates that a) Presence of QSN hyperintense hemorrhagic cysts is a biomarker associated with decreased eGFR in ADPKD patients; b) Current relaxation-based MR imaging approaches are highly non-specific to hemorrhage, not being able to differentiate presence of blood products and proteinaceous fluids; c) Renal QSM is feasible, can be efficiently acquired without significant prolongation of the MRI exam time, and can be used for identification of hemorrhagic cysts.
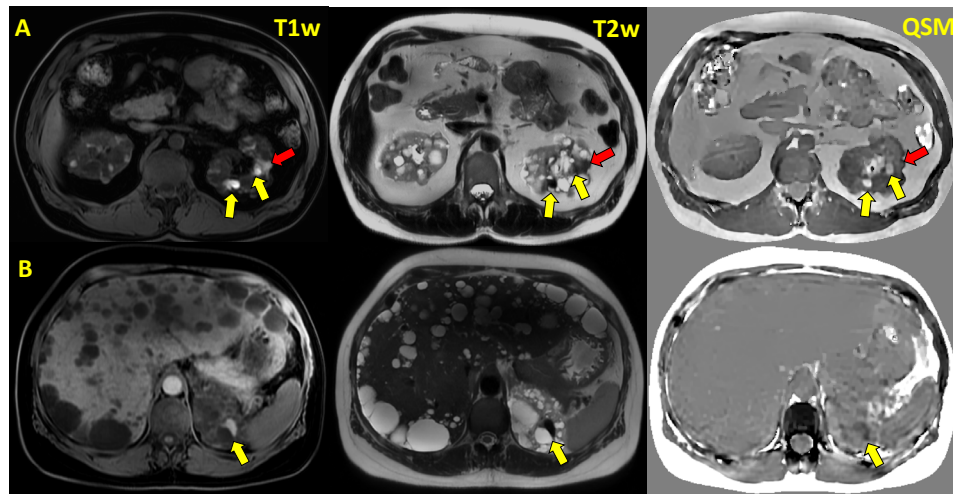
Fig.1. Examples of T1 hyperintense/T2 hypointense cysts with different magnetic properties as visualized by QSM. A) Paramagnetic, QSM hyperintense cysts strongly suggestive of chronic hemorrhage (yellow arrows) along an isointense cyst (red arrow); B) Diamagnetic, QSM hypointense cyst. QSM iso- and hypointensity is indicative of non-hemorrhagic nature of T1/T2 shortening and different cysts composition
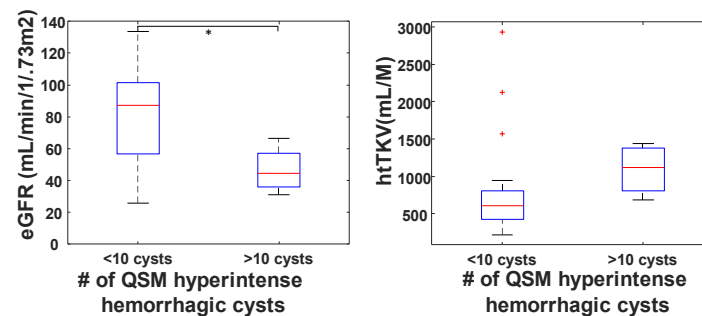
Fig.2. Patients with >10 QSM hyperintense cysts have eGFR reduced by 50% without statistically significant increase in htTKV.

References:

1. Torres VE, Harris PC, Pirson Y. Autosomal dominant polycystic kidney disease. *Lancet*. Apr 14 2007;369(9569):1287-1301. doi:10.1016/S0140-6736(07)60601-1

2. Chebib FT, Torres VE. Assessing Risk of Rapid Progression in Autosomal Dominant Polycystic Kidney Disease and Special Considerations for Disease-Modifying Therapy. *Am J Kidney Dis*. Aug 2021;78(2):282-292. doi:10.1053/j.ajkd.2020.12.020

3. Chapman AB, Bost JE, Torres VE, et al. Kidney volume and functional outcomes in autosomal dominant polycystic kidney disease. *Clin J Am Soc Nephrol*. Mar 2012;7(3):479-86. doi:10.2215/CJN.09500911

4. Kline TL, Korfiatis P, Edwards ME, et al. Image texture features predict renal function decline in patients with autosomal dominant polycystic kidney disease. *Kidney Int*. Nov 2017;92(5):1206-1216. doi:10.1016/j.kint.2017.03.026

5. Riyahi S, Dev H, Blumenfeld JD, et al. Hemorrhagic Cysts and Other MR Biomarkers for Predicting Renal Dysfunction Progression in Autosomal Dominant Polycystic Kidney Disease. *J Magn Reson Imaging*. Feb 2021;53(2):564-576. doi:10.1002/jmri.27360

6. Cornec-Le Gall E, Audrezet MP, Rousseau A, et al. The PROPKD Score: A New Algorithm to Predict Renal Survival in Autosomal Dominant Polycystic Kidney Disease. *J Am Soc Nephrol*. Mar 2016;27(3):942-51. doi:10.1681/ASN.2015010016

7. Marotti M, Hricak H, Fritzsche P, Crooks LE, Hedgcock MW, Tanagho EA. Complex and simple renal cysts: comparative evaluation with MR imaging. *Radiology*. Mar 1987;162(3):679-84. doi:10.1148/radiology.162.3.3809481

8. Bradley WG, Jr. MR appearance of hemorrhage in the brain. *Radiology*. Oct 1993;189(1):15-26. doi:10.1148/radiology.189.1.8372185

9. Pei Y, Obaji J, Dupuis A, et al. Unified criteria for ultrasonographic diagnosis of ADPKD. *J Am Soc Nephrol*. Jan 2009;20(1):205-12. doi:10.1681/ASN.2008050507

10. Ravine D, Gibson RN, Walker RG, Sheffield LJ, Kincaid-Smith P, Danks DM. Evaluation of ultrasonographic diagnostic criteria for autosomal dominant polycystic kidney disease 1. *Lancet*. Apr 2 1994;343(8901):824-7. doi:10.1016/s0140-6736(94)92026-5

Importance of R2 accuracy for susceptibility separation methods

Tereza Beatriz Oliveira Assunção[1], Nashwan Naji[2], Alan Wilman[1,2]

[1]Dept. of Biomedical Engineering; [2]Dept. of Radiology and Diagnostic Imaging (University of Alberta, Edmonton, Canada)

Summary: Acquiring transverse relaxation rate (R2) maps can be lengthy and its impact on the quality of susceptibility separation is not known. We evaluated the importance of R2 map accuracy for two susceptibility separation methods.

Introduction: Susceptibility separation allows the mapping of paramagnetic and diamagnetic sources independently [1]. It has been applied in the human brain to quantify iron and myelin in healthy subjects and assess disease progression in neurodegenerative disorders such as multiple sclerosis [2,3]. Different models have been proposed to separate susceptibility sources, with the original χ-separation method using R2' (=R2*-R2). However, acquiring an adequate R2 map, which is required to calculate the R2' map accurately, can be lengthy and its importance for the final separation maps remains uncertain. Furthermore, fitting of R2 decay curves can be complex owing to stimulated echoes, with simple fitting approaches leading to errors. Thus, this work aims to evaluate how R2 map errors can bias the paramagnetic and diamagnetic outputs of two susceptibility separation methods that require R2' as input.

Methods: Eleven healthy subjects (36 ± 15 years, 7 females) were scanned at 3T (Siemens Prisma, Erlangen, Germany) with the following sequences: 2D dual echo Turbo Spin Echo: TR = 2500 ms, TE1 = 10 ms, TE2 = 93 ms, $0.9 \times 0.9 \times 3.0$ mm^3 resolution; 3D MEGE: TR = 47 ms, TE1 = 5.0 ms with echo spacing 7.1 ms, 6 echoes, $0.6 \times 0.7 \times 2.0$ mm^3 resolution; and a Bloch-Siegert B1$^+$ map with $1.3 \times 1.3 \times 3.0$ mm^3 resolution. R2 maps were reconstructed using Bloch modeling of the actual flip angles, determined from the pulse sequence and B1$^+$ map [4]. To evaluate the importance of R2 accuracy for susceptibility separation, R2 maps were altered by a global multiplication factor (ranging from 75% to 125% in steps of 1%, which produces errors from -25% to 25% of the true R2 value) prior to forming R2' maps which were used as input for two separation methods, χ-separation [1] and χ-sepnet [5]. Both methods rely on phase and R2' as input, with χ-sepnet using a deep learning approach. For both separation methods, the total, positive and negative χ maps generated with the altered R2' inputs, caused by introduced R2 errors, were compared to an unaltered pipeline. The mean percentage error (MPE) within deep gray matter (DGM) and white matter (WM) regions of interest (ROIs) was used to compare results.

Results: Figure 1 shows an example of susceptibility separation outputs of the two methods using accurate R2. Both paramagnetic maps highlighted iron-rich areas, such as DGM, while the diamagnetic maps highlighted WM regions with increased myelin content. χ-sepnet more effectively reduced the artifacts from air-tissue interfaces in the frontal brain, which arose from the MEGE sequence and were present in the R2* map. Overall, χ-separation produced maps with higher contrast than χ-sepnet. Figure 2 shows plots for the MPE generated by the altered R2 maps averaged across all subjects. The effect of R2 error on R2' error is highest in structures with lower R2* (typically about ±15% R2' output error for ±5% input error in R2) and their relationship is mostly linear, except when R2 overestimation introduced negative values of R2' which were zeroed prior to the separation algorithm. χ-separation outputs exhibited increased error over χ-sepnet for both DGM and WM ROIs, reaching MPE error values greater than 25% for values as small as ~12% R2 error in most regions. For χ-sepnet, most of the curves stayed close to ±25% output MPE even for higher R2 input error.
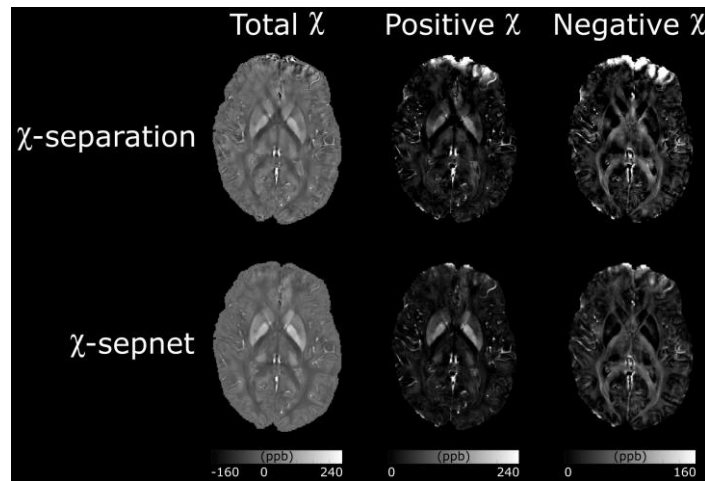
Figure 1 – Representative output maps for both susceptibility separation methods with the unaltered pipeline (accurate R2 values) from a 26-year-old male healthy subject.
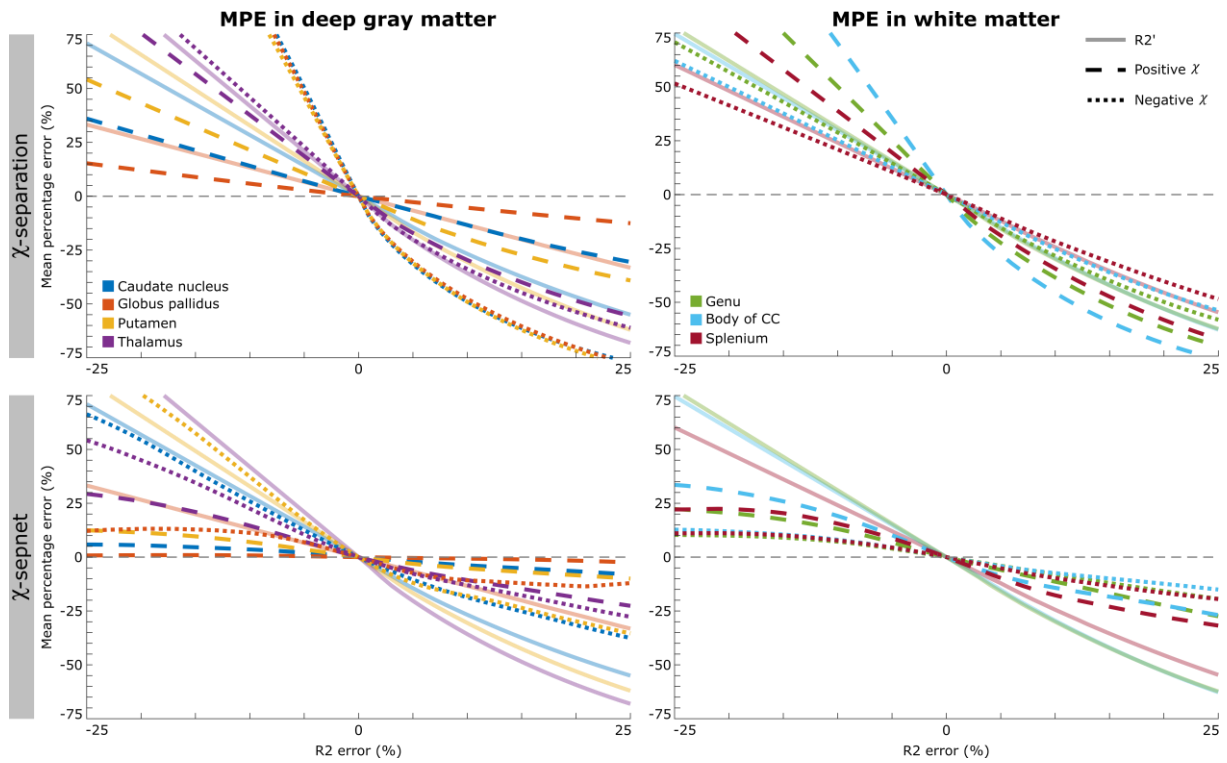
Figure 2 – Mean MPE of R2' and para and diamagnetic susceptibility maps in the 11 subjects versus R2 error for χ-separation (upper row) and χ-sepnet (bottom row) within deep gray matter (left column) and white matter (right column) regions-of-interest. Solid, dashed and dotted lines represent R2', positive χ and negative χ, respectively. R2' lines were the same for both methods as it is an input value. χ-sepnet percentage errors were consistently less than R2', while χ-separation percent errors were generally similar or greater than R2'.

Discussion and Conclusions: Errors in R2, which translate into R2' input errors, were shown to play a significant role in yielding increased errors in para and diamagnetic susceptibility maps. R2' is overestimated with R2 underestimation, while R2 overestimation causes R2' underestimation. The trends on MPE for the χ maps versus R2 error behaved similarly across both methods and ROIs. All of them followed their respective R2' trend, with R2' overestimation causing overestimation on both output maps, the same applies to underestimation. However, the influence of R2' error was different between methods, ROIs and maps. For both methods, DGM ROIs presented greater errors on the negative χ map, while WM had more errors on positive χ maps. These errors are due to the fact that negative χ for paramagnetic sources and positive χ for diamagnetic sources are expected to be low, increasing the MPE. All WM ROIs behaved similarly to each other in both methods. For DGM ROIs, in both methods globus pallidus (GP) was less sensitive to R2 input errors as R2' is dominated by R2* in this iron-rich region, while much lower R2* in thalamus was the most sensitive to R2 errors. χ-sepnet reduced the air-tissue artifact in the frontal brain, generating χ maps with less artifact than χ-separation, as expected from the findings reported by [5]. Comparing the plots for both methods, χ-separation showed steeper lines than χ-sepnet for all ROIs, which means that the former is more sensitive to R2 input errors, as MPE reached higher values for smaller R2 errors. Even though χ-sepnet presented a higher tolerance to global R2 error and resolved local artifacts from the MEGE sequence better than χ-separation, its sensitivity for *local* R2 errors requires further investigation. The effects of local R2 errors for both methods can be evaluated in future work. In conclusion, both methods were affected by R2 errors, indicating that R2 map accuracy is important to properly separate susceptibility sources when using separation methods dependent on complete R2' measurement.

References:
[1] Shin H G et al. (2021), "χ-separation: Magnetic susceptibility source separation toward iron and myelin mapping in the brain" *NeuroImage*, vol. 240, 118371, doi: 10.1016/j.neuroimage.2021.118371.
[2] Lao G et al. (2023), "Sub-voxel quantitative susceptibility mapping for assessing whole-brain magnetic susceptibility from ages 4 to 80" *Hum. Brain Mapp.*, doi: 10.1002/hbm.26487
[3] Ziyan Z et al. (2024), "MR Susceptibility Separation for Quantifying Lesion Paramagnetic and Diamagnetic Evolution in Relapsing–Remitting Multiple Sclerosis" *J Magn Reson Imaging*, doi: 10.1002/jmri.29266
[4] McPhee K C, Wilman A H (2015) "T2 quantification from only proton density and T2-weighted MRI by modelling actual refocusing angles" *NeuroImage*, vol. 118, pp. 642–650, doi: 10.1016/j.neuroimage.2015.05.079.
[5] Kim M et al. (2022) "Chi-sepnet: Susceptibility source separation using deep neural network" *Joint Annual Meeting ISMRM-ESMRMB ISMRT 31st Annual Meeting*

DeepSepSTI-R2*: R2-Free Anisotropic Susceptibility Source Separation in Susceptibility Tensor Imaging with Deep Learning

Zhenghan Fang[1,4], Hyeong-Geol Shin[2,3], Peter van Zijl[1,2,3], Jeremias Sulam[1,4], and Xu Li[2,3]

[1]Department of Biomedical Engineering, Johns Hopkins University, Baltimore, USA; [2]Department of Radiology and Radiological Sciences, Johns Hopkins University School of Medicine, Baltimore, USA; [3]F.M. Kirby Research Center for Functional Brain Imaging, Kennedy Krieger Institute, Baltimore, USA; [4]Johns Hopkins Kavli Neuroscience Discovery Institute, Baltimore, USA

Summary: DeepSepSTI-R2* enhances anisotropic susceptibility source separation by eliminating the need for extra R2 measurement, i.e., using only R2* and phase maps derived solely from gradient echo data, thereby reducing scan time without significantly compromising performance.

Introduction: Multiple tissue sources contribute to the bulk tissue magnetic susceptibility. These sources can be categorized into paramagnetic, such as iron, and diamagnetic, such as myelin and calcium, and can coexist in an MR imaging voxel. Recently, chi-separation [1] was proposed to separate the intra-voxel paramagnetic and diamagnetic sources by combining gradient echo (GRE) phase and R2' measures (derived from R2* with multi-echo GRE data and R2 maps from spin echo sequences, i.e. R2' = R2* - R2). The need for extra R2 measurement increases scan time and makes less practical, especially for clinical studies. R2* based susceptibility source separation has also been proposed [6,7]. In addition, most previous susceptibility source-separation approaches assumed isotropic tissue susceptibility thus ignoring the anisotropy of certain tissue structures like the diamagnetic myelin sheath in white matter fibers. More recently, a new approach, namely DeepSepSTI [2], was developed, which allows anisotropic susceptibility source separation using a second-order tensor model for the diamagnetic sources following the convention in susceptibility tensor imaging [3,4], while the paramagnetic part is assumed to be isotropic. DeepSepSTI estimates the para- and dia-magnetic sources from a combination of phase, R2* and R2 maps, similar to chi-separation. The inverse problem is solved by a deep learning model using neural network that resembles the proximal operator of a learned regularizer [5]. By separating paramagnetic and diamagnetic sources while considering susceptibility anisotropy, DeepSepSTI can provide more information about pathological changes and potentially help improve tensor reconstruction accuracy.

However, like chi-separation, the need for R2 measurements in DeepSepSTI significantly prolongs scan time and introduces potential co-registration errors. This problem is more pronounced for anisotropic susceptibility separation, where the scans are already very long when multiple head orientations need to be acquired. Therefore, it is highly desirable to eliminate the need for R2 acquisition in anisotropic susceptibility source separation.

In this work, we present DeepSepSTI-R2*, an improvement over DeepSepSTI that uses only R2* and phase measurements, without R2. To achieve this, we developed a new deep learning model to jointly estimate susceptibility sources *and* R2 given R2* and phase. Preliminary results on both simulation and *in vivo* data show good potential of this approach.

Methods: We represent the diamagnetic source as a second-order tensor image, x_{neg}, and the paramagnetic source as a scalar image, x_{pos}, because the paramagnetic component is mainly generated by tissue iron and generally considered isotropic. Denote the local phase measurement at jth orientation by δB_j. The underlying physics model can be written as

$$\delta B_j = F^{-1}D_jF\big(Ix_{pos} + x_{neg}\big), \qquad R_{2,j}^* = Dr\big(x_{pos} - H_jx_{neg}\big) + R_2$$

where F is the Fourier transform, D_j is the corresponding dipole kernel, I maps the scalar image x_{pos} to a tensor image with a scaled identity matrix at each voxel (hence $\chi = Ix_{pos} + x_{neg}$ represents the bulk susceptibility tensor), Dr is the relaxometry constant (114 Hz/ppm), and H_j maps the tensor image x_{neg} to a scalar image by projecting the tensor onto the B0 direction (i.e., $h_{0j}^T\chi h_{0j}$, where h_{0j} is a unit vector representing the jth B0 direction in the subject's frame of reference). Each voxel in x_{pos} is a positive scalar, and in x_{neg} a negative semi-definite tensor. R_2 is assumed to be an orientation independent scalar. Different from DeepSepSTI which uses R_2 as observation, here we treat R_2 as an additional unknown to estimate. The resulting inverse problem is estimating x_{pos}, x_{neg}, and R_2, given the δB and R_2^* measurements at potentially multiple orientations.

To solve the inverse problem, we resort to the deep learning method previously presented in [5], which has shown excellent performance for STI reconstruction using fewer orientations. Thanks to the flexibility of the approach, we adapted it to the new inverse problem defined in this work. Let y be the combination of all the observations, δB and R_2^*, and x be all the unknowns, i.e., x_{pos}, x_{neg}, and R_2. The above inverse problem can be summarized as $y = Ax$, where A is the linear forward operator. In general, we can solve the inverse problem by solving the minimization problem: $\min_x 1/2\|y - Ax\|_2^2 + R(x)$, with an appropriately chosen regularizer R. The minimization problem can be solved via proximal gradient descent, which iteratively applies gradient descent on the data-fidelity term and the proximal operator of R. In the deep learning method, a neural network f_θ is used to approximate the proximal operator of R, leading to the following iterative learned proximal gradient descent update: $\hat{x}_{i+1} = f_\theta\big(\hat{x}_i + A^H(y - A\hat{x}_i)\big)$, where $\hat{x}_i$ is the estimation at the i-th iteration and A^H is the Hermitian transpose of A. The algorithm is run for a fixed number of iterations, and the last iteration is used as final reconstruction. Training is performed end-to-end using supervised learning, using simulated data from computational brain phantoms generated from *in vivo* human brain measurements. We used the same dataset

as in [2], including 13 subjects, with 6-11 orientations each; 10 subjects are used for training, 1 for validation, and the remaining 2 for testing.

Results: Fig. 1a shows the reconstruction results of x_{pos}, and mean magnetic susceptibility (MMS) of x_{neg} on *in vivo* human data using 3 head orientations. DeepSepSTI-R2* achieves comparable result to DeepSepSTI – both match closely the reference from COSMOS based chi-separation (with 6 orientations). Additionally, DeepSepSTI-R2* exhibits less noise than DeepSepSTI. Fig. 1c shows the estimated R2 map by DeepSepSTI-R2*, showing good agreement with the acquired R2. Table 1a shows the performance metrics for susceptibility tensor estimation using both simulation and in vivo data. Table 1b shows similar quantitative results for x_{pos}, MMS of x_{neg} and R2 map in vivo. DeepSepSTI-R2* performs worse than DeepSepSTI on tensor reconstruction, but better in the estimation of x_{pos} and MMS of x_{neg}. These results collectively suggest that DeepSepSTI-R2* may achieve comparable results for anisotropic susceptibility source separation without R2 measurement while reducing the scan time in practice.

Discussion and Conclusions: We propose DeepSepSTI-R2*, an upgrade in time use to the DeepSepSTI framework, and demonstrate its feasibility to conduct anisotropic susceptibility source separations without extra R2 acquisition, making it more practical clinically. Further improvements on the physical model and network trainings are warranted in the future.
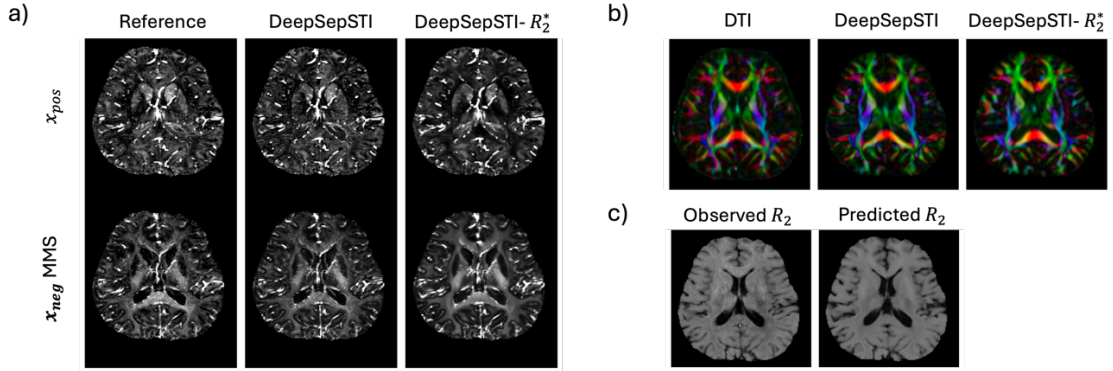
Figure 1 – Visual results for *in vivo* data. (a) Predictions of x_{pos} and MMS of x_{neg}; (b) Predictions of PEV; (c) Acquired R_2 map and that predicted by DeepSepSTI-R2*.

a)

Method	Simulation				In Vivo		
	PSNR (↑)	SSIM (↑)	ECSE (↓)	wPSNR (↑)	ECSE (↓)	MSA R-squared (↑)	MSA Pearson's Correlation (↑)
DeepSTI [5]	45.8 (1.3)	0.981 (0.002)	0.070 (0.008)	24.23 (0.52)	0.097 (0.013)	0.66 (0.03)	0.81 (0.02)
DeepSepSTI [2]	45.5 (1.1)	0.984 (0.002)	0.062 (0.004)	25.40 (0.30)	0.095 (0.012)	0.71 (0.04)	0.84 (0.02)
DeepSepSTI-R2*	44.0 (2.2)	0.981 (0.004)	0.085 (0.044)	24.18 (1.16)	0.136 (0.023)	0.71 (0.04)	0.84 (0.02)

b)

Method	In Vivo					
	x_{pos}		x_{neg} (MMS)		R_2	
	PSNR (↑)	SSIM (↑)	PSNR (↑)	SSIM (↑)	PSNR (↑)	SSIM (↑)
DeepSepSTI [2]	38.31 (6.20)	0.949 (0.041)	42.25 (5.44)	0.960 (0.031)	-	-
DeepSepSTI-R2*	41.52 (1.73)	0.979 (0.005)	42.90 (2.69)	0.982 (0.006)	41.54 (0.88)	0.981 (0.003)

Table 1 – Quantitative results for simulation and *in vivo* data averaged over 1 to 6 orientations. (a) Metrics for susceptibility tensor reconstruction. ECSE: eigenvector cosine similarity error. wPSNR: PSNR of anisotropy-weighted PEV map. MSA R-squared and correlation are evaluated against DTI FA. (b) Accuracies for susceptibility source separation, using a COSMOS approach as reference, and accuracy for R2 estimation. ↑: Higher is better; ↓: lower is better.

References:
[1] Shin, Hyeong-Geol, et al. "χ-separation: Magnetic susceptibility source separation toward iron and myelin mapping in the brain." Neuroimage 240 (2021): 118371.
[2] Fang, Zhenghan, et al. "DeepSepSTI: Improved Susceptibility Tensor Reconstruction by Anisotropic Susceptibility Source Separation." ISMRM 2024.
[3] Liu, Chunlei. "Susceptibility tensor imaging." Magnetic Resonance in Medicine 63.6 (2010): 1471-1477.
[4] Li, Wei, et al. "Susceptibility tensor imaging (STI) of the brain." NMR in Biomedicine 30.4 (2017): e3540.
[5] Fang, Zhenghan, et al. "DeepSTI: towards tensor reconstruction using fewer orientations in susceptibility tensor imaging." Medical image analysis 87 (2023): 102829.
[6] Dimov, Alexey V., et al. "Susceptibility source separation from gradient echo data using magnitude decay modeling." Journal of Neuroimaging 32.5 (2022): 852-859.
[7] Chen, Jingjia, et al. "Decompose quantitative susceptibility mapping (QSM) to sub-voxel diamagnetic and paramagnetic components based on gradient-echo MRI data." Neuroimage 242 (2021): 118477.

Preliminary Phase-Based EPT in Parkinson's Disease: Effects of Open-Ended Fringe Lines

Oriana V. Arsenov[1], Jierong Luo[1], George E.C. Thomas[2], Rimona S. Weil[2], Karin Shmueli[1]

[1]Medical Physics and Biomedical Engineering, University College London, London, United Kingdom; [2]Dementia Research Centre, Institute of Neurology, University College London, London, United Kingdom

Summary: Phase-based electrical properties tomography (EPT) was calculated from ME-EPI images suffering from open-ended fringe lines in a Parkinson's disease study. After removing the brain region, affected by this artifact, we observed a significant increase in conductivity in CSF and white matter, and a significant decrease in gray matter, in this preliminary group of patients compared to healthy controls.

Introduction: Parkinson's disease (PD) is the second most common progressive neurodegenerative disorder[1] and is characterized by the aggregation of a protein, α-synuclein, into structures called Lewy bodies[2]. Lewy bodies are mainly found in the substantia nigra pars compacta (SNc) but can be present in other brain regions. Elevated levels of metal ions, particularly Ca^{2+}, are found in these structures[2,3]. Changes in the Ca^{2+} ion concentrations are caused by disruptions of calcium homeostasis.

MRI electrical properties tomography-(MR-EPT) reconstructs the tissue electrical conductivity which, at high frequencies, is related to the tissue ion content, and could provide clinically useful information for diagnosing and monitoring disease progression. In this study, we used a multiple-echo 2D gradient-echo echo-planar imaging (ME-GRE-EPI) acquisition to investigate conductivity values in patients with Parkinsons's disease compared to healthy controls (HC).

Methods: <u>MRI Acquisition</u>: As part of an ongoing study of PD we acquired 2D ME-EPI brain images using a sequence with multi-echo capability[4] on a 3T Siemens Prisma, with a 64-channel head coil, with 1.3 mm isotropic resolution, matrix size=184x168x126, BW= 1812 Hz/Pixel, FA=90°, 3 TEs, TE1/ΔTE/TE5=14.80/24.53/63.86 ms and TR=4034 ms, with multiband 3 and GRAPPA 4 for 70 volumes. Here, we present results from all 4 PD participants (M/F: 3/1, age: 63.7±7.6 years) and 6 healthy controls (HC) (M/F: 5/1, age: 72.2±3.6 years) acquired to date.

<u>EPT pipeline</u>: The phase offset at TE=0 (φ_0) was extrapolated from a non-linear fit[5] of the complex data over all echoes and unwrapped[6]. A mask was generated using FSL BET[7], refined by thresholding[8,9], and eroded by 1 voxel to reduce brain edge artifacts. Slice-to-slice inconsistencies in φ_0 were corrected by subtracting the median in each axial slice in the brain[10]. EPT on masked φ_0 maps, used the integral approach (differentiation kernel: 17 voxels, surface integral kernel: 39 voxels) with magnitude-weighted and segmentation-based edge preservation[11] using the echo-combined magnitude[12]. High quality structural conductivity maps (σ) were calculated by taking the median of positive values in each voxel of co-registered EPT reconstructions over all 70 timepoints.

Results and Discussion: All phase data acquired so far suffers from open-ended fringe lines that propagate into the extrapolated φ_0 (pink arrow Fig. 1b), and from Moire interference of aliasing artifacts[13] (green arrow Fig. 1b). The open-ended fringe lines appear in the lower part of the brain, where slice-to-slice inconsistencies also appear more pronounced.

a. Magnitude   b. φ_0 c. σ (1 volume)   d. Median σ (70 volumes)

-3   rad   3   0   S/m   2.5
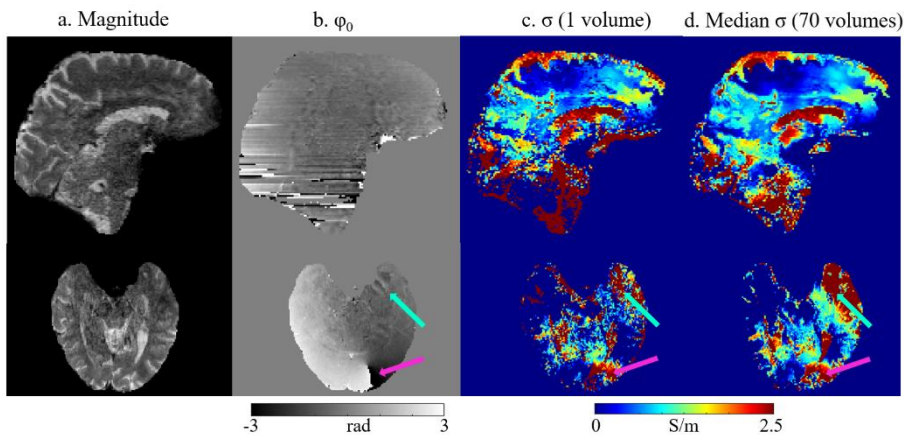
Figure 1. Open-ended fringe lines (pink arrow) and aliasing artifact (green arrow) in φ_0 (b), create artifacts in the conductivity maps at each timepoint (c) and the median conductivity over all timepoints (d).

Therefore, we removed a lower section of the brain from φ_0 in every volume. The difference between median σ reconstructed from the full and cropped φ_0 (Figure 2) shows that artifacts in σ propagate upwards towards the middle of the brain but did not affect the upper part of the brain. The width of this difference was consistent across subjects and similar to the 20-voxel radius of the integral kernel.

A. Healthy control

B. Parkinson's patient
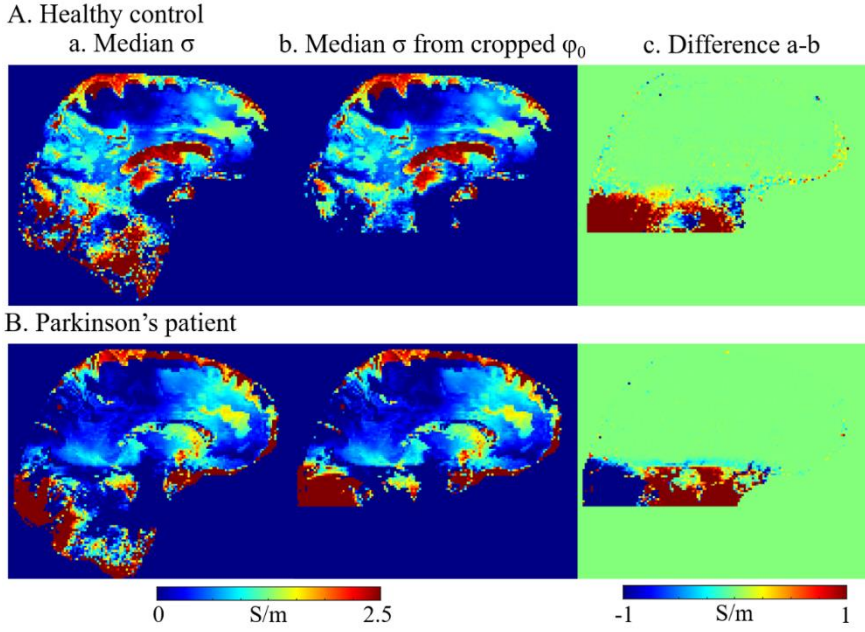
Figure 2. Median conductivity maps reconstructed from the whole φ_0 (a) and cropped φ_0 (b) and the difference maps (c) in one healthy control (A) and one PD participant (B).

Conductivity distributions from the cropped φ_0 for each subject in cerebrospinal fluid (CSF), gray matter (GM), and white matter (WM) are displayed in Figure 3 with negative conductivity values and those > 1.5 times the interquartile range above the third quartile[14] excluded. A t-test between PD and HC values was computed and showed a significant ($p < 0.001$) increase in σ for Parkinson's patients in CSF and WM of 2.2% and 1.9%, respectively, and a significant decrease in GM of 3.5%.
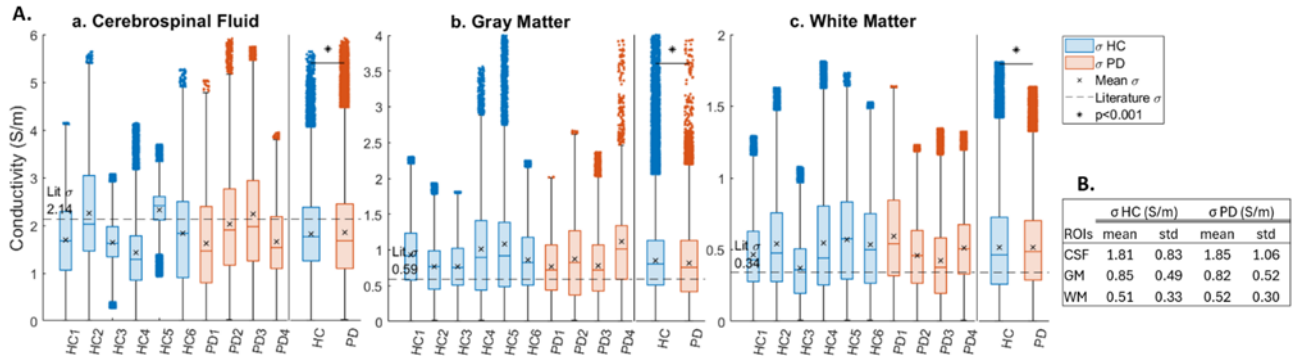
Figure 3. σ distribution in each PD and HC together with distributions across subjects (A) and mean σ values $\pm$ standard deviations (B) in PD compared to HC participants. Literature value measured ex-vivo in healthy tissue [15] is indicated by the dashed line in each region of interest, CSF (a), GM (b), and WM (c). p-values showing significant differences are displayed for each region. Negative conductivity values and values greater than 1.5 times the interquartile range above the third quartile were excluded.

Conclusions: Open-ended fringe lines, likely caused by imperfect complex coil combination, represent a challenge for EPT reconstruction. We removed the areas most affected by this artifact from the input φ_0 images to improve EPT reconstructions. In this small preliminary data set, reconstructed conductivities were significantly increased in CSF and white matter regions, and significantly decreased in gray matter in participants with Parkinson's disease compared to healthy controls. As more subjects continue to be acquired as part of this study, further work will include investigating the effect of higher-order shimming on open-ended fringe lines and evaluating conductivity changes in gray matter sub-regions to better understand conductivity changes in Parkinson's disease.

References: [1] Lamptey RN et al (2022), *International journal of molecular sciences*, 23(3):1851. [2] Zaichick SV et al (2017), *Disease models & mechanisms*, 10(5):519-35.9. [3] Moons R et al (2020), *Scientific reports*, 10(1):16293. [4] CMRR C2P (2022), https://www.cmrr.umn.edu/ multiband/. [5] Liu T et al (2013), *Magnetic resonance in medicine*, 69(2):467-76. [6] Karsa A et al (2018), *IEEE transactions on medical imaging*, 38(6):1347-57. [7] Smith SM et al (2002), *Human Brain Mapping*, 17(3):143-55. [8] Karsa A et al (2020), *Magnetic resonance in medicine*, 84(6):3206-22. [9] Kiersnowski OC et al (2023), *BIC-ISMRM PG Symposium*. [10] Arsenov OV et al (2024), *ISMRM & SMRT Annual Meeting*. [11] Karsa A et al (2021). *ISMRM & SMRT Annual Meeting*. [12] Poser BA et al (2009), *Neuroimage*, 45(4):1162-72. [13] Stadler A et al (2007), *European radiology*, 17:1242-55. 14. Rousseeuw PJ et al (1993), *Journal of the American Statistical association*, 88(424):1273-83. [15] Gabriel C et al (1996), *Phys. Med. Biol*, 41:2271-93.

Systematic analysis of relaxometric constants in brain tissue using temperature-dependent transverse relaxometry and magnetic susceptibility: Toward 7T chi-separation

Hyeong-Geol Shin[1,2], Yuto Uchida[1], Javier Redding-Ochoa[3], Kengo Onda[1], Alexander Barrett[3], Adnan Bibic[2], Juan C. Troncoso[3], Peter van Zijl[1,2], Kenichi Oishi[1], and Xu Li[1,2]

[1]Department of Radiology, Johns Hopkins University School of Medicine, Baltimore, USA; [2]F.M. Kirby Research Center, Kennedy Krieger Institute, Baltimore, USA; 3Department of Pathology, Johns Hopkins University School of Medicine, Baltimore, USA

Summary: This work systematically investigates the temperature and field strength dependency of the relaxometric constant (D_r) in human brain tissue, enhancing our understanding of the effects of susceptibility sources on bulk susceptibility and relaxometry. A proposed super-linear field-strength correction for D_r can help improve the accuracy of susceptibility source separation at ultra-high field.

Introduction: Recent developments in magnetic susceptibility source separation[1–3] have demonstrated the potential of imaging separately the paramagnetic and diamagnetic susceptibility (χ_{para} and χ_{dia}), giving more specific measures of paramagnetic iron versus diamagnetic myelin. Most susceptibility source separation methods rely on a relaxometric constant (D_r) to link χ_{para} and χ_{dia} to their induced reversible relaxation (R2'). Theoretically, D_r is dependent on source characteristic frequency (plus field strength),[2,4] temperature,[5,6] and the underlying susceptibility source geometry (size, shape, etc.)[4], necessitating accurate estimation of D_r in tissue. D_r can be easily measured in phantoms[1,2], but measuring in-vivo values is challenging. In previous studies, *in-vivo* brain D_r was empirically measured at 3T using R2' and susceptibility measures in basal ganglia (137 Hz/ppm) for chi-separation[1], assumed to be the theoretical maximum by ignoring diffusion (324 Hz/ppm)[3], or iteratively fitted[7]. The relaxometric constant is expected to largely influence the χ_{para} and χ_{dia} values obtained from source separation, but it has not been physically measured in human brain tissue in a systematic way. Here, a comprehensive study of D_r was conducted using a postmortem brain sample at both 3T and 7T, using quantitative susceptibility mapping (QSM)[8] and R2' imaging at multiple temperature points (6-35°C). Considering the field strength- and temperature-dependent D_r, a better field-strength correction is suggested to perform more accurate brain susceptibility source separation at 7T.

Theory: Assuming a voxel containing both paramagnetic and diamagnetic susceptibility inclusions, within the static dephasing regime, its bulk magnetic susceptibility χ_{bulk} and R2' (sensitized by water) can be described as follows[1,4]:

$$\chi_{bulk} = \zeta_{para}\Delta\chi_{para} + \zeta_{dia}\Delta\chi_{dia} = \zeta_{para}\chi_{para,inc} + \zeta_{dia}\chi_{dia,inc} - (\zeta_{para} + \zeta_{dia})\chi_{water} \qquad [Eq.1],$$

$$R2' = D_{r,para}\zeta_{para}\Delta\chi_{para} + D_{r,dia}\zeta_{dia}|\Delta\chi_{dia}| = D_{r,para}\zeta_{para}\chi_{para,inc} - D_{r,dia}\zeta_{dia}\chi_{dia,inc} - (D_{r,para}\zeta_{para} - D_{r,dia}\zeta_{dia})\chi_{water} \qquad [Eq.2]$$

where $\Delta\chi_{para/dia,inc}$ is susceptibility difference between water (χ_{water}) and para/dia magnetic inclusion ($\chi_{para/dia,inc}$), $\zeta_{para/dia}$ the volume fraction of para/dia-magnetic inclusion, and $D_{r,para/dia}$ relaxometric constant for $\chi_{para/dia,inc}$. Eqs. 1-2 suggest that the temperature dependency of χ_{bulk} and R2' may not be solely attributed to its paramagnetic inclusion and its paramagnetism (i.e., by Curie's law), due to the contribution of diamagnetic inclusions and the temperature-dependent χ_{water} ($\Delta\chi_{water} = -0.05$ ppm for increase of 40°C)[9], which was usually ignored in previous studies [5,6,10]. In real tissue, D_r is a complex function of source geometry, diffusivity, and field strength[1,4,11], but the combination of Eq.1 and 2 suggest D_r could be better determined when there is a single susceptibility source.

Methods: [Data Acquisition] A postmortem hemibrain (57y/o, male) was scanned at 3T and 7T at 7 different temperatures (from 6°C to 35°C). To achieve a uniform temperature across the specimen, it was embedded in a water bath at a certain temperature at least 3 hours before MRI and encapsulated inside a thermally insulated 3D-printed container during MRI. MRI at each temperature included multi-orientational multi-echo gradient echo (MEGE) for R2* and local frequency map (MEGE; resolution=1-mm-isotropic, TR/TE1/ΔTE@3T=40/7/7ms[4-echo], TR/TE1/ΔTE@7T=40/3/3ms[5-echo], 4 orientations per temperature) and multi-echo spin-echo for R2 (resolution=2-mm-isotropic, TE1/ΔTE@3T=11/11ms[8-echo], TE1/ΔTE@3T=12/12m[5-echo]). **[Processing]** For each temperature, R2 map, multi-orientation local frequency (obtained after unwrapping[12], echo combination[13], and background field removal[14]), and R2* maps were reconstructed and co-registered. χ_{bulk} was estimated using COSMOS (CSF-referenced), and R2' by subtracting R2 from R2* (orientationally-averaged). **[ROI analysis]** Six gray matter (GM) ROIs were segmented using SynthSeg[15] and 17 white matter (WM) ROIs were manually segmented using DTI.

Results: Fig. 1. shows normalized R2', R2*, and χ_{bulk} values in GM and WM, which decrease over temperature at both 3T and 7T (normalized by each parameter at 6°C). χ_{bulk} shows small temperature dependency, independent of field strength, while relaxometry shows large temperature dependency varying across field strengths as well as relaxometry (R2' vs. R2*), as expected by theory. Notably, χ_{bulk} in WM increases (becoming less diamagnetic) with temperature, which has not yet been reported before (as Curie's law expects χ_{bulk} decreasing with temperature), suggesting the potential contribution of temperature-dependent χ_{water} (Fig .1B; note that here χ_{bulk} in WM is normalized by negative value [χ_{bulk} at 6°C]).

When investigating D_r in GM ROIs having paramagnetic iron as a dominant susceptibility source, $D_{r,para}$ exhibits dependency on both field strength and temperature (Fig. 2). Given diffusivity is independent on field strength, larger normalized $D_{r,para}$ values at 7T compared to 3T indicate a super-linear increase in R2' over field strength[11,16]. This agrees with the theory that we may have a closer to ideal static dephasing regime at higher field[4,11,16]. In addition, the relaxometric constant measured around body temperature is observed to be much lower than theoretical maximum predicted in ideal static dephasing regime (48% at 3T and 78% at 7T), consistent with previous observations[1]. All these results suggest a field-specific D_r measurements may be needed for accurate source separation.

When R2' and χ_{bulk} are compared between 3T and 7T, 7T R2' shows higher values than that expected from 3T with linear scaling by field strength, while χ_{bulk} is in good agreement with theoretical expectation (Fig. 3). These higher 7T R2' values over linear scaling are also consistent with the super-linear behavior of D_r over field strength in Fig.2. In addition, strong linearity without intercept ($p<0.01$) between 3T and 7T measures (χ_{bulk} and R2') shows the feasibility of linear modeling using D_r to describe the effects of susceptibility on R2' at both 3T and 7T as in Eq. 2. Fig.4. shows the 3T and 7T chi-separation comparison results when D_r at 7T is scaled linearly from 3T (i.e. scaled with 7T/3T) or directly measured (assuming non-linear behavior). When D_r is scaled linearly, both χ_{dia} and χ_{para} at 7T show overestimation compared to 3T results. Conversely, using D_r scaled by the corrected scaling factor as in Fig.3, 7T chi-separation results highly correspond to those at 3T, indicating the efficacy of the super-linear field strength correction. The measured 3T D_r in the brain sample is 157 Hz/ppm at 35°C, agreeing in general with previous in-vivo measurements[1].
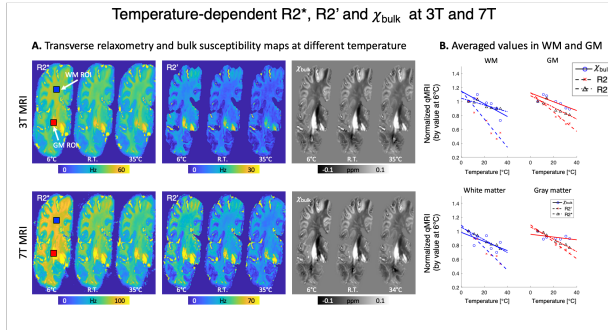

Fig 1. A. R2*, R2' and χ_{bulk} maps at 6° C, room temperature, and 35° C at 3T (top) and 7T (bottom). B. Temperature dependence of normalized R2*, R2' and χ_{bulk} (divided by the parameter at 6° C) were linearly fitted in GM (red) and WM (blue) area.
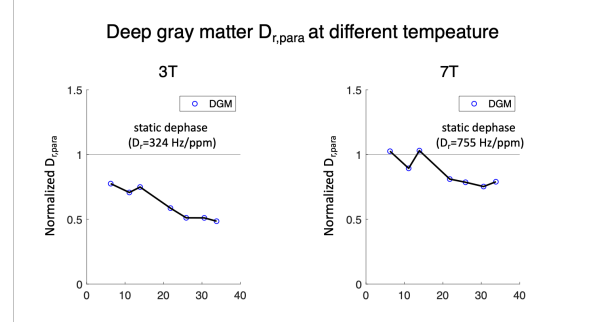
Fig 2. Estimated relaxometric constant $D_{r,para}$ in deep gray matter (DGM) as a function of temperature at 3T (left) and 7T (right). D_r values are normalized to their physical maximum.
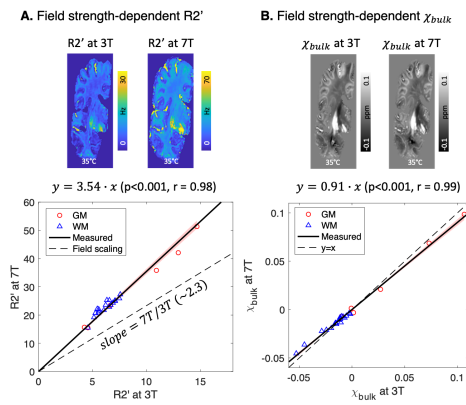
Fig 3. R2' (A) and χ_{bulk} maps (B) acquired at 35°C at 3T and 7T and the corresponding linear regressions of the parameters at the two field strengths.
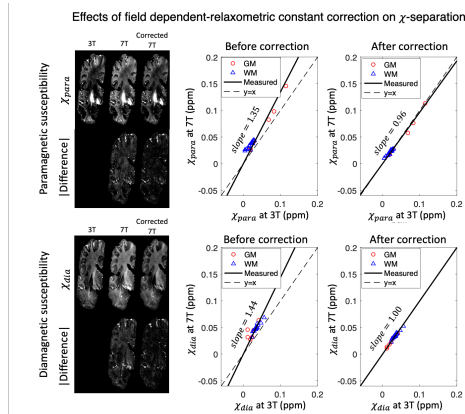
Fig 4. Comparison of 7T chi-separation results ($\chi_{para/dia}$ in the top/bottom row) using a simple linear field-strength scaling (=7T/3T) for D_r versus using the proposed super-linear correction (Corrected 7T).

Discussion and Conclusions: We systematically analyzed the relaxometric constant in human brain by measuring relaxometry and susceptibility at different temperatures and field strengths, proposing a field-strength correction to achieve more accurate brain chi-separation results at 7T.

References: [1] Shin HG (2021), NeuroImage, 240:118371; [2] Emmerich J, (2121), J Magn Reson. 2021;330:107033; [3] Chen J (2021). Neuroimage, 242:118477; [4] Yablonskiy DA, Magnet Reson Med, 32(6):749 763; [5] Birkl C (2015), Magnet Reson Med, 73(3):1282-1288; [6]. Birkl C (2017), Magnet Reson Med, 79(3):1609-1615; [7] Li Z (2023), NeuroImage;274:120148; [8] Liu T (2009), Magnet Reson Med. 61(1):196-204; [9] Cini R (1968), J Chem Phys. 1968;49(6):2826-2830. doi:10.1063/1.1670491; [10]. Kan H (2020), Magn Reson Imaging, 73:55-61; [11] Turner R (1993), Magn Reson Med. 1993;29(2):277-279; [12] Abdul-Rahman HS (2007), Appl Opt 46(26):6623-6635; [13] Wu B (2012), NeuroImage, 59(1):297-305; [14]. Wu B (2012), Magnet Reson Med, 67(1):137 147; [15] Billot B (2023), Méd Image Anal, 86:102789; [16]. Peters AM (2007), Magn Reson Imaging 25(6):748-753.

In vivo measurements of tibiofemoral knee articular cartilage electrical conductivity in a healthy patient cohort by magnetic resonance electrical properties tomography

Pablo Argote[1], Emily Y. Miller[2], Hongtian Zhu[1], Woowon Lee[1], Timothy Lowe[1], Corey P. Neu[1,2]

[1]Paul M. Rady Department of Mechanical Engineering, University of Colorado Boulder, Boulder, CO; [2]Biomedical Engineering Program, University of Colorado Boulder, Boulder, CO, USA

Summary: This study presents an optimized Helmholtz phase-based method for mapping knee cartilage conductivity using MR-EPT, validated through *in silico* models, phantoms, and *in vivo* data. The method aims to serve as a novel biomarker for early osteoarthritis detection and enhance clinical decision-making.

Introduction: Knee osteoarthritis (OA) is a major cause of disability, affecting over 50 million Americans [1]. The irreversible cartilage degradation often necessitates painful surgeries, imposing significant socioeconomic burdens. Earlier detection allows for faster intervention, improving people's quality of life. Quantitative Magnetic Resonance Imaging (qMRI) helps OA diagnosis by measuring tissue properties, including electrical conductivity [2-6]. Conductivity correlates with streaming potential, which results from charged fluid movement through cartilage under pressure, as during gait. Conductivity deviations may suggest early OA. Proteoglycans in the cartilage matrix create an electronegative environment, aiding tissue hydration and its mechanical response [7]. This study uses MR-EPT to optimize and validate a quantitative conductivity mapping method using computational models and phantoms and measure quantitative conductivity maps (QCMs) of tibiofemoral knee articular cartilages in a patient cohort. The goal is to develop a robust knee health metric using cartilage conductivity as a biomarker, enhancing clinical decision-making, improving patient outcomes, and paving the way for new therapies.

Methods: <u>*Phantoms, Human Subjects, MR Imaging*</u>: Conductivity phantoms were prepared with a 1.28 S/m conductivity standard (HI7030L, Hanna Instruments) and 0.5 S/m solution (0.32 w/v% NaCl). Healthy human subjects (N=12 [6 females, 6 males], age=28.3±4.7 years) were recruited with institutional review board approval. A 3T Siemens Magnetom Prismafit MRI system with a Tx/Rx Knee 15 Flare Coil was used, employing a 3D balanced steady state free precession (bSSFP) sequence. The sequence parameters were TR=5.69 ms, TE=2.84 ms, flip angle: 25°, XY-resolution: 0.625mm/pixel, slice thickness: 0.6mm/slice, number of averages: 5, field of view: 160x160 mm^2, bandwidth: 610 Hz/pixel. The total scan was less than 5 minutes.

<u>*Quantitative Conductivity Mapping*</u>: Analysis was conducted on MATLAB. Regions of interest (ROIs) were manually segmented to outline phantoms and the medial femoral condyle and tibial plateau of human subjects. Conductivity calculations used the Helmholtz phase-based method (Eq. 1) [2-5] with the transceiver phase assumption (i.e., $\varphi^{\pm} = \varphi/2$) and a Laplacian algorithm to estimate the 2nd order spatial derivative by convolution of a tri-variate 2nd order polynomial. For edge-aware processing, phase voxels that deviated past the threshold from the central phase voxel were excluded (Eq. 2). Voxels with negative conductivities were zeroed, and all QCMs were smoothed using 3D Gaussian smoothing.

$$\sigma = \frac{\nabla^2 \varphi^{\pm}(x,y,z)}{\omega\mu} \quad (1)$$

$$R = \left| \frac{A(r)}{A(r_{target})} - 1 \right| \leq R_{thresh} \quad (2)$$

<u>*Parameter Optimization, Forward Model & Statistical Analysis*</u>: Parameters of interest included the Laplacian pad size, deviation threshold, and Gaussian smoothing parameters (standard deviation, kernel size, and iterations). The *in silico* forward model was created by fitting the phase image of a homogeneous phantom solution to a global tri-variate 2nd order polynomial to obtain a new phase profile. Parameter optimization was conducted using pad sizes (5, 10, 20, 25 voxels), deviation thresholds (5, 10, 20, 40%), and Gaussian parameters (sigma: 0.5, 1, 2; kernel: 5, 7, 11 voxels). Noise measurements of 0.3% were obtained from phase images of human knee cartilage ROIs. To further validate parameter sensitivity in the forward model, lower and higher levels of Gaussian noise (0.1% and 0.9%) were applied. Metrics of percent error from the expected value (1.9 S/m) and precision were used for comparisons. A two-way ANOVA was conducted on mean regional conductivities with factors being sex (male vs. female) and cartilage region (femoral vs. tibial) with significance set at $p < 0.05$.

Results: The forward model demonstrated the sensitivity of QCM parameters in accurately reconstructing the ground truth conductivity. Small pad size (< 10 voxels) resulted in noisy data, while too large pad sizes (> 20 voxels) increased percent error (>5%) but maintained precision under 0.2 S/m. Excessive Gaussian 3D smoothing beyond 5 rounds was not favorable. Optimizing the post-processing determined a pad size of 10, a deviation threshold of 10-20%, and three rounds of 3D Gaussian smoothing to minimize error (Fig. 1A). The ground truth phantom conductivity profiles were successfully reconstructed with errors (<5%) (Fig. 1B). In the *in vivo* cohort, subtle differences were noted in the conductivity between the femoral and tibial regions, yet not significant. Mean conductivities were male: 0.95 ± 0.80 S/m (femoral) and 1.34 ±

1.01 S/m (tibial); female: 1.00 ± 0.75 S/m (femoral) and 1.51 ± 0.86 S/m (tibial), respectively (Fig. 1D). The *p-values* for the two-way ANOVA were Gender (p=0.7628), Region (p=0.2174) and Gender*Region (p=0.8716).
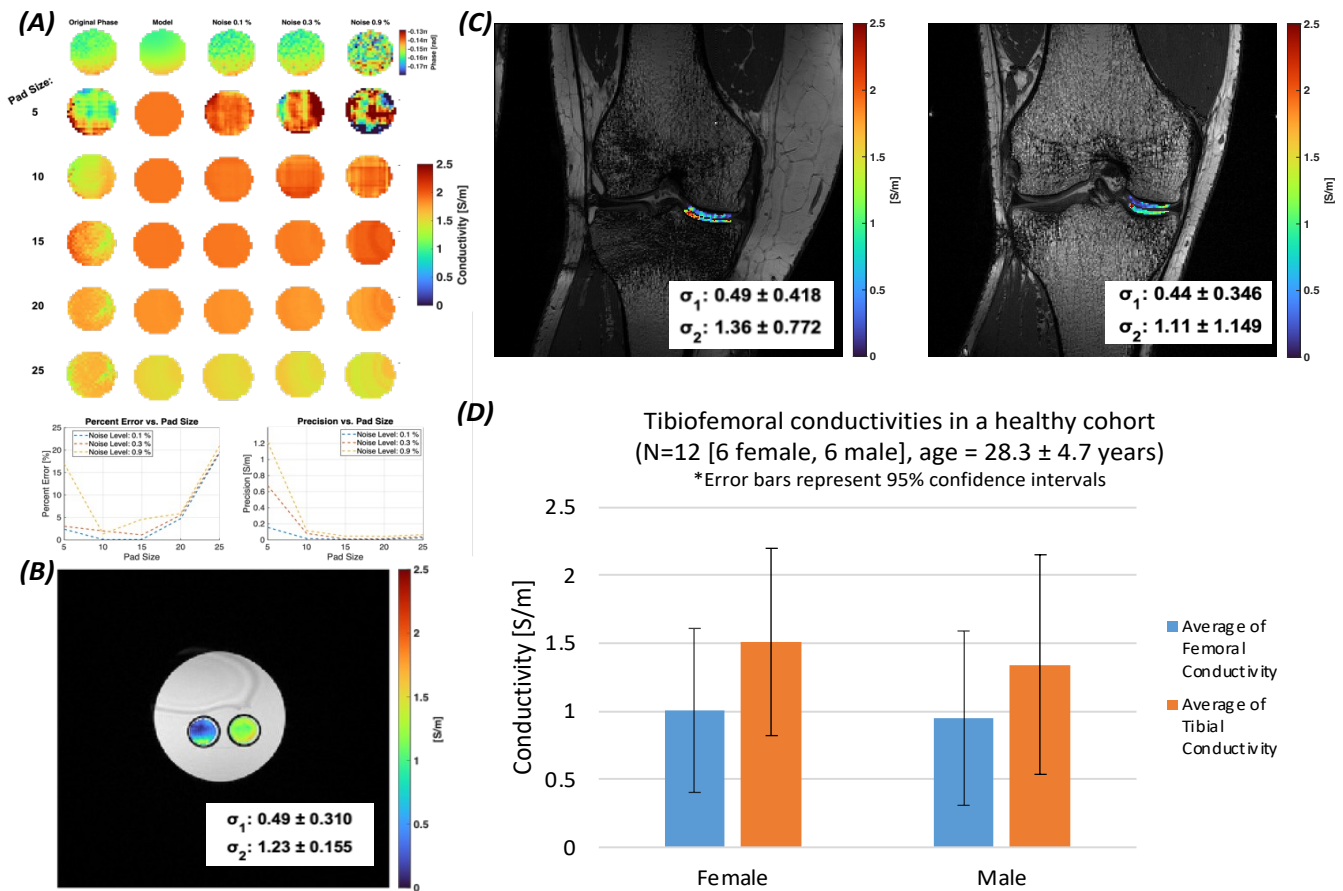
Figure 1: (A) *In silico* model with added noise levels, showing percent error and precision against pad size, **(B)** Multi-phantom data, successfully reconstructing expected conductivities. **(C)** Magnitude images with superimposed QCMs of medial tibiofemoral cartilages in example female (left) and male (right) subjects. **(D)** Mean regional conductivities of the healthy patient cohort.

Discussion and Conclusions: The optimal parameters were a pad size of 10, deviation threshold of 10-20%, and three rounds of 3D Gaussian smoothing with a standard deviation of 0.5-1 and kernel size of 5-11 pixels for all noise levels. The *in vivo* conductivities did not show significant difference between the femur and tibia in both males and females. These results align with literature values for cartilage conductivity, which range from 1.12-2.98 S/m [5], 0.51-1.15 S/m [8], and 0.48 S/m at 128 MHz [6]. The observed variation in bulk conductivities may indicate physiological phenomena related to cartilage health. This study validates conductivity mapping in computational models, ground truth phantoms and *in vivo* articular cartilage of a healthy cohort using MR-EPT. We hypothesize that QCMs serve as potential biomarkers for early osteoarthritis detection. Further experimentation is required to understand how these variations correlate with disease states and the phenomena of articular cartilage under load, especially concerning regional heterogeneity.

References:
[1] Barbour, K. E., *et al*. (2017), "Vital Signs: Prevalence of Doctor-Diagnosed Arthritis and Arthritis-Attributable Activity Limitation-United Sates, 2013-2015," Morb. *Mortal Wkly. Rep.*, vol. 66, no. 9, pp.246-253. doi: 10.15585/mmwr.mm6609e1
[2] Haacke, E. M., *et al*. (1991), "Extraction of conductivity and permittivity using magnetic resonance imaging," *Phys. Med. Biol.,* vol. 36, no. 6, pp. 723-734, doi: 10.1088/0031-9155/36/6/002
[3] Stehning, C., *et al*. (2011), "Real-Time Conductivity Mapping using Balanced SSFP and Phase-Based Reconstruction," *Proc. Intl. Soc. Mag. Reson. Med*., Abstract, pp. 128, 2011.
[4] Kim, D-H., *et al*. (2014), "Simultaneous imaging of in vivo conductivity and susceptibility," *Magn. Reson. Med.,* vol. 71, no. 3, pp. 1144-1150, Mar. 2014, doi: 10.1002/mrm.24759
[5] Lee, J-H., *et al*. (2022), "In vivo electrical conductivity measurement of muscle, cartilage, and peripheral nerve around knee joint using MR-electrical properties tomography," *Sci. Rep.*, vol. 12, no. 73, doi: 10.1038/s41598-021-03928-y
[6] Gabriel, S., *et al.* (1996), "The dielectric properties of biological tissues: II. Measurements in the frequency range 10 Hz to 20 GHz," *Phys. Med. Biol.*, vol. 41, no. 11, pp. 2251-2269, doi: 10.1088/0031-9155/41/11/002
[7] Grodzinsky, A. J., *et al*. (1978), "Electromechanical properties of articular cartilage during compression and stress relaxation," *Nature*, vol. 275, no. 5679, pp.448-450, doi: 10.1038/275448a0
[8] Binette, J.S., et al. (2004), "Tetrapolar measurement of electrical conductivity and thickness of articular cartilage," *J. Biomech. Eng.*, vol. 126, no. 4, pp.475-484, doi: 10.1115/1.1785805.

Using Quantitative Susceptibility Mapping (QSM) as a biomarker for neurodegeneration after repeated Traumatic Brain Injury (rTBI).

Carly Skudin[1], Alexandra G. Roberts[1], Dominick Romano[1], Kelly M. Gillen[1], Ilhami Kovanlikaya[1], Tracy Butler[1], Jonathan P. Dyke[1], Pascal Spincemaille[1], Yi Wang[1]

[1] Department of Radiology, Weill Cornell Medicine, New York, NY, USA

Summary: Increased iron accumulation in specific regions of interest (ROIs) have been observed in neurodegenerative diseases. In this study, we investigated whether these same regions display increased susceptibility in repeated Traumatic Brain Injury (rTBI) patients, particularly in victims of interpersonal violence (IPV), defined by behaviors that exert power and control over another, who have had repeated traumatic brain injuries[11]. The underserved and sparsely studied IPV cohort was of particular interest for this work. We found that QSM paramagnetic susceptibilities may help identify areas of potential neurodegeneration in this cohort. As such, QSM may be a promising biomarker in probing the lasting impact of rTBI in victims of IPV.

Introduction: Traumatic Brain Injury (TBI) is a common and deleterious form of head injury which can cause pathological and structural changes in the brain. Survivors suffer from progressive complications years after the acute injury, including neuronal death, brain atrophy, and a slew of cognitive and behavioral issues[1,2]. Individuals who have sustained repeated TBI (rTBI) are at even higher risk for post-traumatic neurodegeneration. Repeated injuries have been linked to the later development of Chronic Traumatic Encephalopathy (CTE), Frontotemporal dementia (FTD), Parkinson's Disease (PD), and Alzheimer's disease (AD)[1,3-5]. Iron accumulation is one of the several post-injury pathologies which can cause harm to the brain. Iron deposition can lead to axonal damage, tau phosphorylation, and cell death. Iron deposition has also infamously been implicated in the aforementioned neurodegenerative diseases[2-6]. QSM is a useful imaging tool for measuring iron levels in clinical and research settings. This quantitative technique has demonstrated that certain regions of interest (ROIs) have significantly increased iron accumulation in patients with neurodegenerative diseases like PD and AD, compared to healthy controls[4,7-10]. There are particularly vulnerable subsets of patient populations who experience rTBI at an alarming rate, such as victims of interpersonal violence (IPV). As domestic violence is still a relatively newly recognized research issue, measuring rTBI in these patients may provide them with a better outcomes[11]. Quantifying iron in patients with rTBI may serve as a biomarker for measuring brain damage or predicting neurodegeneration after multiple head injuries[4,9].

Methods: QSM images were analyzed retrospectively in 14 subjects, n=8 rTBI patients (41.9 ± 9.4 years) and n=6 healthy, age-matched healthy controls (HC, 38.0 years ± 8.0 years). The rTBI cohort was broken into two subgroups: athletes with rTBI and victims of IPV with rTBI. All participants were scanned on 3T clinical MRI scanners (GE Healthcare) using the product head coil. The QSM imaging parameters were: 3D multi-echo gradient echo (GRE), voxel size 0.58 mm × 0.58 mm × 3.0 mm, field of view 24 cm, matrix size of 416 x 320 x 56, six echo times with TE1=4.5 ms and ΔTE=9.9ms, repetition time TR = 58.5 ms, flip angle = 20 degrees, RBW = 244 Hz/pixel, elliptical k-space sampling and 0.80 phase field of view. QSM images were reconstructed using morphology enabled dipole inversion (MEDI)[12].

Images were segmented with ITK-SNAP[13]. Five regions of interest (ROIs) were identified and segmented manually: Red Nucleus (RN), Substantia Nigra (SN), Globus Pallidus (GP), Head of Caudate Nucleus (CN), and Putamen (P). Segmented regions were reviewed by a neuroradiologist, and the mean susceptibility values were calculated in ITK-SNAP for each region. Individual t-tests were performed on each of the five ROI groups to compare mean susceptibility values in individual voxels of each ROI in the two cohorts, rTBI and HC. An additional post-hoc Bonferroni correction was performed to correct for multiple comparisons. We considered *p<0.05* to indicate statistical significance.

Results: Compared to healthy controls (SN: 62.9 ± 22.6; RN: 43.1 ± 18.6), a statistically significant higher susceptibility was observed in the SN (*p=0.007*) (rTBI: 122.5 ppm ± 31.4 ppm) and RN (*p=0.03*) (rTBI: 89.2 ppm ± 32.0 ppm) in the rTBI cohort, suggesting increased accumulation of iron. Within the rTBI group, the IPV subset demonstrated a mean susceptibility in the SN of 143.2 ppm ± 25.1 ppm and in the RN of 98.2 ppm ± 44.6 ppm. The athlete subset of the rTBI cohort demonstrated a mean susceptibility in the SN of 110.0 ppm ± 30.0 ppm and in the RN of 83.7 ppm ± 26.5 ppm). QSM identified marginally significant differences in susceptibility in the GP in the rTBI cohort as compared to healthy controls *(p=0.06).*
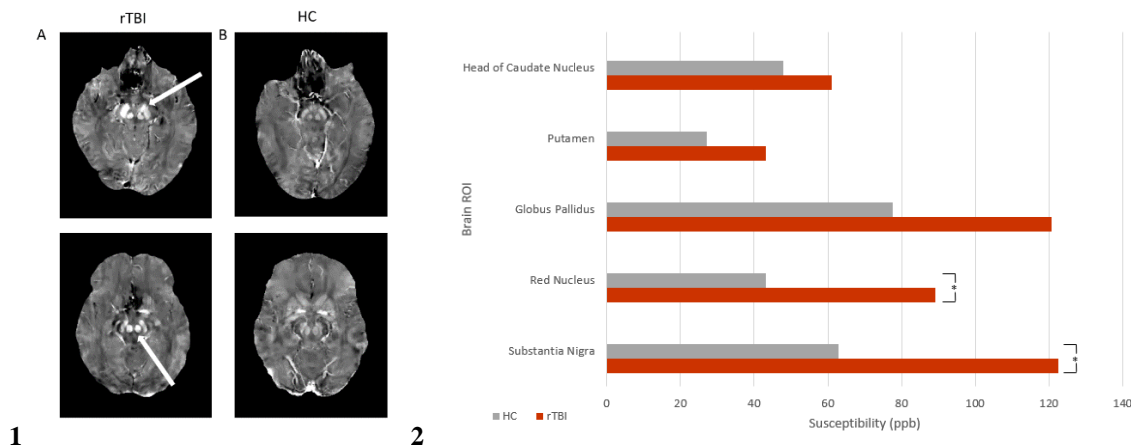
Figures – Figure 1. QSM images of 2 rTBI patients (A) and 2 HCs (B). The top arrow is noting the hyperintensity in the substantia nigra in the rTBI patient as compared to the healthy control. The bottom arrow is noting the hyperintensity in the red nucleus in the rTBI patient as compared to the healthy control (a); **Figure 2.** Average susceptibility values of the selected segmented regions of interest. Red bars denote RTBI patients and gray bars denote HCs. Statistical significance was set at $p<0.05$ (b)

Discussion and Conclusions: Our work demonstrates iron accumulation in subjects with rTBI. These subjects, particularly the IPV group, had significantly increased magnetic susceptibility in the SN and RN, as compared to healthy controls. This is likely to be of clinical relevance, given that iron accumulation in these ROIs is also observed in patients with AD and PD. QSM imaging in rTBI patients may be used as a clinical tool for assessing damage after injury or predicting regions of potential neurodegeneration. This may be a particularly vital and useful technique for underserved and underrepresented populations For example, IPV cohorts will greatly benefit from research, awareness, and increased education on this issue. Our results indicate that quantifying iron with QSM may be useful for the assessment of iron accumulation after head injury and may be a biomarker in specific regions for monitoring neurodegeneration.

References:
[1] Barker S, Paul BD, Pieper AA (2023), "Increased Risk of Aging-Related Neurodegenerative Disease after Traumatic Brain Injury," *Biomedicines,* no. 4: 1154, https://doi.org/10.3390/biomedicines11041154
[2] Huang S, Li S, Feng H, Chen Y (2021), "Iron metabolism disorders for cognitive dysfunction after mild traumatic brain injury," *Frontiers in Neuroscience*, 15, https://doi.org/10.3389/fnins.2021.587197
[3] Faden AI, Loane DJ (2015) "Chronic neurodegeneration after traumatic brain injury: Alzheimer disease, chronic traumatic encephalopathy, or persistent neuroinflammation?" *Neurotherapeutics*. vol 12, pp. 143-50, doi: 10.1007/s13311-014-0319-5. PMID: 25421001; PMCID: PMC4322076.
[4] Nisenbaum EJ, Novikov DS, Lui YW (2014), "The presence and role of iron in mild traumatic brain injury: an imaging perspective," *J Neurotrauma*, vol 31, pp. 301-7, doi: 10.1089/neu.2013.3102.
[5] Daglas M, Adlard PA (2018), "The Involvement of Iron in Traumatic Brain Injury and Neurodegenerative Disease," *Frontiers in Neuroscience*, 12, https://doi.org/10.3389/fnins.2018.00981
[6] Raz E, Jensen JH, Ge Y, Babb JS, Miles L, Reaume J, Grossman RI, Inglese M (2011), "Brain iron quantification in mild traumatic brain injury: a magnetic field correlation study," *AJNR Am J Neuroradiol*, vol 32, pp. 1851-6, doi: 10.3174/ajnr.A2637.
[7] Wang Y, Spincemaille P, Liu Z, Dimov A, Deh K, Li J, Zhang Y, Yao Y, Gillen KM, Wilman AH, Gupta A, Tsiouris AJ, Kovanlikaya I, Chiang GC, Weinsaft JW, Tanenbaum L, Chen W, Zhu W, Chang S, Lou M, Kopell BH, Kaplitt MG, Devos D, Hirai T, Huang X, Korogi Y, Shtilbans A, Jahng GH, Pelletier D, Gauthier SA, Pitt D, Bush AI, Brittenham GM, Prince MR (2017), "Clinical quantitative susceptibility mapping (QSM): Biometal imaging and its emerging roles in patient care," *J Magn Reson Imaging*, vol 46, pp. 951-971. doi: 10.1002/jmri.25693.
[8] Li KR, Avecillas-Chasin J, Nguyen TD, Gillen KM, Dimov A, Chang E, Skudin C, Kopell BH, Wang Y, Shtilbans A (2021), "Quantitative evaluation of brain iron accumulation in different stages of Parkinson's disease," *J Neuroimaging*, vol 32, pp. 363-371. doi: 10.1111/jon.12957.
[9] Ravanfar P, Loi SM, Syeda WT, Van Rheenen TE, Bush AI, Desmond P, Cropley VL, Lane DJ, Opazo CM, Moffat BA, Velakoulis D, Pantelis C (2021), "Systematic review: Quantitative susceptibility mapping (QSM) of Brain Iron Profile in neurodegenerative diseases," *Frontiers in Neuroscience*, 15. https://doi.org/10.3389/fnins.2021.618435
[10] Gozt A, Hellewell S, Ward PGD, Bynevelt M, Fitzgerald M (2021), "Emerging Applications for Quantitative Susceptibility Mapping in the Detection of Traumatic Brain Injury Pathology," *Neuroscience,* vol 467, pp. 218-236. doi: 10.1016/j.neuroscience.2021.05.030.
[11] Costello K, Greenwald BD (2022), "Update on Domestic Violence and Traumatic Brain Injury: A Narrative Review," *Brain Sci* vol 12, pp. 122. doi: 10.3390/brainsci12010122.
[12] De Rochefort L, Liu T, Kressler B, et al (2010), "Quantitative susceptibility map reconstruction from MR phase data using Bayesian regularization: Validation and application to brain imaging," *Magnetic Resonance in Medicine*, vol 63, pp. 194-206. doi:10.1002/mrm.22187
[13] Yushkevich PA, Piven J, Hazlett HC, Smith RG, Ho S, Gee JC, Gerig G (2006), "User-guided 3D active contour segmentation of anatomical structures: significantly improved efficiency and reliability," *Neuroimage*, vol 31, pp. 1116-28. doi: 10.1016/j.neuroimage.2006.01.015.

Stack-of-Spiral Cardiac Quantitative Susceptibility Mapping in One Breath-Hold for Differential Heart Chamber Blood Oxygenation

Jiahao Li[1], Pablo Villar-Calle[2], Mahniz Reza[2], Lily Jin[2], Thanh D. Nguyen[3], Yi Wang[1,3], Jiwon Kim[2],
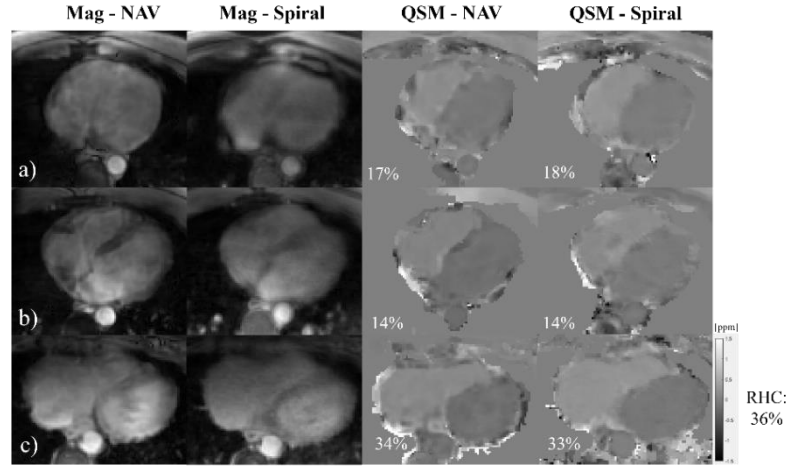
Jonathan W. Weinsaft[2], Pascal Spincemaille[3]

[1]Biomedical Engineering (Cornell University, Ithaca, USA); [2]Medicine and [3]Radiology (Weill Cornell Medicine, New York, USA)
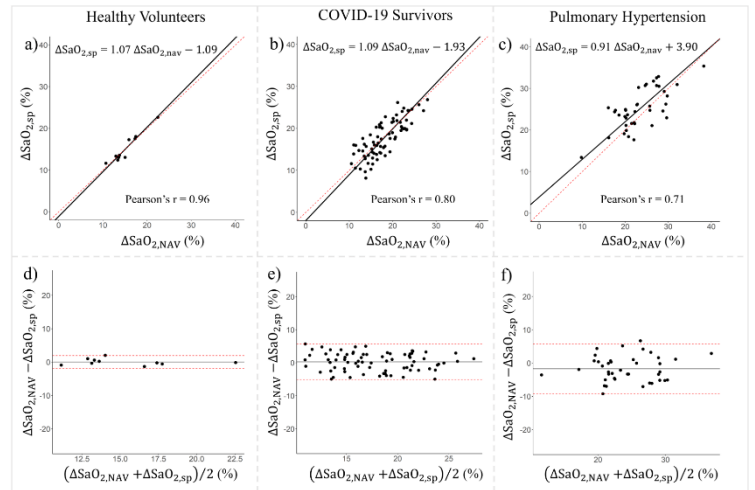
Summary: We developed a 3D stack-of-spiral sequence for cardiac quantitative susceptibility mapping to acquire multi-echo gradient echo images in one breath-hold. The resulting differential blood oxygenation between the right/left heart was observed to be similar to that obtained using a previous navigator based Cartesian acquisition and validated through right heart catheterization.

Introduction: Differential blood oxygen saturation between the right and left heart (ΔSaO_2) is a key measure in pulmonary hypertension (PH) prognosis and clinical outcome prediction [1]. The current clinical practice for measuring cardiovascular blood oxygenation relies on right heart catheterization (RHC), which is an invasive procedure and entails the risk of ionizing radiation. Cardiac quantitative susceptibility mapping (QSM) is a novel cardiac magnetic resonance imaging technique for directly

Figure1 – Representative cases of NAV and spiral combined echo magnitude and QSM images in healthy volunteer (a), COVID-19 survivors (b) and pulmonary hypertension (c). Estimated ΔSaO_2 is at the lower-left corner of QSM; PH RHC reference is 36%.

quantifying tissue magnetic susceptibility by utilizing the deoxygenated blood induced susceptibility contrast [2]. Previously, cardiac QSM used a prospective 1D diaphragmatic navigator and ECG-triggered 3D Cartesian multi-echo gradient echo data acquisition [3]. However, navigator setup can be complicated, and the acquisition times can be long. Here, we developed a 3D stack-of-spiral sequence for cardiac QSM to accelerate the data acquisition in one breath-hold and compared the results with navigator based cardiac QSM in terms of the ΔSaO_2 quantification.

Methods: A 3D spoiled multi-echo stack-of-spiral sequence was with golden angle rotated variable density spiral trajectory was used for data acquisition [4]. The same spiral trajectory was repeatedly and continuously sampled within one TR for multi-echo signal and across all the slice encodes before moving on to the next leaf. The FOV was set up in the axial plane covering the heart. Imaging parameters were: number of leaves 36, readout length 1096, readout bandwidth ±125kHz, flip angle 12º, number of echoes 3, $TE_1/TR/\Delta TE = 0.4/17.8/5.9$msec, reconstructed matrix size 256×256×24, image resolution $1.8\times1.8\times5mm^3$. Prior to the multi-echo acquisition, a reference free induction decay (FID) signal was acquired along kz encoding for off-resonance correction [5]. With the above setting, spiral QSM can be acquired under 20sec within one breath-hold.

Figure2 – Comparison between ΔSaO_2 from spiral and NAV QSM in healthy volunteer (a,d), COVID-19 survivors (b,e) and PH subjects (c,f) for Deming Regression and Bland Altman plot.

For comparison, the navigator based Cartesian QSM (NAV QSM) was performed with the same FOV, reconstructed matrix size and resolution. Other imaging parameters were: readout bandwidth ±83.33kHz, flip angle 15º, number of echoes 5, $TE_1/TR/\Delta TE = 1.4/18.7/3.4$msec. A GRAPPA factor of 2 was implemented to reduce scan time.

For QSM reconstruction, both spiral QSM and NAV QSM followed the same post-processing as below. An initial field map was fitted form the complex multi-echo gradient echo data, unwrapped using the graph-cut based method [6]. Then

iterative decomposition of water and fat with echo asymmetry and least squares estimation (IDEAL) [7] was applied to get the water, fat and field map. QSM was computed using total field inversion (TFI+0) [3, 8] with L2 based regularization to minimize the blood pool susceptibility variation:

$$y^* = \underset{y}{\operatorname{argmin}} \|w(f - DPy)\|_2^2 + \lambda\|M_G \nabla Py\|_1 + \sum_i \mu_i \|M_i P(y - \bar{y}^i)\|_2^2 \qquad (1)$$

Where M_i are the heart chamber masks segmented from the magnitude images using a 3D U-Net based deep neural network. The final QSM is derived as $\chi = Py^*$. Then, ΔSaO_2 was estimated from the difference between the mean susceptibility in right/left ventricle blood pools and scaled by individual hematocrit.

Healthy volunteers, COVID-19 survivors and PH subjects were scanned on a 3T scanner (GE MR750) and a 3T clinical scanner (GE PET/MR). Deming Regression and Bland-Altman plot were used for comparison among ΔSaO_2 from spiral and NAV QSM, and RHC (which was available in the PH cohort only).

Results: Representative images are shown in Figure 1. All N=10 healthy volunteers (age: 30±8, 20% female) were images successfully. Among the COVID-19 survivors, N=75 subjects (age: 53±16, 56% female) successfully underwent both spiral and NAV QSM. In the same group, 13 additional subjects did not have NAV QSM acquired due to the limited exam schedule and/or subjects' unavailability for longer scan time. The average NAV QSM scan time was 415±140sec with navigator efficiency 39.2±11.1%, versus 20sec spiral QSM and 100% efficiency. In both cohorts, Deming regression and Bland-Altman plot shows similar ΔSaO_2 between spiral and NAV QSM (healthy volunteers: $\Delta SaO_{2,sp} = 1.07\Delta SaO_{2,NAV} - 1.09$ (%), r=0.96; COVID-19 survivors: $\Delta SaO_{2,sp} = 1.09\Delta SaO_{2,NAV} - 1.93$(%), r=0.80) in Figure 2.
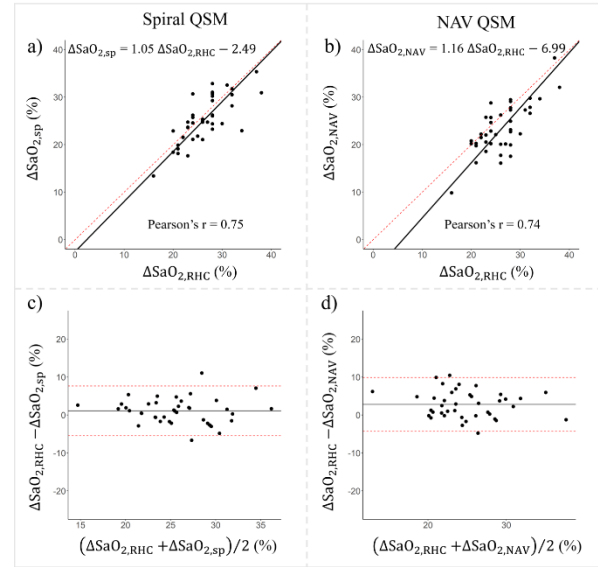
In the PH cohort, N=40 subjects successfully underwent both spiral and NAV QSM and had RHC performed within 2months prior to MRI, NAV QSM had an average scan time of 428±189sec and 38.9±14.4% navigator efficiency, whereas spiral QSM was 20sec and 100% efficiency. Method comparison between spiral and NAV QSM in terms of quantification showed good agreement (Figure 2C, $\Delta SaO_{2,sp} = 0.91\Delta SaO_{2,NAV} + 3.90$ (%), r=0.71). By comparing each imaging method with clinical reference value from RHC, it demonstrated that spiral QSM slightly outperformed NAV QSM with better correlation and lower limits of agreements (Figure 3, spiral $\Delta SaO_{2,sp} = 1.05\Delta SaO_{2,RHC} - 2.49$ (%), r=0.75; NAV $\Delta SaO_{2,NAV} = 1.16\Delta SaO_{2,RHC} - 6.99$ (%), r=0.74).

Figure3 – Spiral QSM (a, c) and NAV QSM (b, d) estimated ΔSaO_2 w.r.t. RHC in PH cohort for Deming Regression and Bland Altman plot.

Discussion and Conclusions: The proposed non-gated spiral cardiac QSM achieved data acquisition within one breath-hold and 100% scan efficiency in our multi-cohort study. Limitations include the lack of cardiac gating and/or triggering, which induces a degree of image blurring. Nevertheless, our results in all three cohorts showed well-aligned agreement between spiral and NAV QSM for ΔSaO_2 quantification. Additionally, cardiac QSM based ΔSaO_2 estimation was validated using RHC derived oxygenation in the PH cohort. These results suggest the feasibility of including cardiac QSM as part of a clinical CMR exam in PH patients.

References:
[1] Gallet R, et al, *Arch Cardiovasc Dis.*, 2012;105(1):5-12, doi: 10.1016/j.acvd.2011.10.005.
[2] Wen Y, et al, *Magn Reson Med*, 2018;79(3):1545-1552, doi: 10.1002/mrm.26808.
[3] Wen Y, et al, *J Cardiovasc Magn Reason*, 2019;21(1):70, doi: 10.1186/s12968-019-0579-7.
[4] Xu B, et al, *Magn Reson Med*, 2013;69(2):370-381, doi: 10.1002/mrm.24253.
[5] Sarah Eskreis-Winkler, et al., "Time-Efficient Approximate Inhomogeneity Correction Algorithm for 3D Spiral Contrast Enhanced Imaging of the Liver," *Proc Intl Soc Magn Reson Med* 2012.
[6] Dong J, et al, *IEEE Trans Med Imaging*, 2015;34(2):531-540, doi: 10.1109/TMI.2014.2361764.
[7] Reeder SB, et al, *Magn Reson Med*, 2005;54(3):636-644, doi: 10.1002/mrm.20624.
[8] Liu Z, et al, *Magn Reson Med*, 2017;78(1):303-315, doi: 10.1002/mrm.26331.

Automatic Chamber Segmentation for Cardiac Quantitative Susceptibility Mapping

Jiahao Li[1,2], Pablo Villar-Calle[3], Yi Wang[1,2], Jiwon Kim[3], Jonathan W. Weinsaft[3], Pascal Spincemaille[2]

[1]*Biomedical Engineering (Cornell University, Ithaca, USA);* [2]*Radiology and* [3]*Medicine (Weill Cornell Medicine, New York, USA)*

Summary: A deep neural network was developed for cardiac chamber segmentation to facilitate an automated cardiac quantitative susceptibility mapping processing pipeline suitable for clinical studies.

Introduction: Cardiac Quantitative Susceptibility Mapping (QSM) provides is a non-invasive method for measuring the blood oxygen saturation difference (ΔSaO_2) between the right and left heart [1]. A previously validated cardiac QSM method uses total field inversion (TFI+0) [2-4] combined regularization term that imposes signal uniformity on the cardiac chambers. The same chamber segmentations are also required for the right-left heart ΔSaO_2 measurements. In this method, this segmentation was performed manually preventing this method from wider clinical use. Deep neural networks have emerged as a mainstream data-driven approach for automatic medical image segmentation in various imaging modalities and scenarios [5]. However, most existing segmentation methods or public cardiac datasets are either focused on short-axis view or using balanced steady-state free-precession (bSSFP) based images [6-8]. In contrast, cardiac QSM uses multi-echo gradient-echo (mGRE) often in axial orientation. Due to the intrinsic low signal-to-noise ratio in mGRE, a customized 3D deep learning segmentation network is needed to make the cardiac QSM pipeline fully automatic.

Methods: A retrospective dataset consisting of N=120 cardiac QSM exams performed on COVID-19 survivors on a 3T clinical scanner (GE PET/MR) is constructed for this study. The cardiac QSM data were acquired using a free-breathing ECG-triggered 3D spoiled multi-echo gradient echo sequence with 1D diaphragmatic navigator on axial plan covering the whole heart to pulmonary arteries. Imaging parameters are as follows: $TE_1/TR/\Delta TE$ = 1.4/18.7/3.4msec, number of echoes N_e = 5, flip angle FA = 15°, readout bandwidth ±83.33kHz, image resolution 1.8×1.8×5mm³, reconstructed matrix size 256×256 with on average 24 slices. All subjects were provided consent for this IRB approved protocol.

For each exam, a combined multi-echo gradient echo magnitude image was used to manually segmented out eight chambers and vessels including left ventricle (LV), right ventricle (RV), left atrium (LA), right atrium (RA), ascending aorta (AAo), descending aorta (DAo), main pulmonary artery (PA) and superior vena cava (SVC). All masks were reviewed by an experienced cardiologist. The corresponding QSM was reconstructed with this mask using TFI+0:

$$y^* = \underset{y}{\operatorname{argmin}} \|w(f - DPy)\|_2^2 + \lambda\|M_G \nabla Py\|_1 + \sum_i \lambda_i \|M_i P(y - \bar{y}^i)\|_2^2$$

Where blood pool susceptibility uniformity was imposed in each of the aforementioned regions as denoted by M_i. ΔSaO_2 was then estimated by taking the difference of the LV and RV mean susceptibility and scaled by the hematocrit.

Two U-Net architecture based 3D deep neural networks were trained to perform automated chamber segmentation on this dataset: 1) unetVgg using convolutional layers, and 2) unetRes using residual blocks within each convolution. The dataset was randomly split into 84/24/12 training/validation/test sets. Both models were trained with a 5-fold cross-validation on the training/validation sets using stochastic gradient descent in 2000 epochs. During each epoch training, the network was fed a 3D combined-echo magnitude image with random location cropping and rotation for data augmentation. A multi-class cross entropy was chosen as the loss function to match the manually segmented labels. An ensemble model was constructed using the average probability map taking from each fold of the trained model resulting in the final output of the auto-segmented labels. Dice scores on each cardiac chamber were
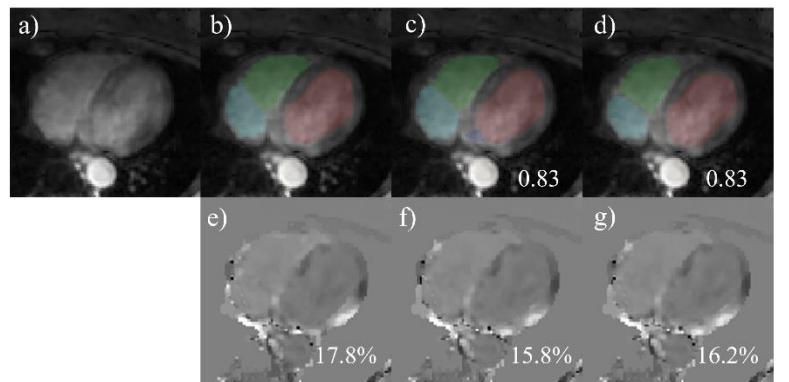
Figure1 – A representative case in the test set (combined echo magnitude image, a) with segmentation from manual label (b), unetVgg (c) and unetRes (d); and their corresponding QSM. The number in (c) and (d) indicates the average dice for unetVgg and unetRes segmentation, respectively. The numbers on QSM indicates $\Delta SaO2$ estimated by using manual label (e), unetVgg (f) and unetRes (g) segmentation.

computed for each segmentation. Both segmentations were then used to recompute a cardiac QSM and the associated ΔSaO_2. The latter were compared with the manually obtained values using Bland-Altman analysis and Deming regression.

The deep learning network was implemented in python3 using pyTorch on NVIDIA GPUs. QSM reconstruction was conducted using MATLAB R2020b. Statistical analysis was performed using R 4.3.0.

Results: A representative case with manual segmentations, both model segmentations and their corresponding QSM are shown in Figure 1. The dice scores across all the classes and the mean dice measures are summarized in Figure 2 across the test cases, where the mean dice scores from unetVgg vs unetRes are 0.79 ± 0.042 vs 0.78 ± 0.045 using the manual segmentation as the ground-truth. The derived oxygen saturation difference from both models and the manual segmentation are compared in Figure 3 in the test cases. The regression of each model to manual are: $\Delta SaO_{2,vgg} = 1.30\Delta SaO_{2,m} - 5.41$ (%), Pearson's r = 0.75; $\Delta SaO_{2,res} = 1.11\Delta SaO_{2,m} - 2.95$ (%), Pearson's r = 0.81.

Discussion and Conclusions: The results shown here demonstrate the ability of unetVgg and unetRes models to segment the designated cardiac chamber with a comparable result compared to the manual labels in terms of dice comparison as well as in this specific study, the ΔSaO_2 quantification. Although dice-wise, unetRes resulted in a slightly lower performance across all the chambers, it provided a ΔSaO_2 closer to the manually obtained value. This shows that a ResNet based 3D U-Net neural network can be suited for heart chamber segmentation in the context of cardiac QSM study. This is a promising first step to making cardiac QSM fully automated.
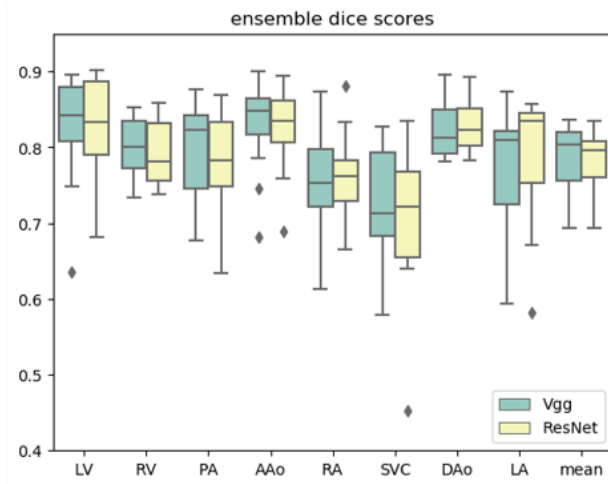
Figure2 – The average dice scores (mean ± sd) across all the segmented chambers in the ensemble unetVgg and unetRes model.
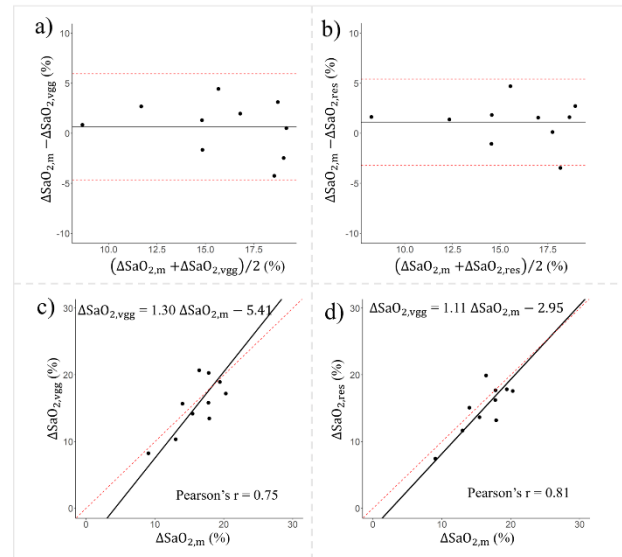
Figure3 – Bland-Altman plot (first row) and Deming regression (second row) for ΔSaO_2 comparison by using the unetVgg (a, c) and unetRes (b, d) segmentation in the test set w.r.t. the manual labels.

References:
[1] Wen Y, et al, *Magn Reson Med*, 2018;79(3):1545-1552, doi: 10.1002/mrm.26808.
[2] Wen Y, et al, *J Cardiovasc Magn Reason*, 2019;21(1):70, doi: 10.1186/s12968-019-0579-7.
[3] Liu Z, et al, *Magn Reson Med*, 2017;78(1):303-315, doi: 10.1002/mrm.26331.
[4] Liu Z, et al, *Magn Reson Med*, 2018;79:2795-2803, doi: 10.1002/mrm.26946.
[5] Hesamian MH, et al, *J Digit Imaging,* 2019;32(4):582-596, doi: 10.1007/s10278-019-00227-x.
[6] Chen C, et al, *Front Cardiovasc Med*, 2020;7:25, doi: 10.3389/fcvm.2020.00025.
[7] Bernad O, et al, *IEEE transactions on medical imaging*, 2018;37(11):2514-2525.
[8] Isensee F, et al, *Nat Methods*, 2021;18(2):203-211, doi: 10.1038/s41592-020-01008-z.

Characterizing the Temporal Signal-to-Noise Ratio in Simultaneous Functional MRI, QSM and EPT

Jierong Luo, Jannette Nassar, Patrick Fuchs, Oriana Arsenov, and Karin Shmueli

*Department of Medical Physics and Biomedical Engineering (University College London, London, United Kingdom)*

Summary: We have characterized the temporal signal-to-noise ratio of BOLD fMRI, fQSM and fEPT time series, acquired simultaneously using a multi-echo (ME) GRE-EPI sequence in the human brain. The novel QSM and EPT based tSNR distributions reflect the conventional magnitude tSNR, with some noticeable high tSNR "hot spots" and low tSNR in the cerebellum for EPT.

Introduction: In fMRI, the temporal signal-to-noise ratio (tSNR) is a measure of data quality over time and depends on the MRI acquisition parameters[1-5]. It determines the sensitivity of an acquisition to activation-induced blood oxygen level dependent (BOLD) signal changes[2,4], and consequently affects the statistics in fMRI time series analysis[1,6]. Recent advances in tissue electro-magnetic properties imaging have enabled functional activations to be probed via tissue susceptibility and electrical conductivity changes. Reconstructed from the MRI phase, functional quantitative susceptibility mapping (fQSM)[6-10] and functional electrical properties tomography (fEPT)[11-16] have shown promise in detecting neuronal activations.

Although significant fQSM and fEPT activations have been observed using a typical general linear modeling approach[6], the tSNRs in the fQSM and fEPT time series have not been characterized. Moreover, these tSNRs could help interpret variations between subjects and aid comparisons of studies using different acquisition hardware and protocols[6-16]. Therefore, here we calculated tSNRs of fQSM and fEPT and compare them with the fMRI tSNR, acquired simultaneously using a ME GRE-EPI sequence[17].

Methods: Three healthy volunteers (HVs) were scanned on a 3T Prisma (Siemens, Erlangen, Germany) using a ME 2D GRE-EPI sequence[17], with 1.3 mm isotropic resolution, GRAPPA = 4, MB = 3, TR = 4034 ms, TEs = 15.6, 41.6, 67.6 ms, seventy volumes were acquired with a block design visual stimulus paradigm[17]. For fMRI, echo images within each volume were combined for optimal BOLD contrast[18]. QSM was calculated from the complex data using an optimised reconstruction pipeline as described previously[10]. We extrapolated the MR transceive phase (φ_0) from the complex data[16] and then reconstructed the EPT time series using a surface integral method with MagSeg magnitude and segmentation kernels[19] derived from the mean echo-combined[18] magnitude images over all 70 volumes. The resulting fMRI, fQSM and fEPT were registered across the time-series, and the tSNR map for each time series was calculated as the temporal mean over the temporal standard deviation in each voxel.

Results and Discussion: Fig. 1 shows the echo-combined magnitude (a), QSM (b) and EPT (c) of a single volume their temporal means over the 70 coregistered volumes, and the corresponding tSNR maps (d-f) in a representative subject. Compared with the conventional echo-combined magnitude tSNR (Fig. 1d), the EPT time series showed a more inhomogeneous tSNR distribution (Fig. 1f) with the lowest tSNR observed in CSF. This may be because the reconstructed conductivity values in the CSF are highly variable and often either negative or extremely high.
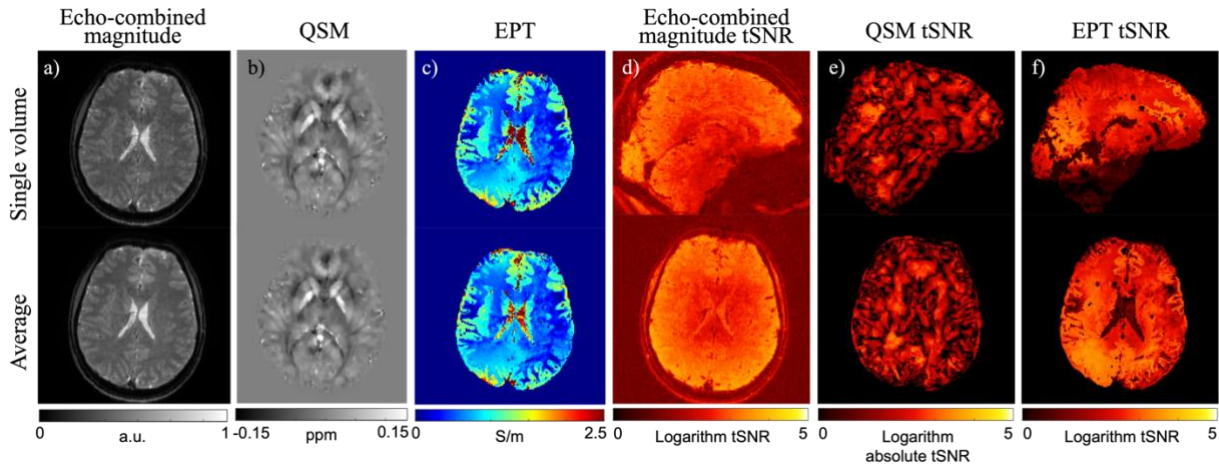

Figure 1 – Single volume (top) and mean images over 70 volumes (bottom) for echo-combined magnitude (a), QSM (b) and EPT (c) in HV1. Temporal SNR (tSNR) calculated for echo-combined magnitude (d), QSM (e) and EPT (f) time series in HV1. Note that the absolute value of the QSM tSNR is shown so that all tSNRs could be shown on the same (natural logarithm) scale.

The EPT tSNR was very low in the cerebellum due to residual slice-to-slice phase inconsistency artefacts[17,20]. The magnitude had the highest tSNR (Fig. 2a) with the highest values at the (posterior) brain edges, reflecting the RF coil sensitivity distribution. The QSM tSNR is more difficult to interpret due to the presence of both paramagnetic (positive) and diamagnetic (negative) tissues and regions in between having tSNR values close to zero, even in the absolute QSM tSNR maps shown. Despite this, the QSM tSNR maps show a similar distribution to the EPT tSNR maps, with the highest values in the back of the brain.

Conclusions: We characterized the tSNR of fQSM and fEPT for the first time and compared them with the tSNR of conventional BOLD fMRI. The distinct tSNR maps for the fQSM and fEPT time series may facilitate the interpretation of these novel functional contrasts and provide a tool to assess the acquisition quality for these modalities.

Figure 2 – Maximum intensity projections of the tSNR of echo-combined magnitude (a), QSM (b) and EPT (c) in three HVs.

References:
[1] Parrish T B, et al., (2000), "Impact of signal-to-noise on functional MRI," *Magn. Reson. Med.*, vol. 44, pp. 925-932, doi: 10.1002/1522-2594(200012)44:6<925::AID-MRM14>3.0.CO;2-M.
[2] Krüger G and Glover G H, (2001), "Physiological noise in oxygenation-sensitive magnetic resonance imaging," *Magn. Reson. Med.*, vol. 46, pp. 631-637, doi: 10.1002/mrm.1240.
[3] Murphy K, et al., (2007), "How long to scan? The relationship between fMRI temporal signal to noise ratio and necessary scan duration," *NeuroImage.*, vol. 34, pp. 565-574, doi: 10.1016/j.neuroimage.2006.09.032.
[4] Triantafyllou C, et al., (2011), "Physiological noise and signal-to-noise ratio in fMRI with multi-channel array coils," *NeuroImage*, vol. 55, pp. 597-606, doi: 10.1016/j.neuroimage.2010.11.084.
[5] Welvaert M and Rosseel Y, (2013), "On the definition of signal-to-noise ratio for fMRI data," *PLoS ONE*, vol. 8, pp. e77089, doi: 10.1371/journal.pone.0077089.
[6] Friston K J, et al., (1995), "Statistical Parametric Maps in Functional Imaging: A General Linear Approach," *Hum. Brain Mapp.*, vol. 2, pp. 189-210, doi: 10.1002/hbm.460020402.
[7] Balla D Z et al., (2014), "Functional quantitative susceptibility mapping (fQSM)," Neuroimage, vol. 100, pp. 112–124, doi: 10.1016/j.neuroimage.2014.06.011.
[8] Sun H, et al., (2017), "Structural and functional quantitative susceptibility mapping from standard fMRI studies," *NMR Biomed.*, vol. 30, pp. e3619, doi: 10.1002/nbm.3619.
[9] Lancione M et al., (2021), "Complementing canonical fMRI with functional quantitative susceptibility mapping (fQSM) in modern neuroimaging research," *Neuroimage*, vol. 244, pp. 118574, doi: 10.1016/j.neuroimage.2021.118574.
[10] Nassar J et al., (2023), "Preliminary Functional Quantitative Susceptibility Mapping with Multi-Echo EPI", *Proc. Ann. Meeting ISMRM 2023*, Abstract 2533.
[11] Helle M and Katscher U (2019), "Electrical Properties Tomography based Functional Magnetic Resonance Imaging (EPT-fMRI)," *Proc. Ann. Meeting ISMRM 2019*, Abstract 3759.
[12] Schmidt R (2019), "Electrical conductivity as a potential mean to decouple the hemodynamic response from fMRI," *Proc. Ann. Meeting ISMRM 2019*, Abstract 3777.
[13] Jung K J, et al. (2023), "Investigation of electrical conductivity changes during functional activity of the brain via phase-based MR-EPT: Preliminary observation," *Proc. Ann. Meeting ISMRM 2023*, Abstract 0922.
[14] Jahng G H, et al. (2023), "High-frequency Conductivity Signal Changes Measured with Functional MREPT during Visual Stimulation," *Proc. Ann. Meeting ISMRM 2023*, Abstract 0923.
[15] Rae C D, et al. (2024), "Functional conductivity imaging: quantitative mapping of brain activity," *Proc. Ann. Meeting ISMRM 2024*, Abstract 1293.
[16] Luo J, et al. (2024), "Preliminary Whole-Brain Functional Electrical Properties Tomography using Gradient-Echo Echo-Planar Imaging," *Proc. Ann. Meeting ISMRM 2024*, Abstract 3681.
[17] Kiersnowski O C, et al. (2024), "Rapid high resolution integrated structural and functional susceptibility and conductivity mapping in the human brain," *Proc. Ann. Meeting ISMRM 2024*, Abstract 188.
[18] Poser B A, et al. (2006), "BOLD contrast sensitivity enhancement and artifact reduction with multiecho EPI: parallel-acquired inhomogeneity-desensitized fMRI," *Magn. Reson. Med.*, vol. 55, pp. 1227–1235, doi: 10.1002/mrm.20900.
[19] Karsa A, and Shmueli K (2021), "New approaches for simultaneous noise suppression and edge preservation to achieve accurate quantitative conductivity mapping in noisy images," *Proc. Ann. Meeting ISMRM 2021*, Abstract 3774.
[20] Arsenov O, et al., (2024), "Artifact reduction for rapid phase-based EPT in the human brain in vivo using a multi-echo 2D EPI sequence," *Proc. Ann. Meeting ISMRM 2024*, Abstract 3675.
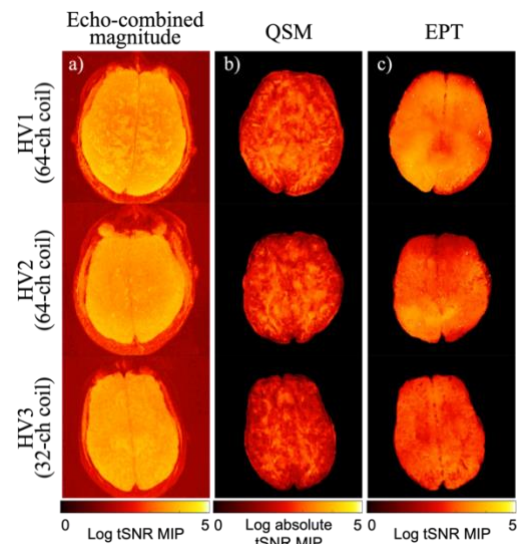
Radiomic Prediction of Parkinson's Disease Deep Brain Stimulation Surgery Motor and Non-motor Outcomes using Quantitative Susceptibility Mapping

Alexandra G. Roberts[1,2], Jinwei Zhang[3], Sema Akkus[4], Dominick Romano[2], Brian H. Kopell[4], Pascal Spincemaille[2], Yi Wang[1,2]

1 Electrical and Computer Engineering, Cornell University; 2 Department of Radiology, Weill Cornell Medicine; 3 Electrical and Computer Engineering, Johns Hopkins University; 4 Department of Neurosurgery, Mount Sinai Hospital

Summary: Radiomic features extracted from preoperative quantitative susceptibility maps predict both motor and non-motor numerical outcomes of deep brain stimulation surgery to treat Parkinson's disease.

Introduction: Deep brain stimulation (DBS) in the subthalamic nucleus (STN) is a treatment for motor symptoms in advanced Parkinson's disease (PD) [1]. Predicting DBS outcomes (particularly non-motor symptoms such as depression) to optimize patient selection is an important unmet clinical need. The current state of the art is preoperative levodopa challenge test (LCT) [2], which is subjective and has poor predictive power [3]. In addition to its role in presurgical planning [4] and disease progression [5], recent work demonstrates correlation between radiomic features of quantitative susceptibility maps (QSM) and DBS binary outcomes [6]. This work demonstrates that QSM radiomic features can predict both motor and nonmotor DBS outcomes as continuous variables using the least absolute shrinkage operator [7] (Lasso) combined with a novel label noise compensation approach.

Methods: This was a retrospective study approved by the Mount Sinai Hospital ethics committee and informed consent was obtained from all patients. Thirty-one patients undergoing bilateral STN-DBS were recruited based on: 1) diagnosis of idiopathic PD, 2) demonstrated response to levodopa, 3) motor complications impacting quality of life despite optimal medical management, 4) intact cognitive functioning, and 5) presence of medication-refractory tremors. Exclusion criteria were: 1) atypical parkinsonian disorders, 2) severe psychiatric illness, 3) dementia, 4) diffuse cerebral ischemic changes on brain MRI, and 5) systemic comorbidities. QSM was acquired from multi-echo gradient echo (mGRE) data and reconstructed with MEDI-L$_1$. [8] Presurgical metrics were UPDRS scores on and off medication according to LCT. Postsurgical metrics are UPDRS scores on stimulation and off medication. [9] The predicted variable y was UPDRS-III improvement defined as $y = \frac{u_{presurgical} - u_{postsurgical, on\ stimulation}}{u_{presurgical}}$. The substantia nigra (SN) and STN were segmented using a patient specific atlas and nonlinear registration with the Advanced Normalization Tools (ANTS) toolbox. Per ROI, 1595 features were extracted using a PyRadiomics [10][11]. Recursive feature selection was conducted and a Lasso model was fit using least angle regression (SciKit-Learn [12][13] to find the optimal weights $w^* = \text{argmin} \frac{1}{2N} \|y - X_\Phi w\|_2^2 + \lambda \|w\|_1$. Hyperparameters included splits k, selected features m and Lasso regularization parameter λ. The proposed pipeline is in Figure 1. Nested cross-validation was used to train and test the model. For the outer loop, given the sample sizes, a leave-one-out approach [14, 15] was used where the model was trained with $N - 1$ subjects and was tested on the excluded subject. This was repeated for each subject. For the inner loop, the splits k, recursively selected (step size 1000) features m, and regularization λ were chosen by minimizing the training error. Each feature of the $N - 1$ training samples was standardized and the training error for cross-validation stratified splits $k = \{2, 3, 4\}$ and regularization parameters λ were computed. The minority class ($y_{train} < 0.3$) [16] was resampled to allow stratified split $k_{max} = 5$. The dataset was augmented by factor $Q = 3$ and label noise multiplier $\eta = 2.326$ with label noise to compensate [17] for human rater variability in UPDRS-III [18]. The model was retrained over the entire dataset using m^* features, optimal split k^*, and optimal regularization parameter λ^*. The predictive power of LCT and Lasso with noise compensation was evaluated using linear regression (correlation r, slope m, intercept b, significance p). This process also used in the 25 patients with complete scores to predict nonmotor symptoms as measured by the Beck Depression Inventory [19] after Tukey outlier rejection [20] for sample sizes smaller than 30 ($N_{outliers} = 6$). Noise compensation used parameters $Q = 1, \eta = 1.5$ to retrain the pipeline on $N_{samples} = 19$.

Results: Radiomic predictions of motor outcomes are shown in Figure 2a ($r = 0.73, p < 0.01$), in addition to radiomic correct binary classification of all cases as success (improvement greater than or equal to 0.3) or failure, while LCT failed on both numerical prediction ($r = -0.11, p = 0.57$) and binary classification. Figure 2b a similar trend for nonmotor outcomes $r = 0.62, p < 0.01$ for the radiomic model while LCT failed to predict outcomes ($r = 0.25, p > 0.01$). Features with predictive value are shown in Figure 3. Note that motor predictions rely on age, disease duration and high-frequency content features consistent with previous findings [21].

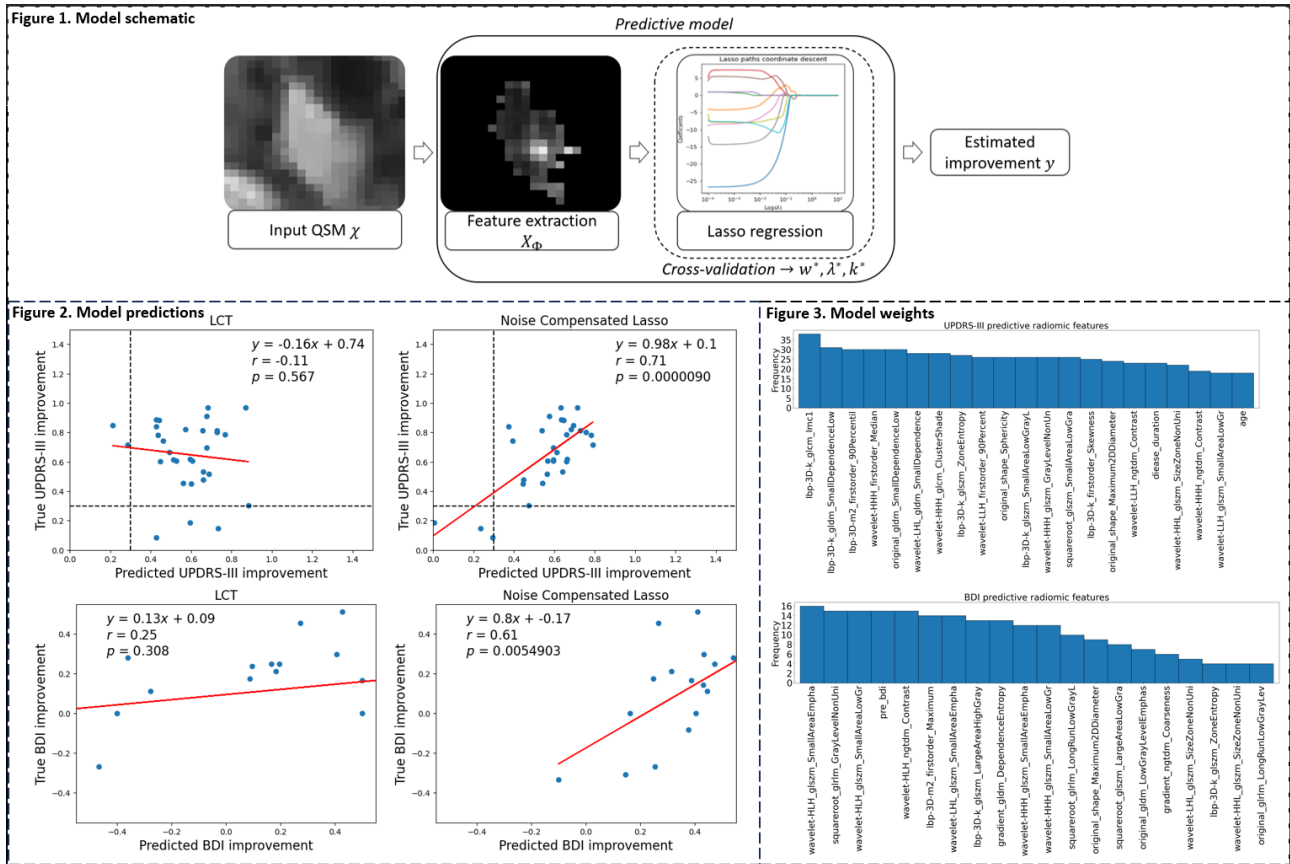**Discussion and Conclusions:** Radiomic features on QSM improve predictions of both motor and nonmotor outcomes of deep brain stimulation surgery.

Figures: Figure 1. Model schematic demonstrating QSM input, feature extraction, training and prediction for each model.
Figure 2. Predicted improvement for UPDRS-III and BDI metrics after DBS surgery.
Figure 3. Predictive features grouped by frequency in N models.

Figure 1. Model schematic

Predictive model

Input QSM χ → Feature extraction X_Φ → Lasso regression

Cross-validation → w^*, λ^*, k^*

Estimated improvement y

Figure 2. Model predictions

LCT
$y = -0.16x + 0.74$
$r = -0.11$
$p = 0.567$

Noise Compensated Lasso
$y = 0.98x + 0.1$
$r = 0.71$
$p = 0.0000090$

LCT
$y = 0.13x + 0.09$
$r = 0.25$
$p = 0.308$

Noise Compensated Lasso
$y = 0.8x + -0.17$
$r = 0.61$
$p = 0.0054903$

Figure 3. Model weights

References:

[1]   S. J. Groiss, L. Wojtecki, M. Südmeyer, and A. Schnitzler, "Review: Deep brain stimulation in Parkinson's disease," *Therapeutic Advances in Neurological Disorders,* vol. 2, no. 6, pp. 379-391, 2009, doi: 10.1177/1756285609339382.

[2]   G. Saranza and A. E. Lang, "Levodopa challenge test: indications, protocol, and guide," *Journal of Neurology,* 2020, doi: 10.1007/s00415-020-09810-7.

[3]   L. Lachenmayer *et al.*, "Subthalamic and pallidal deep brain stimulation for Parkinson's disease-meta-analysis of outcomes," *npj Parkinsons Disease,* vol. 7, 09/06 2021, doi: 10.1038/s41531-021-00223-5.

[4]   A. V. Dimov, A. Gupta, B. H. Kopell, and Y. Wang, "High-resolution QSM for functional and structural depiction of subthalamic nuclei in DBS presurgical mapping," *Journal of Neurosurgery,* vol. 131, no. 2, pp. 360-367, 2019, doi: 10.3171/2018.3.jns172145.

[5]   X. Guan, M. Lancione, S. Ayton, P. Dusek, C. Langkammer, and M. Zhang, "Neuroimaging of Parkinson's disease by quantitative susceptibility mapping," *NeuroImage,* vol. 289, p. 120547, 2024/04/01/ 2024, doi: https://doi.org/10.1016/j.neuroimage.2024.120547.

[6]   Y. Liu *et al.*, "Predicting Motor Outcome of Subthalamic Nucleus Deep Brain Stimulation for Parkinson's Disease Using Quantitative Susceptibility Mapping and Radiomics: A Pilot Study," (in eng), *Front Neurosci,* vol. 15, p. 731109, 2021, doi: 10.3389/fnins.2021.731109.

[7]   R. Tibshirani, "Regression Shrinkage and Selection Via the Lasso," *Journal of the Royal Statistical Society: Series B (Methodological),* vol. 58, no. 1, pp. 267-288, 1996, doi: https://doi.org/10.1111/j.2517-6161.1996.tb02080.x.

[8]   L. De Rochefort *et al.*, "Quantitative susceptibility map reconstruction from MR phase data using bayesian regularization: Validation and application to brain imaging," *Magnetic Resonance in Medicine,* vol. 63, no. 1, pp. 194-206, 2010, doi: 10.1002/mrm.22187.

[9]   Z. Lin *et al.*, "Revisiting the L-Dopa Response as a Predictor of Motor Outcomes After Deep Brain Stimulation in Parkinson's Disease," *Frontiers in Human Neuroscience,* vol. 15, 2021, doi: 10.3389/fnhum.2021.604433.

[10]   J. J. M. Van Griethuysen *et al.*, "Computational Radiomics System to Decode the Radiographic Phenotype," *Cancer Research,* vol. 77, no. 21, pp. e104-e107, 2017, doi: 10.1158/0008-5472.can-17-0339.

[11]   A. G. Roberts *et al.*, "QRadAR: An Open-source Toolbox for Quantitative Magnetic Resonance Radiomics Analysis and Reproducibility," presented at the International Society of Magnetic Resonance in Medicine (Submitted), Singapore, 2023.

[12]   F. Pedregosa *et al.*, "Scikit-learn: Machine Learning in Python," *arXiv pre-print server,* 2018-06-05 2018

[13]   B. Efron, T. Hastie, I. Johnstone, and R. Tibshirani, "Least angle regression," *The Annals of Statistics,* vol. 32, no. 2, pp. 407-499, 2004

[14]   Z. Cui, M. Su, L. Li, H. Shu, and G. Gong, "Individualized Prediction of Reading Comprehension Ability Using Gray Matter Volume," (in eng), *Cereb Cortex,* vol. 28, no. 5, pp. 1656-1672, May 1 2018, doi: 10.1093/cercor/bhx061.

[15]   X. Li *et al.*, "Predicting the Post-therapy Severity Level (UPDRS-III) of Patients With Parkinson's Disease After Drug Therapy by Using the Dynamic Connectivity Efficiency of fMRI," *Frontiers in Neurology,* vol. 10, 2019, doi: 10.3389/fneur.2019.00668.

[16]   V. Torres *et al.*, "Image-guided programming deep brain stimulation improves clinical outcomes in patients with Parkinson's disease," *npj Parkinson's Disease,* vol. 10, no. 1, 2024, doi: 10.1038/s41531-024-00639-9.

[17]   A. G. Roberts *et al.*, "Radiomic Prediction of Parkinson's Disease Deep Brain Stimulation Surgery Outcomes using Quantitative Susceptibility Mapping and Label Noise Compensation," presented at Neuromodulation, New York City, 2024.

[18]   M. Richards, K. Marder, L. Cote, and R. Mayeux, "Interrater reliability of the unified Parkinson's disease rating scale motor examination," *Movement Disorders,* vol. 9, no. 1, pp. 89-91, 1994, doi: 10.1002/mds.870090114.

[19]   A. T. e. a. Beck, "An Inventory for Measuring Depression," *Archives of General Psychiatry,* vol. 4, no. 6, pp. 561-571, 1961, doi: 10.1001/archpsyc.1961.01710120031004.

[20]   J. Tukey, *Exploratory Data Analysis*. Springer New York, 1977.

[21]   W. Zhao *et al.*, "Relationship Between Iron Distribution in Deep Gray Matter Nuclei Measured by Quantitative Susceptibility Mapping and Motor Outcome After Deep Brain Stimulation in Patients With Parkinson's Disease," *Journal of Magnetic Resonance Imaging,* vol. 58, no. 2, pp. 581-590, 2023, doi: 10.1002/jmri.28574.

Investigating the correspondence between the paramagnetic component of brain magnetic susceptibility and iron distribution

Fábio Seiji Otsuka[3], José Henrique Monteiro de Azevedo[1,2], André Avanzine[1], Roberta Diehl Rodriguez[3,4], Vanessa Cristina de Oliveira Souza[5], Fernando Barbosa Jr.[5], Maria Concepción Garcia Otaduy[3], Carlos Ernesto Garrido Salmon[1,2,6]

[1]*InBrain, Department of Physics, FFCLRP-USP, Ribeirão Preto, Brazil;*
[2]*Graduate Program Neurology, FMRP-USP, Ribeirão Preto, Brazil;*
[3]*LIM 44, InRad, FMUSP, São Paulo, Brazil;*
[4]*Behavioral and Cognitive Neurology Group, Department of Neurology, FMUSP, São Paulo, Brazil;*
[5]*Department of Clinical Analyses, Toxicology and Food Sciences, FCFRP, Ribeirão Preto, Brazil,*
[6]*Department of Medical Imaging, Hematology and Clinical Oncology , FMRP-USP, Ribeirão Preto, SP, Brazil*

Summary: In this study, we investigated the paramagnetic components (PCS) of the magnetic susceptibility (QSM) of brain tissue and its relationship to total iron concentration as measured by mass spectrometry. Compared to QSM, the PCS revealed a stronger correlation to iron, including structures where QSM failed to show a correlation with iron. Our results reinforce the idea that PCS reflects better the iron distribution in the brain.

Introduction: The sensitivity of Quantitative Susceptibility Mapping (QSM) to iron distribution in the brain has been thoroughly investigated in postmortem studies using many different iron quantification techniques [1], where strong correlation was found on iron-rich structures. Recently, the development of robust techniques for sub voxel source separation of diamagnetic and paramagnetic components [2-3] has opened a venue for further investigation of brain's magnetic properties. However, quantitative validation of these techniques using ground truth references has not been performed yet. In this study, we evaluated the relationship between the paramagnetic components from the DECOMPOSE-QSM [2] and compared the results against conventional QSM.

Methods: The research ethics committee of the Medical School of the University of São Paulo (approval number 14407) approved this study. For this study, 12 *postmortem* subjects were included (mean age of 66.53 ± 15.91 years old). Subjects underwent MRI with *postmortem* interval between 11h and 24h. A 3D-GRE multiecho sequence was used with the following parameters: flip angle of 10º, 5 echoes (1st 3cho 5ms; echo interval 4ms), 25ms repetition time, resolution of $0.5x0.5x1.0$ mm^3 and Field of View of $203x224x128$ mm^3.

For each subject, 8 regions of interest (ROI) from the Gray Matter (GM) were manually segmented by visual inspection comparing the images to photographs taken during sample extraction. The following structures were included: Caudate Nucleus (CN); Pre-Central Cortex (CPR); Entorhinal Cortex (ENT); Globus Pallidus (GP); Hippocampus (HIP); Putamen (PUT); Red Nucleus (RN) and Substantia Nigra (SN). Total iron concentration was measured using Inductively Coupled Plasm Mass Spectrometry (ICP-MS).

QSM maps were processed using the following pipeline: nonlinear fitting of phase images; phase unwrapping (Laplacian algorithm); background field filter (V-SHARP) and dipole inversion (STAR-QSM). Paramagnetic (PCS) and diamagnetic (DCS) components maps were generated using the DECOMPOSE-QSM algorithm, preprocessing steps were the same as for conventional QSM. For the analysis, mean values of QSM and PCS maps at each ROI was compared against iron concentration. A correlation test (correcting for multiple comparison) and linear regression was performed.

Results: Figure 1 shows the QSM, PCS and DCS from two different subjects. Figure 2 shows the linear plot between QSM and PCS against iron concentration by including all ROIs (A and B) and individually per ROI (C and D).
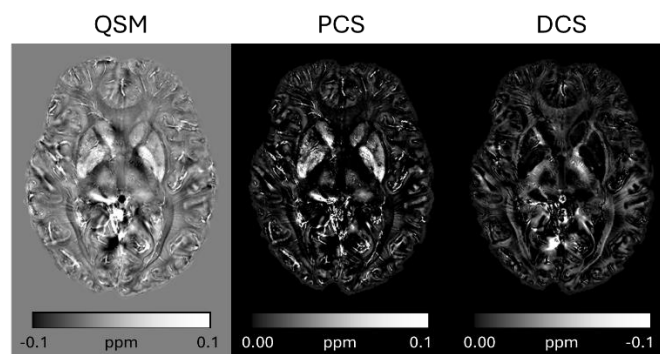
Figures

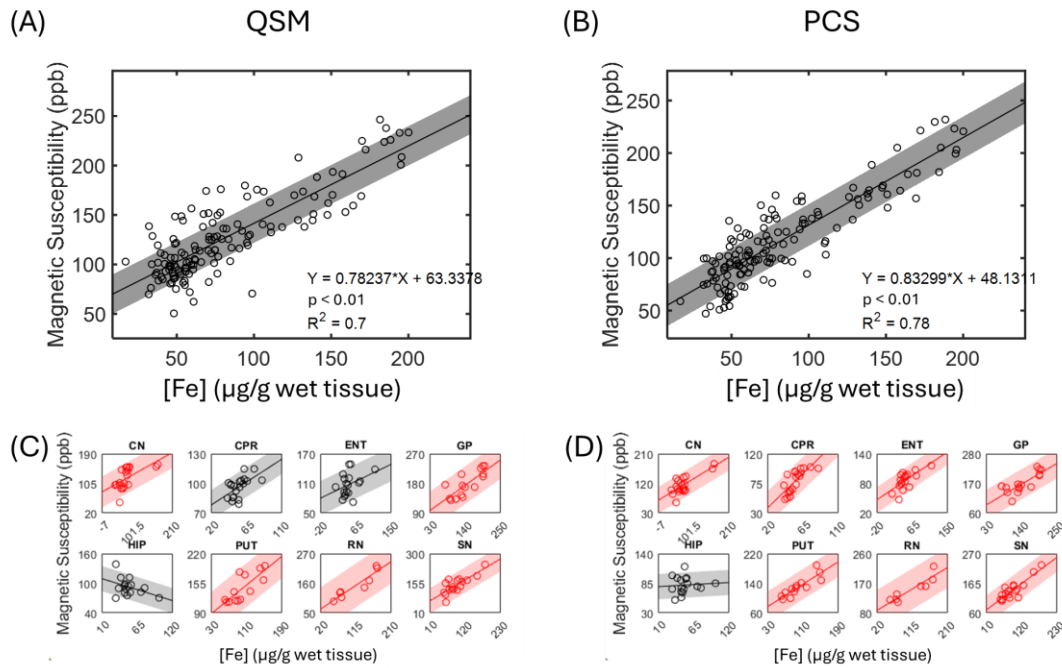Figure 1: The QSM, PCS and DCS maps processed for one postmortem subject.

Figure 2: Linear plot, correlation and linear regression between QSM (left, A and C), PCS (right, B and D) versus iron concentration. A and B show the overall relationship between QSM/PCS and iron. C and D show the relationship per ROI, whereby red plots indicate a statistically significant correlation

Discussion and Conclusions: The results show that the PCS showed an increase in the correlation to iron, when compared to QSM. The linear regression of the overall relationship between PCS and iron yielded a slope slightly higher than conventional QSM (0.83 compared to 0.78), however it is still lower than theoretical prediction for the ferritin's contribution to susceptibility, estimated to be around 1.25 at the temperature range of postmortem subjects. Additionally, more correlations that were not observed on conventional QSM (the CPR and ENT structures) were observed on PCS. These results suggest increased sensitivity to iron when considering only the paramagnetic component. The only exception was the HIP structure that did not show any correlation even for the PCS maps.

References:
[1] Langkammer C et al. "Quantitative susceptibility mapping (QSM) as means to measure brain iron? A post mortem validation study," NeuroImage, vol. 62 (2012), pp. 1593–1599.
[2] Chen J et al. "Decompose quantitative susceptibility mapping (QSM) to sub-voxel diamagnetic and paramagnetic components based on gradient-echo MRI data." NeuroImage vol. 242 (2021): 118477.
[3] Li Z et al. "APART-QSM: An improved sub-voxel quantitative susceptibility mapping for susceptibility source separation using an iterative data fitting method." NeuroImage vol. 274 (2023): 120148.

Comparison of χ-separation results for different methods for obtaining R2'

Chungseok Oh[1], Minjun Kim[1], Jongho Lee[1]

[1]*Laboratory for Imaging Science and Technology, Seoul National University, Seoul, Republic of Korea*

Summary: In this study, we compared χ-separation results according to different methods for obtaining R2'.

Introduction: The recently developed χ-separation method provides the distribution of susceptibility sources within the brain, which contains rich information about brain structures [1]. In χ-separation, paramagnetic and diamagnetic susceptibility maps can be reconstructed from a phase map and an R2' (= $R2^*$ - R2) map. However, obtaining an R2 map is challenging due to SAR limits or long scan time of multi-echo spin echo (MESE) scans (e.g. a MESE scan with a resolution of $1\times1\times2$ mm^3 takes 13.5 minutes [2]). Accordingly, several studies have tried to acquire low quality R2 maps within short scan time [3], or estimate R2' without acquiring R2 maps [4,5]. In this study, we compared χ-separation results for different methods for obtaining R2' maps, either with acquiring low quality R2 maps or without acquiring R2 maps. The comparison results may provide guidelines for acquisition or processing for R2 (or R2') in χ-separation.

Methods: In this study, we compared a total of five different methods of obtaining R2' maps, where two methods utilize low quality R2 maps, and three methods estimate R2' maps without using R2 maps. The first two methods are using R2 maps acquired from low-resolution MESE data or acquired from turbo spin echo (TSE) data. These two methods were investigated using retrospectively generated data from the fully sampled MESE data. The other three methods are using nominal value for R2, using linear approximation for obtaining R2' from $R2^*$, and using neural network to reconstruct R2' from $R2^*$.

For the reference data, we utilized four subjects from Chi-sepnet dataset [2] which contains multi-echo gradient-recalled echo (mGRE) data and MESE data. The mGRE data was acquired with the following scan parameters: resolution=$1\times1\times1$ mm^3, TR=38 ms, TE$_1$/ΔTE/TE$_6$=7.7/5.0/32.8 ms, matrix size=$256\times224\times176$. The MESE data was acquired with following scan parameters: in-plane resolution=1×1 mm^2, slice thickness=2 mm, TR=7800 ms, TE$_1$/ΔTE/TE$_6$=15/15/90 ms, matrix size=256×204, number of slices=76. From mGRE data and MESE data, paramagnetic (χ_{para}) and diamagnetic (χ_{dia}) susceptibility maps were reconstructed using χ-separation toolbox [6] with following processing methods: ROMEO for phase unwrapping, V-SHARP for background field removal, ARLO for $R2^*$ fitting, dictionary-based fitting for R2 fitting, and *Chi-separation (MEDI)* reconstruction for susceptibility imaging [1]. The reconstructed susceptibility maps were regarded as reference susceptibility maps for comparison.

To investigate the case of using low-resolution MESE data, a low-resolution MESE data with 1×3 mm^2 of in-plane resolution was generated from original MESE data by truncation on k-space data along the phase encoding direction (expected scan time = 4.5 min). After that, susceptibility maps were reconstructed using the same processing methods as described above.

For the investigation of the case of using TSE data, a dual echo TSE data was generated from MESE data with a readout scheme of TE$_1$/TE$_2$=15/90 ms and ETL=6 (expected scan time = 4.5 min). Because the dual echo TSE data have only two echoes, B1 was set to 1 in dictionary-based fitting for R2 mapping. Susceptibility maps were reconstructed using the same processing methods as above.

To investigate the case of using nominal value, R2 was set to 13 Hz considering typical T2 values in the white matter and gray matter are 60-100 ms in 3T [7].

For the case of using linear approximation, R2' was estimated using a linear approximation model between $R2^*$ and R2' ($R2^*= \alpha R2'$) as suggested in the previous paper [5]. By linear regression of R2' and R2* values in 8 ROIs in a representative subject, the coefficient α was estimated as 2.7646. This estimated coefficient value was applied in all subjects.

To explore the case of using neural network for R2' reconstruction, the R2Pnet, which reconstructs R2' maps from $R2^*$ maps, was utilized. This network was trained using pairs of an R2' map and an $R2^*$ map from 6 subjects.

For quantitative evaluation of susceptibility maps from each method, RMSE, SSIM, and HFEN were measured with respect to reference susceptibility maps. Also, we performed linear regression analyses in 24 ROI regions (11 regions for χ_{para} and 13 regions for χ_{dia}) from four subjects between reference susceptibility maps and other susceptibility maps.

Results: When using low resolution MESE data, RMSE and SSIM, and linear regression analysis results showed the best metric compared to the other methods. When using TSE data, it showed best HFEN metrics, however, the slope in linear

regression analysis results in χ_{dia} was 0.84, implying that underestimation in χ_{dia} values in ROI regions. When using nominal value or linear approximation, it showed relatively large reconstruction errors compared to other methods. When an R2 map is not utilized, using a neural network for obtaining R2' maps showed the best metric in RMSE, SSIM, and HFEN compared to other two methods.

Discussion and Conclusions: In this study, we compared five different methods of acquiring R2' maps in short scan time or no scan for R2 mapping. Each of the five methods has pros and cons. Using the low-resolution MESE data can be an effective method to reduce scan time. Using the TSE data can yield a good quality of susceptibility maps, however, susceptibility values can be underestimated especially in χ_{dia}. When an R2 map is unavailable, using neural network based R2' reconstruction method yielded best results among three methods. However, this study has several limitations. First, our investigation on the two cases of using low quality R2 maps were performed on retrospectively generated images. Second, this study investigated a limited case of each method (e.g. low-resolution MESE data were downsampled by a factor of 3). In further study, a more detailed investigation for each method needs to be considered.

		Utilizing low quality R2 maps		Not using R2 maps		
	Original	R2 from low resolution MESE	R2 from TSE	Nominal value	Linear approximation	Neural network
(a) χ_{para}						
Quantitative metrics of χ_{para} RMSE (↓)		**11.4 ± 0.2**	12.6 ± 0.5	24.0 ± 2.0	43.0 ± 2.1	17.3 ± 0.7
SSIM (↑)		**0.9957 ± 0.0008**	0.9837 ± 0.0026	0.9659 ± 0.0082	0.9223 ± 0.0144	0.9860 ± 0.0035
HFEN (↓)		11.8 ± 0.5	**8.8 ± 0.4**	27.4 ± 2.8	47.6 ± 2.9	20.7 ± 1.5
Linear regression analysis on χ_{para} Slope		1.00	0.96	1.15	0.95	1.06
R^2		1.00	1.00	0.99	0.99	1.00
(b) χ_{dia}						
Quantitative metrics of χ_{dia} RMSE (↓)		**12.8 ± 0.3**	14.9 ± 0.6	28.4 ± 2.2	52.6 ± 2.8	20.1 ± 1.4
SSIM (↑)		**0.9951 ± 0.0014**	0.9833 ± 0.0027	0.9620 ± 0.0119	0.9015 ± 0.0238	0.9836 ± 0.0051
HFEN (↓)		14.2 ± 0.7	**10.6 ± 0.5**	34.1 ± 3.9	61.1 ± 3.3	25.9 ± 2.8
Linear regression analysis on χ_{dia} Slope		0.98	0.85	1.06	1.03	1.04
R^2		1.00	0.99	0.80	0.90	0.96

Figures –The representative slices, quantitative metrics, and linear regression analysis results of (a) χ_{para} and (b) χ_{dia} maps.

References:
[1] Shin, Hyeong-Geol, et al. "χ-separation: Magnetic susceptibility source separation toward iron and myelin mapping in the brain." Neuroimage 240 (2021): 118371.
[2] Kim, Minjun, et al. "Chi-sepnet: susceptibility source separation using deep neural networks." Joint Annual Meeting ISMRM-ESMRMB & ISMRT 31st Annual Meeting. Vol. 2464. 2022.
[3] Park, Beomsoo, et al. "Assessing the Reproducibility of χ-separation: Comparative Analysis of Two Modeling Approaches with Quantitative Susceptibility Mapping." Annual Meeting ISMRM & ISMRT 33rd Annual Meeting. 2024.
[4] Kim, Jiye, et al. "A feasibility study of susceptibility source separation via chi-separation in amyotrophic lateral sclerosis patients at 7T." Annual Meeting ISMRM & ISMRT 32nd Annual Meeting. 2023.
[5] Dimov, Alexey V., et al. "Susceptibility source separation from gradient echo data using magnitude decay modeling." Journal of Neuroimaging 32.5 (2022): 852-859.
[6] https://github.com/SNU-LIST/chi-separation
[7] Stanisz, Greg J., et al. "T1, T2 relaxation and magnetization transfer in tissue at 3T." Magnetic Resonance in Medicine: An Official Journal of the International Society for Magnetic Resonance in Medicine 54.3 (2005): 507-512.

Susceptibility source separation algorithms in postmortem human brain: A comparison study

José Henrique Monteiro de Azevedo[1,2], Fábio Seiji Otsuka[3], André Avanzine[1], Maria Concepción Garcia Otaduy[3], Carlos Ernesto Garrido Salmon[1,2,4]

[1]*InBrain, Department of Physics, FFCLRP-USP, Ribeirão Preto, Brazil;*
[2]*Graduate Program Neurology, FMRP-USP, Ribeirão Preto, Brazil;*
[3]*LIM 44, InRad, FMUSP, São Paulo, Brazil;*
[4]*Department of Medical Imaging, Hematology and Clinical Oncology, FMRP-USP, Ribeirão Preto, SP, Brazil;*

Summary: By comparing two susceptibility source separation techniques on human *postmortem* brain tissue, it was found a good agreement between methods for the paramagnetic component, whereas the diamagnetic component showed disagreements on some white matter structures. Weak correlations were found between both diamagnetic maps by using the diffusion fractional anisotropy values as a measure of tissue anisotropy and myelination.

Introduction: Iron is the primary source of paramagnetic susceptibility in the brain, while myelin is the main source of diamagnetism [1]. Myelin is predominantly found in white matter, but also in gray matter, especially, in basal ganglia structures [2]. Conventional Quantitative Susceptibility Mapping (QSM) cannot separate the opposing effects of iron and myelin, recent methods such as APART-QSM and DECOMPOSE have been developed to address this issue [3, 4, 5]. These methods can provide a more specific analysis of iron and myelin's roles in neurodegenerative diseases considering specific Regions of Interest (ROI). Fractional anisotropy (FA) values can be related to myelin content [6]. This study compares ROI to ROI the APART-QSM and DECOMPOSE methods for separating susceptibility in *postmortem* data.

Methods: The research ethics committee of the Medical School of the University of São Paulo (approval number 14407) approved this study. MRI scans were conducted on 45 *postmortem* subjects aged 31 to 91 using a 7T MR scanner. The APART-QSM[3] and DECOMPOSE[4] methods derived paramagnetic and diamagnetic susceptibility values across 9 deep gray and 7 white matter regions (Figure 1). ROI segmentation was done automatically using *first* FSL and a specific atlas (https://github.com/SNU-LIST/chi-separation-atlas). All the maps, including FA, were linearly transformed from native to 3D T1-weighted image space using ANTS software. Pearson correlation was used to analyze the correlations between methods.
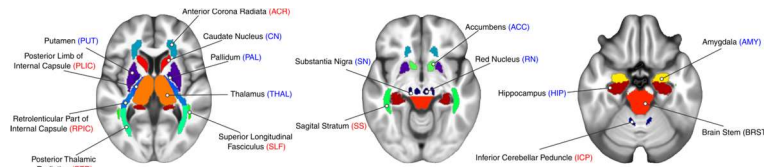

Figure 1 Regions of interest in white (WM) (red) and grey matter (GM) (blue)
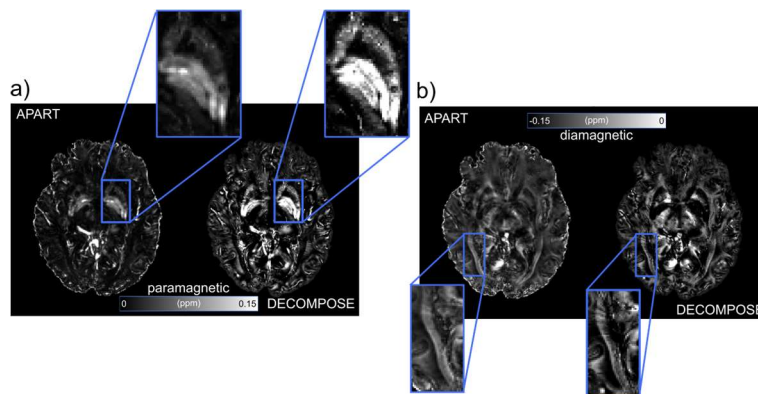
Results:

Figure 2 Examples of paramagnetic (a) and diamagnetic (b) susceptibility maps obtained with both methods.

Paramagnetic susceptibility values show a good correlation between the methods (R^2=0.78) (Fig. 3 b). All structures show a Pearson correlation coefficient above 0.6 (Fig. 3 a). On the other hand, the diamagnetic components were less correlated (R^2=0.44), as in some structures of white matter regions we did not find significant correlations (Fig. 3a). The linear

regression between methods yielded angular coefficients of 1.06 and 1.27 for the paramagnetic and diamagnetic components, respectively (Figs. 2.b-c).

The association of diamagnetic values and fractional anisotropy in all studied regions did not show significant correlations for both APART (R^2=0.04) or DECOMPOSE (R^2=0.05). However, the individual ROI analysis show some significant associations (Fig. 4). For APART-QSM 7/18 regions were significant associated, while for DECOMPOSE, only 4/18 regions.
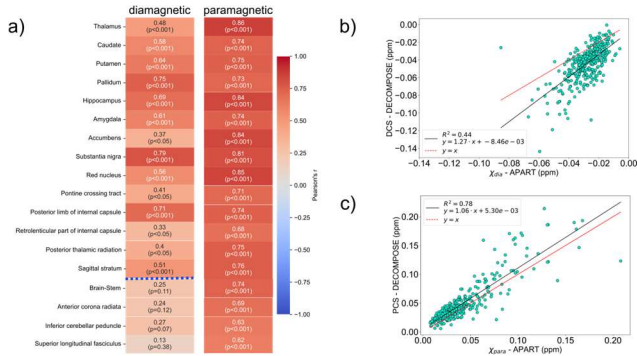

Figure 3 Correlation between susceptibility values obtained with APART-QSM and DECOMPOSE (a) Table with Pearson's correlations for each ROI comparing both separation methods (b) All susceptibility values for paramagnetic (b) and diamagnetic components (c)
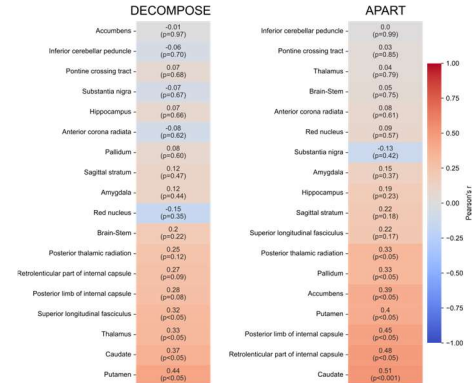
Figure 4 Correlation analysis for each ROI between diamagnetic susceptibility, obtained with APART-QSM or DECOMPOSE, and fractional anisotropy values.

Discussion and Conclusions: Both methods showed an overall consistent correlation between results, with the paramagnetic components displaying a better correlation compared to the diamagnetic components. By evaluating each ROI separately, it was found that the diamagnetic components displayed no correlation on some WM structures.

The results suggest that the paramagnetic components are less affected by the sub-voxel modeling of the signal. The diamagnetic component, on the other hand, is less consistent and indicates a strong sensitivity to the method used. Furthermore, the effect of anisotropy and orientation may have also influenced the results since these effects may interfere with the initial consideration of the linear relationship between R2* or R2' and susceptibility used by both methods.

By comparing the diamagnetic components to the FA maps, a weak negative correlation was observed for both methods; however, when evaluating per ROI, some structures showed a significant correlation. While diffusion and susceptibility anisotropy originate from different biophysical mechanisms, there are some similarities between these quantities throughout the brain. However, unlike diffusion, susceptibility values may change from negative to positive depending on the fibers' relative orientation, which could also have influenced the results from the FA comparison.

References:
[1] Schweser, Ferdinand et al. "Foundations of MRI phase imaging and processing for Quantitative Susceptibility Mapping (QSM)." Zeitschrift fur medizinische Physik vol. 26,1 (2016): 6-34.
[2] Lao, Guoyan et al. "Sub-voxel quantitative susceptibility mapping for assessing whole-brain magnetic susceptibility from ages 4 to 80." Human brain mapping vol. 44,17 (2023): 5953-5971.
[3] Li, Zhenghao et al. "APART-QSM: An improved sub-voxel quantitative susceptibility mapping for susceptibility source separation using an iterative data fitting method." NeuroImage vol. 274 (2023): 120148.
[4] Chen, Jingjia et al. "Decompose quantitative susceptibility mapping (QSM) to sub-voxel diamagnetic and paramagnetic components based on gradient-echo MRI data." NeuroImage vol. 242 (2021): 118477.
[5] Shin, Hyeong-Geol et al. "χ-separation: Magnetic susceptibility source separation toward iron and myelin mapping in the brain." NeuroImage vol. 240 (2021): 118371.
[6] Lazari, Alberto, and Ilona Lipp. "Can MRI measure myelin? Systematic review, qualitative assessment, and meta-analysis of studies validating microstructural imaging with myelin histology." NeuroImage vol. 230 (2021): 117744.

MRI quantification of liver fibrosis using diamagnetic susceptibility: An ex-vivo feasibility study.

Chao Li[1,2], Jinwei Zhang[1,3], Alexey V. Dimov[1], Anne K. Koehne de González[4], Gary M. Brittenham[5], Martin R. Prince[1], Dominick Romano[1,3], Jiahao Li[1,3], Pascal Spincemaille[1], Thanh D. Nguyen[1], and Yi Wang[1]

1. Radiology, Weill Cornell Medicine, New York, NY, United States
2. Applied and Engineering Physics, Cornell University, Ithaca, NY, United States
3. Meinig School of Biomedical Engineering, Cornell University, Ithaca, NY, United States
4. Department of Pathology, Columbia University , New York, NY, United States
5. Department of Pediatrics, Columbia University, New York, NY, United States

Summary: This work develops a non-invasive method to evaluate liver fibrosis using MRI. Diamagnetic sources are separated from paramagnetic sources using a biophysical model and multi echo gradient echo data. The value of the diamagnetic sources can be used to quantify the amount of accumulation of collagen due to liver fibrosis. Significant differences in liver negative susceptibility were observed between non-fibrotic/mild-stage fibrosis (F0, F1), medium stage fibrosis (F2, F3), and cirrhosis (F4).

Introduction: Liver fibrosis is a pathological condition characterized by the excessive accumulation of extracellular matrix proteins, particularly collagen, as a response to chronic liver injury (1). The extracellular matrix proteins and collagens are diamagnetic. Therefore, the amount of diamagnetic susceptibility sources may be used to evaluate the stage of liver fibrosis. However, the coexistence of paramagnetic contents such as iron in some patients with liver fibrosis makes measuring the diamagnetic content difficult. Recently, a biophysical model was proposed that separates the paramagnetic and diamagnetic sources in MRI by utilizing QSM and additional R_2' information (2-3). In this work, we demonstrate that the diamagnetic susceptibility can be useful to quantify the fibrotic tissues in the liver. In this work, we compare different MRI parameters including R2*, R2, R2', QSM, PDFF and χ^- (negative susceptibility sources) in their ability to differentiate non-fibrotic/mild-stage fibrosis (F0, F1), medium stage fibrosis (F2, F3), and cirrhosis (F4).

Theory: The relaxation of the collagen fibers and iron granules, which manifest as micro-cylinders and micro-spheres respectively, can be modeled with the static dephasing model (3). R2'(r) is given by:

$$R_2'(r) = \alpha R_2^*(r) = D_r^+|\chi^+(r)| + D_r^-|\chi^-(r)| \quad (1)$$

Where $\chi^+(r)$ and $\chi^-(r)$ are the positive and negative susceptibility sources respectively. The QSM, $\chi(r)$ can be written as

$$\chi(r) = |\chi^+(r)| - |\chi^-(r)| \quad (2)$$

Where $D_r^+ = D_r^-$ are the relaxometric constants of the positive and negative susceptibility sources respectively. The reconstruction of $\chi^+(r)$ and $\chi^-(r)$ are detailed in (3).

Method: Liver explant samples from 20 patients were collected, scanned, and analyzed (Table 1). The liver samples also underwent histopathological analysis using hematoxylin and eosin (H&E), Masson's trichrome and Prussian Blue stains for histology, fibrosis, and iron evaluation, respectively. MRI imaging parameters were (1) 3D mGRE at 3T (GE Healthcare, Waukesha, WI, USA), 8 echoes, flip angle = 15, TE1 = 2.6 ms, ΔTE = 2.7 ms, TR = 24.43 ms, reconstructed voxel size = 0.88 $\times$ 0.88 $\times$ 1 mm3, bandwidth = 390 Hz/pixel, reconstructed matrix = 256 $\times$ 256 x 74-128. From mGRE, water-fat separation (4-5) was performed, and QSM (6-9) and R2* (10) were calculated. Masks are drawn on the scanned liver samples, and average R2*, R2, R2', χ, PDFF and $|\chi^-|$ were calculated within the masks.

Results: Figure 1 shows a representative example of QSM, $|\chi^+|$ and $|\chi^-|$ as well as hematoxylin and eosin (H&E), Prussian Blue and Masson's trichrome stains in the same liver sample. Figure 3 compares R2*, R2, R2', χ, PDFF and $|\chi^-|$ for the samples without fibrosis or with mild fibrosis (F0-1), samples with medium stage fibrosis (F2-3) and samples with cirrhosis (F4). Only average absolute negative susceptibility and R2* are significantly different between F0-1 and F2-3. For negative susceptibility, p = 0.017677 between F0-1 and F2-3. For R2*, p = 0.04798 between 0.04798 and p = 0.020513 between 0.020513.

Discussion: This study shows that the susceptibility values of diamagnetic can be used to quantify the fibrotic tissues in liver, which may allow a non-invasive evaluation of fibrosis stage in patients.

	All (n = 20)	F0-1 (n = 5)	F2-3 (n = 7)	F4 (n = 8)
Age (y)	43 (0-80)	13 (0-80)	45 (24-61)	57 (49-66)
Sex				
-Male	13	4	4	5
-Female	7	1	3	3
Iron deposition				
-None	10	4	5	1
-Grade 0	1	0	1*	0
-Grade 0-1	1	0	1	0
-Grade 1	1	1	0	2
-Grade 2	1	0	0	1
-Grade 2-3	3	0	0	3
-Grade 3	1	0	0	1
Steatosis				
-None	9	2	6	1
-Stage 0 (<5%)	5	1	0	4
-Stage 1 (5-33%)	4	1	1	2
-Stage 2 (34-66%)	1	1	0	0
-Stage 3 (>66%)	1	0	0	1

*In one sample where grade-0 iron was found in the hepatocytes, iron was observed in the Kupffer cells.
Figure 1 Demographic and histopathologic characteristics of the liver sample
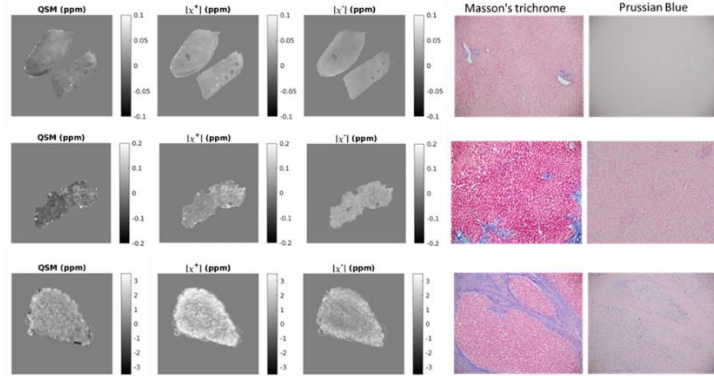

Figure 2: A representative example: QSM, $|\chi^+|$ and $|\chi^-|$ are shown in the first row. Hematoxylin and eosin (H&E), Prussian Blue and Masson's trichrome stains for this example are shown in the second row
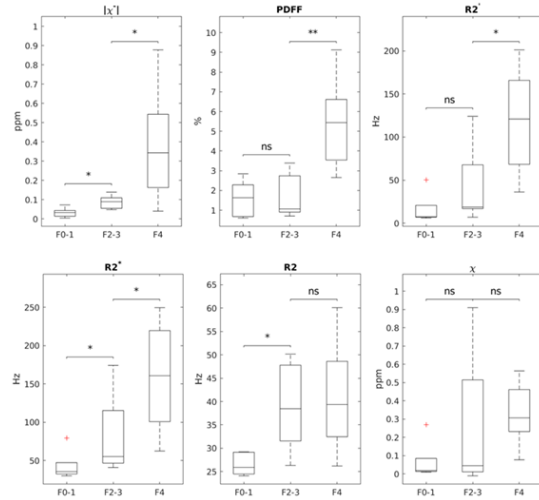

Figure 3: Comparison of $|\chi^-|$, R2*, χ (QSM), PDFF, R2' and R2 in liver samples with no or mild fibrosis (F0-1), medium stage fibrosis (F2-3) and cirrhosis (F4). P-values (Mann–Whitney U test) are shown as well.

Reference:

(1) Bataller R, Brenner DA. Liver fibrosis. J Clin Invest. 2005;115(4):1100-. doi: Doi 10.1172/Jci200524282c1. PubMed PMID: WOS:000228145700044.

(2) Shin HG, Lee J, Yun YH, Yoo SH, Jang J, Oh SH, Nam Y, Jung S, Kim S, Fukunaga M, Kim W, Choi HJ, Lee J. chi-separation: Magnetic susceptibility source separation toward iron and myelin mapping in the brain. Neuroimage. 2021;240:118371. doi: 10.1016/j.neuroimage.2021.118371. PubMed PMID: 34242783.

(3) Dimov AV, Gillen KM, Nguyen TD, Kang J, Sharma R, Pitt D, Gauthier SA, Wang Y. Magnetic Susceptibility Source Separation Solely from Gradient Echo Data: Histological Validation. Tomography. 2022;8(3):1544-51. Epub 20220614. doi: 10.3390/tomography8030127. PubMed PMID: 35736875; PMCID: PMC9228115.

(4) Chen J, Gong NJ, Chaim KT, Otaduy MCG, Liu C. Decompose quantitative susceptibility mapping (QSM) to sub-voxel diamagnetic and paramagnetic components based on gradient-echo MRI data. Neuroimage. 2021;242:118477. doi: 10.1016/j.neuroimage.2021.118477. PubMed PMID: 34403742; PMCID: PMC8720043.

(5) Yablonskiy DA, Haacke EM. Theory of NMR signal behavior in magnetically inhomogeneous tissues: the static dephasing regime. Magn Reson Med. 1994;32(6):749-63. doi: 10.1002/mrm.1910320610. PubMed PMID: 7869897.

(6) Dong J, Liu T, Chen F, Zhou D, Dimov A, Raj A, Cheng Q, Spincemaille P, Wang Y. Simultaneous phase unwrapping and removal of chemical shift (SPURS) using graph cuts: application in quantitative susceptibility mapping. IEEE Trans Med Imaging. 2015;34(2):531-40. doi: 10.1109/TMI.2014.2361764. PubMed PMID: 25312917.

(7) Reeder SB, McKenzie CA, Pineda AR, Yu H, Shimakawa A, Brau AC, Hargreaves BA, Gold GE, Brittain JH. Water-fat separation with IDEAL gradient-echo imaging. J Magn Reson Imaging. 2007;25(3):644-52. doi: 10.1002/jmri.20831. PubMed PMID: 17326087.

(8) Liu T, Khalidov I, de Rochefort L, Spincemaille P, Liu J, Tsiouris AJ, Wang Y. A novel background field removal method for MRI using projection onto dipole fields (PDF). Nmr Biomed. 2011;24(9):1129-36. doi: 10.1002/nbm.1670. PubMed PMID: 21387445; PMCID: PMC3628923.

(9) Liu J, Liu T, de Rochefort L, Ledoux J, Khalidov I, Chen WW, Tsiouris AJ, Wisnieff C, Spincemaille P, Prince MR, Wang Y. Morphology enabled dipole inversion for quantitative susceptibility mapping using structural consistency between the magnitude image and the susceptibility map. Neuroimage. 2012;59(3):2560-8. doi: 10.1016/j.neuroimage.2011.08.082. PubMed PMID: WOS:000299494000057.

(10) Liu Z, Spincemaille P, Yao Y, Zhang Y, Wang Y. MEDI+0: Morphology enabled dipole inversion with automatic uniform cerebrospinal fluid zero reference for quantitative susceptibility mapping. Magn Reson Med. 2018;79(5):2795-803. doi: 10.1002/mrm.26946. PubMed PMID: 29023982; PMCID: PMC5821583.

(11) Liu Z, Kee Y, Zhou D, Wang Y, Spincemaille P. Preconditioned total field inversion (TFI) method for quantitative susceptibility mapping. Magn Reson Med. 2017;78(1):303-15. doi: 10.1002/mrm.26331. PubMed PMID: 27464893; PMCID: PMC5274595.

(12) Pei M, Nguyen TD, Thimmappa ND, Salustri C, Dong F, Cooper MA, Li J, Prince MR, Wang Y. Algorithm for fast monoexponential fitting based on Auto-Regression on Linear Operations (ARLO) of data. Magn Reson Med. 2015;73(2):843-50. doi: 10.1002/mrm.25137. PubMed PMID: 24664497; PMCID: PMC4175304.

Oxygen Extraction Fraction (OEF) Estimation using U-net Trained with Synthetically Generated Multi Gradient Echo Data

Mert Şişman[1,2], Hangwei Zhuang[2,3], Alexey V. Dimov[2], Alexandra Roberts[1,2], Pascal Spincemaille[2], Thanh Nguyen[2] and Yi Wang[2,3]

[1]Department of Electrical and Computer Engineering, Cornell University, Ithaca, NY, USA; [2]Department of Radiology, Weill Cornell Medicine, New York, NY, USA; [3]Meinig School of Biomedical Engineering, Cornell University, Ithaca, NY, USA

Summary: Oxygen extraction fraction (OEF) mapping is an important biomarker of tissue viability. Here, we propose a novel framework for deep neural network training with synthetically generated data based on biophysical signal modeling for OEF estimation from multi-echo gradient echo data.

Introduction: OEF measures the fraction of oxygen extracted from the blood, and therefore can signal important information about the tissue health. It is known that oxygen metabolism in several diseases such as Parkinson's disease [1], Alzheimer's disease [2], and multiple sclerosis [3] changes either globally or locally. The current gold standard of OEF measurements is positron emission tomography (PET) using three ^{15}O tracers [4] which is challenging to perform and not widely available. MRI is a noninvasive clinical imaging technique and several MRI-based OEF measurement techniques have been developed, such quantitative blood oxygenation-dependent (qBOLD)-OEF [5] or quantitative susceptibility mapping (QSM)-OEF [6]. Recently, a combined estimation method called qBOLD-QSM (QQ)-OEF was developed showing promise [7]. QQ-OEF works with routine multi gradient-echo measurements which makes it possible to employ it in clinical practice with ease. However, QQ-OEF assumes a closed form equation for signal evolution following qBOLD and suffers from long computation times. Here, we propose a novel deep learning approach where the training data is created using biophysical modeling of the mGRE signal while the use of neural network allows for a fast estimation of OEF.

Methods: The mGRE signal simulation composed of two parts: 1) Phase signal simulation via QSM modeling and 2) magnitude signal simulation based on R2* decay and local dephasing of spins due to deoxygenated blood carrying capillaries, myelin sheaths inside white matter tracts with anisotropic properties, off-resonance effects due to non-uniform field inside voxels. As the baseline for the brain anatomy, T1/T2/proton density (PD) - weighted images from the IXI dataset (http://brain-development.org/ixi-dataset/) were used.

For QSM generation, steps designated by the QSM reconstruction challenge 2.0 [8] were followed with slight modifications as T2* maps were not available. For white matter (WM), gray matter (GM), and cerebrospinal fluid (CSF) segmentations, FSL FAST algorithm [9], for the deep gray nuclei segmentations, Allen brain atlas [10], and for the air/tissue/skull segmentations, probability maps from Statistical Parametric Mapping (SPM) toolbox [11] were utilized. OEF and venous blood volume (v) maps were created as blurred piecewise constant random distributions. Large veins are obtained from a brain vein atlas [12] with susceptibilities estimated from the local OEF values. Phase data is then generated from the field data estimated via dipole convolution [13].

For magnitude signal generation, R2* is estimated from the empirical R2 map obtained from the T2-weighted and PD weighted images, and R2′ map simulated by scaling absolute QSM values. For estimation of the local dephasing due to deoxygenated blood, numerical simulations were conducted using randomly distributed solid cylinders with susceptibilities determined by blood oxygenation and background susceptibility. Off-resonance effects due to large susceptibility sources outside of the brain were also included. For fast estimation of these effects for each voxel during data generation, a fully-connected neural network is trained. Finally, fiber orientation dependent signal decay effects were also included [14].

50 such synthetic mGRE data sets with known OEF and blood volume v were generated. A 3D U-net [15] was trained on this data using a 40/5/5 training/validation/testing split. The training done for 1000 epochs with MSE loss and 1e-4 learning rate.

For in vivo evaluation, data from 2 healthy subjects were acquired on a 3T MRI scanner (Prismafit, Siemens Healthineers, Erlangen, Germany) using a monopolar 3D mGRE acquisition with parameters: FOV = 25.6 cm, phase FOV factor = 81.3%, TR = 41 ms, $TE_1/\Delta TE$ = 2.2/3.25 ms, number of TEs = 7, voxel size = 1 mm^3 isotropic, RBW = 260 Hz/pixel, FA = 15°.

Results: Figure 1(a) shows the U-net architecture, and (b) shows the plot of the training and validation loss over epochs. Figure 1(c) shows the true OEF map and OEF estimations by the proposed method and the QQ[16] in a synthetic test case. Error metrics also provided for each case. The estimated OEF maps of experimentally measured mGRE data are shown in Figure 1(d).
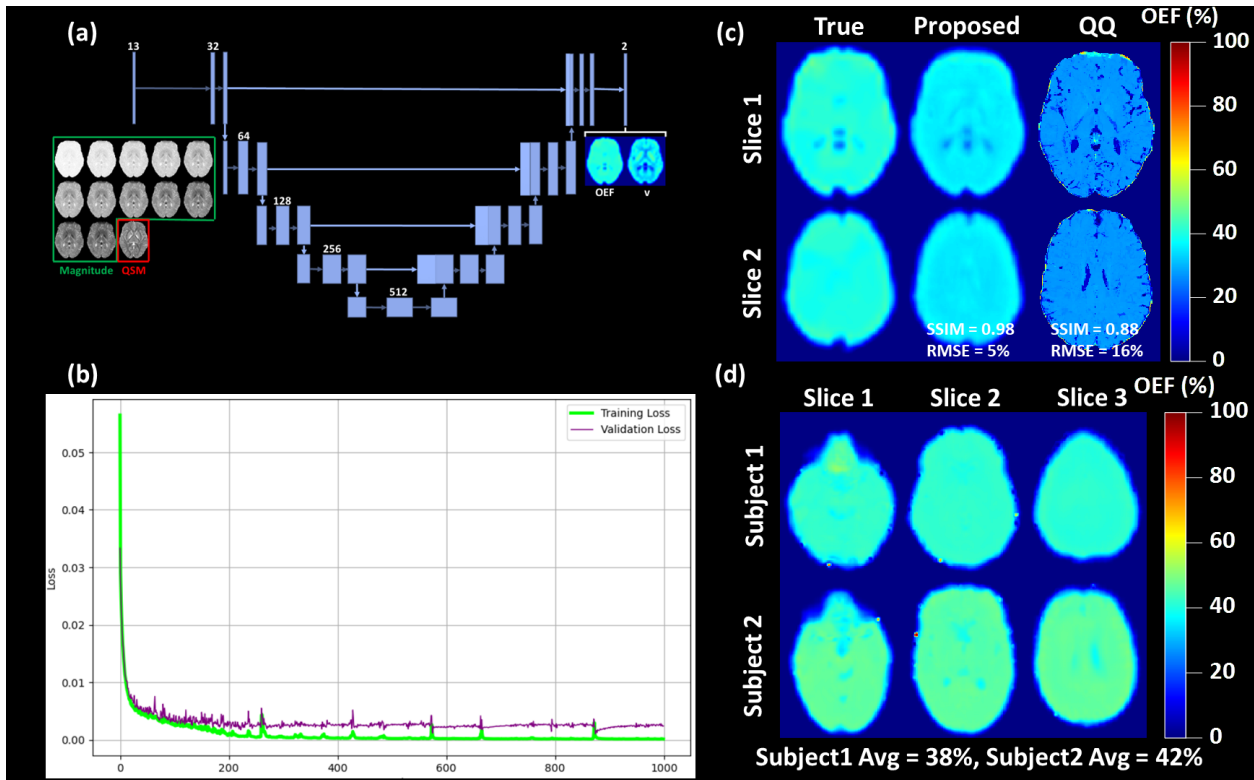
Figure 1 – U-net architecture trained for OEF estimation (a); Training and Validation losses over 1000 epochs of training (b); Example OEF result from the test dataset (synthetic) (c); OEF maps of two healthy subjects (d).

Discussion and Conclusions: Here, we proposed a novel approach for the fast and biophysics-based estimation of the OEF distribution and showed its feasibility in experimental settings. The lower error values obtained via the proposed method compared to the QQ demonstrates that the proposed method is able to provide higher accuracy due to the physics motivated modeling of the tissue microstructure. The in vivo OEF values were within the expected range for healthy controls. Further improvements will focus on the enlargement of the training dataset and inclusion of various pathologies for accurate estimation of OEF in patient data.

References:
[1]   P. Borghammer, M. Vafaee, K. Ostergaard, A. Rodell, C. Bailey, and P. Cumming, "Effect of memantine on CBF and CMRO2 in patients with early Parkinson's disease," *Acta Neurol Scand,* vol. 117, no. 5, pp. 317-23, May, 2008.
[2]   K. Nagata, R. J. Buchan, E. Yokoyama, Y. Kondoh, M. Sato, H. Terashi, Y. Satoh, Y. Watahiki, M. Senova, Y. Hirata, and J. Hatazawa, "Misery perfusion with preserved vascular reactivity in Alzheimer's disease," *Ann N Y Acad Sci,* vol. 826, pp. 272-81, Sep 26, 1997.
[3]   D. J. Brooks, K. L. Leenders, G. Head, J. Marshall, N. J. Legg, and T. Jones, "Studies on regional cerebral oxygen utilisation and cognitive function in multiple sclerosis," *J Neurol Neurosurg Psychiatry,* vol. 47, no. 11, pp. 1182-91, Nov, 1984.
[4]   M. A. Mintun, M. E. Raichle, W. R. Martin, and P. Herscovitch, "Brain oxygen utilization measured with O-15 radiotracers and positron emission tomography," *J Nucl Med,* vol. 25, no. 2, pp. 177-87, Feb, 1984.
[5]   X. He, and D. A. Yablonskiy, "Quantitative BOLD: mapping of human cerebral deoxygenated blood volume and oxygen extraction fraction: default state," *Magn Reson Med,* vol. 57, no. 1, pp. 115-26, Jan, 2007.
[6]   J. Zhang, D. Zhou, T. D. Nguyen, P. Spincemaille, A. Gupta, and Y. Wang, "Cerebral metabolic rate of oxygen (CMRO2) mapping with hyperventilation challenge using quantitative susceptibility mapping (QSM)," *Magn Reson Med,* vol. 77, no. 5, pp. 1762-1773, May, 2017.
[7]   J. Cho, Y. Kee, P. Spincemaille, T. D. Nguyen, J. Zhang, A. Gupta, S. Zhang, and Y. Wang, "Cerebral metabolic rate of oxygen (CMRO2) mapping by combining quantitative susceptibility mapping (QSM) and quantitative blood oxygenation level-dependent imaging (qBOLD)," *Magn Reson Med,* vol. 80, no. 4, pp. 1595-1604, Oct, 2018.
[8]   J. P. Marques, J. Meineke, C. Milovic, B. Bilgic, K. S. Chan, R. Hedouin, W. van der Zwaag, C. Langkammer, and F. Schweser, "QSM reconstruction challenge 2.0: A realistic in silico head phantom for MRI data simulation and evaluation of susceptibility mapping procedures," *Magn Reson Med,* vol. 86, no. 1, pp. 526-542, Jul, 2021.
[9]   Y. Zhang, M. Brady, and S. Smith, "Segmentation of brain MR images through a hidden Markov random field model and the expectation-maximization algorithm," *IEEE Trans Med Imaging,* vol. 20, no. 1, pp. 45-57, Jan, 2001.
[10]   S. L. Ding, J. J. Royall, S. M. Sunkin, L. Ng, B. A. Facer, P. Lesnar, A. Guillozet-Bongaarts, B. McMurray, A. Szafer, T. A. Dolbeare, A. Stevens, L. Tirrell, T. Benner, S. Caldejon, R. A. Dalley, N. Dee, C. Lau, J. Nyhus, M. Reding, Z. L. Riley, D. Sandman, E. Shen, A. van der Kouwe, A. Varjabedian, M. Wright, L. Zöllei, C. Dang, J. A. Knowles, C. Koch, J. W. Phillips, N. Sestan, P. Wohnoutka, H. R. Zielke, J. G. Hohmann, A. R. Jones, A. Bernard, M. J. Hawrylycz, P. R. Hof, B. Fischl, and E. S. Lein, "Comprehensive cellular-resolution atlas of the adult human brain," *J Comp Neurol,* vol. 524, no. 16, pp. 3127-481, Nov 01, 2016.
[11]   J. Ashburner, "Computational anatomy with the SPM software," *Magn Reson Imaging,* vol. 27, no. 8, pp. 1163-74, Oct, 2009.
[12]   P. G. D. Ward, N. J. Ferris, P. Raniga, D. L. Dowe, A. C. L. Ng, D. G. Barnes, and G. F. Egan, "Combining images and anatomical knowledge to improve automated vein segmentation in MRI," *Neuroimage,* vol. 165, pp. 294-305, Jan 15, 2018.
[13]   Y. Wang, and T. Liu, "Quantitative susceptibility mapping (QSM): Decoding MRI data for a tissue magnetic biomarker," *Magn Reson Med,* vol. 73, no. 1, pp. 82-101, Jan, 2015.
[14]   S. Wharton, and R. Bowtell, "Gradient echo based fiber orientation mapping using R2* and frequency difference measurements.," *Neuroimage,* vol. 83, pp. 1011-1023, 2013.
[15]   O. Ronneberger, P. Fischer, and T. Brox, "U-Net: Convolutional Networks for Biomedical Image Segmentation." pp. 234-241.
[16]   J. Cho, P. Spincemaille, T. D. Nguyen, A. Gupta, and Y. Wang, "Temporal clustering, tissue composition, and total variation for mapping oxygen extraction fraction using QSM and quantitative BOLD," *Magn Reson Med,* vol. 86, no. 5, pp. 2635-2646, Nov, 2021.

Feasibility of Thin-slab Susceptibility Source Separation in Human Brain

Nashwan Naji[1], Alan Wilman[1,2]

[1]*Dept. of Radiology and Diagnostic Imaging;* [2]*Dept. of Biomedical Engineering (University of Alberta, Edmonton, Canada)*

Summary: The thin-slab technique offers substantial acquisition time reduction in focal high-resolution susceptibility imaging applications by enabling robust diamagnetic and paramagnetic maps from a thin slab of as few as 8 slices. This technique utilizes an additional rapid low-resolution GRE acquisition with extended spatial coverage to estimate the missing field information outside the imaged thin slab.

Introduction: The susceptibility source separation (χ-Sep) technique was recently introduced to explore sub-voxel diamagnetic and paramagnetic components by capitalizing on both the magnitude and phase of multi-echo gradient echo (mGRE) images (to compute R2* and phase shift, respectively), and ideally the magnitude of multi-echo spin-echo (mSE) images (to compute R2') [1-3]. For accurate susceptibility measurement, adequate spatial coverage is required to resolve the 3D convolution relationship between the phase shift and the underlying sources [4-6]. This requirement makes applying χ-Sep at sub-millimeter resolution and/or ultra-high field strength ($\geq$ 7T) challenging due to prolonged acquisition time (and SAR limit when mSE is used). Although several techniques have been introduced to accelerate mGRE/mSE acquisition [7-9], enabling χ-Sep from a thin slab would further reduce the scan time and/or allow exploring higher spatial resolution with reduced time penalty. Recently, we introduced a technique to perform QSM from thin slabs in brain with aid from a lower-resolution acquisition of extended coverage [6], and here we investigate extending its applicability to χ-Sep.

Methods: A) Imaging Protocol: To perform the thin-slab technique, two sets of axial 3D mGRE with different spatial resolutions were collected at 3T from 3 healthy volunteers. The first set had resolution of 0.54×0.54×0.65 mm^3 and through-plane coverage of 78 mm (120 slices acquired in 16.28 min) centered on putamen. Thin slabs were then produced retrospectively from this acquisition by truncating the number of slices to 24, 16, and 8. The second set had brain coverage of 80 mm (40 slices, 1.68 min), and its resolution was lowered to 2.18×1.09×2.0 mm^3. Both sets used 7 echoes, TE1/ΔTE/TR of 4.14/6.13/47 ms, 178×210 mm^2 in-plane FOV, and 17° flip-angle.

B) Susceptibility Mapping and Separation: Susceptibility maps were produced using i) a typical QSM processing (V-SHARP background removal [10] and MEDI dipole inversion [11]) and using ii) the thin-slab technique described in [6]. Briefly, the thin-slab approach uses the low-resolution data to estimate and remove the background field and to regularize the dipole inversion step. In all cases, phase unwrapping was performed using ROMEO [12], and R2* maps were calculated using the Quantitative Mapping Tools [13]. Afterwards, source separation was performed using χ-Sep toolbox [1] with initial susceptibility either from i) or ii) and R2' being approximated as 0.52×R2* [3]. Finally, ten grey and white matter regions were manually segmented on one central slice and used for measurement.

Results: Similar to what was reported in QSM [4-6], attempting source separation from thin slabs using conventional methods resulted in inaccurate estimation of the underlying paramagnetic and diamagnetic components, as shown in Figure 1A (Typical Method). Using the proposed method, however, susceptibility mapping (and separation) from as few as 8 slices was achieved with comparable quality to those obtained using the typical approach with extended spatial coverage, as illustrated in Figure 1A (Proposed Method). Quantitatively, the average absolute error of all subjects (with respect to measurements with the widest slab) using the proposed method was (mean $\pm$ SD) 2.05±0.97 ppb, compared to 15.0±12.12 ppb for the typical reconstruction, as shown in Figure 1B. Similar findings were also found when true R2' measurements (i.e., with mSE acquisition) were used in the source separation (results not shown).

Discussion and Conclusions: The shortcoming of the conventional approach originates from the non-sufficient truncated field information used to invert the convolution with dipole field. The proposed technique addresses this by utilizing a low-resolution version of the field map with extended spatial coverage to help the inversion algorithm understand the field distribution outside the imaged thin slab. The extra low resolution supporting data had coarser resolution by a factor of 24, meaning that it can be acquired with extended spatial coverage in 5% the time that would be needed for the full coverage high-resolution acquisition. Thus, performing source separation from few targeted slices using the proposed method offers 60% to 90% reduction in acquisition time on top of utilized pulse sequence acceleration techniques, which can further reduce sensitivity to motion artifacts and enhance patient experience. Alternatively, the saved time can be used to achieve maps of higher resolution within a reasonable time frame. To conclude, the thin-slab technique offers further scan time reduction in acquiring the data required for susceptibility source separation when the targeted region can be covered with only a few slices.
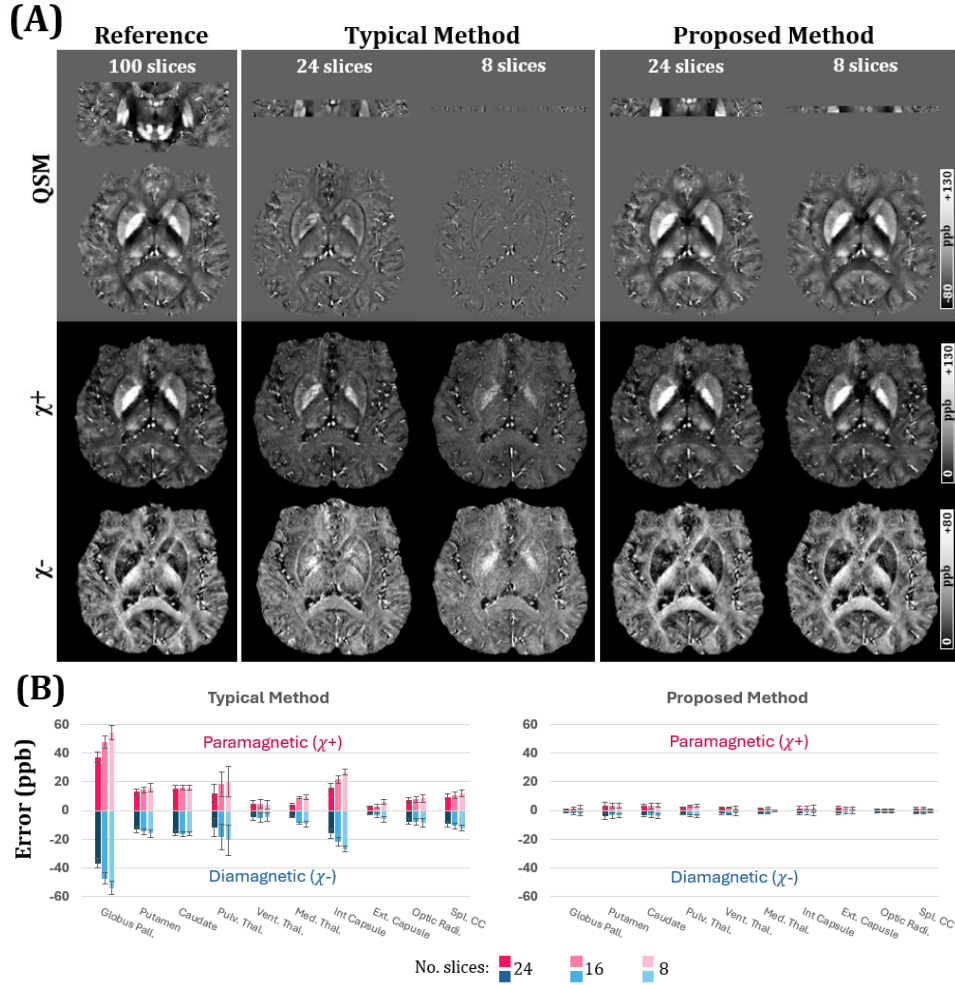
Figure 1: A) An illustration of the obtained susceptibility maps in-vivo from one subject using the typical approach with extended spatial coverage (first column), the typical approach from a thin slab of 24 slices and 8 slices (middle 2 columns), and the proposed approach from a thin slab of 24 slices and 8 slices (last 2 columns). B) Average absolute error over all subjects of paramagnetic and diamagnetic measurements in 10 ROIs at different slab widths (color-coded), with respect to the full-width slab measurements.

References:

[1] Shin HG, Lee J, Yun YH, et al (2021), "χ-separation: Magnetic susceptibility source separation toward iron and myelin mapping in the brain", *Neuroimage*, vol. 240, pp. 118371.

[2] Chen J, Gong NJ, Chaim KT, et al (2021), "Decompose quantitative susceptibility mapping (QSM) to sub-voxel diamagnetic and paramagnetic components based on gradient-echo MRI data", *Neuroimage*, vol. 242, pp. 118477.

[3] Dimov AV, Nguyen TD, Gillen KM, et al (2022), "Susceptibility source separation from gradient echo data using magnitude decay modeling", *Journal of Neuroimaging*, vol. 32, pp. 852-859.

[4] Elkady AM, Sun H, Wilman AH (2016), "Importance of extended spatial coverage for quantitative susceptibility mapping of iron-rich deep gray matter", *Magn. Reason. Imaging*, vol. 34, pp. 574-578, doi: 10.1016/j.mri.2015.12.032.

[5] Karsa A, Punwani S, Shmueli K (2019), "The effect of low resolution and coverage on the accuracy of susceptibility mapping", *Magn. Reason. Med.*, vol. 81, pp. 1833-1848, doi: 10.1002/mrm.27542.

[6] Naji N, Wilman A (2023), "Thin slab quantitative susceptibility mapping", *Magn. Reason. Med.*, vol. 90, pp. 2290-2305.

[7] Sun H, Wilman AH (2015), "Quantitative susceptibility mapping using single-shot echo-planar imaging", *Magn. Reason. Med.*, vol. 73, pp. 1932-1938, doi: 10.1002/mrm.25316.

[8] Bilgic B, Gagoski B, Cauley SF, et al (2015), "Wave-CAIPI for Highly Accelerated 3D Imaging"; *Magn Reson Med*, vol.73, pp. 2152-2162 doi: 10.1002/mrm.25347.

[9] Barth M, Breuer F, Koopmans PJ, et al (2016), "Simultaneous multislice (SMS) imaging techniques", *Magn Reson Med*, vol. 75, pp.63-81. doi: 10.1002/mrm.25897.

[10] Li W, Wu B, Liu C (2011), "Quantitative susceptibility mapping of human brain reflects spatial variation in tissue composition" *Neuroimage*, vol. 55, pp. 1645–56.

[11] Liu J, Liu T, de Rochefort L, et al (2012), "Morphology enabled dipole inversion for quantitative susceptibility mapping using structural consistency between the magnitude image and the susceptibility map", *Neuroimage*, vol. 59, pp. 2560-2568.

[12] Dymerska B, Eckstein K, Bachrata B, et al (2021), "Phase unwrapping with a rapid opensource minimum spanning tree algorithm (ROMEO)", *Magn Reson Med*, vol. 85, pp. 2294-2308. doi: 10.1002/mrm.28563.

[13] Naji N (2024), Quantitative Mapping Tools, https://github.com/MRItech/Quantitative-Mapping-Tools.

Transformer-Based Super-Resolution of χ-separation Maps with Anisotropic Voxel Leveraging In-Plane High-Resolution Information and Uncertainty Estimation

Hayeon Lee[1], Sooyeon Ji[1], Kyeongseon Min[1], Chungseok Oh[1], Taechang Kim[1], Jongho Lee[1]

[1]Department of Electrical and Computer Engineering (Seoul National University, Seoul, Korea, Republic of)

Summary: We present a novel transformer-based super-resolution framework that leverages high-resolution in-plane information and uncertainty estimation to enhance the through-plane resolution of χ-separation maps, achieving superior performance.

**Introduction:** χ-separation [1] quantifies paramagnetic and diamagnetic susceptibility sources within brain tissue using gradient echo (GRE) data. Due to time and cost constraints in clinical settings, acquiring GRE data with isotropic high-resolution (HR) voxels is often impractical, leading to the acquisition of anisotropic voxels with through-plane low-resolution (LR). For instance, GRE data acquired for Susceptibility Map-Weighted Imaging (SMWI) [2] typically has a voxel size of 0.5 mm x 0.5 mm x 1 mm. In this study, we propose a transformer-based super-resolution framework that utilizes in-plane HR information and an uncertainty estimation to enhance the through-plane resolution, converting anisotropic voxels into HR isotropic voxels. Inspired by SMORE [3], we trained a model using HR axial slices and applied it to LR sagittal slices to obtain through-plane HR data. Furthermore, we employed the state-of-the-art Hybrid Attention Transformer (HAT) [4][5], known for its superior performance in super-resolution tasks. Additionally, we integrate loss terms utilizing uncertainty estimation, previously demonstrated to be effective in CNN-based super-resolution tasks [6], to enhance performance of our model.

Methods: All χ-separation maps were processed using the χ-separation toolbox (https://github.com/SNU-LIST/chi-separation). For the super-resolution task, we employed the HAT transformer architecture, combining self-attention, channel attention, and overlapping cross-attention (OCA), to map LR to HR and activate more pixels for high-quality image restoration. Furthermore, we integrated uncertainty estimation (as illustrated in Figures (a) and (b)) to enforce the model focusing on challenging parts of the image, such as textured and edge pixels with high uncertainty. Our approach consists of two main steps: First, a model is trained to estimate uncertainty using the estimating sparse uncertainty (ESU) loss function (L_{ESU}). Second, a new model is trained using the uncertainty-driven loss (L_{UDL}). The formulations for the loss functions are as follows:

$$L_{ESU} = \frac{1}{N} \sum_{i=1}^{N} \exp(-s_i) \, \|y_i - f(x_i)\|_1 + 2s_i$$

$$L_{UDL} = \frac{1}{N} \sum_{i=1}^{N} \hat{s}_i \|y_i - f(x_i)\|_1$$

where x_i and y_i represent the LR and HR images, respectively, and s_i denotes the estimated log variance. Here, $\hat{s}_i = s_i - \min(s_i)$ is used as the weight for the L1 loss. The s_i values are obtained from the model trained in the first step and are fixed while training the model in the second step. For training, the model was trained using LR-HR paired datasets derived from HR axial slices. LR images in the paired dataset were generated by cropping and filtering k-space, while HR images were the original images. To evaluate our model, we used downsampled 1 mm x 1 mm x 2 mm resolution data from χ-separation maps with 1 mm isotropic voxels, creating LR-HR pairs for sagittal slices. The trained model was then applied to the sagittal slices to obtain through-plane HR data. These results were compared to interpolated images using k-space zero padding, with quantitative metrics such as PSNR and SSIM. The χ-separation maps with 1 mm isotropic voxels served as the reference for evaluation.

Results: The proposed framework outperformed interpolation using k-space zero padding, demonstrating superior performance in enhancing the through-plane resolution of χ-separation maps with anisotropic voxels. While the integration of uncertainty-driven loss functions ($L_{ESU} + L_{UDL}$) led to slight improvements in PSNR and SSIM metrics compared to using only L1 loss, the overall visual quality of the super-resolved images was enhanced. The super-resolved χ-separation maps exhibited improved clarity and sharpness, with reduced errors observed in the difference maps. These results highlight the potential of the proposed approach to enable the generation of χ-separation maps with isotropic HR voxels that hold significant value for both clinical applications and future research.
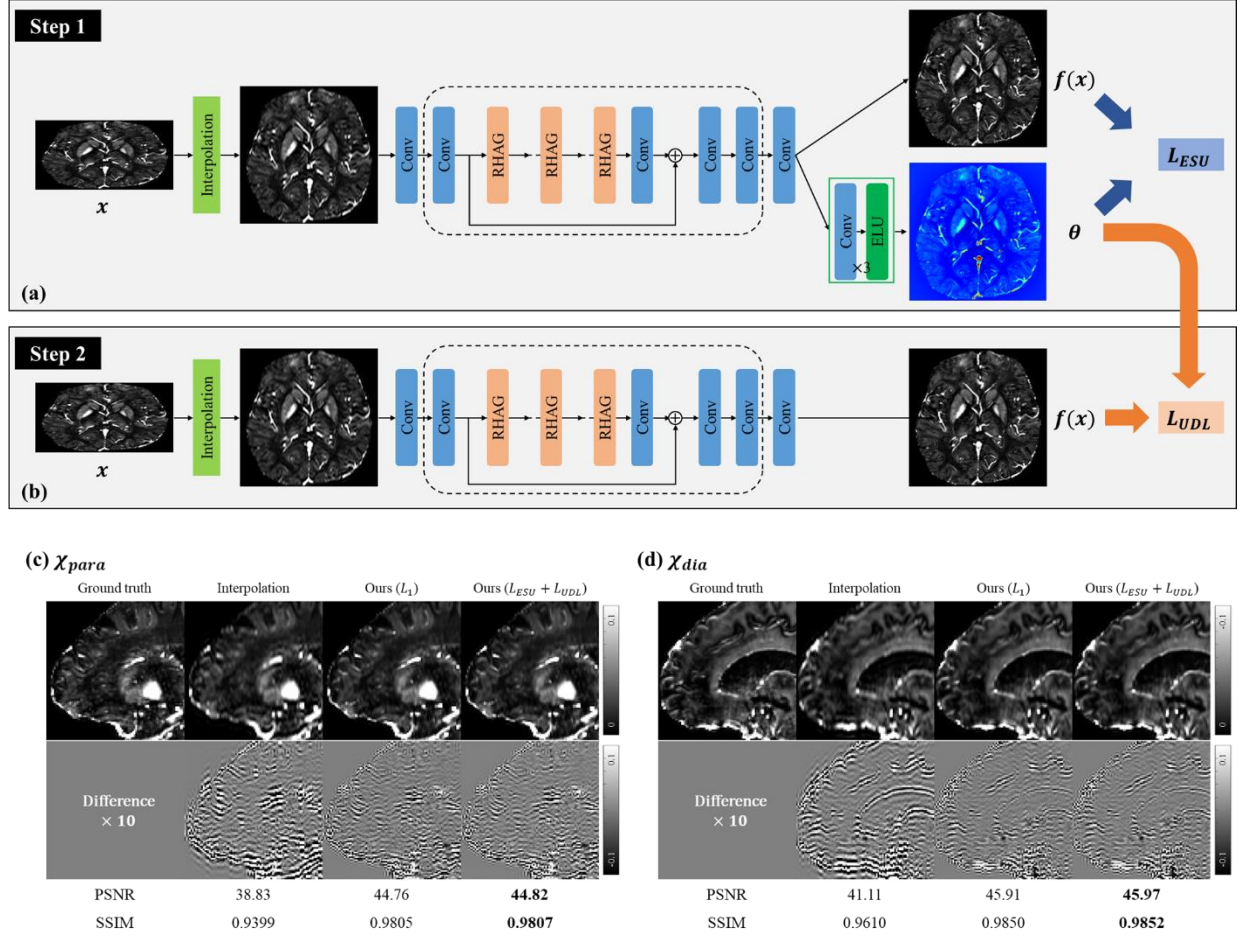
Figures – The overall framework (a) Step 1: The initial LR image (x) undergoes interpolation before being input into the model. The model is trained to estimate uncertainty using the loss function L_{ESU}. **(b) Step 2:** The model is trained using the uncertainty-driven loss L_{UDL}, which leverages the previously calculated uncertainty to prioritize high-uncertainty regions and further enhance image quality. **(c) χ_{para}** and **(d) χ_{dia}:** Super-resolution results in both χ_{para} and χ_{dia} and their respective difference maps showcase the effectiveness of the proposed framework in enhancing visual clarity and sharpness.

Discussion and Conclusions: Our proposed method enables the conversion of χ-separation maps with anisotropic voxels into χ-separation maps with isotropic HR voxels, demonstrating significant improvements in visual clarity and potential diagnostic utility. The framework's effectiveness was demonstrated through both quantitative metrics (PSNR, SSIM) and qualitative assessments, showcasing superior performance compared to interpolation. However, it is important to note that this study utilized a synthetic LR-HR paired dataset generated through downsampling, rather than actual acquired anisotropic voxels. Future work will focus on validating the framework's performance on real-world data with anisotropic voxels.

References:
[1] Shin, H.-G. et al., 2021, χ-separation: Magnetic susceptibility source separation toward iron and myelin mapping in the brain: NeuroImage, v. 240, p. 118371, doi:10.1016/j.neuroimage.2021.118371.
[2] Nam, Y., S. Gho, D. Kim, E. Y. Kim, and J. Lee, 2017, Imaging of nigrosome 1 in substantia nigra at 3T using multiecho susceptibility map-weighted imaging (SMWI): Journal of Magnetic Resonance Imaging, v. 46, no. 2, p. 528–536, doi:10.1002/jmri.25553.
[3] Zhao, C., B. E. Dewey, D. L. Pham, P. A. Calabresi, D. S. Reich, and J. L. Prince, 2021, SMORE: A Self-Supervised Anti-Aliasing and Super-Resolution Algorithm for MRI Using Deep Learning: IEEE Transactions on Medical Imaging, v. 40, no. 3, p. 805–817, doi:10.1109/tmi.2020.3037187.
[4] Chen, X., X. Wang, J. Zhou, Y. Qiao, and C. Dong, 2022, Activating More Pixels in Image Super-Resolution Transformer: arXiv, doi:10.48550/arxiv.2205.04437.
[5] Chen, X., X. Wang, W. Zhang, X. Kong, Y. Qiao, J. Zhou, and C. Dong, 2023, HAT: Hybrid Attention Transformer for Image Resto-ration: arXiv, doi:10.48550/arxiv.2309.05239.
[6] Ning, Q. et al., 2024, Uncertainty-Driven Loss for Single Image Super-Resolution, NeurIPS 2024

Single-training physics-informed u-net for dipole inversion

Hangwei Zhuang[1,2], Pascal Spincemaille[2], Thanh Nguyen[2] and Yi Wang[1,2]

¹Cornell University, Ithaca, USA; ²Weill Cornell Medical College, New York, USA;

Summary: We proposed a single-training physics informed u-net for dipole inversion.

Introduction: As deep learning has gained popularity across various fields, and demonstrated significant success and potential, it has been a popular tool to improve the longstanding QSM problem. Much research dedicated to solving dipole inversion, the crucial step in QSM, using various network architectures and training schemes such as 2D and 3D unet, variational networks, generative adversarial networks, training with clinical data, synthetic data or combined [1-6]. Although the forward model loss has been combined in several methods for training or fine tuning, we propose in this study a fast and efficient deep learning model utilizing the 3D unet architecture and only the physical model to solve the dipole inversion inverse problem.

Methods: Network Architecture: a standard 3D unet model with 4 downsample blocks and 4 upsample blocks was implemented using Pytorch. The kernel size of all convolutional layers was 3*3*3 and ReLu activation and dropout = 0.5 were utilized. Forward Model: The dipole convolution was formulated as $f_{local} = D * \chi$ and implemented for pytorch tensors as k-space multiplication. Network Training: The network was trained for 2000 epochs on the input local field map. Adam optimizer with learning rate = 0.0005, betas = (0.9,0.999) was used. The loss function was defined by the mean squared error between the input f_{lcoal} and the output convolved with the dipole $\chi_{out} * D$. The model was trained and validated on the 2016 QSM reconstruction challenge data with background field-corrected tissue phase as input and χ_{33} from STI as the ground truth.[7] Statistical Analysis: normalized root mean squared error (NRMSE), high-frequency error norm(HFEN) and XSIM[8] between the result and the ground truth were calculated.

Results: Axial slices from different levels in the brain of the input local field, ground truth χ_{33} and our result were shown in Figure. 1. The NRMSE between the model estimation and the ground truth is 55.99, the HFEN is 80.54 and the XSIM is 0.87.
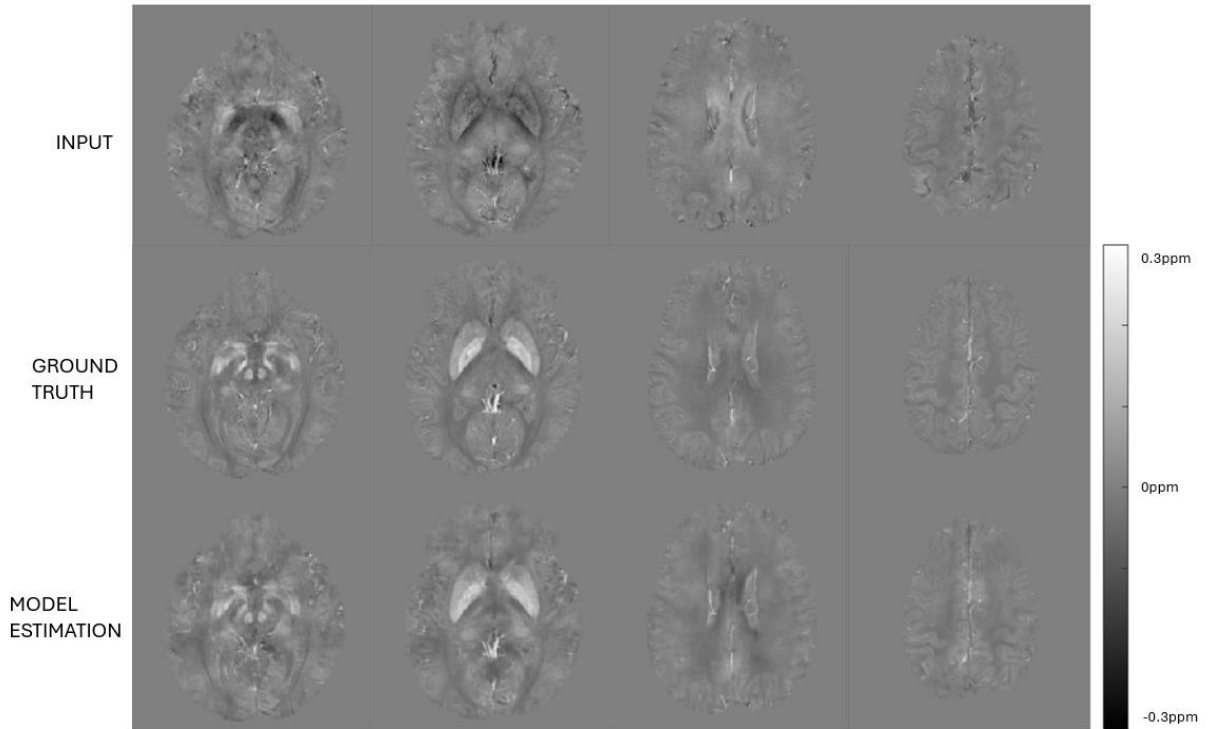
Figure.1 – different slices of the input local field map (top), ground truth susceptibility map (middle) and the susceptibility map estimated from the network (bottom)

Discussion and Conclusions: Our method achieves comparable image quality as other dipole inversion methods and requires considerably less computation resources. Our method does not learn from either in-vivo or synthetic training data and thus avoids bias introduced by training data class imbalance or error propagation from the simulation process and is

more suitable for subject specific susceptibility mapping. Without iterating over a substantial number of images, our method takes only ~30 minutes to finish the single training using and nvidia RTX A6000 GPU. The simplicity of the forward model loss term reduces the need for tuning weights of various loss terms. Our result has a slightly high HFEN indicating the performance in high spatial frequency regions can still be improved. Spatial regularization terms and noise could be added to more completely model the forward problem.

References:
[1] Jung, W., S. Bollmann and J. Lee (2022). "Overview of quantitative susceptibility mapping using deep learning: Current status, challenges and opportunities." NMR Biomed 35(4): e4292..
[2] Yoon, J., E. Gong, I. Chatnuntawech, B. Bilgic, J. Lee, W. Jung, J. Ko, H. Jung, K. Setsompop, G. Zaharchuk, E. Y. Kim, J. Pauly and J. Lee (2018). "Quantitative susceptibility mapping using deep neural network: QSMnet." Neuroimage 179: 199-206..
[3] Bollmann, S., K. G. B. Rasmussen, M. Kristensen, R. G. Blendal, L. R. Ostergaard, M. Plocharski, K. O'Brien, C. Langkammer, A. Janke and M. Barth (2019). "DeepQSM - using deep learning to solve the dipole inversion for quantitative susceptibility mapping." Neuroimage 195: 373-383.
[4] Chen, Y., A. Jakary, S. Avadiappan, C. P. Hess and J. M. Lupo (2020). "QSMGAN: Improved Quantitative Susceptibility Mapping using 3D Generative Adversarial Networks with increased receptive field." Neuroimage 207: 116389.
[5] Zhang, J. W., Z. Liu, S. Zhang, H. Zhang, P. Spincemaille, T. D. Nguyen, M. R. Sabuncu and Y. Wang (2020). "Fidelity imposed network edit (FINE) for solving ill-posed image reconstruction." Neuroimage 211.
[6] Zhang, M., R. Feng, Z. Li, J. Feng, Q. Wu, Z. Zhang, C. Ma, J. Wu, F. Yan, C. Liu, Y. Zhang and H. Wei (2024). "A subject-specific unsupervised deep learning method for quantitative susceptibility mapping using implicit neural representation." Med Image Anal 95: 103173.
[7] Langkammer, C., F. Schweser, K. Shmueli, C. Kames, X. Li, L. Guo, C. Milovic, J. Kim, H. Wei, K. Bredies, S. Buch, Y. Guo, Z. Liu, J. Meineke, A. Rauscher, J. P. Marques and B. Bilgic (2018). "Quantitative susceptibility mapping: Report from the 2016 reconstruction challenge." Magn Reson Med 79(3): 1661-1673.
[8] Milovic C., Tejos C., Irarrazaval P., Shmueli K.(2020) XSIM, a susceptibility-optimised similarity index metric: Validation with 2016 and 2019 QSM reconstruction challenge datasets

Low Frequency Electrical Conductivities Predicted by Diffusion Microstructure Methods.

Rosalind Sadleir, Sasha Hakhu, Scott Beeman, Saurav Z. K. Sajib

Arizona State University, Tempe, USA

Summary: We assessed the effect of tissue microstructure model on predicted low frequency (LF) conductivities. We found that predicted conductivities varied greatly and found differences in LF conductivities predicted in the left and right hippocampus compared to hippocampus substructures.

Introduction: Most diffusion microstructure models are focused on white matter, with properties of other structures going relatively understudied. This is of relevance to conductivity tensor imaging (CTI) [1], as it leverages output of similar models to construct a scaling factor translating diffusion to conductivity tensors. Therefore, we performed an investigation into the conductivities of gray and white matter predicted by three different microstructure models: NODDI [2], Spherical Mean [3] and SANDI [4].

Methods: Data from two databases containing microstructure diffusion MRI data were used. The WU-Minn HCP dataset provides diffusion data for 1200 healthy young adults with b-values (s/mm^2) = 0 (18 directions), 1000 (90 directions), 2000 (90 directions) and 3000 (90 directions) on a 3T scanner (TR/TE 5520/89.5 ms; 1.25 mm isotropic voxels) and allows for NODDI and SMT model fitting. The first 199 subjects of the WU-Minn HCP data set were processed. The MGH HCP dataset includes diffusion data for 35 healthy adults with b-values (s/mm^2) = 0 (40 directions), 1000 (64 directions), 3000 (64 directions), 5000 (128 directions) and 10000 (246 directions) on 3T scanner (TR/TE 8800/57 ms; 1.5 mm isotropic voxels) and allows for the SANDI model fitting. All MGH HCP data were used.

The relationship between conductivities were evaluated in white matter regions of interest (ROIs), cortical ROIs and Subcortical ROIs. Specific ROIs examined are shown in Figure 1 (a).
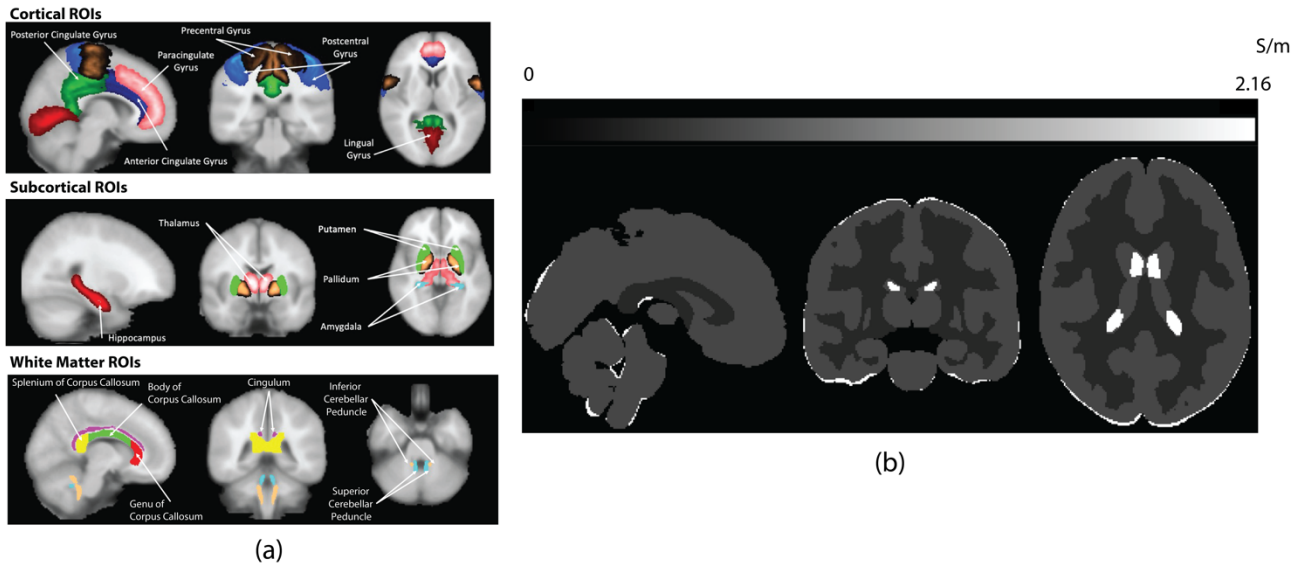
Figure 1 – Cortical, subcortical and white matter ROIs used (a); Model-based EPT conductivities in MNI space. (b)

The relationship between Isotropic LF CTI conductivity $\mathbf{C}_L^{CTI}$ and extracellular diffusivity d_e^w is described by

$$\mathbf{C}_L^{CTI} = \eta^{CTI} d_e^w. \qquad (1)$$

where η^{CTI} is the scaling factor distribution and

$$\eta^{CTI} = \frac{\alpha \sigma_H}{\alpha d_e^w + \beta (1 - \alpha) d_i^w} \qquad (2)$$

Where the factors α, (the extracellular fraction) d_e^w and d_i^w (intracellular diffusivity) were extracted from each microstructure model. The final factor, β, representing intra to extracellular ionic concentration, was assumed to be 0.41. After fitting, all data were transformed into MNI space and means were determined for each subject's predicted conductivity within the compartments shown in **Fig** 1 (a). As this study was concerned only with the effects of diffusion

models, we used model values for EPT white and gray matter conductivities σ_H at 128 MHz (3T) [5]. One slice of this volume in MNI space is shown in **Fig**. 1 (b).

Results: We found that conductivities predicted by each model were somewhat different. Box and whisker plots of one white matter ROI and one cortical ROI structure are shown in **Fig.** 2. As expected, white matter conductivities were predicted to be overall lower than for gray matter but there were differences in predicted values between methods. For example even though identical data were used for NODDI and SMT methods predicted corpus callosum conductivities were different by nearly a factor of two.
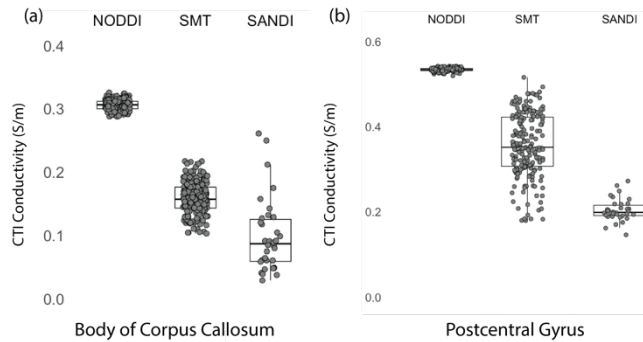
Figure 2. Predicted conductivity in white matter (corpus callosum) (a) and cortical (postcentral gyrus) compartments (b).

Overall, predicted conductivities in all gray and white matter structures showed similar dependences to those shown in **Fig.** 2, reflecting the effects of assumptions made in each microstructure model. Predicted conductivities in gray and white matter for each model were consistent for each model across structures of each type. An interesting case is presented in comparison of the hippocampal substructures presented in **Fig**. 3. Examples of conductivities in the hippocampus overall are shown compared with those found in the substructures CA1, CA23 and CA4/Dentate Gyrus The hippocampus overall had lower conductivity than the substructures. We believe this is because the substructures nominated have proportionally more gray matter.
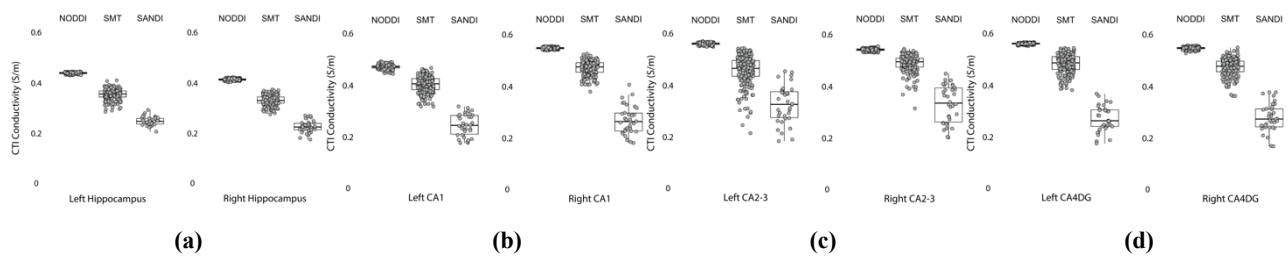
Figures 3 – Predicted conductivities in (a) left and right hippocampus; (b) left and right hippocampus CA1; (c) left and right hippocampus CA2/3 and (d) left and right hippocampus CA4/DG

Discussion and Conclusions: Because the NODDI model makes the most assumptions on tissue structure and focuses primarily on white matter, it may not be an ideal model to use to understand both gray and white matter. The SMT model makes the fewest assumptions on model structure and the greater variability observed in SMT predictions is not surprising. Predictions of SMT and SANDI models should be further explored and compared to actual tissue conductivities to further validate microstructure models used for CTI. The finding of different conductivity predictions different hippocampal substructures compared to the hippocampus overall is intriguing and also warrants further study.

References:
[1]   S. Z. K. Sajib, O. I. Kwon, H. J. Kim, and E. J. Woo, "Electrodeless conductivity tensor imaging (CTI) using MRI: basic and animal experiments," *Biomedical Engineering Letters,* vol. 8, no. 3, pp. 273-282, 2018, doi: https://doi.org/10.1007/s13534-018-0066-3(0123456789().,-volV)(0123456789().,-volV).
[2]   H. Zhang, T. Schneider, C. A. Wheeler-Kingshott, and D. C. Alexander, "NODDI: Practical in vivo neurite orientation dispersion and density imaging of the human brain," *NeuroImage,* vol. 61, pp. 1000-1016, 2012.
[3]   E. Kaden, F. Kruggel, and D. C. Alexander, "Quantitative mapping of the per-axon diffusion coefficients in brain white matter," *Magnetic Resonance in Medicine,* vol. 75, pp. 1752-1763, 2016, doi: doi:10.1002/mrm.25734.
[4]   M. Palombo *et al.*, "SANDI: A compartment-based model for non-invasive apparent soma and neurite imaging by diffusion MRI," *NeuroImage,* vol. 215, p. 116835, 2020.
[5]   S. Gabriel, R. W. Lau, and C. Gabriel, "The dielectric properties of biological tissues: III Parametric models for the dielectric spectrum of tissues," *Physics in medicine and biology,* vol. 41, pp. 2271-2293, 1996.

Feasibility of laminar functional quantitative susceptibility mapping

Sina Straub[1], Xiangzhi Zhou[1], Shengzhen Tao[1], Erin M. Westerhold[1], Jin Jin[2], Erik H. Middlebrooks[1]

[1]*Department of Radiology, Mayo Clinic, Jacksonville, FL, USA;* [2]*Siemens Healthcare, Brisbane, Australia*

Summary: Layer fMRI is an increasingly utilized technique that provides insights into the laminar organization of brain activity. However, both blood-oxygen-level-dependent (BOLD) fMRI and vascular space occupancy data (VASO) have certain limitations, such as bias towards larger cortical veins in BOLD fMRI and high specific absorption rate in VASO. This study aims to explore the feasibility of whole-brain laminar functional quantitative susceptibility mapping (fQSM) at ultra-high field and demonstrates the feasibility of studying layer-dependent activation using submillimeter fQSM. Compared to BOLD fMRI, fQSM exhibits reduced bias towards venous drainage effects on the cortical surface, allowing for better localization of laminar activation.

Introduction: The rapidly expanding field of laminar functional magnetic resonance imaging (fMRI) is dedicated to evaluating functional activation in individual cortical layers (1). Recent advancements in fMRI technology, particularly the utilization of ultra-high field (UHF) have facilitated fMRI with exceptional temporal and spatial resolution (2,3). However, the ability of functional imaging techniques to assess activation in specific layers also relies on the choice of contrast mechanisms. While gradient-echo blood-oxygen-level-dependent (BOLD) fMRI is highly sensitive to functional activation, it is also biased towards venous drainage effects on the cortical surface, limiting its spatial selectivity (4). Techniques based on cerebral blood volume (CBV) and cerebral blood flow (CBF) have demonstrated the ability to better localize activation within the corresponding cortical layers (5) such as vascular space occupancy (VASO) (3-6). The objective of this study is to assess the feasibility of laminar fQSM versus traditional laminar BOLD fMRI and VASO**.**

Methods: In accordance with Institutional Review Board approval, data were acquired in ten healthy volunteers. MRI was performed on a 7T scanner (MAGNETOM Terra, Siemens Healthineers, Erlangen, Germany) using an investigational 8Tx-32Rx head coil (Nova Medical Inc., Wilmington, MA, USA). A segmented, multi-shot gradient-echo 3D EPI research sequence (7) was employed, including skipped-CAIPIRINHA acceleration (8), navigator echoes acquired per excitation, and imaging echoes from the center of the k-space to estimate the zeroth- and first-order phase correction (9). Additionally, VASO data were acquired in three subjects using a research sequence (8,10). The VASO sequence was acquired with inversion times TI1 = 993 ms and TI2 = 1859 ms, four magnetic preparations per shot, and fat suppression. All other sequence parameters are listed in Table 1. A finger-tapping paradigm (Table 1) was performed consisting of alternating blocks of the active task and rest. Complex data were denoised using NOise reduction with DIstribution Corrected (NORDIC) principal component analysis (11). Susceptibility maps were computed from the phase data of each volume. Phase was unwrapped using 3D path-based unwrapping (12). Background field removal was performed with V-SHARP (13) and fourth-order polynomial fitting to correct for radiofrequency transmit-phase offset (14). Dipole inversion was computed using STAR-QSM (15). The brain mask used for susceptibility map computation was generated with FSL-BET. Each volume was referenced to the mean susceptibility value of the whole brain. For all acquisitions, the volumes were aligned to the first measurement of the time series using FSL FLIRT and 3D GRE fMRI and VASO data were co-registered. The VASO data were time-interpolated in Matlab, and BOLD corrected as described in Huber et al. (16). Data were upsampled by a factor of four. z-Scores were computed in Matlab, and masks were manually drawn in the motor (M1) and somatosensory cortex (S1) on fQSM using FSLEyes. These masks were used to segment 20 equidistant layers with the LN_GROW_LAYERS function in laynii (16). For the remainder of this manuscript, it is assumed that for M1 (S1), the segmented Layers 1 and 2 (1-2) approximately correspond to cortical Layer I, 3-5 (3-6) to Layer II, 6-9 (7-10) to Layer III, 10 and 11 (11-14) to Layer Va, 12-15 (15-16) to Layer Vb, and 16-20 (17-20) to Layer VI. LN_LAYER_SMOOTH was used to smooth z-score maps within layers with a full width at half maximum set to 1 mm.

Table 1: Sequence parameters

Protocol	volume TR in ms	TE/TR in ms	Resolution in mm³	matrix size/ FOV in mm³	BW in Hz/pixel	EPI factor/ segments	Partial Fourier (PE, slice)	CAIPIRINHA acceleration (PE×3D-Shift)	Acquisition time in min:sec	Flip angle	measurements	paradigm
3D GRE-EPI	9660	14/23	0.81×0.81×0.81	272×218×212/ 220×176×172	1148	7/ 10	7/8, 6/8	3×4-2	7:22	10	45	rarararararararar
VASO	10665	15.6/43.3	0.82×0.82×0.82	216×234×80/ 177×192×66	926	29/ 2	6/8, -	3×2-1	8:05	30	45	rarararararararar

Results: For M1, the magnitude of the activation-dependent susceptibility decrease was comparable across Layers I to VI, with an average of approximately -0.001 ppm for each layer (Figure 1a). However, for fMRI, the superficial layers showed the largest activation-dependent signal increase (Figure 1b). Average signal increase for Layer I was approximately 2.6% compared to 1.3% for Layer VI (Figure 1b). Comparing the time-evolution of different layers for fQSM, fMRI and VASO data (Figure 1c-e), it was evident that fMRI exhibited the largest activation-dependent signal increase in the most superficial layer, while a corresponding signal decrease was

not observed to the same extent for fQSM or VASO. The z-scores were higher for fMRI and VASO compared to fQSM (Figure 2); however, z-scores were distributed closer to the cortex-CSF boundary in fMRI compared with fQSM and VASO (Figure 2).
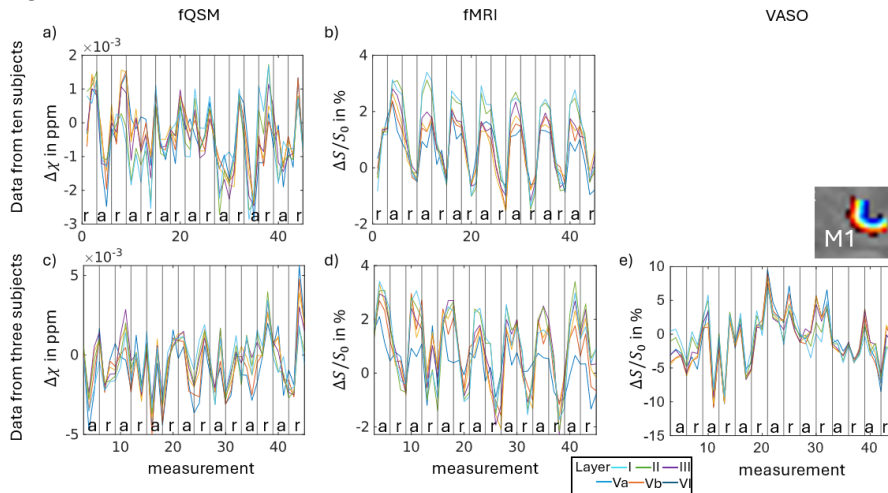
Figure 1 – Subject-averaged fQSM (Fig. 1a), fMRI (Fig. 1b) and VASO (Fig, 1c) signal evolutions for Layers I (cyan) to VI (blue) are displayed for the motor cortex (M1). The top row displays data from all ten subjects, whereas in the bottom row only data of subjects in whom VASO data were acquired is shown.
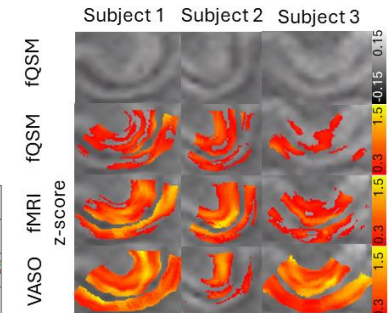
Figure 2 – z-Score maps are presented for fQSM, fMRI and VASO data in one subject overlaid on time-averaged fQSM.

Discussion and Conclusions: Compared to BOLD fMRI, fQSM showed less bias towards the superficial cortical layers and yielded results that were more comparable to the VASO data. However, as it quantifies activation-dependent BOLD susceptibility changes, which are also the basis for BOLD fMRI, fQSM can still be expected to exhibit some bias towards the venous drainage on the cortical surface, in contrast to CBF- or CBV-based methods provided these methods are not contaminated by BOLD effect. One advantage of laminar 3D-EPI-fQSM compared to VASO is the lower specific absorption rate and the relative ease of achieving whole-brain coverage. In conclusion, our findings demonstrate the feasibility of studying layer-dependent activation using submillimeter fQSM. Compared to BOLD fMRI, fQSM exhibits reduced bias towards venous drainage effects on the cortical surface, allowing for better localization of laminar activation.

References:
[1] Norris DG, Polimeni JR., Laminar (f)MRI: A short history and future prospects. Neuroimage 2019;197:643-649.
[2] Feinberg DA, Beckett AJS, Vu AT, et al. Next-generation MRI scanner designed for ultra-high-resolution human brain imaging at 7 Tesla. Nature Methods 2023;20(12):2048-2057.
[3] Huber L, Tse DHY, Wiggins CJ, et al. Ultra-high resolution blood volume fMRI and BOLD fMRI in humans at 9.4 T: Capabilities and challenges. Neuroimage 2018;178:769-779.
[4] Huber L, Handwerker DA, Jangraw DC, et al. High-Resolution CBV-fMRI Allows Mapping of Laminar Activity and Connectivity of Cortical Input and Output in Human M1. Neuron 2017;96(6):1253.
[5] Jin T, Kim SG. Cortical layer-dependent dynamic blood oxygenation, cerebral blood flow and cerebral blood volume responses during visual stimulation. Neuroimage 2008;43(1):1-9.
[6] Huber L, Goense J, Kennerley AJ, et al. Cortical lamina-dependent blood volume changes in human brain at 7 T. Neuroimage 2015;107:23-33.
[7] Jin J, Tourell M, Sati P, et al. Segmented 3D EPI with CAIPIRINHA for Fast, High-Resolution T2*-weighted Imaging. Proceedings of the 2021 ISMRM & SMRT Annual Meeting & Exhibition Volume 2021. p. 4190.
[8] Stirnberg R, Stocker T. Segmented K-space blipped-controlled aliasing in parallel imaging for high spatiotemporal resolution EPI. Magn Reson Med 2021;85(3):1540-1551.
[9] Pfeuffer J, Van de Moortele PF, Ugurbil K, Hu XP, Glover GH. Correction of physiologically induced global off resonance effects in dynamic echo-planar and spiral functional imaging. Magnetic Resonance in Medicine 2002;47(2):344-353.
[10] Huber L, Finn ES, Chai Y, et al. Layer-dependent functional connectivity methods. Prog Neurobiol 2021;207:101835.
[11] Moeller S, Pisharady PK, Ramanna S, et al. NOise reduction with DIstribution Corrected (NORDIC) PCA in dMRI with complex-valued parameter-free locally low-rank processing. Neuroimage 2021;226:117539.
[12] Abdul-Rahman HS, Gdeisat MA, Burton DR, Lalor MJ, Lilley F, Moore CJ. Fast and robust three-dimensional best path phase unwrapping algorithm. Appl Opt 2007;46(26):6623-6635.
[13] Li W, Wu B, Liu C. Quantitative susceptibility mapping of human brain reflects spatial variation in tissue composition. Neuroimage 2011;55(4):1645-1656.
[14] Chan KS, Marques JP. SEPIA-Susceptibility mapping pipeline tool for phase images. Neuroimage 2021;227:117611.
[15] Wei H, Dibb R, Zhou Y, et al. Streaking artifact reduction for quantitative susceptibility mapping of sources with large dynamic range. Nmr Biomed 2015;28(10):1294-1303.
[16] Huber LR, Poser BA, Bandettini PA, et al. LayNii: A software suite for layer-fMRI. Neuroimage 2021;237:118091.

Investigating Prostate Cancer Using QSM In Vivo

Laxmi Muralidharan[1], Manju Mathew[2], Adam Retter[2], Joey Clemente[2], Lucy Caselton[2], Sumandeep Kaur[2], Julia Markus[2], Shonit Punwani[2], Karin Shmueli[1]

[1]Department of Medical Physics and Biomedical Engineering, University College London, United Kingdom

[2]Centre for Medical Imaging, University College London, United Kingdom

Summary: A high resolution QSM sequence and optimized pipeline to compare the susceptibility values in lesion v. negative MRI suggests that QSM could be limited to detecting calcifications and hemorrhages in prostate.

Introduction: Previous QSM studies in prostate cancer (PCa) have investigated the potential to detect intraprostatic calcifications to use as fiducial markers for radiotherapy[1] and post biopsy[2] but none have assessed subtle tissue susceptibility changes. Blood's susceptibility is directly proportional to its deoxygenation[3], and low oxygenation (hypoxia) is thought to occur early in the evolution of PCa and is linked to an aggressive phenotype[4]. All this underpins our aim to investigate whether QSM can help detect and classify cancerous lesions in the prostate.

Methods: 27 subjects undergoing PCa screening were recruited as part of a clinical study [5] and scanned on a 3T Philips Ingenia using a 4x4 channel receive coil array on the front with a 4x4 array in the table. All subjects were given Buscopan to reduce rectal gas and bowel motion. 7 patients had lesions and underwent prostatectomy (*surgical* group), 8 patients had malignant lesions on biopsy and underwent other treatment (*non-surgical* group) and 12 patients had radiologically negative MR results for prostate cancer (*control* group).

Optimised 3D GRE parameters [6] included: FOV 420 x 320 x 128 mm, 1 mm isotropic resolution, 5 in-phase echoes: TE1 4.6 ms, ΔTE 6.9 ms, and SENSE factor 3. A QSM pipeline was optimized in 9 control subjects and applied to all subjects: The complex signal was denoised using Marchenko-Pastur Principal Component Analysis (MP-PCA) [7]. Total field maps from a non-linear fit of the denoised complex data [8] underwent Laplacian unwrapping [9]. Background field removal was performed using VSHARP [10, 11] with a maximum kernel width of 25 mm and a whole prostate mask contoured (MIM software[12]) on the T2-weighted
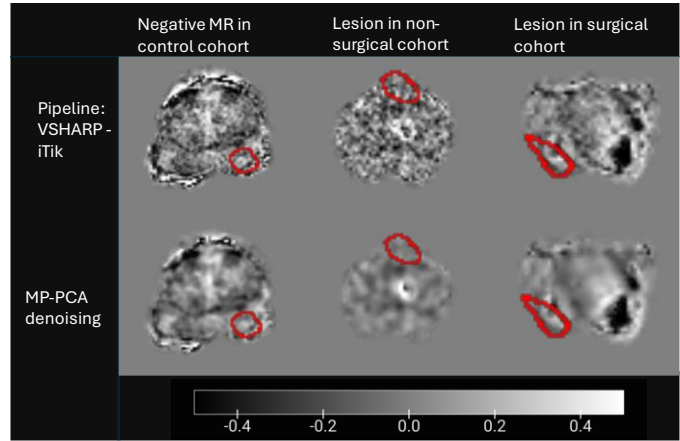

Figure 1: Susceptibility maps and ROI contours (red) with and without the MP-PCA denoising in noisy datasets in the different cohorts
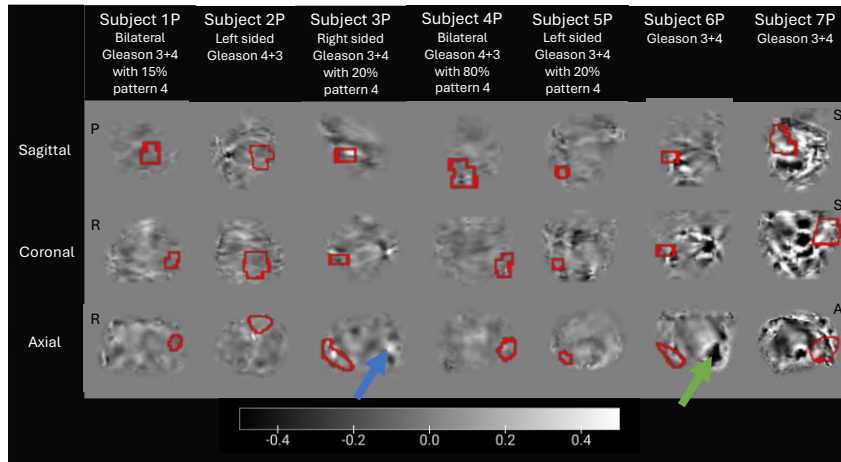

Figure 2: Susceptibility maps and **lesion** ROI contours (red) in the surgical cohort. The Gleason grade of the lesions for each subject is included. There are no salient lesion susceptibility differences on visual inspection.

images acquired in the same session/different session (FOV 180x180x96.6 mm, reconstructed voxel size 0.375x0.375x3 mm) by an experienced radiologist and transformed into the QSM space using the global registration of T2w and echo-combined [13] magnitude GRE images (NiftyReg[14, 15]). Susceptibility calculation was performed using iterative Tikhonov regularization[16] with the default regularization parameter α=0.05. Cancerous **Lesion** ROIs in the surgical (9) and non-surgical (10) groups, and **negative MRI** ROIs in the control (12) and non-surgical (3) groups were obtained in a similar manner to the whole prostate contour. To minimize partial volume effects, ROI masks were eroded by 1 voxel using a spherical kernel. A t-test was performed to compare the ROI mean susceptibility values between lesions and negative MRI ROIs.
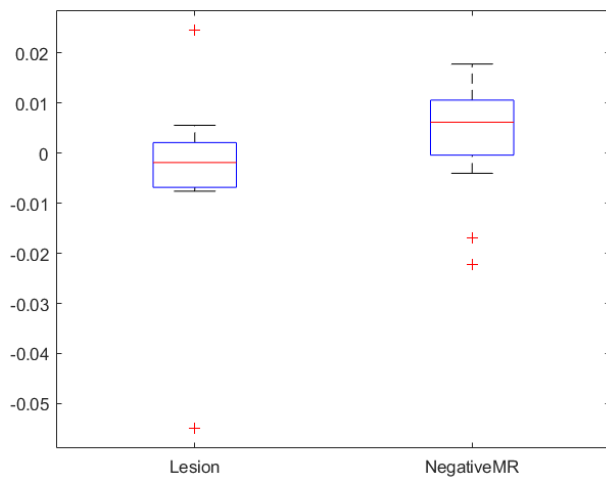
Figure 3: Box plot of mean susceptibility values in cancerous **lesion** ROIs (surgical and non-surgical groups) and **negative MRI** ROIs (control and non-

Results and Discussion: Paramagnetic regions (blue arrows), likely to be haemorrhages and diamagnetic regions (green arrows), likely to be calcium-rich secretion residues, were observed in the prostates of several subjects (Figure 2). Visually, there were no clear susceptibility differences in ROI susceptibilities between the groups. We found no significant difference in the mean susceptibility values (t(32)= -1.4620, p=0.16). Although we would hypothesise that hypoxia in cancerous lesions would lead to increased susceptibility, there seems to be general trend of lower mean susceptibility values in the **lesions** compared to **negative MR**. These results could be attributed to prostate cancers' poor vasculature compared to other tumours such as renal carcinomas [17, 18].

Conclusion: An optimized high-resolution sequence and processing pipeline were used to obtain prostate susceptibility maps to investigate any tissue susceptibility differences between cancerous lesions and control regions of non-cancerous tissue. We found no difference in the mean susceptibility values in the cancerous lesions compared to the negative MRI non-cancerous tissue. More data are being acquired to improve the statistical power of this preliminary study.

References: 1. Kan, H., et al., *Delineation of prostatic calcification using quantitative susceptibility mapping: Spatial accuracy for magnetic resonance-only radiotherapy planning.* J Appl Clin Med Phys, 2021.

2. Straub, S., et al., *Potential of quantitative susceptibility mapping for detection of prostatic calcifications.* J Magn Reson Imaging, 2017. **45**(3): p. 889-898.

3. Jain, V., et al., *Investigating the magnetic susceptibility properties of fresh human blood for noninvasive oxygen saturation quantification.* Magn Reson Med, 2012. **68**(3): p. 863-7.

4. Fraga, A., et al., *Hypoxia and Prostate Cancer Aggressiveness: A Tale With Many Endings.* Clin Genitourin Cancer, 2015. **13**(4): p. 295-301.

5. Singh, S., et al., *Histo-MRI map study protocol: a prospective cohort study mapping MRI to histology for biomarker validation and prediction of prostate cancer.* BMJ Open, 2022. **12**(4): p. e059847.

6. Muralidharan L, M.M., Clemente J, Caselton L, Kaur S, Brizmohun M, Punwani S, Shmueli K *An Optimized High Resolution Acquisition and Processing Pipeline for QSM in the Prostate.* in *ISMRM & ISMRT Annual meeting* 2023. Toronto, Canada.

7. Does, M.D., et al., *Evaluation of principal component analysis image denoising on multi-exponential MRI relaxometry.* Magn Reson Med, 2019. **81**(6): p. 3503-3514.

8. Liu, T., et al., *Nonlinear formulation of the magnetic field to source relationship for robust quantitative susceptibility mapping.* Magn Reson Med, 2013. **69**(2): p. 467-76.

9. Schweser, F., et al., *Toward online reconstruction of quantitative susceptibility maps: superfast dipole inversion.* Magn Reson Med, 2013. **69**(6): p. 1582-94.

10. Schweser, F., et al., *Quantitative imaging of intrinsic magnetic tissue properties using MRI signal phase: an approach to in vivo brain iron metabolism?* Neuroimage, 2011. **54**(4): p. 2789-807.

11. Wu, B., et al., *Whole brain susceptibility mapping using compressed sensing.* Magn Reson Med, 2012. **67**(1): p. 137-47.

12. *MIM Software Inc.*; Available from: https://www.mimsoftware.com/.

13. Kundu, P., et al., *Multi-echo fMRI: A review of applications in fMRI denoising and analysis of BOLD signals.* Neuroimage, 2017. **154**: p. 59-80.

14. Computing, C.f.M.I. *NiftyReg*. 2019; Available from: http://cmictig.cs.ucl.ac.uk/wiki/index.php/NiftyReg.

15. Rueckert, D., et al., *Nonrigid registration using free-form deformations: application to breast MR images.* IEEE Trans Med Imaging, 1999. **18**(8): p. 712-21.

16. Karsa, A., S. Punwani, and K. Shmueli, *An optimized and highly repeatable MRI acquisition and processing pipeline for quantitative susceptibility mapping in the head-and-neck region.* Magn Reson Med, 2020. **84**(6): p. 3206-3222.

17. Zhang, K. and D.J. Waxman, *Impact of tumor vascularity on responsiveness to antiangiogenesis in a prostate cancer stem cell-derived tumor model.* Mol Cancer Ther, 2013. **12**(5): p. 787-98.

18. Eberhard, A., et al., *Heterogeneity of angiogenesis and blood vessel maturation in human tumors: implications for antiangiogenic tumor therapies.* Cancer Res, 2000. **60**(5): p. 1388-93.

QSM in the presence of nondipolar phase shifts

Thomas Jochmann,[1,2] Fahad Salman,[2] Michael G. Dwyer,[2,3]
Niels Bergsland,[2,3] Robert Zivadinov,[2,3] Jens Haueisen,[1] Ferdinand Schweser[2,3]

[1]*Department of Computer Science and Automation, Technische Universität Ilmenau, Ilmenau, Germany;* [2]*Buffalo Neuroimaging Analysis Center, Department of Neurology, Jacobs School of Medicine and Biomedical Sciences at the University at Buffalo, The State University of New York, Buffalo, NY, USA;* [3]*Center for Biomedical Imaging, Clinical and Translational Science Institute, University at Buffalo, The State University of New York, Buffalo, NY, USA.*

Summary: The impact of nondipolar phase shifts from white matter microstructure on susceptibility maps calculated with state-of-the-art QSM methods was compared to DEEPOLE QUASAR. DEEPOLE QUASAR provided more robust and accurate susceptibility estimates in simulations. In vivo, a shift of deep gray matter susceptibility was observed relative to QSM methods.

Introduction: All quantitative susceptibility mapping methods are built on the assumption that *isotropic* magnetic susceptibility is the only source of observed MRI phase shifts, which produces the characteristic *dipole* phase contrast [1]. Experimental evidence and theoretical considerations suggest additional *nondipolar* contributions from tissue microstructure [2], [3] and chemical exchange [4] in the brain. The QUASAR model [5] describes nondipolar contributions with an additive term f_ρ: $f = d * \chi + f_\rho$.

We recently presented DEEPOLE QUASAR and demonstrated that it can separate susceptibility-induced phase shifts from nondipolar shifts [6], [7]. In the present work, we studied the effect of nondipolar phase shifts on susceptibility maps computed with different state-of-the-art QSM methods.

Methods: <u>QSM algorithms</u>: (1) DEEPOLE QUASAR; (2) DEEPOLE QSM (similar to DeepQSM [8] but based on the identical pipeline as DEEPOLE QUASAR), to study the immediate effect from the physical model; (3) MEDI [9], for being a widely recognized and applied QSM algorithm; (4) FANSI [10], for being the top-scoring algorithm in the 2019 QSM challenge (NRMSE at Stage 2) [11]; and (5) SDI [12], for being an algorithm that directly solves the inversion problem without iterative refinements or regularization which makes SDI particularly prone to model mismatch and thereby serves as a canary for violations to the QSM model.

<u>Adding nondipolar contributions to the 2019 QSM Challenge Model:</u> We extended the original brain model with nondipolar frequency contributions in the white matter, derived from diffusion images according to Wharton et al. [13], as proposed by the authors of the original challenge dataset [14]. **Fig. 1A** shows cross-sections of the created phantom.

<u>In vivo assessment:</u> *N*=8 subjects (two healthy volunteers and six with multiple sclerosis) were imaged at 3T (Philips MR 7700; 32-channel brain coil) using an accelerated 3D GRE mFFE PDw sequence, CS factor = 5, 512×512×144 matrix size, 0.5×0.5×1 mm³ nominal resolution (FOV=256×184×144 mm³), flip angle=15°, TR/TE/ΔTE = 50 ms/3.7 ms/6 ms, 8 echoes, bandwidth = 283.9 kHz). Scanner-reconstructed phase images were unwrapped with a best-path algorithm [15], and background fields were removed with RESHARP [16]. ROIs: Hybrid multi-atlas fusion technique, ANTs JLF.
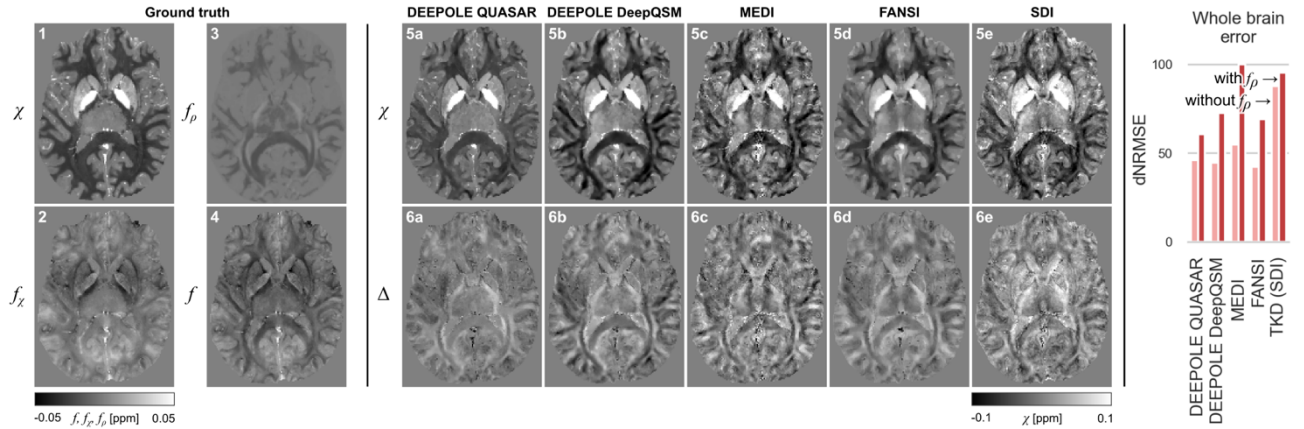
Fig. 1. Comparison of susceptibility estimates from different algorithms in a realistic digital brain model. **Left**: Tiles 1-4 show axial slices of the digital brain (ground truth). Susceptibility was estimated from the purely susceptibility-induced field (2; susceptibility estimates not shown) and from the field with nondipolar contributions (4; estimates in 5, errors in 6). **Right**: demeaned and normalized root-mean-squared error (dNRMSE).
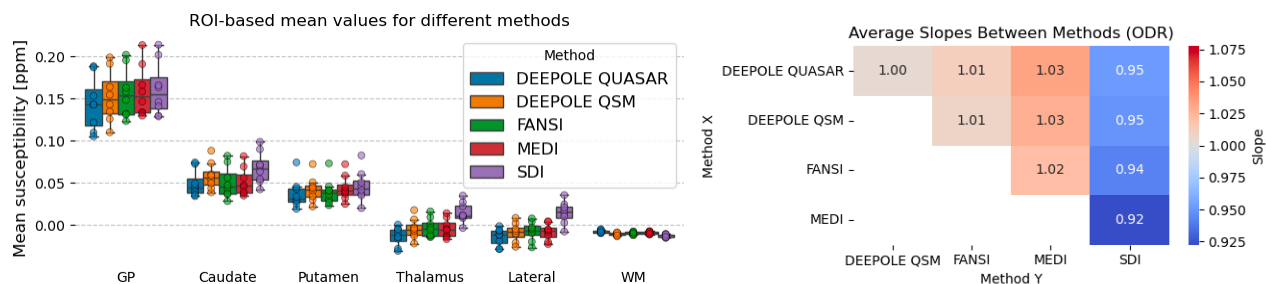
Fig. 2. Left: In vivo susceptibility in different brain regions obtained with different algorithms. The boxes denote the quartiles of the magnetic susceptibility over the eight subjects and the whiskers span from the minimal to the maximal value. **Right:** Slope between the susceptibility estimates in deep gray matter from the different algorithms.

Results: Fig. 1 shows the simulated brain phantom, the estimated susceptibility maps from the different algorithms, and their difference to the ground truth, as well as dNRMSE values. In the simulation *without* microstructure, the results from DEEPOLE QUASAR, DEEPOLE QSM, MEDI, and FANSI were comparable both visually and in various metrics (results not depicted). In the simulation *with* microstructure, the estimates from all algorithms demonstrated substantially higher discrepancies. DEEPOLE QUASAR was least affected among all methods in each of the metrics.

Fig. 2 shows the mean magnetic susceptibilities in different brain regions obtained with the different algorithms. In the deep gray matter regions, DEEPOLE QUASAR yielded lower values than any of the other methods (left panel). The slope between the different algorithms, however, was nearly identical (right panel), suggesting that nondipolar did not lead to systematic over- or underestimation.

Discussion and Conclusions: In the digital brain phantom experiment, the DEEPOLE QUASAR algorithm, which integrates an extended model to account for nondipolar phase shifts, achieved more robust and accurate susceptibility estimates than state-of-the-art QSM algorithms. For the in vivo susceptibility estimates in the highly clinically relevant deep gray matter, we found an offset between DEEPOLE QUASAR and the conventional QSM methods, but the slope between the methods was close to 1.0. The results point toward the choice of the reference value [17] as a critical topic, and the potential effect of nondipolar phase contributions on referencing.

References:
[1] F. Schweser *et al.*, "Foundations …," *Z. Für Med. Phys.*, 2016, doi: 10.1016/j.zemedi.2015.10.002.
[2] D. A. Yablonskiy *et al.*, "Biophysical mechanisms of MRI …," *Proc. Natl. Acad. Sci.*, 2012, doi: 10.1073/pnas.1206037109.
[3] S. Wharton *et al.*, "Fiber orientation-dependent …," *Proc. Natl. Acad. Sci.*, 2012, doi: 10.1073/pnas.1211075109.
[4] K. Shmueli *et al.*, "Investigating lipids as a source of chemical exchange-induced MRI frequency shifts," *NMR Biomed.*, vol. 30, no. 4, p. e3525, 2017, doi: https://doi.org/10.1002/nbm.3525.
[5] F. Schweser *et al.*, "Quantitative susceptibility mapping (QSM) with an extended physical model … (QUASAR) mapping," *NMR Biomed.*, vol. 31, no. 12, p. e3999, 2018, doi: 10.1002/nbm.3999.
[6] T. Jochmann *et al.*, "U2-Net for DEEPOLE QUASAR …," presented at the International Society of Magnetic Resonance in Medicine (ISMRM) 27th Annual Meeting, Montreal, Canada, May 13, 2019.
[7] T. Jochmann *et al.*, "Quantitative mapping of susceptibility and non-susceptibility frequency with DEEPOLE QUASAR," in *International Society of Magnetic Resonance in Medicine (ISMRM) 29th Annual Meeting*, 2021.
[8] S. Bollmann *et al.*, "DeepQSM …," *NeuroImage*, vol. 195, pp. 373–383, Jul. 2019, doi: 10.1016/j.neuroimage.2019.03.060.
[9] J. Liu *et al.*, "Morphology …," *NeuroImage.*, 2012, doi: 10.1016/j.neuroimage.2011.08.082.
[10] C. Milovic *et al.*, "Fast nonlinear susceptibility inversion …," *Magn. Reson. Med.*, 2018, doi: 10.1002/mrm.27073.
[11] QSM Challenge 2.0 Organization Committee *et al.*, "QSM reconstruction challenge 2.0: Design and report of results," *Magn. Reson. Med.*, vol. 86, no. 3, pp. 1241–1255, 2021, doi: https://doi.org/10.1002/mrm.28754.
[12] F. Schweser *et al.*, "Toward online reconstruction of quantitative susceptibility maps: Superfast dipole inversion," *Magn. Reson. Med.*, vol. 69, no. 6, pp. 1581–1593, 2013, doi: 10.1002/mrm.24405.
[13] S. Wharton *et al.*, "Effects of white matter microstructure on phase and susceptibility maps," *Magn. Reson. Med.*, vol. 73, no. 3, pp. 1258–1269, 2015, doi: https://doi.org/10.1002/mrm.25189.
[14] J. P. Marques *et al.*, "QSM reconstruction challenge 2.0 …," *Magn. Reson. Med.*, 2021, doi: 10.1002/mrm.28716.
[15] H. S. Abdul-Rahman *et al.*, "Fast and robust three-dimensional best path phase unwrapping algorithm," *Appl. Opt.*, vol. 46, no. 26, pp. 6623–6635, Sep. 2007, doi: 10.1364/AO.46.006623.
[16] H. Sun *et al.*, "Background field removal using spherical mean value filtering and Tikhonov regularization," *Magn. Reson. Med.*, vol. 71, no. 3, pp. 1151–1157, 2014, doi: 10.1002/mrm.24765.
[17] S. Straub *et al.*, "Suitable reference tissues for quantitative susceptibility mapping of the brain," *Magn. Reson. Med.*, vol. 78, no. 1, pp. 204–214, 2017, doi: 10.1002/mrm.26369.

Single-Orientation Susceptibility Anisotropy Imaging

Thomas Jochmann[1,2], Ahmad Omira[1], Niklas Kügler[1], Robert Zivadinov[2,3], Jens Haueisen[1], Ferdinand Schweser[2,3]

[1]Technische Universität Ilmenau, Department of Computer Science and Automation, Ilmenau, Germany; [2]Buffalo Neuroimaging Analysis Center, Department of Neurology at the Jacobs School of Medicine and Biomedical Sciences, University at Buffalo, The State University of New York, Buffalo, NY, United States; [3]Center for Biomedical Imaging, Clinical and Translational Science Institute, University at Buffalo, The State University of New York, Buffalo, NY, United States

Summary: We present an approach for extracting susceptibility tensor components from a single orientation scan. The technique allows assessing structural tissue integrity, particularly in the white matter. Requiring only a single orientation renders the method clinically feasible.

Introduction: Imaging tissue anisotropy can yield relevant information about structural integrity [1]. The magnetic susceptibility of brain tissue depends on the orientation of the tissue in the magnetic field [2]. In white matter, the anisotropy is strongly related to the myelin lipid bilayer, which plays a key role in early brain development and is compromised in diseases like multiple sclerosis [1]. The 3×3 susceptibility tensor can be mapped via susceptibility tensor imaging (STI) [3]. STI, however, requires measuring the brain under multiple different head orientations, which renders the method clinically infeasible. Under a (clinically feasible) *single orientation*, the *apparent* susceptibility is affected by three out of the nine susceptibility tensor components:

$$f = f_{33} + f_{23} + f_{13} = (\chi_{33} * d_{33}) + (\chi_{23} * d_{23}) + (\chi_{13} * d_{13}).$$

The field perturbations f_{ij} induced by each of these three components follow characteristic spatial fingerprints (kernels) (**Fig. 1**).

In this work, we present a fitting technique that separates these three susceptibility tensor components based on a single MRI scan. We focused on χ_{13} and χ_{23}, because these off-diagonal elements of the susceptibility tensor are potentially more sensitive to structural breakdown of aligned fibers than the bulk isotropic component on the main diagonal, and imaging of χ_{33} is already widely established through conventional QSM [4].

Methods: Fitting the STI model with a physics-informed neural network: We borrowed from deep learning methodology to fit the three susceptibility components in the equation above for each subject without involving separate training data (**Fig. 2**). Three randomly initialized *U-Nets* are iteratively optimized to map f to the estimates χ_{ij} (dipole inversion) such that the forward simulation (dipole convolution with the three kernels, summation) matches the input f (**Fig. 3**).

Ill-posedness, regularization, and calibration: Separating the sources is underdetermined because the kernels (d_{13}, d_{23}, d_{33}) are not orthogonal (e.g., f_{33} could be explained with $\chi_{23} * d_{23}$). We mediated the amplitude of the three susceptibility components with a loss-term based on their Frobenius norm and three weighting factors, because in real tissue, χ_{33} is vastly larger than the other two components. Using a dataset with recordings from 29 orientations [5], these weighting factors where calibrated such that the single-orientation estimates matched the STI solution.

Validation: We validated the method on another STI dataset with (*i*) the original phase measurements and (*ii*) a phantom with perfect phase data simulated from the STI solutions.
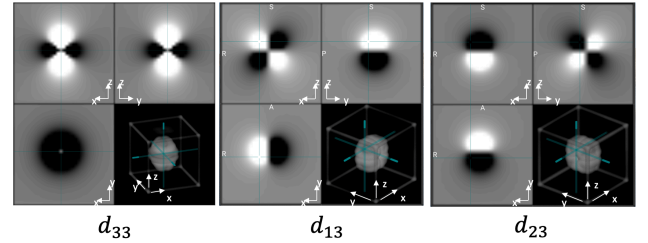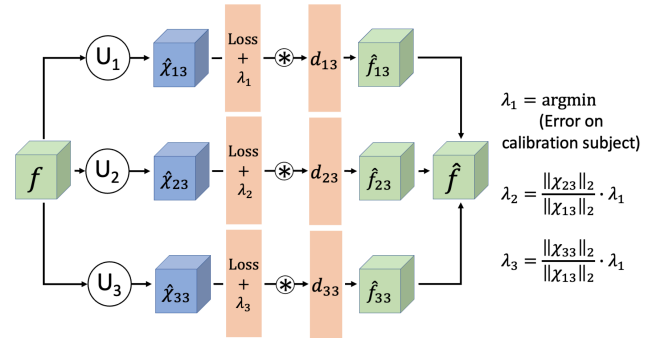

d_{33} d_{13} d_{23}

Fig. 1. Kernels d_{33}, d_{13}, and d_{23}.

$\lambda_1 = \text{argmin}$ (Error on calibration subject)

$\lambda_2 = \dfrac{\|\chi_{23}\|_2}{\|\chi_{13}\|_2} \cdot \lambda_1$

$\lambda_3 = \dfrac{\|\chi_{33}\|_2}{\|\chi_{13}\|_2} \cdot \lambda_1$

Fig. 2. Physics-informed network and loss weights to balance χ_{13}, χ_{23}, and χ_{33}.

input f (measured)   output $\hat{f}$ error $\hat{f} - f$
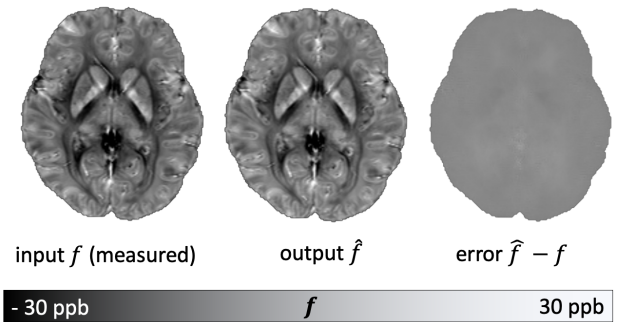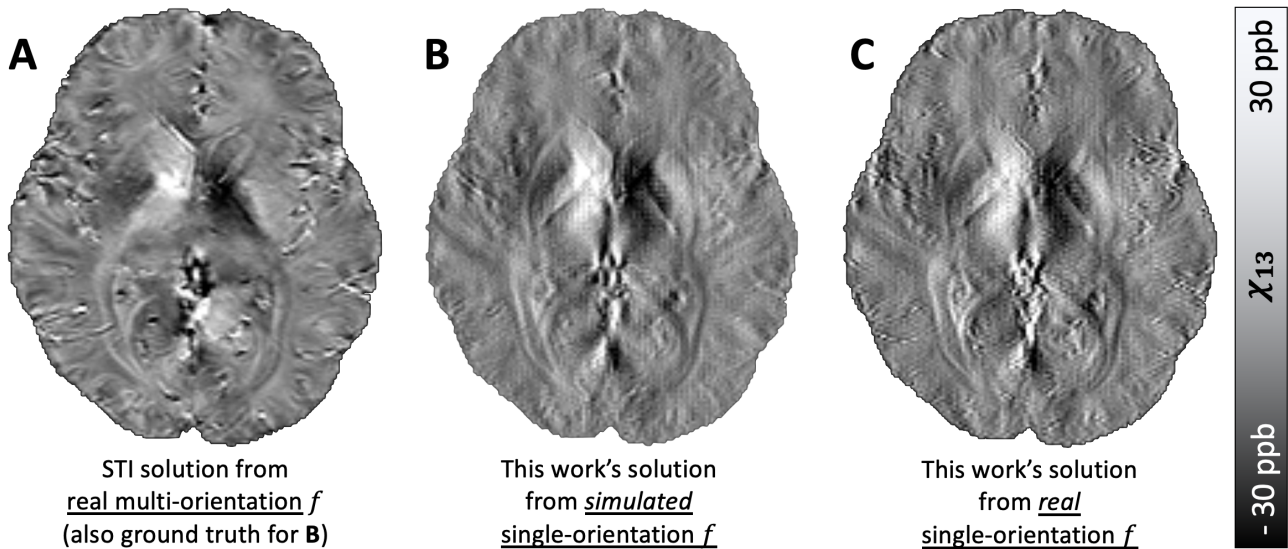
- 30 ppb f 30 ppb

Fig. 3. Upon convergence, the output field map matches the input, indicating mathematically valid solutions for χ_{ij} under the STI model.

Fig. 4. Estimated off-diagonal susceptibility tensor component χ_{13} from STI (gold standard) and this work. Similar to the STI solution, the off-diagonal solution visualizes deep gray matter nuclei and dense white matter tracts (optic radiations).

Results: <u>Phantom experiment and comparison to STI (gold standard):</u> **Fig. 4** shows how the single-orientation estimates of χ_{13} from a simulated f resemble the ground truth and the single-orientation estimates of χ_{13} from a real, measured f resemble the STI estimates. Results for χ_{23} were similar.

Discussion and Conclusions: The presented approach offers an alternative to STI by facilitating the isolation of only specific tensor components, χ_{13} and χ_{23}, from a single acquisition orientation. The method provides a novel basis for structural integrity assessment in white matter. A key challenge addressed by this approach is the ambiguity inherent in this source separation problem, especially given the small magnitude of χ_{13} and χ_{23} relative to χ_{33}.

From six or more available orientations, STI yields three more components of the symmetric susceptibility tensor: χ_{11}, χ_{22}, and to χ_{12}. Single-orientation phase data do not contain information about these components, making it mathematically impossible to determine them from a single orientation without additional assumptions about the tissue. Nevertheless, changes in any of the tensor components might typically not occur solitarily and imaging only three of the components might suffice to detect most of the potential tissue alterations.

This study provides a novel approach to STI that sidesteps the need for multiple head orientations, optimizing patient comfort and clinical utility. Despite the potential influence of χ_{33} on the smaller tensor components, our strategy for source separation demonstrates a high degree of precision in estimating χ_{13} and χ_{23}. Validated against established STI protocols and through phantom experiments, the method shows promise for studying white matter integrity.

References:
[1] D. A. Yablonskiy, J. Luo, A. L. Sukstanskii, A. Iyer, and A. H. Cross, "Biophysical mechanisms of MRI signal frequency contrast in multiple sclerosis," *Proc. Natl. Acad. Sci.*, vol. 109, no. 35, pp. 14212–14217, Aug. 2012, doi: 10.1073/pnas.1206037109.
[2] X. He and D. A. Yablonskiy, "Biophysical mechanisms of phase contrast in gradient echo MRI," *Proc. Natl. Acad. Sci.*, vol. 106, no. 32, pp. 13558–13563, Aug. 2009, doi: 10.1073/pnas.0904899106.
[3] C. Liu, "Susceptibility tensor imaging," *Magn. Reson. Med.*, vol. 63, no. 6, pp. 1471–1477, 2010, doi: 10.1002/mrm.22482.
[4] F. Schweser, A. Deistung, B. W. Lehr, and J. R. Reichenbach, "Differentiation between diamagnetic and paramagnetic cerebral lesions based on magnetic susceptibility mapping," *Med. Phys.*, vol. 37, no. 10, pp. 5165–5178, 2010, doi: 10.1118/1.3481505.
[5] Y. Shi, R. Feng, Z. Li, J. Zhuang, Y. Zhang, and H. Wei, "Towards in vivo ground truth susceptibility for single-orientation deep learning QSM: A multi-orientation gradient-echo MRI dataset," *NeuroImage*, vol. 261, p. 119522, Nov. 2022, doi: 10.1016/j.neuroimage.2022.119522.

Orientation dependency of white matter magnetic susceptibility with the QUASAR model

Thomas Jochmann[1,2], Niklas Kügler[1], Ahmad Omira[1], Robert Zivadinov[2,3], Jens Haueisen[1], Ferdinand Schweser[2,3]

[1]Technische Universität Ilmenau, Department of Computer Science and Automation, Ilmenau, Germany; [2]Buffalo Neuroimaging Analysis Center, Department of Neurology at the Jacobs School of Medicine and Biomedical Sciences, University at Buffalo, The State University of New York, Buffalo, NY, United States; [3]Center for Biomedical Imaging, Clinical and Translational Science Institute, University at Buffalo, The State University of New York, Buffalo, NY, United States

Summary: This study establishes the substantial influence of nondipolar frequency shifts on MRI phase contrast anisotropy, questioning established assumptions from susceptibility tensor imaging and quantitative susceptibility mapping, thereby paving the way for more accurate brain tissue characterization.

Introduction: Experimental evidence and theoretical considerations suggest that, in brain tissue, the formation of phase shifts depends not only on bulk isotropic magnetic susceptibility (with *dipolar* phase shifts) but also on tissue orientation, microstructure, and chemical exchange [1] with *nondipolar* phase. We recently presented a deep learning-based solution approach to the QUASAR model that includes these nondipolar frequency shifts that are not accounted for in the conventional QSM model (**Fig. 1**) [2].

In this work, we further investigated the underpinnings of phase contrast in the brain by studying the magnetic susceptibility and nondipolar frequency shifts under different orientations relative to the main magnetic field.

Methods: <u>Solution techniques:</u> We used our deep learning-based method DEEPOLE QUASAR to estimate magnetic susceptibility and nondipolar frequency shifts from frequency maps [2]. For comparison with the conventional QSM model, we used an identical deep learning-based approach but with QSM as the underlying physical model (in-house improved version [3] of DeepQSM [4]).
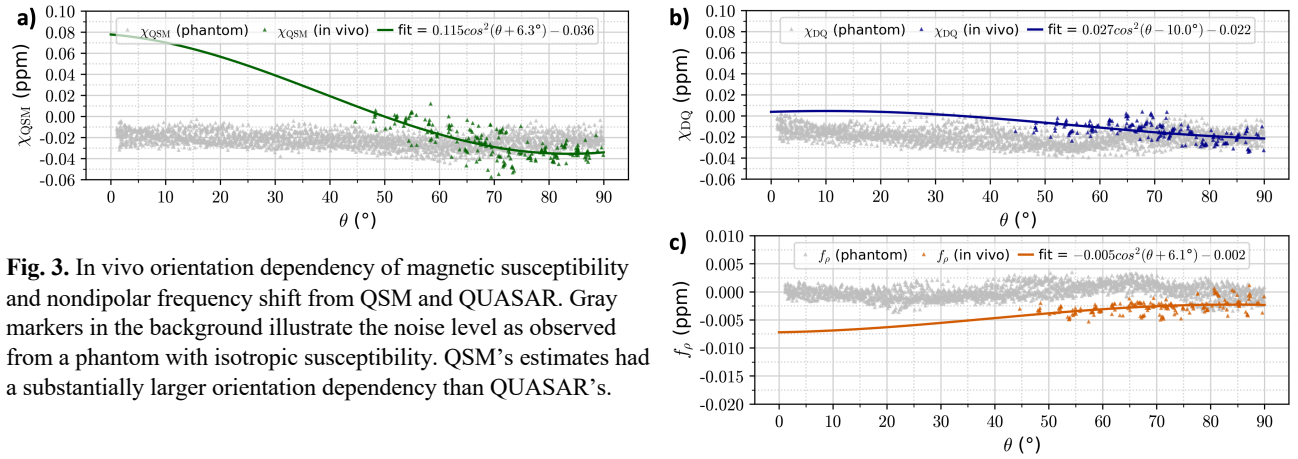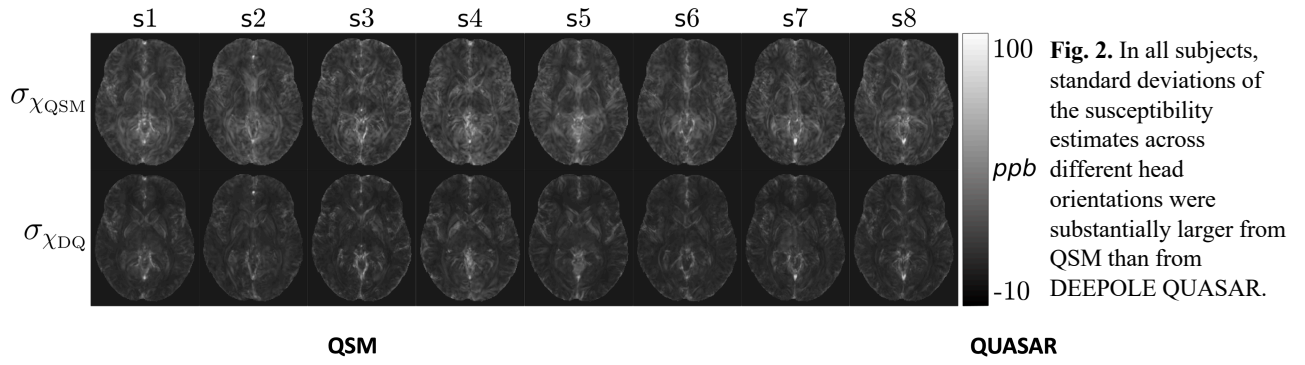
<u>Methods validation:</u> We first confirmed that in the absence of orientation dependency in the sources, the methods do not hallucinate any orientation dependency (**Fig. 3**, light gray markers in the background). We used a realistic brain susceptibility map and simulated phase data under different magnetic field orientations.

<u>Real phase data:</u> We studied the orientation dependence in regions of the brain that are known to be structurally anisotropic. We evaluated the voxel values of highly directional white matter fiber bundles (corpus callosum, optic radiations, and internal capsule) with regards to the underlying fiber orientation relative to the main magnetic field. We used MRI scans from eight patients, measured under 11-29 orientations to the main magnetic field [5].

Results: The orientation dependency with QSM was substantially stronger than with DEEPOLE QUASAR (**Fig. 3**). Neither DEEPOLE QUASAR's susceptibility estimate, nor its nondipolar frequency shift maps showed substantial orientation dependence. **Fig. 1** shows solutions of both methods from a representative subject under 8 different head orientations. **Fig. 2** shows the standard deviations across the solutions under different oblique head orientations from 8 subjects. **Fig. 3** shows the orientation dependence of the susceptibility and nondipolar frequency shift in the corpus callosum region of the same subject. We made comparable observations in the two studied corpus callosum regions, two optic radiation regions, and two internal capsule regions.
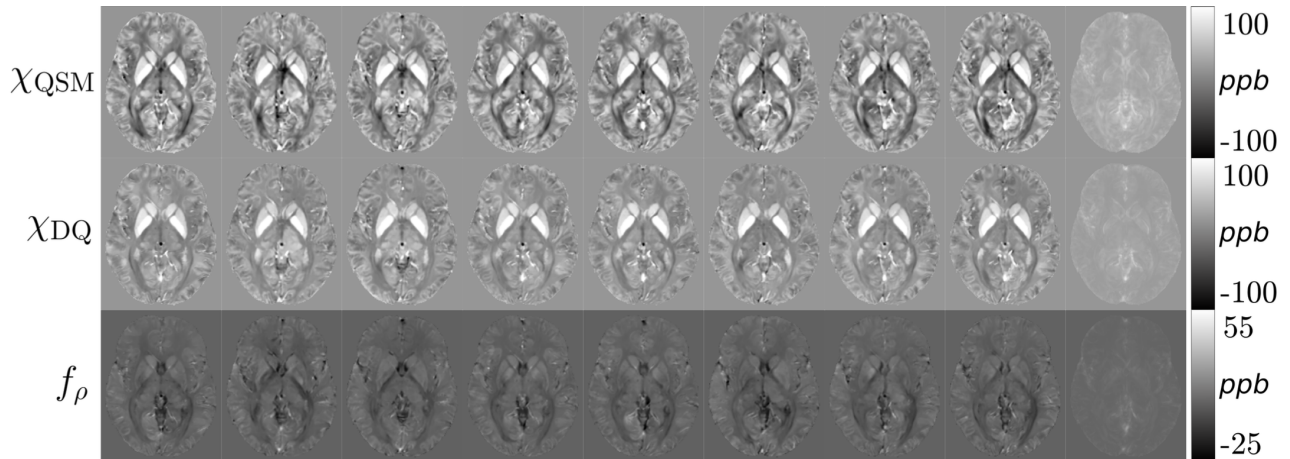
Fig. 1. Comparison of estimated sources under eight different head orientations (top row: QSM, middle and bottom row: DEEPOLE QUASAR). The rightmost column shows the standard deviation across 29 head orienations.

Fig. 2. In all subjects, standard deviations of the susceptibility estimates across different head orientations were substantially larger from QSM than from DEEPOLE QUASAR.

Fig. 3. In vivo orientation dependency of magnetic susceptibility and nondipolar frequency shift from QSM and QUASAR. Gray markers in the background illustrate the noise level as observed from a phantom with isotropic susceptibility. QSM's estimates had a substantially larger orientation dependency than QUASAR's.

Discussion and Conclusions: Our findings with DEEPOLE QUASAR suggest that anisotropy in frequency shifts is not solely attributable to magnetic susceptibility but potentially a misinterpretation of nondipolar frequency shifts, which are neglected by the conventional QSM model. Our findings suggest that QSM and STI may require to incorporate nondipolar contributions into their physical models.

The limited range of head tilt angles achievable in typical MRI scans, however, constrains our observations of the full angular spectrum, indicating the need for dedicated MRI protocols that can capture a wider range of orientations for a more comprehensive analysis.

The study presents a reassessment of quantitative susceptibility mapping considering the previously ignored, yet theoretically and experimentally shown nondipolar frequency shifts. Solutions from DEEPOLE QUASAR, a novel technique for mapping susceptibility and nondipolar shifts suggest that susceptibility anisotropy in white matter is smaller than previously thought and might instead be the result of a misinterpretation of nondipolar shifts, which could stem from chemical exchange or tissue microstructure.

References:
[1] F. Schweser and R. Zivadinov, "Quantitative susceptibility mapping (QSM) with an extended physical model for MRI frequency contrast in the brain: a proof-of-concept of quantitative susceptibility and residual (QUASAR) mapping," *NMR Biomed.*, vol. 31, no. 12, p. e3999, 2018, doi: 10.1002/nbm.3999.
[2] T. Jochmann, J. Haueisen, R. Zivadinov, and F. Schweser, "U2-Net for DEEPOLE QUASAR–A Physics-Informed Deep Convolutional Neural Network that Disentangles MRI Phase Contrast Mechanisms," presented at the International Society of Magnetic Resonance in Medicine (ISMRM) 27th Annual Meeting, Montreal, Canada, May 13, 2019.
[3] T. Jochmann, J. Haueisen, and F. Schweser, "How to train a Deep Convolutional Neural Network for … (QSM)," in *International Society of Magnetic Resonance in Medicine (ISMRM) 28th Annual Meeting, Virtual Conference*, 2020.
[4] S. Bollmann *et al.*, "DeepQSM - using deep learning to solve the dipole inversion for quantitative susceptibility mapping," *NeuroImage*, vol. 195, pp. 373–383, Jul. 2019, doi: 10.1016/j.neuroimage.2019.03.060.
[5] Y. Shi, R. Feng, Z. Li, J. Zhuang, Y. Zhang, and H. Wei, "Towards in vivo ground truth susceptibility for single-orientation deep learning QSM: A multi-orientation gradient-echo MRI dataset," *NeuroImage*, vol. 261, p. 119522, Nov. 2022, doi: 10.1016/j.neuroimage.2022.119522.

Fast and High-Resolution Whole Brain SWI and QSM with CAIPIRINHA 3D-EPI and Deep-Learning Reconstruction

Jin Jin[1], Josef Pfeuffer[2], Dominik Nickel[2], Monique Tourell[3], Ashley Stewart[3], Steffen Bollmann[3], Saskia Bollmann[3], Markus Barth[3], Kieran O'Brien[1]

[1] *Siemens Healthcare Pty Ltd, (Brisbane, Australia);* [2] *Siemens Healthineers AG, Application Development, Erlangen, Germany;* [3] *The University of Queensland, (Brisbane, Australia)*

Summary: To address the strong clinical desire for fast and in-line Susceptibility Weighted Imaging (SWI) and Quantitate Susceptibility Mapping (QSM) images, a flow-compensated, CAIPIRINHA-accelerated 3-dimensional echo planar imaging (3DEPI) research sequence with deep learning-based image reconstruction and super-resolution was developed. The sequence can acquire sub-millimetre resolution, whole-brain images in under 80 seconds, while providing high image quality and anatomical detail in T2*, SWI, QSM, and (susceptibility map weighted images) SMWI images.

Introduction: SWI is a mature technique that combines the T2*w magnitude and filtered-phase images from a 3D T2*-weighted acquisition to visualize the influence of local magnetic field changes in tissues[1]. SWI is playing an increasingly vital role in visualizing pathological conditions, such as stroke, vascular malformation, neurodegenerative disorders, and tumour[2]. The more recently developed QSM can utilise the same T2*w acquisitions but aims to better differentiate paramagnetic tissues from diamagnetic tissues by differentiating between local and background effects on the measured phase[3]. In T2*w acquisitions, the sensitivity of the MR signal to tissue susceptibility increases with echo time (TE). Hence, relatively long TEs are typically used in SWI and QSM acquisitions (e.g., TE-optimized for SWI are approximately 40 ms and 20 ms for 1.5T and 3T, respectively[3,4]). When a typical 3D gradient echo (3DGRE) sequence is used for high-resolution, whole-brain acquisitions, scan times can be as long as 5-10 minutes. As a result, there is a strong clinical desire to shorten the scan time without compromising image quality. In this work, we aim to substantially accelerate the high-resolution susceptibility-sensitive acquisitions combining a fast 3DEPI sequence[5,6] with deep learning (DL) reconstruction to enhance image quality.

Methods: All experiments were performed on a 3T clinical scanner (MAGNETOM Vida, Siemens Healthcare, Erlangen, Germany) with two healthy volunteers. This study employed a segmented, flow-compensated 3DEPI research sequence that is highly flexible in EPI train length, acceleration factor and CAIPIRINHA acceleration sampling patterns[5,7]. Table 1 provides the imaging protocol with 0.82 mm isotropic resolution and whole-brain coverage in 79 seconds. The fast acquisition was facilitated by 4× CAIPIRINHA acceleration and EPI acquisition with an echo-train length of 5.

The magnitude and phase images are reconstructed inline using either a conventional GRAPPA or DL-based[8] reconstruction. The DL reconstruction comprises two independent, sequential processing steps. Firstly, images are generated on the acquired resolution using a variational network architecture with six iterations that alternate between parallel imaging reconstruction and 3D image regularizations using U-nets[8]. The network parameters were determined through supervised training based on about 500 fully sampled 3D datasets of head, abdomen, and pelvis from healthy volunteers (no 3DEPI data included). Secondly, the obtained images were interpolated using a DL-based super-resolution algorithm[9], with a factor-of-two interpolation in all spatial dimensions. Both steps were implemented in PyTorch, trained on a dedicated GPU cluster. The obtained network parameters were exported for prospective use in the scanner reconstruction pipeline.

Following image reconstruction, the research sequence offers further inline processing, including SWI, minimum intensity projection (mIP), QSM and a susceptibility map weighted image (SMWI)[10]. The in-line QSM processing mostly follows the same methods as the off-line QSM pipeline QSMxT[11].

Table 1 *3DEPI imaging protocols with 0.82×0.82×0.82 mm³ isotropic resolution.*

Figures	FOV read (mm)	FOV phase	base res	Reconstruction	Recon. Resolution (mm)	slices	slice thickness (mm)	FA (°)	TE (ms)	TR (ms)	Acceleration	BW (Hz/Px)	EPI	TA (min:sec)
Fig.1A	222	87.50%	277	GRAPPA	0.82 iso	192	0.82	15	21	41	4	288	5	1:19
Fig.1B			544	DL	0.41 iso									

Results: 3DEPI+GRAPPA (Fig.1A) produced high anatomical details across the brain regions. Specifically, blood vessels and surrounding tissues appeared sharp in the 3DEPI SWI/mIP images. DL reconstruction (Fig.1B) further improved the image fidelity for the 3DEPI scans, hence recovering even more details of tissues and vessels. The substantia nigra is better defined in Fig1.B, compared with Fig.1A, while the vessels are notably more delineated with DL recon compared with GRAPPA counterparts.

Fig.1A and 1B display the subsequent inline processing using the GRAPPA and DL images respectively, providing filtered phase, SWI, mIP, QSM and SMWI. The DL-QSM is of significantly higher quality than GRAPPA-QSM throughout the FOV, especially around the centre of the FOV (e.g., substantia nigra). Consequently, the DL-SMWI appears to have enhanced contrast thanks to the improved susceptibility maps. The phase, filtered phase, and QSM maps of different views are provided in Fig.1C and Fig.1D for GRAPPA and DL reconstructions, respectively, where the enhanced quality is better appreciated, such as, around basal ganglia.
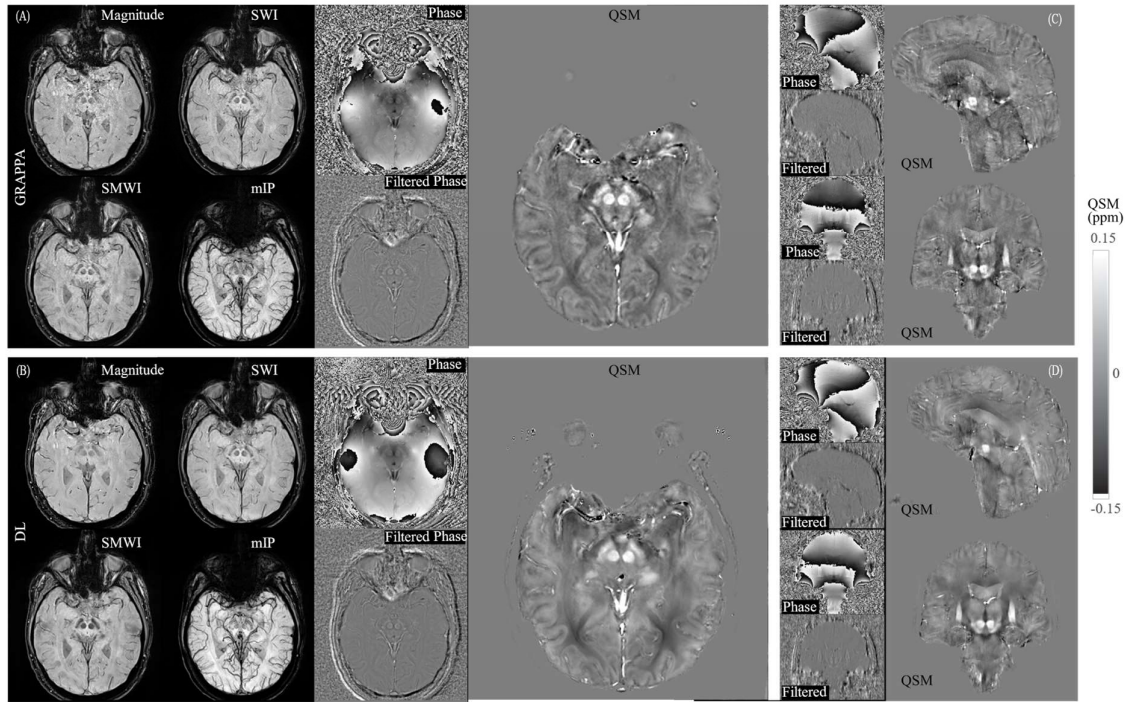
Figure 1 Isotropic 3DEPI scans with QSM processing. (A): The acquisition was reconstructed using GRAPPA reconstruction. (B) The same acquisition was reconstructed using DL reconstruction. (C) and (D); The phase, filtered phase and QSM images of (A) and (B) are shown in sagittal and coronal orientation. The QSM images are shown in linear scaled between -0.15 to 0.15 ppm.

Conclusions: The fast 3DEPI acquisition and the DL reconstruction techniques indicate considerable potential to explore the benefit of shorter scan times and/or enhancement of image quality to further elucidate the clinical value for both SWI and QSM contrasts.

References:

1. Haacke, E. M., Xu, Y., Cheng, Y.-C. N. & Reichenbach, J. R. Susceptibility weighted imaging (SWI). *Magnetic Resonance in Medicine* **52**, 612–618 (2004).
2. Mittal, S., Wu, Z., Neelavalli, J. & Haacke, E. M. Susceptibility-Weighted Imaging: Technical Aspects and Clinical Applications, Part 2. *American Journal of Neuroradiology* **30**, 232–252 (2009).
3. Haacke, E. M. *et al.* Quantitative susceptibility mapping: current status and future directions. *Magnetic Resonance Imaging* **33**, 1–25 (2015).
4. Haacke, E. M., Mittal, S., Wu, Z., Neelavalli, J. & Cheng, Y.-C. N. Susceptibility-Weighted Imaging: Technical Aspects and Clinical Applications, Part 1. *American Journal of Neuroradiology* **30**, 19–30 (2009).
5. Jin Jin *et al.* Segmented 3D EPI with CAIPIRINHA for Fast, High-Resolution T2*-weighted Imaging. in *Proc. Annu. Meeting ISMRM* (2021).
6. Tourell, M. *et al.* Three-dimensional EPI with shot-selective CAIPIRIHANA for rapid high-resolution quantitative susceptibility mapping at 3 T. *Magnetic Resonance in Medicine* **92**, 997–1010 (2024).
7. Monique Tourell *et al.* Submillimeter, Sub-Minute Quantitative Susceptibility Mapping using a Multi-Shot 3D-EPIwith 2D CAIPIRINHA Acceleration. in *Proc. Annu. Meeting ISMRM* (2021).
8. Hammernik, K. *et al.* Learning a variational network for reconstruction of accelerated MRI data. *Magnetic Resonance in Medicine* **79**, 3055–3071 (2018).
9. Almansour, H. *et al.* Deep Learning-Based Superresolution Reconstruction for Upper Abdominal Magnetic Resonance Imaging: An Analysis of Image Quality, Diagnostic Confidence, and Lesion Conspicuity. *Investigative Radiology* **56**, (2021).
10. Gho, S.-M. *et al.* Susceptibility map-weighted imaging (SMWI) for neuroimaging. *Magnetic Resonance in Medicine* **72**, 337–346 (2014).
11. Stewart, A. W. *et al.* QSMxT: Robust masking and artifact reduction for quantitative susceptibility mapping. *Magnetic Resonance in Medicine* **87**, 1289–1300 (2022).

Conformal Quantitative Susceptibility Mapping

Mathias Lambert[1], Carlos Milovic[1]

[1]Pontificia Universidad Católica de Chile

Summary: Current QSM reconstruction techniques typically do not provide statistical guarantees against errors and hallucinations in the model. By applying conformal prediction to QSM it's possible to identify which structures are real and which are artifacts.

Introduction: Currently, black-box machine learning models are frequently employed in high-risk contexts, such as medical diagnostics, where uncertainty quantification is necessary to prevent unexpected model failures. A simple paradigm for producing statistically rigorous uncertainty sets or intervals for the predictions of such models is conformal prediction[1], often known as conformal inference. In this paper we explore the application of the conformal prediction framework to a neural network to reconstruct susceptibility maps.

Methods: We apply the image-to-image conformal regression framework[2] to a simple 3D U-net type network, with 6 layers and leakyrelu activation function. We train the network with 26000 forward simulations formed from the composition of geometric shapes (sphere, prism, cone, torus), 15 epoch. The loss function used was:

$$L(x, y) = 2 \cdot |x - y|_1 + \varphi_{\frac{\alpha}{2}}(l(x), y) + \varphi_{1-\frac{\alpha}{2}}(u(x), y)$$

Where $l(x)$ indicates a pixel that could have a much lower value than the prediction, $u(x)$ indicates a pixel that could have a much higher value than the prediction, α is the risk level and φ_α is the quantile loss or pinball loss.

We tested the network against a forward simulation based on COSMOS, with complex noise at SNR 100. In addition, we tested the same simulation with a 2π peak in the center.
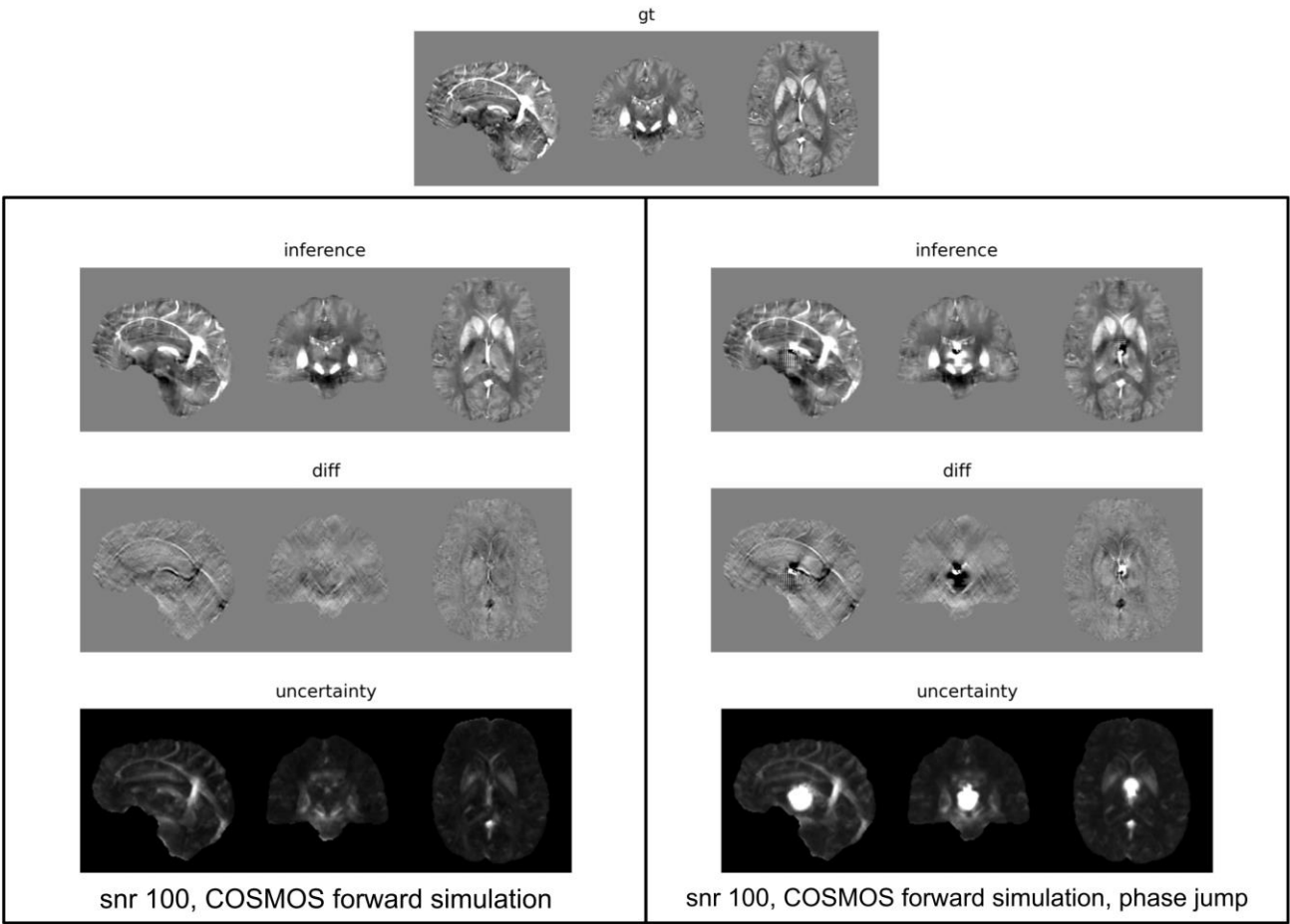
Results: The network obtained an RMSE of 45.34 for the COSMOS simulation and an RMSE of 60.80 for the simulation with the phase inconsistency at the center.

Discussion and Conclusions: The results show that the network can identify areas where artefacts are generated as areas of high uncertainty and blood vessels as areas of uncertainty. The last point is interesting as the reconstruction quality of these areas is usually measured visually, so the conformal prediction framework might allow a better evaluation of the reconstructions and consequently an improvement in the reconstruction methods.

References:
[1]Angelopoulos, A. N. and Bates, S., "A Gentle Introduction to Conformal Prediction and Distribution-Free Uncertainty Quantification", arXiv e-prints, 2021. doi:10.48550/arXiv.2107.07511.
[1]Angelopoulos, A. N., "Image-to-Image Regression with Distribution-Free Uncertainty Quantification and Applications in Imaging", arXiv e-prints, 2022. doi:10.48550/arXiv.2202.05265.

Figures -

gt

inference

diff

uncertainty

snr 100, COSMOS forward simulation

inference

diff

uncertainty

snr 100, COSMOS forward simulation, phase jump

Evaluation of the diamagnetic and paramagnetic maps of the Locus Coeruleus

Fábio Seiji Otsuka[1], Pedro Burlacchini Sanches Marinho[1], Bruno Fracchini Pastorello[1], Chunlei Liu[2], Roberta Diehl Rodriguez[1], Maria Concepción García Otaduy[1]

[1]LIM44, Instituto e Departamento de Radiologia, HC-FMUSP, Sao Paulo, Brazil; [2]Department of Electrical Engineering and Computer Sciences, Helen Wills Neuroscience Institute, University of California, Berkeley, Berkeley, CA, USA;

Summary: Here we describe magnetic susceptibility properties of the locus coeruleus for different stages of Alzheimer's disease (AD) pathology. Diamagnetic (DCS) and paramagnetic (PCS) components were processed and compared with the respective Braak index. A significant association was observed with the QSM and DCS maps, and the stratification into Low Braak (LB) and High Braak (HB) index was also significant with QSM and DCS using the mean values.

Introduction: The Locus Coeruleus (LC) is a small structure rich in neuromelanin (NM), being the main producer of noradrenaline in the brain. It is known that AD neuropathology begins years before the onset of disease-defining-symptoms, and the locus coeruleus (LC) is one of the first brain structures to be affected by the pathology [1], which makes it a potential biomarker for early disease diagnosis. Unfortunately, LC structure is very small and difficult to visualize by MRI, making it very challenging to use it as an imaging biomarker. Also, it is still of debate what is the origin for the LC contrast observed on the NM sensitive images, which difficult interpretation of the results. Here we proposed to analyze the magnetic susceptibility properties of the MR signal within the LC and compare it with histological results to gain insight about how AD pathology burden affects LC MRI signal

Methods: 12 *postmortem* subjects (7 male, mean age of 78 +/- 14) were recruited by the City Death Verification Service after the family signed informed consent. The research ethics committee of the Medical School of the University of São Paulo (approval number 14407) approved this study. All subjects presented no known neurological disease or presence of focal brain lesions. *Postmortem in situ* brain MRI was performed with a Magnetom 7T scanner (Siemens, Germany) and a 32ch head coil (Nova Medical, USA). QSM acquisition was based on a 3D FAT SAT GRE multi-echo sequence, with five echoes (first echo 5ms, ΔTE of 4ms), flip angle of 10º, 25ms TR, 2 mm axial thick sections, and 0.4mm in plane resolution. The *postmortem* interval was between 11h and 20h. The QSM, diamagnetic (DCS) and paramagnetic (PCS) components maps were calculated using the DECOMPOSE algorithm, with phase pre-processing steps using the functions included in the STISuite toolbox. Mean and median values were obtained by applying an LC mask to the corresponding maps. The LC was segmented manually from the 1st echo magnitude images identified as the brightest circular structure (on axial planes) located bilaterally to the fourth ventricle, caudally to the substantia nigra, with subsequent corrections made on the sagittal and coronal planes to avoid overlap with other structures. Upon autopsy, the whole brain was procured and fixed in buffered 10% formalin. Alzheimer's pathological staging was performed according to Braak stage for AD pathology [2], by evaluating the presence and distribution of the main proteinopathies underlying neurodegenerative diseases: hyperphosphorylated tau protein (AT8), amyloid-β (4G8), phosphor TDP-43 (1D3/TDP43), α-synuclein phosphor (81a). The analyzed brain area sections were the superior frontal gyrus, middle and inferior temporal gyri, hippocampus at the level of geniculate body, amygdala and occipital cortex. To assess correlation between Braak staging and QSM, PCS and DCS the Kendall's tau test was used. To compare QSM, PCS and DCS for groups of different AD pathology burden, we divided subjects in two groups: group of lower Braak (LB), with Braak spanning from 0 to 3; and group of higher Braak (HB), with Braak spanning from 4 to 6. Comparison between both groups was assessed by the Mann-Whitney U test. Statistical significance was considered when p<0.05.

Results: After Braak staging, subjects were divided in two groups, LB and HB, with n=7 and n=5, respectively. Figure 1 shows the manually segmented LC mask superimposed to the GRE image for a single subject. Figure 2 shows an example of QSM, PCS and DCS maps for a subject. Table 1 shows results from the correlation of QSM, PCS and DCS with Braak staging using Kendall's tau test. Table 2 shows results for the comparison between lower (LB) and higher Braak (HB) group using Mann-Whitney test.

| Corr with Braak	mean QSM (ppm)	median QSM (ppm)	mean PCS (ppm)	median PCS (ppm)	mean DCS (ppm)	median DCS (ppm)
Kendall's tau b	0.582	0.554	0.291	0.453	0.453	0.420
p value	**0.012**	**0.017**	0.207	**0.050**	**0.050**	0.068

Table 1 - Kendall's tau b and p-value for the Kendall's tau test, between the Braak stage and the mean and median values of QSM, PCS and DCS maps.

Braak groups	mean QSM (ppm)	median QSM (ppm)	mean PCS (ppm)	median PCS (ppm)	mean DCS (ppm)	median DCS (ppm)
LB (0-3)	-0.116	-0.099	0.028	0.006	-0.138	-0.105
HB (4-6)	0.006	-0.006	0.061	0.039	-0.055	-0.039
p value	**0.018**	**0.034**	0.343	0.106	**0.030**	**0.030**

Table 2 - mean values and median of the QSM, PCS and DCS maps for the LB (1st row) and HB (2nd row), and the p-values of the Mann-Whitney test (3rd row).
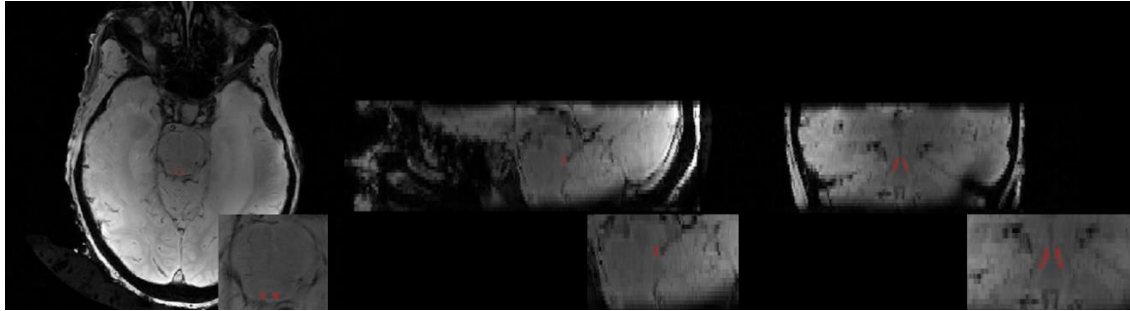
Figure 1 - Gradient echo image (1st echo) at three orthogonal planes (axial, sagittal and coronal, from left to right). ROI mask of the LC is shown superimposed in red.
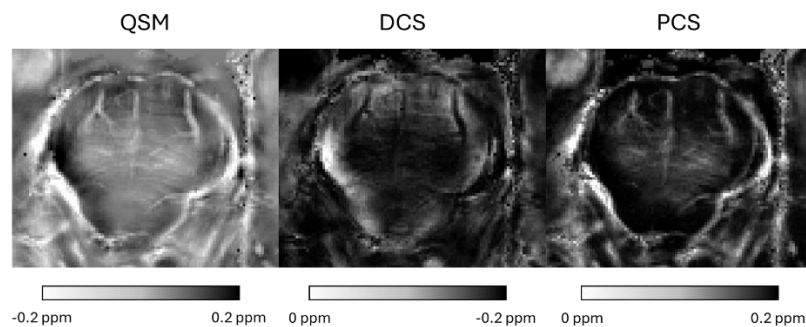
Figure 2 - QSM, DCS and PCS maps processed for a subject at the level of the LC.

Discussion and Conclusions: It is still not completely elucidated what drives MRI contrast within the LC on the NM sensitive images, which are commonly based on T1- and MT-weighted images. NM itself is paramagnetic and its concentration is associated with neuronal density, which is reduced with pathology. Therefore, QSM could be an interesting tool to evaluate LC composition during aging and pathology progression. However, QSM is also affected by other paramagnetic components (i.e. iron and copper), and diamagnetic components (myelin and proteins), which varies with age and pathology progression. Using DECOMPOSE algorithm we were able to disentangle the paramagnetic from the diamagnetic component of the QSM signal. We observed that the main component which was driving the changes in QSM was the DCS, as shown in Table 1. Although PCS was slightly higher for higher Braak staging, as indicated by the positive correlation between median PCS and Braak, the differences in PCS for both evaluated groups was not significant. Since we expect to have a lower NM concentration for the HB group, we hypothesize that the lack of significant changes in PCS with pathology might be due to the counteracting effect of NM decrease and iron deposition during neurodegeneration. On the other hand, the significant increase of DCS might be associated to a loss of myelin during disease progression. A point-to point correlation of these maps results with histopathology results, with iron, protein and myelin quantification would contribute to complement the interpretation of the results. However, these preliminary results already highlight the potential of QSM to evaluate AD disease progression in vivo.

References:

[1] Jack CR, Knopman DS, Jagust WJ, Petersen RC, Weiner MW, Aisen PS, et al. Tracking pathophysiological processes in Alzheimer's disease: An updated hypothetical model of dynamic biomarkers. The Lancet Neurology. 2013.

[2] Braak, H. & Braak, E. Staging of Alzheimer's disease-related neurofibrillary changes. *Neurobiol. Aging* 16, 271–278 (1995).

Impact of angulated acquisitions in QSM reconstructions

Nestor Muñoz[1,2,3], Carlos Milovic[1,2], Cristian Tejos[1,2,3]

[1]Biomedical Imaging Center (Pontificia Universidad Católica de Chile, Santiago, Chile); [2]Department of Electrical Engineering (Pontificia Universidad Católica de Chile, Santiago, Chile); [3]Millennium Institute Millennium Institute for Intelligent Healthcare Engineering (iHEALTH)(Chile)

Introduction: Quantitative Susceptibility Mapping (QSM) is a novel technique that provides a scalar value for the magnetic susceptibility in human tissue [1], [2]. QSM have been applied to study neurological disorders like Parkinson Disease, multiple sclerosis, psychosis, among others [3], [4], [5].All these studies made dozens of QSM reconstructions, assuming a complete alignment of the head with the direction of the main magnetic field [2]. Tilting the head may affect the expected susceptibility value, due to the susceptibility anisotropy that exists in human brain [6], [7]. In this work, we aim to analyze the influence of rotating the head in QSM reconstructions under realistic circumstances.

Methods: For this work, we used the Susceptibility Tensor Imaging (STI) brain phantom, designed by an eigen-decomposition of simulated eigenvalues and reconstructed eigenvectors [8], [9]. Using the STI brain phantom, we simulated 30 directions of the head that followed rotations of the head in the left-right (θ_{LR}) and antero-posterior (θ_{AP}) axis. Rotations followed a gaussian distribution, with zero mean and standard value of $4°$ and $2.6°$ for θ_{LR} and θ_{AP} respectively [10]. Afterwards, we simulated 30 acquisitions that followed the simulated directions using Eq. 1 and Eq. 2.

$$\delta_n(r) = FT^{-1}\left(A_n \cdot FT(\chi(r))\right) (1)$$

where δ_n corresponds to the local field at a certain orientation n with respect to the main magnetic field, χ a vectorized form of the susceptibility tensor, and $A_n = [a_{11,n} \quad a_{12,n} \quad a_{13,n} \quad a_{22,n} \quad a_{23,n} \quad a_{33,n}]$ is the system matrix of size 1×6, with elements $a_{ii,n}$ and $a_{ij,n}$ described as,

$$a_{ii,n} = \frac{H_{i,n}H_{i,n}}{3} - \frac{k^T \hat{H}_n\left(k_i H_{i,n}\right)}{\|k\|^2}, a_{ij,n} = \frac{2H_{i,n}H_{j,n}}{3} - \frac{k^T \hat{H}_n\left(k_i H_{j,n} + k_j H_{i,n}\right)}{\|k\|^2} (2)$$

where $\hat{H}_n$ is the unit vector of the main magnetic field. We reconstructed QSM maps using the NDI algorithm [11] without adding noise was the the local field simulations. Finally, we analized the influence of rotating the head in each brain tissue that compose the STI brian phantom.

Results and Discussions: Fig. 1 shows the comparison between two local field simulations (first row) and their respective QSM image (second column) at two rotated acquisitions (first and second column). Looking at the differences in simulated local field and QSM images (Fig.1, third column) and standard deviation (Fig.1, fourth column), we can see a clear difference in deep brain nuclei (yellow arrows) rather than in white matter. This indicates that deep brain nuclei might be more affected to rotated acquisitions than white matter. Boxplots of local field simulations (Fig. 2) and QSM images (Fig. 3) also shows a bigger difference in deep brain nuclei, such as substantia nigra, putamen or globus pallidus. This observation could indicate the presence of anisotropy within these nuclei, and it is essential to consider this aspect when acquiring GRE acquisitions for magnetic susceptibility studies. Compared to the QSM image aligned to the main magnetic field, the amygdala reached a difference over 24%, and hippocampus reached a difference over 16%, even with rotations of the head only at $5°$ out of the main magnetic field.

Conclusions: We effectively studied the impact of minor rotations of the head in the scanning process of a QSM typical clinical study. Acquisitions with the head rotated might have a big impact in the results, because of the susceptibility anisotropy that exists inside the brain.

References:
[1]   K. Shmueli, "Quantitative Susceptibility Mapping," vol. 1, pp. 819–838, Jan. 2020, doi: 10.1016/B978-0-12-817057-1.00033-0.
[2]   QSM Consensus Organization Committee *et al.*, "Recommended implementation of quantitative susceptibility mapping for clinical research in the brain: A consensus of the ISMRM electro-magnetic tissue properties study group," *Magn Reson Med*, vol. 91, no. 5, pp. 1834–1862, Jan. 2024, doi: 10.1002/MRM.30006.
[3]   C. Langkammer *et al.*, "Quantitative Susceptibility Mapping in Multiple Sclerosis," *Radiology*, vol. 267, no. 2, pp. 551–559, May 2013, doi: 10.1148/radiol.12120707.
[4]   C. Langkammer *et al.*, "Quantitative Susceptibility Mapping in Parkinson's Disease," *PLoS One*, vol. 11, no. 9, pp. 1–13, Sep. 2016, doi: 10.1371/journal.pone.0162460.
[5]   M. García Saborit *et al.*, "Quantitative Susceptibility Mapping MRI in Deep-Brain Nuclei in First-Episode Psychosis," *Schizophr Bull*, Apr. 2023, doi: 10.1093/SCHBUL/SBAD041.
[6]   C. Liu, "Susceptibility tensor imaging," *Magn Reson Med*, vol. 63, no. 6, pp. 1471–1477, 2010, doi: 10.1002/mrm.22482.

[7]   W. Li, C. Liu, T. Q. Duong, P. C. M. van Zijl, and X. Li, "Susceptibility tensor imaging (STI) of the brain," *NMR Biomed*, vol. 30, no. 4, Apr. 2017, doi: 10.1002/nbm.3540.

[8]   N. Muñoz, C. Milovic, C. Langkammer, and C. Tejos, "Microstructure simulation in susceptibility tensor brain phantom," in *2022 Joint Workshop on MR phase, magnetic susceptibility and electrical properties mapping*, Lucca, Oct. 2022.

[9]   N. Muñoz, C. Milovic, and C. Tejos, "Realistic brain phantom for Susceptibility Tensor Imaging," in *ISMRM & ISMRT Annual Meeting & Exhibition*, London, 2022.

[10]   P. Prabhu *et al.*, "Content-Based Estimation of Brain MRI Tilt in Three Orthogonal Directions," *J Digit Imaging*, doi: 10.1007/s10278-020-00400-7.

[11]   D. Polak *et al.*, "Nonlinear dipole inversion (NDI) enables robust quantitative susceptibility mapping (QSM)," 2020, doi: 10.1002/nbm.4271.
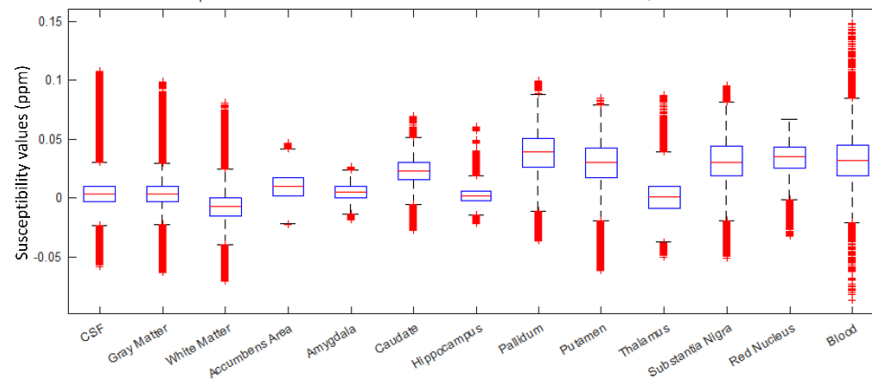
Figures:
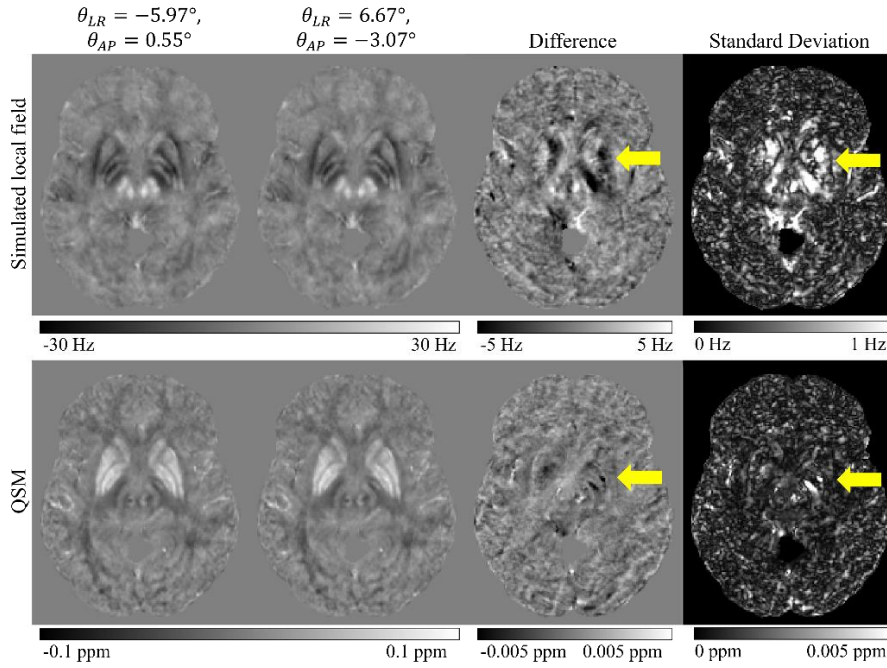
Figure 1. Local field simulations (first row) and QSM images (second row) at different acquisition orientations (first and second column). Difference of both orientations is shown in third column, and the standard deviation of both, simulated local field and QSM images is shown in fourth column.
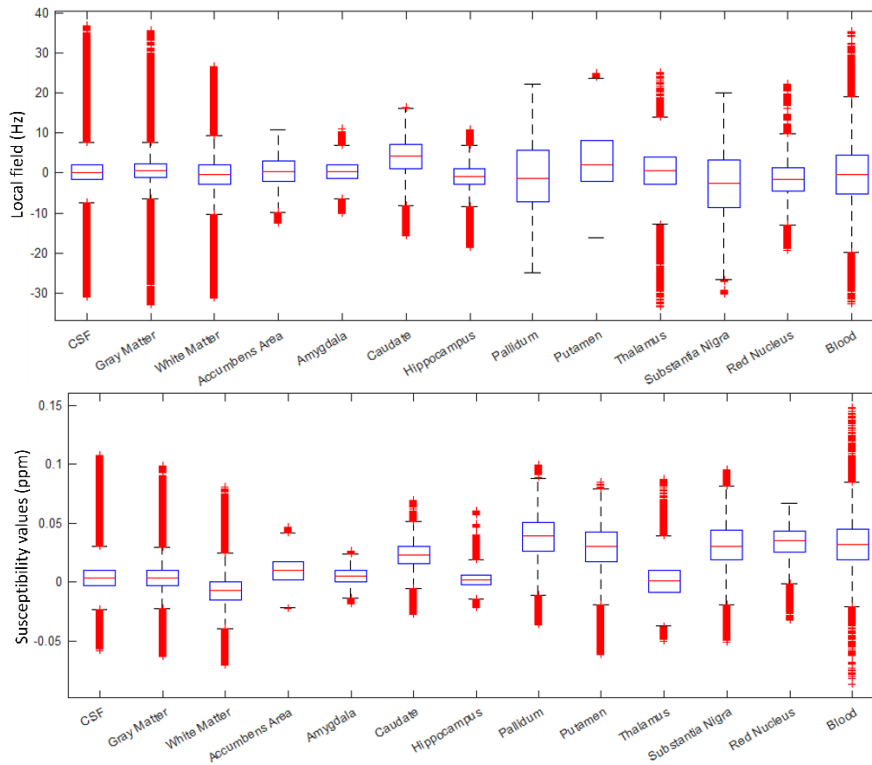
Figure 2. Boxplot of the local field (Hz) simulations at different orientations for multiple brain tissue.

Figure 3. Boxplot of the susceptibility mapping images (ppm) at different orientations for multiple brain tissue.

Interpretable Machine Learning Model for Characterizing Magnetic Susceptibility-based Biomarkers in First Episode Psychosis

Pamela Franco[1,2], Cristian Montalba[3,4,5], Raúl Caulier-Cisterna[6], Carlos Milovic[7], Alfonso González[8,9], Juan Pablo Ramirez-Mahaluf[8], Juan Undurraga[8,10], Rodrigo Salas[1,3], Nicolás Crossley[3,4,8], Cristian Tejos[3,4,12], Sergio Uribe[13]

[1] Biomedical Engineering School (Universidad de Valparaíso, Valparaíso, Chile); [2] Physics Department, Faculty of Sciences (Universidad de Santiago, Santiago, Chile); [3] Millennium Institute for Intelligent Healthcare Engineering (Santiago, Chile) ; [4] Biomedical Imaging Center (Pontificia Universidad Católica de Chile, Santiago, Chile); [5] Radiology Department (Pontificia Universidad Católica de Chile, Santiago, Chile; [6] Department of Informatics and Computing (Universidad Tecnológica Metropolitana, Santiago, Chile); [7] School of Electrical Engineering (Pontificia Universidad Católica de Chile, Valparaíso, Chile); [8] Department of Psychiatry (Pontificia Universidad Católica de Chile, Santiago, Chile); [9] School of Medicine (Universidad Finis Terrae, Santiago, Chile); [10] Pharmacovigilance (Instituto Psiquiátrico Dr. J. Horwitz Barak, Santiago, Chile); [11] Biomedical Engineering School (Universidad de Chile Valparaíso, Valparaíso, Chile); [12] Department of Electrical Engineering (Pontificia Universidad Católica de Chile, Santiago, Chile); [13] Department of Medical Imaging and Radiation Sciences (Monash University, Queensland, Australia)

Summary: The study investigates dopamine dysfunction in the brains of psychosis patients using Quantitative Susceptibility Mapping (QSM) MRI to measure iron levels, a co-factor in dopamine pathways. A machine learning approach, specifically a Random Forest model, was applied to distinguish between healthy individuals and First-Episode Psychosis (FEP) patients, as well as to predict their response to antipsychotic treatment. The SHAP framework was used for feature interpretation, and hierarchical clustering identified feature correlations. Our models could predict FEP patients and their response to antipsychotics with 76.48 ± 10.73% (four features selected) and 76.43 ± 12.57% (four) accuracy. Predicting treatment response will allow us to design alternative management for FEP patients resistant to standard treatments.

Introduction: Recent publications highlighted the changes in brain iron concentrations with a co-factor in dopamine pathways in psychosis patients[1]. Insights about the quantification of iron concentrations in the brain are available now by effective transverse relaxation rate (R2*) and quantitative susceptibility mapping (QSM), calculated from multi-echo gradient-echo (GRE) sequences[2]. As iron is the cofactor in neurotransmitter biosynthesis, the functions of the Grey Matter (GM) nuclei are susceptible to changes in iron concentration. Considering the limited number of dopamine pathways (nigrostriatal and tuberoinfundibular pathways) retrieved from the QSM image, it is possible to refine disease monitoring and improve patient risk stratification[3]. The present study aims to pinpoint potential predictive biomarkers derived from QSM and R2* for individuals experiencing first-episode-psychosis (FEP), along with their response to antipsychotic treatment.

Methods: 3D multi-echo GRE and T1-weight FLAIR of 52 healthy volunteers (HV) and 78 FEP patients (52 RS and 24 TRS) were acquired in a 3T Philips Ingenia MRI scanner. QSM reconstruction was performed as in[4] using Variable Sophisticated Harmonic Artifact Reduction for Phase data (vSHARP)[5] and FAst nonlinear Susceptibility Inversion (FANSI) toolbox[6]. Images were registered and normalized to an NMI space. Twenty-two regions of interest (ROI) of deep GM and subcortical brain nuclei were segmented using the Multicontrast PD25 version 2019[7]. We calculated the mean QSM and R2* values for each ROI. This study developed two machine learning models to analyze brain regions with QSM and R2* values, distinguishing between HV and FEP patients, as well as responders (RS) and treatment-resistant (TRS) patients. The models were built using Python and employed RF with Sequential Forward Selection (SFS) for feature selection, hyperparameter optimization through grid search, and 10-fold cross-validation[16]. SHAP values were used for model interpretation, revealing feature importance[8].

Results: The classification results for the HV vs. FEP classification, four features—right nucleus accumbens R2*, left amygdala R2*, left nucleus accumbens R2*, and right thalamus QSM—yielded an accuracy of 76.48 ± 10.73%. For RS vs. TRS, four features—right hippocampus R2*, left caudate R2*, left putamen R2*, and left amygdala QSM—achieved 76.43 ± 12.57% accuracy. After applying feature selection, treeSHAP analysis was conducted to identify the most important predictors in the model, shown in Figure 1. The SHAP summary plots showed that the key features for HV vs. FEP classification were right nucleus accumbens R2*, left amygdala R2*, left nucleus accumbens R2*, and right thalamus QSM. For RS vs. TRS, the important features were left amygdala QSM, right hippocampus R2*, left caudate R2*, and left putamen R2*. Both classifications use similar features, leading to confusion between classes. The SHAP values indicate the contribution of each feature to the model's predictions, with lower right nucleus accumbens R2* values

increasing the likelihood of being classified as FEP. At the same time, higher left amygdala R2* values favor HV classification. To improve differentiation, a unique feature dedicated to each class is needed. Figure 4 shows the hierarchical clustering analysis revealed that QSM and R2* features were divided into two distinct clusters for both HV vs. FEP and RS vs. TRS classifications. These clusters, which were combined at a high dendrogram distance, can be treated as separate analysis groups.
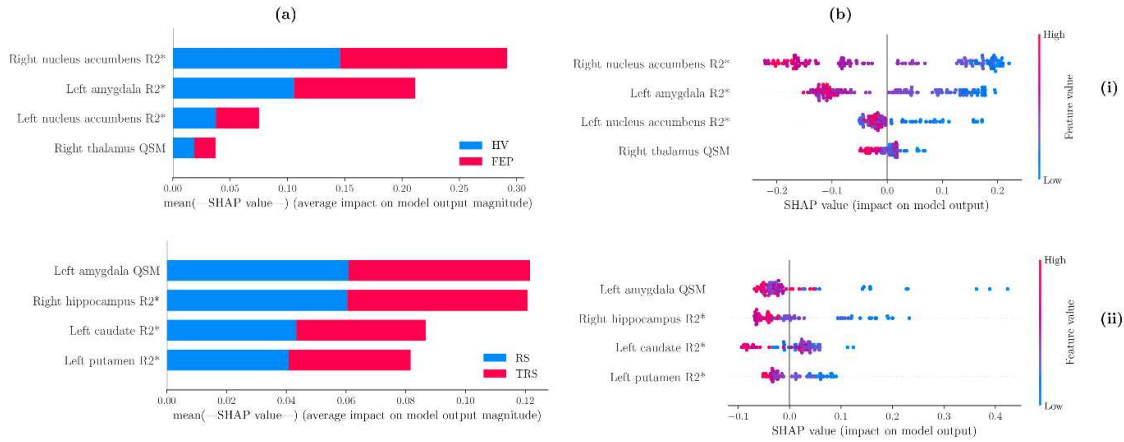
Figure 1. Feature the importance of our models based on SHAP values. (a) The mean absolute SHAP values are depicted to illustrate the importance of global features. (b) The local explanation summary shows the direction of the relationship between a variable and class study. (i) Positive SHAP values push the model to predict FEP patients, and negative values push the model to predict the HV. (ii) Positive SHAP values predict RS patients, and negative values predict TRS patients.

Discussion and Conclusions: This study focused on identifying the most relevant QSM and R2* features for predicting First-Episode Psychosis (FEP) and treatment response using Random Forest (RF) models. Two classification problems were addressed: HV vs. FEP and RS vs. TRS. Feature selection reduced the number of input variables while maintaining model performance, achieving accuracies of 76.48% for HV vs. FEP and 76.43% for RS vs. TRS. SHAP analysis was used for global and local interpretability, revealing the top predictive features, including the right nucleus accumbens R2* and left amygdala QSM. Hierarchical clustering identified two feature clusters, separating QSM and R2* data, confirming their correlation but also highlighting their distinct predictive powers. The study emphasized the complementary nature of QSM and R2* in understanding tissue magnetic properties, particularly regarding brain iron content linked to schizophrenia. Despite some limitations, such as small sample sizes and the use of classical ML algorithms, the study demonstrated the potential of these features for early detection of treatment-resistant schizophrenia, potentially improving clinical outcomes. Future research will explore advanced deep learning methods and larger datasets to further enhance classification performance.

References:

[1] McCutcheon, B. A., Abi-Dargham, A., Howes, O. D. (2019), Schizophrenia, Dopamine, and the Striatum: From Biology to Symptoms. Trends in Neurosciences, vol. 42, no. 3, pp. 205-220.
[2] Wang, Y., Liu, T. (2015), Quantitative Susceptibility Mapping (QSM): Decoding MRI Data for a Tissue Magnetic Biomarker. Magnetic Resonance in Medicine, vol. 73, no. 1, pp. 82-101.
[3] Xu, M., Guo, Y., Cheng, J., et al. (2021), Brain Iron Assessment in Patients with First-Episode Schizophrenia Using Quantita-tive Susceptibility Mapping. Neuroimage: Clinical, vol. 31, p. 102736.
[4] García, M., Muñoz, N., et al. (2019), Quantitative Susceptibility Mapping MRI Shows Changes in Dorsal Striatum in Patients with a First Episode of Psychosis Compared to Controls. ISMRM 27th Annual Meeting & Exhibition.
[5] Kan, H., Arai, N., Takizawa, M., et al. (2018), Background Field Removal Technique Based on Non-Regularized Variable Kernels Sophisticated Harmonic Artifact Reduction for Phase Data for Quantitative Susceptibility Mapping. Magnetic Reso-nance Imaging, vol. 52, pp. 94–101, doi: 10.1016/j.mri.2018.06.006.
[6] Milovic, C., Bilgic, B., Zhao, B., et al. (2018), Fast Nonlinear Susceptibility Inversion with Variational Regularization. Magnetic Resonance in Medicine, vol. 80, no. 2, pp. 814-821.
[7] Xiao, Y., Fonov, V., Bériault, S., et al. (2015), Multi-Contrast Unbiased MRI Atlas of a Parkinson's Disease Population. International Journal of Computer Assisted Radiology and Surgery, vol. 10, no. 3, pp. 329-341.
[8] Kroese, D. P. (2019), Data Science and Machine Learning: Mathematical and Statistical Methods. Chapman and Hall/CRC; 1st edition.

On the validity of the QSM-specific Structural Similarity Index Measure (XSIM) for abdominal QSM

Javier Silva[1,2], Cristián Tejos[1,2,3], Carlos Milovic[1,2]

[1]Department of Electrical Engineering, Pontificia Universidad Católica de Chile, Santiago, Chile; [2]Biomedical Imaging Center, Pontificia Universidad Católica de Chile, Santiago, Chile; [3]Millennium Institute for Intelligent Healthcare Engineering (iHEALTH), Santiago, Chile.

Summary: We extended the analysis of the XSIM metric for tissues with susceptibility values far from zero. Comparisons against RMSE and SSIM pointed out the robustness of this metric in the context of outside-the-brain applications.

Introduction: The Structural Similarity Index Measure (SSIM) [1] has been a popular metric for assessing the quality of QSM reconstructions. SSIM may help to achieve sharper reconstructions [2], but its limited range and unsigned formulation have raised concerns about its validity [3]. In this sense, the QSM-specific SSIM metric (XSIM) was proposed as a re-implementation of SSIM, designed to overcome the biasing and metric-hacking issues related to the signed nature and dynamic range of susceptibility values [4]. Despite having robust internal parameters and preventing bias and metric-hacking, the validity studies of XSIM have been focused on the context of brain QSM, where susceptibility values are still close to the zero-reference tissues. In this study, we extend the analysis of XSIM to an outside-the-brain scenario, with a higher dynamic range between the water and fatty tissue susceptibilities.

Methods: We used the in silico QSM abdominal phantom [5] as ground truth to compare the behavior of the RMSE, SSIM, and XSIM metrics, when each one of them are used as the parameter optimization criteria. We also compared the effects of SSIM and XSIM under an iron overload scenario, to analyze the paramagnetic error penalization and the zero-reference tissue effects in the parameter optimization process. QSM reconstructions were performed using the Fast Nonlinear Susceptibility Inversion with Variational Regularization (FANSI) [6] and Nonlinear Dipole Inversion (NDI) [7] algorithms.

Results: Figure 1 shows the resulting behavior of the nRMSE, SSIM, and XSIM metrics for a regularization weight tunning process with FANSI, using an iron overload simulation. Given the inverse nature of nRMSE (increasing values nRMSE values imply worse reconstructions), we employed the 1-nRMSE values for the plots. The plots showed a significant difference between SSIM and XSIM scores, with a stronger penalization in the latter ones, especially when the liver is used as the zero-reference. Qualitatively, XSIM showed a balance between the over-regularized nRMSE-based reconstructions and the large-scale errors caused by SSIM (Figure 1, left side of the liver reconstruction). Figure 2 shows a comparison between the nRMSE, SSIM, and XSIM metrics for NDI reconstruction of both healthy and iron overload simulations. SSIM results did not present a significant difference between the healthy and the iron overload cases, despite the significant increase in blurring and tissue attenuation in the iron overload reconstructions. In contrast, XSIM showed a clear penalization, which became more pronounced when using the liver as the zero-reference.

Discussion and Conclusions: Compared to RMSE and SSIM-based reconstructions, XSIM showed a better balance between high-frequency and low-frequency details. Additionally, XSIM presented a stronger penalization for paramagnetic errors, particularly when using hepatic tissue as zero-reference. These results validate the robustness of XSIM shown in previous studies, even having its internal parameters calibrated for brain QSM data. Considering these results, we strongly recommend using XSIM to assess QSM reconstructions in the presence of fat or other paramagnetic tissues (e.g., iron overload).
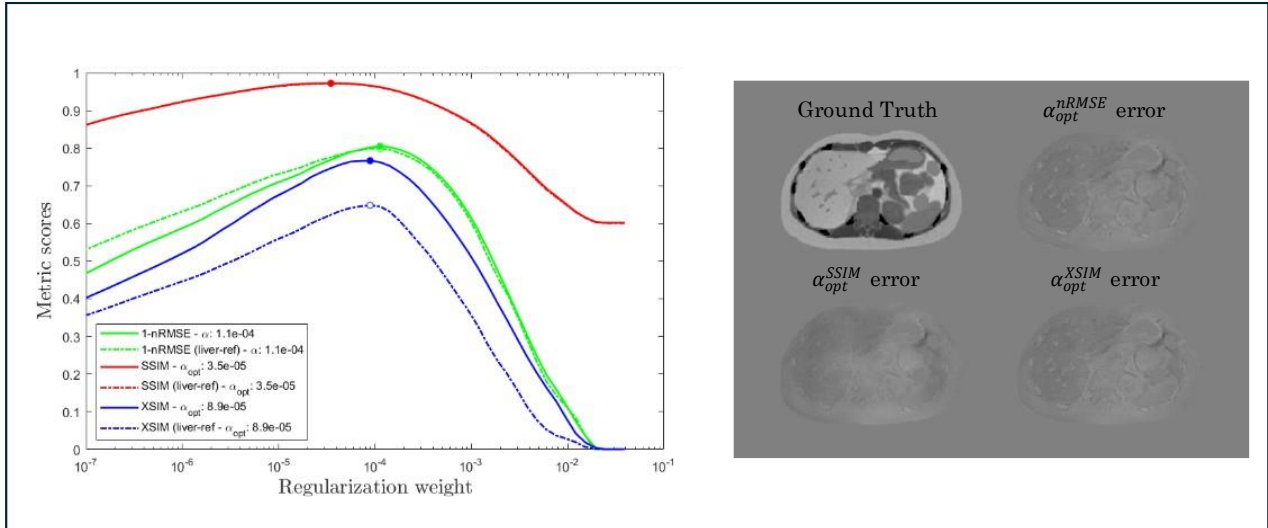
Figure 1. Left: Metric scores for the iron overload phantom reconstructions, using FANSI as the reconstruction method. Right: Ground truth and the corresponding difference images for the optimal values of α using each metric (mean ROI susceptibility as the zero reference).
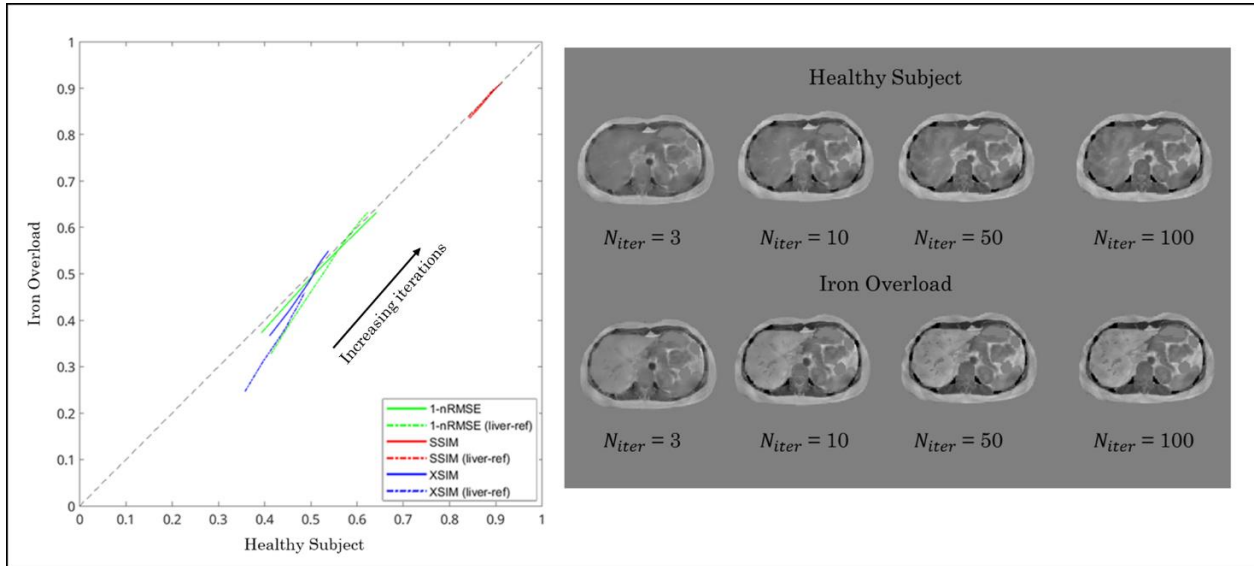
Figure 2. Left: NDI reconstruction metrics (1-nRMSE, SSIM, XSIM) for an increasing number of iterations (from 3 to 100), using the healthy and iron overload simulations of the abdominal QSM phantom. Right: QSM reconstructions of the healthy and iron overload simulations for a different number of NDI iterations (N_{iter}).

Acknowledgements

References:

[1] Wang Z, Bovik AC, Sheikh HR, Simoncelli EP. Image Quality Assessment: From Error Visibility to Structural Similarity. IEEE Trans Image Process. 2004;13(4):600-612. doi:10.1109/TIP.2003.819861

[2] Langkammer C, Schweser F, Shmueli K, Kames C, Li X, Guo L, Milovic C, Kim J, Wei H, Bredies K, Buch S, Guo Y, Liu Z, Meineke J, Rauscher A, Marques JP, Bilgic B; Quantitative Susceptibility Mapping: Report from the 2016 Reconstruction Challenge; Magnetic Resonance in Medicine, 2017 Jul 31. doi: 10.1002/mrm.26830

[3] Langkammer C, Schweser F, Shmueli K, et al. Quantitative susceptibility mapping: Report from the 2016 reconstruction challenge. Magn Reson Med. 2018;79(3):1661-1673. doi:10.1002/mrm.2683

[4] Milovic C, Tejos C, Silva J, Shmueli K, Irarrazaval P. XSIM: A structural similarity index measure optimized for MRI QSM. Magn Reson Med. 2024. doi: 10.1002/mrm.30271

[5] Silva J, Milovic C, Lambert M, et al. Toward a realistic in silico abdominal phantom for QSM. Magn Reson Med. 2023; 89: 2402-2418. doi:10.1002/mrm.29597.

[6] Milovic C, Bilgic B, Zhao B, Acosta-Cabronero J, Tejos C. Fast nonlinear susceptibility inversion with variational regularization. Magn Reson Med. 2018;80(2):814-821. doi:10.1002/mrm.27073

[7] Polak D, Chatnuntawech I, Yoon J, et al. Nonlinear dipole inversion (NDI) enables robust quantitative susceptibility mapping (QSM). NMR Biomed. 2020; 33:e4271.

UNITED IMAGING

uAIFI
AI FOR IMAGING

uMR®
Jupiter 5T

uMR

UNITED IMAGING

uMR 5T

uAIFI

uMR® 670[5]
uAIFI Wide-Bore 1.5T MR

uMR® 680[4]
uAIFI Wide-Bore 1.5T MR

UNITED IMAGING

Comprehensive Portfolio

Covering from clinical to pre-clinical, from middle field to ultra-high field

uPMR® 790
HD TOF PET/MR

uMR® Sagitta[2]
Summit-level whole-body 3T research MR

MAGNETIC RESONANCE

1 Not CE marked, not commercially available in the EU.

2 Not submitted to FDA or CE marked, not commercially available in the U.S. or EU.

3 Research only, not commercially available for clinical use in the US.

4 Detachable table is not CE marked, not commercially available in the EU.

5 Not submitted to FDA, not commercially available in the U.S.

uMR® Jupiter 5T[1]
World's First Whole-Body UHF 5T

uMR® NX Frontier[3]
Ultra-high-gradient Head-only MR

uMR® 9.4T[3]
Ultra-High Field Preclinical MR

uMR® Omega[4]
75cm Ultra-Wide-Bore 3T

uMR® 780
*Clinical 3T*

![RadioDynamic Medical logo]

ABOUT US

RadioDynamic Medical is an AI-driven medical imaging company dedicated to enhancing image quality and optimizing diagnoses through state-of-the-art deep learning and image reconstruction technologies. Our innovative products transform traditional, low-quality, high-radiation medical exams into more efficient, high-quality, and safer medical services. We have introduced the RaDyn reconstructuion and enhancement product line, which includes **RaDynMR, RaDynPET, RaDynSPECT, and RaDynCT,** covering a wide range of medical imaging modalities. Our core team is composed of experts from prestigious universities, including Stanford, UC Berkeley, Duke, Tsinghua and Peking University.

RaDynMR

A deep learning solution that enables MRI scan time reduction, enhancing patient comfort without sacrificing image quality. Leveraging massive amounts of high-quality clinical data and the latest deep learning techniques, **RaDynMR** extracts multi-scale features from MRI scans to reconstruct high-precision medical images. **RaDynMR** is compatible with any brand or model MRI scanner and field strength with no change in workflow.
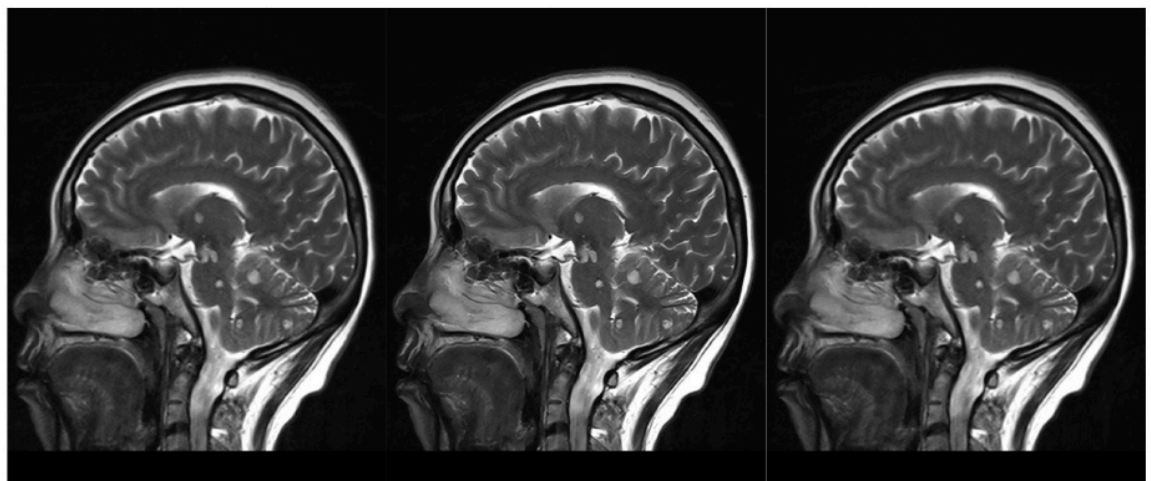

| Accelerated Scan | **Accelerated Scan + RaDynMR** | Conventional Scan |

RaDynCT

Offers both CT denoising and super-resolution capabilities. Utilizing deep learning algorithms, **RaDynCT** removes noise from low-dose CT scans or enhances standard CT images to ultra-high resolution, revealing clearer physiological details. This improvement in image quality directly contributes to higher diagnostic accuracy. **RaDynCT** is applicable across various stages of clinical imaging, including physical exams, disease diagnosis, treatment, and post-treatment follow-up.
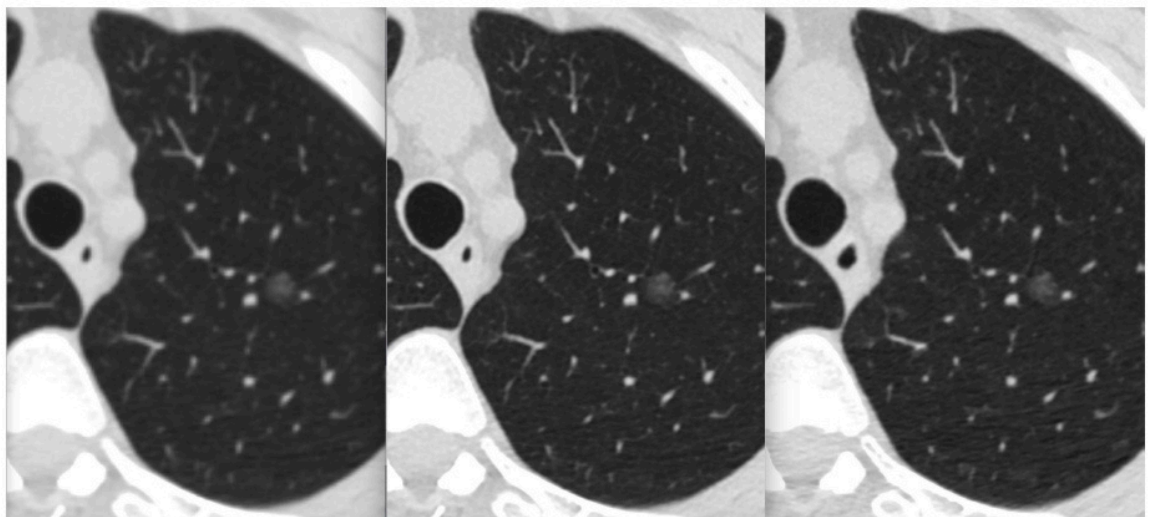
| Low Resolution CT | **Low Resolution CT + RaDynCT** | High Relolution CT |

![Radio Dynamic Medical logo]

RaDynSPECT

An AI-powered solution designed for fast or low-dose SPECT examinations. By utilizing advanced deep learning algorithms, it enhances the resolution and signal-to-noise ratio (SNR) of standard SPECT bone scan images. This technology significantly improves scanning speed, reduces radiation exposure, and enhances image quality. **RaDynSPECT** enables ultra-fast SPECT/CT imaging, reducing acquisition time to 1/7 of the standard while maintaining comparable image quality and diagnostic value through deep learning enhancement.

5min/bed | **5min/bed+RaDynSPECT** | 20min/bed

RaDynPET

Enhances the image quality and reduces the noise of accelerated positron emission tomography (PET) images. The product effectively works on PET scanners that operate at 2-4 times the standard speed, shortening patient examination times. **RaDynPET** also optimizes low-quality images produced by reduced tracer amounts, ensuring that the resulting high-quality images meet clinical diagnostic standards while minimizing radiation risk.

Lowdose | **Lowdose+RaDynPET** | Standard